

FINAL REPORT
U.S. Department of Energy

**LONG-TERM COLLOID MOBILIZATION AND
COLLOID-FACILITATED TRANSPORT OF
RADIONUCLIDES IN A SEMI-ARID VADOSE ZONE**

Principal Investigator:

Markus Flury
Department of Crop and Soil Sciences
Washington State University

Collaborators:

James B. Harsh
Department of Crop and Soil Sciences
Washington State University

Fred Zhang
Pacific Northwest National Laboratory

Glendon W. Gee
Pacific Northwest National Laboratory

Earl D. Mattson
Geocentrifuge Laboratory
Idaho National Laboratory

Peter C. Lichtner
Geoanalysis—Earth and Environmental Sciences
Los Alamos National Laboratory

Grant Number:
DE-FG02-08ER64660

Project Duration:
September 1, 2008 to August 31, 2011
(no-cost extension until August 31, 2012)

Contents

1	Executive Summary	4
2	Comparison of Actual Accomplishments with Goals and Objectives of the Project	7
3	Summary of Project Activities	11
3.1	Motivation	11
3.2	Research Objectives	11
3.3	Overall Research Design	12
3.4	Mechanistic Investigations on Colloid Transport in Unsaturated Porous Media	12
3.4.1	Colloid Interactions with Air-Water Interface	12
3.4.1.1	Motivation	12
3.4.1.2	Materials and Methods	12
3.4.1.3	Principal Results	14
3.4.2	Capillary Forces between Particles and the Air-Water Interface	16
3.4.2.1	Motivation	16
3.4.2.2	Materials and Methods	16
3.4.2.3	Principal Results	20
3.4.3	Interaction between Hanford Colloid and Humic Acids	21
3.4.3.1	Materials and Methods	21
3.4.3.2	Principal Results	21
3.5	Column-Scale Investigations on Transport in Unsaturated Hanford Sediments and Porous Media	22
3.5.1	Using a Geocentrifuge to Elucidate Effects of Flow Rates and Water Content on Colloid Transport and Mobilization	22
3.5.1.1	Motivation	22
3.5.1.2	Materials and Methods	22
3.5.1.3	Principal Results	25
3.5.2	Colloid Mobilization in an Undisturbed Sediment Core under Semi-Arid Recharge Rates	28
3.5.2.1	Motivation	28
3.5.2.2	Materials and Methods	29
3.5.2.3	Principal Results	30
3.6	Field-Scale Eu Colloid Transport at the Semi-Arid Hanford Site	32
3.6.1	Transport of Europium Colloids in Vadose Zone Lysimeters	32
3.6.1.1	Motivation	32

3.6.1.2	Materials and Methods	32
3.6.1.3	Principal Results	36
3.6.2	Field-Scale Conceptual and Numerical Model for Colloid Mobilization and Transport	37
3.6.2.1	Motivation	37
3.6.2.2	Materials and Methods	40
3.6.2.3	Principal Results	43
4	Products Developed	45
4.1	Publications Published in Peer-Reviewed Journals (in inverse chronological order)	45
4.2	Unpublished Reports and Publications in Submission or Preparation	45
4.3	Presentations	46
4.4	Web Sites	47
	Appendix: Reprints of Publications	48

1 Executive Summary

The main purpose of this project was to improve the fundamental mechanistic understanding and quantification of long-term colloid mobilization and colloid-facilitated transport of radionuclides in the vadose zone, with special emphasis on the semi-arid Hanford site. While we focused some of the experiments on hydrogeological and geochemical conditions of the Hanford site, many of our results apply to colloid and colloid-facilitated transport in general. Specific objectives were (1) to determine the mechanisms of colloid mobilization and colloid-facilitated radionuclide transport in undisturbed Hanford sediments under unsaturated flow, (2) to quantify in situ colloid mobilization and colloid-facilitated radionuclide transport from Hanford sediments under field conditions, and (3) to develop a field-scale conceptual and numerical model for colloid mobilization and transport at the Hanford vadose zone, and use that model to predict long-term colloid and colloid-facilitated radionuclide transport.

To achieve these goals and objectives, we have used a combination of experimental, theoretical, and numerical methods at different spatial scales, ranging from microscopic investigations of single particle attachment and detachment to larger-scale field experiments using outdoor lysimeters at the Hanford site. Microscopic and single particle investigations provided fundamental insight into mechanisms of colloid interactions with the air-water interface. We could show that a moving air-water interface (such as a moving water front during infiltration and drainage) is very effective in removing and mobilizing particles from a stationary surface. We further demonstrated that it is particularly the advancing air-water interface which is mainly responsible for colloid mobilization. Forces acting on the colloids calculated from theory corroborated our experimental results, and confirm that the detachment forces (surface tension forces) during the advancing air-water interface movement were

stronger than during the receding movement. Theory indicates that, for hydrophilic colloids, the advancing interface movement generally exerts a stronger detachment force than the receding, except when the hysteresis of the colloid-air-water contact angle is small.

We quantified the interaction forces (capillary forces) between colloids and the air-water interface by using force tensiometry. These measurements showed that capillary forces easily can exceed the attractive forces between colloids and the liquid-solid interface. Natural subsurface particles from the Hanford vadose zone were used for these measurements. Surface coatings and wetting conditions affect the magnitude of the capillary forces, but the most important parameter affecting the capillary force is the surface roughness and shape of the colloids. Irregularly-shaped particles with sharp edges showed the largest capillary forces, because the air-water interface gets pinned at edges. The implication of this phenomenon is that subsurface particles, which often contain edges and are irregularly shaped, are more readily mobilized than spherical model particles. This further emphasizes the important role of capillary forces in fate and transport of colloids in the vadose zone.

Field experiment using a vadose zone lysimeter facility at the Hanford site showed that surface-applied Eu colloids can be translocated rapidly under natural precipitation as well as artificial irrigation. Small amounts of applied colloids were translocated from the surface to a depth of two meters within two months and only 20 mm of cumulative infiltration. Large water infiltration events, mimicking snow melt, enhanced movement of Eu colloids. Nonetheless the majority of Eu colloids remained in the top 30 cm of the soil after 3.5 years of monitoring. These results suggest that colloid and radionuclide transport can occur in the near-surface vadose zone at Hanford under field conditions, but that the magnitude of the transport is less than what has been reported from laboratory studies.

Water flow rates in deep vadose zone sediments at Hanford vary from 0 to 100 mm/year.

We studied colloid mobilization from undisturbed sediment cores under a flow rate of 18 mm/year, a typical low flow rate at Hanford. Under this low flow rate, we observed continuous colloid mobilization from the sediments, although the total amounts of colloids mobilized are small, only 0.5% of available colloids were mobilized during 5 years of observations. These results demonstrate that colloidal particles are mobile even under the low recharge rates found in a semi-arid site like Hanford.

Under higher flow rates, we would expect colloid transport to be even more pronounced. Higher flow rates occur locally at Hanford when flow is channeled because of subsurface layerings or subsurface structures, like the high level waste storage tanks. In such cases, the local recharge due to this “subsurface funnel flow” is much greater than 100mm/yr.

These results of our study are particularly relevant for colloid mobilization and transport related to three process in the vadose zone at Hanford: (1) water infiltration into sediments during rainfall or snowmelt events, (2) groundwater fluctuations as caused by river stage fluctuations, and (3) steady-state, low-flow recharge in deep vadose zone sediments. Transient water flow, like during infiltration or groundwater level fluctuations, are most conducive for colloid mobilization, but even during steady-state, low-flow recharge, colloids can be mobile, although to a much lesser extent. The results of this project have led to a comprehensive and fundamental understanding of colloid transport and mobilization under unsaturated flow conditions at the Hanford site.

2 Comparison of Actual Accomplishments with Goals and Objectives of the Project

Objective 1: Determine the mechanisms of colloid mobilization and colloid-facilitated radionuclide transport in undisturbed Hanford sediments under unsaturated flow

Mechanistic investigations of colloid mobilization and transport were conducted at different spatial scales, both experimentally as well as theoretically.

Systematic studies using confocal microscopy were conducted to determine how effective moving air-water interfaces are in mobilizing colloids from stationary surfaces. Investigations using a single cylindrical flow channel showed that the advancing air-water interface was significantly more effective in detaching colloids from the glass surface than the receding interface. Most of the colloids were detached during the first passage of the advancing air-water interface, while the subsequent interface passages did not remove significant amounts of colloids. Forces acting on the colloids calculated from theory corroborate our experimental results, and confirm that the detachment forces (surface tension forces) during the advancing air-water interface movement were stronger than during the receding movement. Theory indicates that, for hydrophilic colloids, the advancing interface movement generally exerts a stronger detachment force than the receding, except when the hysteresis of the colloid-air-water contact angle is small and that of the channel-air-water contact angle is large. The experiments and theoretical calculations also showed that there is a critical velocity of the air-water interface beyond which no colloids are removed anymore. This velocity is related to the expansion of the water film forming at the solid surface as water and air move through a capillary channel.

Colloids were modified to test the hypothesis that colloid shape has a dominant effect on colloid detachment. To make sure the differently shaped colloids had all the same surface properties, we modified spherical microspheres to form rods, barrels, ellipsoids, and disks. Barrels, which had an edge where the air-water interface was pinned, were removed the most by the moving air-water interface. The pinning of the air-water interface proved to be the most important factor leading to increased colloid removal and mobilization.

Force tensiometry was used to quantify capillary forces as a function of position of the air-water interface on model and natural particles. We have shown that capillary forces exerted at the air-water interface can exceed DLVO and gravity forces, and that moving air-water interfaces during infiltration can mobilize, i.e., detach, soil particles from stationary surfaces. In porous media, while under dry conditions, the capillary force is a strong attachment force of particles to stationary surfaces, under wet conditions, the capillary force becomes a mechanism of detachment of particles from stationary surfaces. Such wet conditions occur during infiltration or drainage. We quantified such detaching capillary forces for differently shaped particles and found that measured capillary forces on natural particles can be approximated by a volume-equivalent ellipsoid. Thus, assuming

an ellipsoidal shape allows us to better predict capillary forces experienced by natural particles in porous media. Capillary forces become more important the smaller the particles are, because the gravity force decreases faster with particle size than the capillary force, and the capillary pressure scales inversely with the particle radius. Thus, particularly for particles in the colloidal size range, the capillary forces will play a dominant role.

Theory was developed to calculate the capillary forces based on particle shape. For non-symmetrical particles, the calculation of the capillary force requires consideration of undulating interface lines, making the theory complex and involved. The theory allows to approximate natural subsurface particles as volume-equivalent ellipsoids.

Objective 2: Quantify in situ colloid mobilization and colloid-facilitated radionuclide transport from Hanford sediments under field conditions

A field experiment was conducted to quantify transport of an intrinsic radionuclide colloid at the Hanford site. As a surrogate for intrinsic Am and Eu colloids, we used non-radioactive Eu-hydroxy-carbonate colloids, $\text{Eu}(\text{OH})(\text{CO}_3)$. The colloids were applied to the surface of field lysimeters and migration of the colloids through the sediments was monitored using wick samplers. The lysimeters were exposed to natural precipitation or artificial irrigation. Wick outflow was analyzed for Eu concentrations and particle counts, supplemented by electron microscopy and energy-dispersive x-ray analysis on selected samples. Small amounts of Eu colloids were detected in the deepest wick sampler (2.14 m depth) 2.5 months after application and cumulative precipitation of only 20 mm. We observed rapid transport of Eu colloids under both natural precipitation and artificial irrigation, i.e., the leading edge of the Eu colloids moved at a velocity of 3 cm/day within the first two months after application. Large water infiltration, mimicking Chinook snowmelt events in late winter/early spring, caused peaks of Eu in the wick outflow. Elevated Eu concentrations were detected in 1.22 and 2.14 m depth 2.5 years after application, which is consistent with long-term recharge estimates at the site. However the main mass of Eu remained in the top 30 cm of the soil. The observed rapid movement of Eu in the homogeneous Hanford Lysimeters was caused by transient water flow near the soil surface. Based on mechanistic laboratory studies, it is likely that the Eu colloids were mobilized and translocated by moving air-water interfaces. The main peak of Eu, however, moved at slower rate, consistent with long-term recharge.

To investigate whether the in situ natural colloids can be mobilized and transported in undisturbed, deep vadose zone sediments at the Hanford site under typical, semi-arid recharge rates, we used an undisturbed sediment core. We sampled an undisturbed sediment core (50 cm i.d., 59.5 cm height) from a depth of 17 m at the Hanford 200 Area. The core was setup as a laboratory lysimeter and exposed to a low infiltration rate of 18 mm/year by applying simulated pore water onto the surface. Particle concentrations were quantified in the column outflow, and selected samples were examined microscopically and for elemental composition (TEM and EDX). Measured water contents and potentials

were used to calibrate a numerical model (Hydrus-1D), which was then applied to simulate colloid mobilization from the sediment core. The results showed that during 5.3 years of monitoring, natural colloids like silicates, aluminosilicates, and Fe-oxides were observed in the core outflows indicating the continuous mobilization of in situ colloids. The total amount of particles mobilized within 5.3 years corresponded to 0.5% of the total dispersible colloids inside the core. The fitted release rate coefficient was six to seven orders of magnitude smaller than coefficients reported from previous studies, where disturbed Hanford sediments and higher flow rates were used. Our findings demonstrate that even under low recharge rates and water contents typical for semi-arid, deep vadose zone sediments, particles can continuously be mobilized, although the total mass of particles is low.

Objective 3: Develop a field-scale conceptual and numerical model for colloid mobilization and transport at the Hanford vadose zone, and use that model to predict long-term colloid and colloid-facilitated radionuclide transport

Colloid and colloid-facilitated contaminant transport mechanisms have been incorporated into the multiphase flow and transport model PFLOTRAN. Our results demonstrate that under field conditions with transient flow, colloid mobilization and transport occurs in Hanford sediments. Small amounts of Eu colloids could be translocated by natural precipitation or irrigation to a depth of 2.14 m within 2.5 months, corresponding to an overall colloid transport velocity of 3 cm/d. Estimates of recharge at the Hanford site range from 1 to 100 mm/year. Considering a volumetric water content of $0.1 \text{ m}^3/\text{m}^3$, the recharge estimates translate to a pore water velocity of 1 to 100 cm/year (equal to 0.003 to 0.3 cm/d), which is considerably slower than what we observed based on the fast Eu transport. This indicates that the near surface transport of a portion of Eu can be rapid, exceeding recharged-based velocity estimates by more than a factor of ten. While a small portion of Eu colloids moved rapidly by preferential flow, the main peak of Eu, however, moved at slower rate, consistent with long-term recharge.

While semi-arid conditions in general are not conducive for colloid transport, the dry summer and wet winter climate at the Hanford site leads to infiltration fronts that penetrate the soil to several meters. These infiltration fronts with their associated moving air-water interfaces provide a means for mobilization and transport of colloids in the near-surface vadose zone.

In the deep vadose zone, we had the premise that particle mobilization is hindered under the low water contents and low steady-state flow rates. However, we did observe continuous particle release. Our study showed that in situ colloid mobilization occurred at a steady-state flow rate of 0.05 mm/d (= 18 mm/y) in an undisturbed sediment core. Although release rate and mass recovery of particles were much lower than reported from previous studies where colloid mobilization from disturbed, sediment columns was reported, we did observe a continuous flux of particles leaving the sediment core.

Our results show that in semi-arid regions, the thick vadose zone with its low water content and flow rates does not necessarily constitute a perfect filter for particle transport. Even under low, steady-state flow rates, particles were mobilized. The continuous particle mobilization observed here may be a possible pathway for colloid-facilitated contaminant transport at the US DOE Hanford site.

3 Summary of Project Activities

This section provides a summary of the experimental methods and results of the project. A detailed account of these activities is given in the attached technical manuscripts in the Appendix.

3.1 Motivation

Radioactive wastes stores at Hanford and other nuclear facilities pose a threat to the environment when waste are accidentally released. Knowledge of fate and transport of waste constituents is a requirement for effective clean-up and long-term management of contaminated sites. While some contaminants, like Cs, Am, Pu, sorb strongly to soil and sediment surfaces and are therefore expected to be retained near the location of their release, it has been shown that colloidal particles can facilitate the movement of these contaminants if the contaminants either associate with the colloids or form colloids themselves. Research from laboratory experiments has shown that colloids can be mobilized from soils and sediments under unsaturated and transient flow. How far-reaching and effective this process is for radionuclide migration in the *vadose zone* at Hanford, however, is not known. In this project we addressed the following major question: How effective are colloids in enhancing the mobility of radionuclides in the Hanford vadose zone, and what is the *long-term* magnitude of this transport process?

3.2 Research Objectives

The general goal of this project was to improve the fundamental mechanistic understanding and quantification of long-term colloid mobilization and colloid-facilitated transport of radionuclides in the vadose zone, with special emphasis on the semi-arid Hanford site. The specific objectives were to:

1. Determine the **mechanisms** of colloid mobilization and colloid-facilitated radionuclide transport in undisturbed Hanford sediments under unsaturated flow.
2. Quantify *in situ* colloid mobilization and colloid-facilitated radionuclide transport from Hanford sediments under **field conditions**.
3. Develop a field-scale conceptual and numerical model for colloid mobilization and transport at the Hanford vadose zone, and use that model to predict **long-term** colloid and colloid-facilitated radionuclide transport.

3.3 Overall Research Design

The objectives of this study were accomplished through a combination of experimental, theoretical, and numerical investigations at different spatial and temporal scales. Spatial scales ranged from microscopic scale, single particle scale, column scale, to the field scale. At the microscale and single particle scale, we used microscopic and tensiometric techniques to elucidate fundamental mechanistic interactions of colloids with the air-water interface. At the column scale, we used (1) a geocentrifuge to separate effects of flow rates and water contents on colloid mobilization, and (2) an undisturbed sediment core to quantify long-term colloid mobilization under flow rates typical for the low recharge in the deep Hanford vadose zone. At the field scale, we studied Eu-colloid transport in several lysimeters located at the Hanford site under natural and artificial precipitation. Theoretical and numerical models were used to analyze and generalize the experimental data.

3.4 Mechanistic Investigations on Colloid Transport in Unsaturated Porous Media

3.4.1 Colloid Interactions with Air-Water Interface

(References: Aramrak et al., 2011; Aramrak et al., 2012)

3.4.1.1 Motivation Previous experiments have shown that when water infiltrates or drains from soil or sediment, colloidal particles tend to be mobilized and leached as the infiltration or drainage fronts moves through the medium. We hypothesized that it is the interaction of the colloids with the moving air-water interface that is responsible for the colloid mobilization.

3.4.1.2 Materials and Methods To determine how effective moving air-water interfaces are in detaching colloids from surfaces, we deposited fluorescent, negatively-charged, carboxylate-modified polystyrene colloids (diameter of 1 μm) into a cylindrical glass channel. Hydrophilic carboxylate-modified microspheres (FluoSpheres, Lot Number 28120W, Molecular Probes Inc., Eugene, OR) were selected as the colloid models. The microspheres had a specific density of 1.055 g/cm³ and surface charge of 0.0175 mol_c/g (Molecular Probes Inc., Eugene, OR). The colloids were hydrophilic with an advancing air-water contact angle of 60 degrees and a receding contact angle of 40 degrees. After colloid deposition, two air bubbles were sequentially introduced into the glass channel and passed through the channel at different velocities (0.5, 7.7, 72, 982, and 10,800 cm/h). The passage of the bubbles represented a sequence of receding and advancing air-water interfaces (Figure 1). Colloids remaining in the glass channel after each interface passage were visualized with confocal microscopy and quantified by image analysis (Figure 2). To check whether the colloids removed by the moving air-water interfaces were initially deposited in the secondary

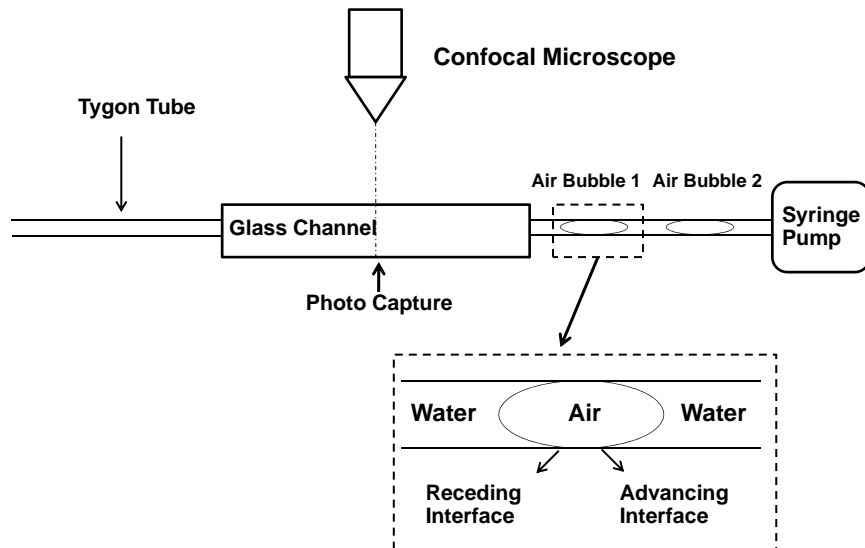


Figure 1. Schematic of experimental setup for air-water interface displacement.

energy minimum (i.e., unfavorable condition) or primary energy minimum, we conducted another set of experiments by changing the solution chemistry. We calculated an appropriate solution chemistry using DLVO theory to determine a solution that will cause the secondary minimum to disappear. We calculated an appropriate solution chemistry using DLVO theory to determine a solution that will cause the secondary minimum to disappear. We deposited the colloids into the channel as described above and then changed the solution chemistry to 0.1 mM CaCl_2 and pH 4.7. Visualization and quantification of colloids deposited on the glass channel was done before and after changing the solution chemistry at all the specific velocities indicated above.

To determine the effect of particle shape on colloid removal, we modified polystyrene colloids to form rods, elliptical disks, and barrels, plate-like, and edge-shaped natural particles. The different shapes were made by encasing microspheres into a film of polyvinyl alcohol (PVA), liquifying the microspheres with either hot oil or toluene, and stretching this film to different aspect ratios using a material tension tester.

Theoretical calculations were performed to determine the expected detachment forces as well as the thickness of the water film as a function of flow velocity. Calculations showed a strong dependence of the detachment forces as a function of contact angle. Calculated shear forces were found to be insignificant compared to detachment forces. We also calculated

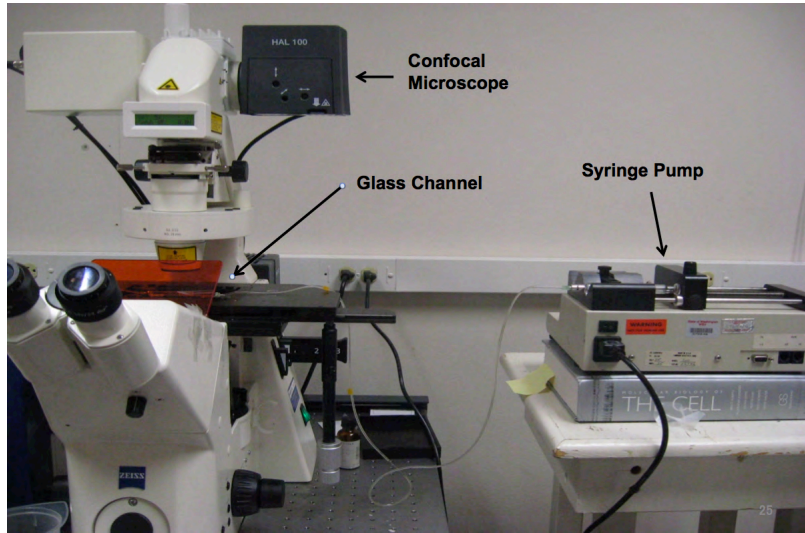


Figure 2. Experimental setup to quantify colloid detachment by moving-air-water interfaces.

contact and induction times during colloid and air-water-interface interactions, i.e., the time it takes for the air-water interface to form a colloid-water-air interface line with a colloid when the air-water interfaces approaches the colloid.

3.4.1.3 Principal Results A typical sequence of confocal images showing colloid deposition and detachment after receding and advancing air-water interface movements is shown in Figure 3. The initial spatial distribution of the colloids on the glass surface represents our reference from which we calculated colloid detachment. After passage of the receding air-water interface, more colloids are visible upstream of the interface, and we consider these colloids being attached the thinning air-water interface trailing the interface front. We could identify the interface location optically because the colloids viewed through water and air phases had different brightness in the confocal microscope. After passage of the advancing air-water interface, only a small fraction of colloids were removed. The following advancing air-water interface showed a pronounced accumulation of colloids at the interface, and after passage of the interface, a large fraction of colloids were removed from the glass surface.

Table 1 shows the quantitative amounts of colloids detached after passage of the air-water interfaces as a function of interface velocity. The hydrodynamic force caused by the flow itself was not able to remove colloids from the glass surface at any velocity, as no colloids were removed during flow in absence of an air bubble, and the surface tension force indeed was the dominant force causing colloid detachment. Colloid detachment was most pronounced at low flow velocities (1, 10, and 100 cm/h). The majority of the colloids

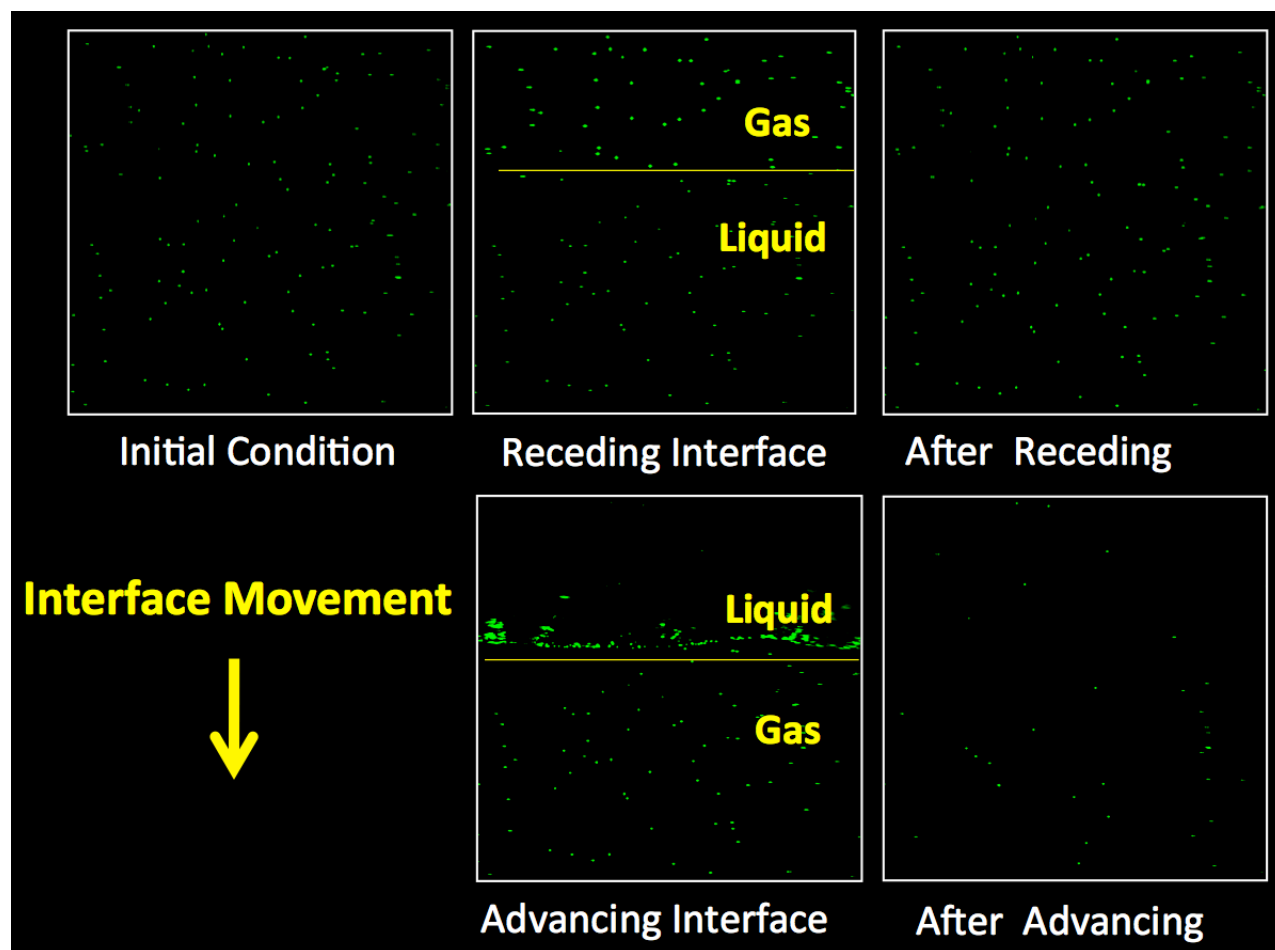


Figure 3. Sequence of confocal images showing colloids deposited on a glass channel before, during, and after air-water interface movements.

Table 1. Colloid detachment (%) from a glass surface after the passages of air-water interfaces.

	Colloid detachment (%) at different velocities				
	1 (0.5)*	10 (7.7)	100 (72)	1000 (982)	10000 (10,800)
	(cm/h)				
Initial state	0 Aa	0 Aa	0 Aa	0 Aa	0 Ab
Flow (no bubble)	0Aa	0.01 ± 0.01 Aa	0.01 ± 0.01 Aa	0.02 ± 0.02 Aa	0.02 ± 0.03 Ab
After receding-1	5 ± 6 Aa	5 ± 5 Aa	9 ± 6 Aa	2 ± 4 Aa	0.4 ± 0.7 Ab
After advancing-1	88 ± 10 Ba	85 ± 10 Ba	80 ± 6 Ba	72 ± 28 Ba	1 ± 2 Bb
After receding-2	0 Aa	0 Aa	0.2 ± 0.5 Aa	1 ± 2 Aa	0.1 ± 0.3 Ab
After advancing-2	3 ± 5 Aa	2 ± 4 Aa	2 ± 2 Aa	12 ± 21 Aa	0.1 ± 0.3 Ab

* Numbers in parentheses are measured velocities. Data represent means and standard deviations measured from 12 replications. Different capital letters (A, B, and C) indicate statistical differences column-wise; and different lower cases (a, b, and c) indicate statistical differences row-wise; both at $\alpha = 0.01$.

were removed by the first advancing interface (advancing-1), and no significant difference in colloid detachment was observed among the three lowest velocities of 1, 10, and 100 cm/h. Indeed for all interface passages, the amounts of colloids detached were not a function of interface velocities in the range of 1 to 100 cm/h; however, for faster velocities (1,000 and 10,000 cm/h), colloid detachment drastically decreased.

Shape-modified colloids showed a preference for removal of colloids with edges (barrels and disks) (Figure 4). The advancing air-water interface was much more effective in removing colloids than the receding interface. Interestingly, even the receding interface could not remove colloids, no matter what shape the colloids had.

3.4.2 Capillary Forces between Particles and the Air-Water Interface

(References: Chatterjee et al., 2012)

3.4.2.1 Motivation In these experiments, we quantified the capillary forces (surface tension forces) acting on natural subsurface particles. No experimental and theoretical quantification of the capillary forces for natural particles have been reported to date, and our data show that the capillary force is a dominant force. We generalize the results by also using a series of standard shaped model particles.

3.4.2.2 Materials and Methods The particles were collected from 20 m depth from a trench face at the Hanford Environmental Restoration Disposal Facility, located 13 km

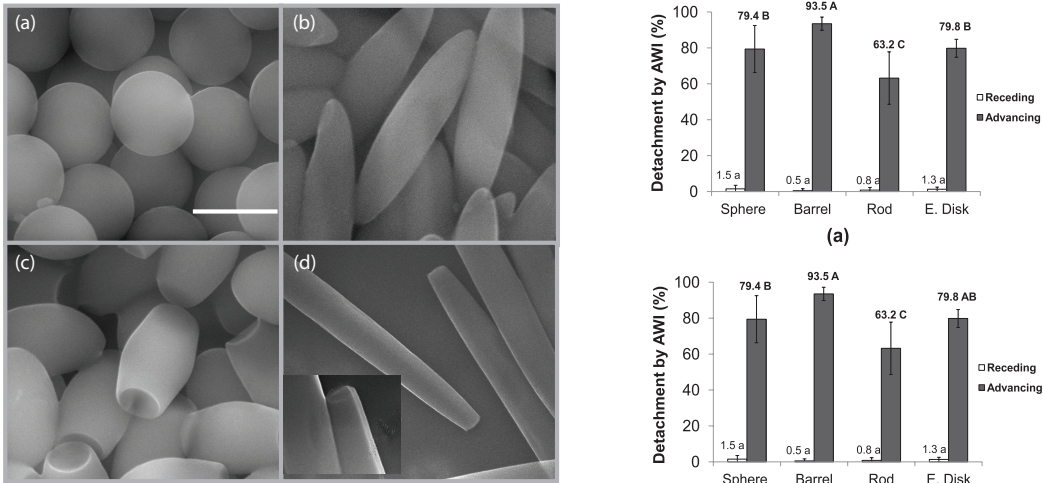


Figure 4. SEM images of four selected shapes of colloids: (a) sphere, (b) rod, (c) barrel, and (d) elliptical disk. (Scale bars: 1 μm) (left) and percentage detachment of deposited colloids as function of shapes by AWI: Different letter indicating statistical difference determined by (a) LSD and (b) Tukey’s at the 95% confidence level (right).

away from the Columbia River between the 200E and 200W areas of the Hanford Reservation. We selected particles with typical mineralogy for the Hanford sediments: basalt, granite, hematite, magnetite, mica, milky quartz, and clear quartz. Standard-shaped model particles were used to delineate the dependency of the measured forces on particle shape. Particles were characterized for air-water contact angles, shape, and surface roughness. The particle outlines in the xy - and xz -planes were determined by scanning electron microscopy and used to quantify the dimensions along the three coordinate axes. The capillary forces between the particles and the air-water interface were measured with a tensiometer (Figure 5). We determined the forces as a function of position of the air-water interface at the particle. Force measurements were made for “as is” particles, i.e., as collected from the field, as well as for particles washed and treated to remove soluble organic surface coatings.

Theory was developed to calculate capillary forces for non-spherical, irregularly-shaped particles. The theory available for spherical particles was expanded to ellipsoidal particles and is based on a force balance approach:

$$f = f_{\text{DLVO}} + f_w + f_s + f_b + f_p \quad (1)$$

where the terms are the DLVO force (f_{DLVO}), the gravity force (f_w), the surface tension force (f_s), the buoyancy force (f_b), and the hydrostatic pressure force (f_p). If the particle is

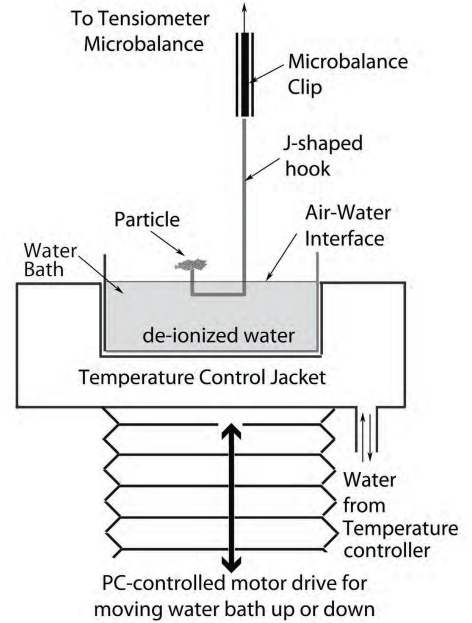


Figure 5. Process tensiometer and schematic of capillary force measurements for natural subsurface particles.

symmetric, the force balance f is parallel to the z -direction (Figure 6a), but if the particle is asymmetric, the directions of f_s and f_p forces are determined by the contact angle of the air-water interface at the particle surface. Further, for asymmetric particles, the interface line is undulating in quadrupolar fashion. If $f < 0$ the particle will be detached from the solid surface, if $f > 0$ the particle will remain pinned to the solid surface.

We further developed the theory for a spherical particle to a triaxial ellipsoid. Theoretical calculations of capillary forces on ellipsoidal particles showed that the contact line is of an undulating, elliptic shape rather than a flat ellipse. The force balance on an ellipsoidal particle is then given as:

$$f = 4a\kappa E(e_{xy})\gamma \cos \beta \sin \phi_c + \pi ab\Delta\rho g z_c \cos^2 \beta - \frac{\pi}{3}\Delta\rho g abc(2 + 3 \sin \beta - \sin^3 \beta) \quad (2)$$

where a , b , and c are the semi-principal axes of the ellipsoid along the three coordinate axes x , y , and z , respectively, κ is the ratio representing increase in contact line due to undulation, $E(e_{xy})$ is the complete elliptic integral of the second kind with eccentricity e_{xy} , β is the parametric latitude, γ is the surface tension of water, ϕ_c is the angle of inclination of the undistorted air-water interface at the three-phase contact line, $\Delta\rho = (\rho_l - \rho_g)$ is the difference between the two fluid densities ρ_l (water) and ρ_g (air), g is the acceleration due to gravity, and z_c is the deflection depth (position of the average contact line on the z -axis).

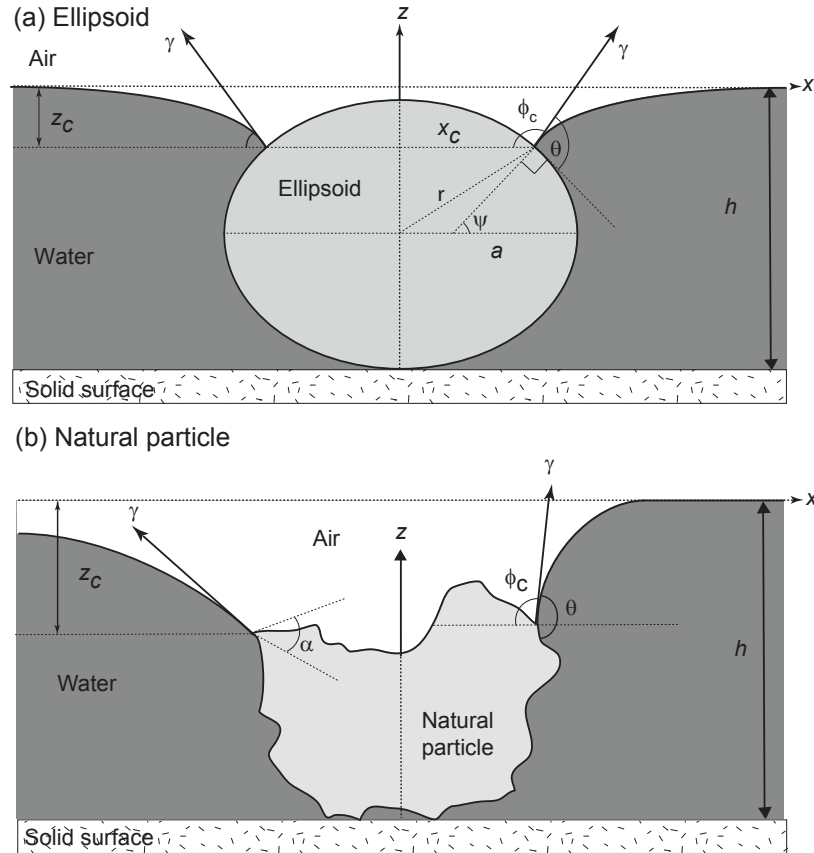


Figure 6. Forces acting (a) on a smooth, ellipsoidal particle with semi-principal radii a , b , c , and (b) on an asymmetric, rough particle in contact with an air-water interface, where $\psi = (\frac{3\pi}{2} - \theta - \phi_c)$ and α is the wedge angle for a sharp point on a surface where pinning occurs.

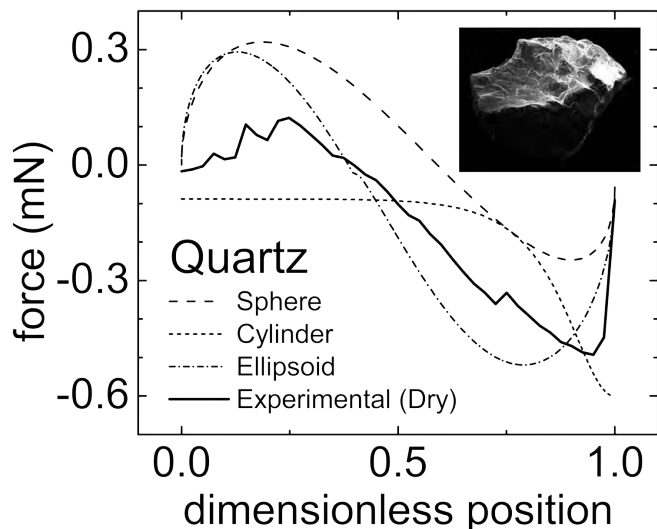


Figure 7. Force-position curves of sphere, circular cylinder, and ellipsoid (theoretical) and a dry, uncleaned quartz particle (experimental) during immersion.

3.4.2.3 Principal Results Figure 7 shows the dimensionless force-position curves for the dry PTFE particles of standard shapes and for the quartz particle. We use quartz as example here to illustrate the behavior of a natural sediment particle. The shape of the curves for the standard particles are related to their geometries. The curves for the PTFE sphere and disk are symmetrical with the immersion and emersion curves almost exact mirror images. Both particles show a large snap-off force, with the disc showing the most pronounced snap-off effect due to interface pinning. The tent and the quartz particle also show snap-off force, due to interface pinning. However, during emersion, there was no snap-in for both the tent and the quartz particle, as the interacting surface area of the particle with the air-water interface is small.

For the natural particles, the snap-off forces are, in general, smaller than the maximum capillary forces, but in some cases the snap-off force equals the maximum force. This occurs when the air-water interface is pinned at the particle surface strong enough so that snap-off happens under conditions represented by the Gibbs extension of the Young Equation. The more pronounced the pinning, the more likely the air-water interface snaps off at the maximum capillary force.

Theoretical and experimental values of capillary forces were of similar order of magnitude. The sphere gave the smallest theoretical capillary force, and the circular cylinder had the largest force due to pinning of the air-water interface. Pinning was less pronounced for natural particles when compared to the circular cylinder. Ellipsoids gave the best agreement with measured forces, suggesting that this shape can provide a reasonable estimation

of capillary forces for many natural particles.

3.4.3 Interaction between Hanford Colloid and Humic Acids

3.4.3.1 Materials and Methods Colloids (operationally defined in this work as particles with diameters less than $2\ \mu\text{m}$) were isolated from fine Hanford sediments representative of those found underneath the Hanford radioactive waste tank farms. An aliquot of the prepared colloid stock solution was treated with 30% vol/vol H_2O_2 to serve as an OM-free control suspension. Total metal e.g., Al, Ca, Fe, Mg, Mn (microwave-assisted HNO_3/HF digestion followed by ICP-OES), C and N (C/N analyser) concentrations were determined for the isolated colloids. Sorption isotherm experiments were carried out using Suwannee River FA and Aldrich HA standard materials. Sorption experiment solutions (pH 7, 1 mM CaCl_2 background) with colloid concentrations of $1\ \text{g L}^{-1}$ and FA or HA concentrations ranging from 0 to $48\ \text{mg L}^{-1}$ were used. No-colloid control solutions were also used. Sorption experiment suspensions were equilibrated on a shaker (17 hours, room temperature) and aliquots of reacted suspensions were used for characterization. Colloids were then centrifuged out of solution and metal (ICP-OES), C and N (TOC analyzer) concentrations in the equilibrium aqueous phases were determined. Natural, FA/HA-reacted and H_2O_2 -treated colloids were characterized using FTIR spectroscopy and SEM-EDAX. Changes in colloid particle size (at pH 7 and 1 mM CaCl_2) and electrophoretic mobility at different values of pH (4, 5, 7, 8, 9, 10) and sorption experiment solution ionic strength (0.01, 0.1 and 1 mM CaCl_2) were measured using dynamic light scattering.

3.4.3.2 Principal Results Results from this investigation indicated that the maximum sorption capacity of Suwannee River FA on Hanford colloids was about $4\ \text{mg C/g}$ and a Langmuir type adsorption isotherm shape was observed, suggesting monolayer sorption of FAs on these colloids. At pH 7 and 1 mM CaCl_2 ionic strength, no differences in particle size were observed between the natural colloids and FA-reacted colloids but a greater particle size was found for the H_2O_2 -treated colloids, suggesting aggregation of particles in absence of organic matter coatings. Also, under these conditions, the natural and FA-reacted colloids had more negative electrophoretic mobility values than the H_2O_2 -treated colloids. Furthermore, electrophoretic mobility values for the FA-reacted colloids generally became increasingly negative with increasing FA reaction concentration. These findings suggest that OM stabilizes the Hanford colloids. Results from this investigation of the interactions between Hanford colloids and HS indicate that natural OM and HS do have a stabilizing effect on colloids from the Hanford radioactive waste repository. The impact of these findings is that OM has the potential to increase the reactivity of Hanford colloids towards contaminants and ultimately influence their participation in colloid-facilitated contaminant transport.

3.5 Column-Scale Investigations on Transport in Unsaturated Hanford Sediments and Porous Media

3.5.1 Using a Geocentrifuge to Elucidate Effects of Flow Rates and Water Content on Colloid Transport and Mobilization

(References: Knappenberger et al., 2012)

3.5.1.1 Motivation Water content and flow rate play an important role in colloid mobilization in unsaturated porous media. It is important to determine the role and the interplay of these factors to obtain a mechanistic understanding of the colloid mobilization process. Unfortunately, under normal gravity, water content and flow rate cannot be independently controlled (the relationship between water content and hydraulic conductivity is hysteretic, but we do not have experimental control over hysteresis). Only with geocentrifuges we can vary each factor independently.

3.5.1.2 Materials and Methods In unsaturated porous media water flow is described by the Darcy-Buckingham-law:

$$q_w = -K(\psi_m) \left(\frac{\partial \psi_m}{\partial z} + 1 \right) \quad (3)$$

where q_w is the flux density, $K(\psi_m)$ is the unsaturated hydraulic conductivity and ψ_m is the matric potential of the media. After Eqn. 3 the water flow is a function of the unsaturated hydraulic conductivity and the gradient of matric and gravimetric potential. The gradient of the gravimetric potential is 1 under gravity. If an unsaturated water flow is developed in a centrifugal field, Eqn. 3 can be rewritten as:

$$q_w = -K(\psi_m) \left(\frac{\partial \psi_m}{\partial r} - \rho \omega^2 r \right) \quad (4)$$

where ρ is the density of the liquid, ω is the angular speed, and r is the radius from the center of rotation. In a centrifugal field it is possible to realize different flux densities q_w at constant matric potentials ψ_m and hence constant water contents by varying the angular speed. Or, a flux density can be realized at different matric potentials ψ_m and water contents, respectively. Consequently, in a centrifugal field, it is possible to overcome the limitations of the Darcy-Buckingham-law of only realizing a certain flux density at a certain water content. In terms of colloidal research, this means that effects of water content and pore water velocity can be considered independently by performing unsaturated flow experiments in a centrifugal field.

Column Setup: We used a plexiglass column with an inner diameter of 5.08 cm and a

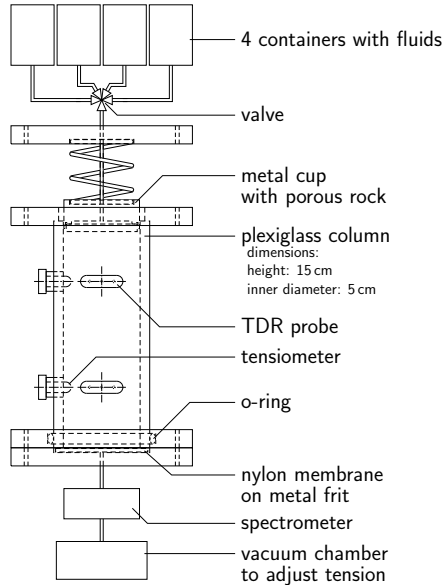


Figure 8. Column setup and principal arrangement of data acquisition devices.

length of 15 cm (Figure 8). At the bottom we used a nylon membrane, mesh size 500 on top of a metal frit. The suction was applied with a vacuum pump via a vacuum chamber. The applied suction on the bottom of the column was controlled with a pressure sensor under the metal frit. In a distance of 4 and 11 cm from the bottom we installed tensiometers and TDR probes to measure the water potential and the water content. The suction on the tensiometers was measured with pressure sensors. The reflection curve on the TDR probes was measured with a Tektronix cable tester and logged with a data logger. We designed the TDR probes to fit the column and used state-of-the-art 3D printing techniques to produce the probes. The liquids were introduced into the column through a porous stone to ensure an even distribution over the whole cross-sectional area of the column.

Porous Media: We used Baker silica sand as a porous medium. The sand was pretreated with 2 M HCl at 90 °C temperature for 24 h to remove organic components and has a porosity of $\epsilon = 0.377$ and a bulk density of $\rho_b = 1.65 \text{ g/cm}^3$. The saturated pore volume (pv_s) in the column is 114.62 cm^3 .

Model Colloids: We used two kinds of carboxylate modified polystyrene colloids with a diameter of 26 and 220 nm. We used a concentration of $2.5 \cdot 10^{15}$ particles/L for the 26 nm colloids and a concentration of 10^{12} particles/L for the 220 nm colloids.

Nitrate Tracer and Solution Chemistry: A 0.2 M NaNO_3 solution was used as a tracer to evaluate the unsaturated flow conditions. We applied the NaNO_3 prior to the colloid experiments to check for uniformity of the flow conditions between single experiments. The solution chemistry was changed during our experiments to vary colloid attachment

Table 2. Sequence of liquids applied in colloid experiments.

Phase	Pore Volumes	Description
A	2	nano pure water
B	4	0.2 mM NaNO ₃
C	2	nano pure water
D	2	1.67 mM NaHCO ₃ , 1.67 mM Na ₂ CO ₃ , 100 mMol NaCl
E	7	1.67 mM NaHCO ₃ , 1.67 mM Na ₂ CO ₃ , 100 mMol NaCl, colloids
F	5	1.67 mM NaHCO ₃ , 1.67 mM Na ₂ CO ₃ , 100 mMol NaCl
G	10	nano pure water

conditions. We used a total of three different solutions for colloid transport: nano pure water (liquid I), nano pure water with high ionic strength (liquid II), and nano pure water with high ionic strength and colloids (liquid III). Nano pure water with an electrical conductivity of less than $5.5 \cdot 10^{-6} \text{ S m}^{-1}$ acted as a starting liquid (liquid I). We buffered nano pure water at pH 10 (1.67 mM NaHCO₃ and 1.67 mM Na₂CO₃) and added 100 mM NaCl to increase the ionic strength to 106 mMol (liquid II). The stock of liquid II was split and colloids were added to one part (liquid III).

Sequence of Liquids: We introduced nano pure water at the beginning of the experiments and developed a steady state flow. After reaching a steady state flow, we introduced the different liquids in a certain sequence for the two different colloids. Every sequence was repeated three times. First we introduced three sequences of the 220 nm colloids and subsequently we introduced three sequences of the 26 nm colloids. We applied the NaNO₃ prior to the colloid experiments. The sequences of liquids are shown in Table 2.

Experiments Under Gravity and Centrifugal Force: The silica sand was introduced into the water filled column to ensure saturated conditions. The liquids were introduced to the column with a peristaltic pump. After a series of 220 nm and 26 nm colloids experiments, we removed the sand from the column, sonicated and washed it with deionized water. For the experiments under centrifugation we used the geocentrifuge facility at the Idaho National Laboratory (50 g-tonne Actidyn Systemes model C61-3, France). The experimental platform has a size of 70 cm length by 50 cm depth by 60 cm height. The radius of centrifugation is 2 m. The geocentrifuge accepts a pay load of 500 kg and accelerations up to 130 g. The centrifuge experiments were the same as the experiments under gravity but we used a piston pump to introduce the liquids into the column. First, we acquired a calibration curve by setting the centrifuge to different accelerations (2 g, 10 g, 20 g, 30 g and 40 g) and applying different flow rates. Then we calculated the corresponding pore water velocities according to different accelerations (Figure 9). Based on these measurements we designed the experiments accordingly.

Spectrophotometry: We used a spectrophotometer to measure the colloid concentra-

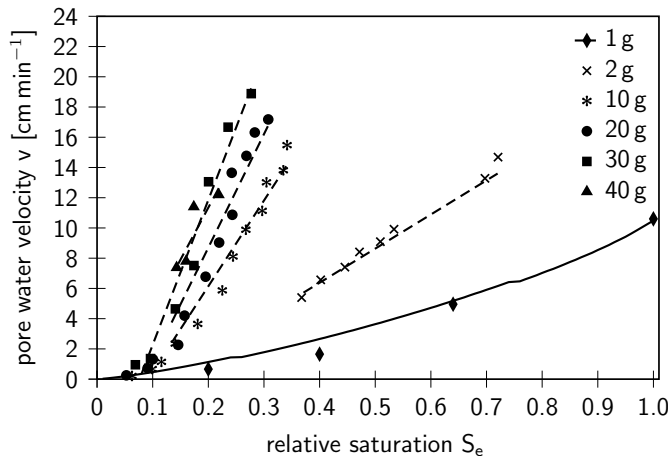


Figure 9. Different pore water velocities over effective saturation (S_e) at different accelerations. The solid line in the 1 g case was calculated based on van Genuchten parameters.

tions in the outflow of the column. Solarization resistant fiber optics were used (QP400-2-SR) to connect the light source to the spectrophotometer. We measured the concentrations of all liquids before every experimental series by injecting the liquid into the flow cell.

3.5.1.3 Principal Results Figure 10 shows the breakthrough and release curves for the 26 and 220 nm colloids and for effective saturations of 0.2, 0.3, 0.6 and 1. Overall, the breakthrough curves decrease with decreasing effective saturation. The first breakthrough curve of a series of three experiments is less pronounced than the second and third breakthrough curve. In case of the 26 nm colloids and an effective saturation of $S_e = 0.3$, no breakthrough occurred for the first run of the series (Figure 10E). The release curves for 220 nm colloids under saturation were very pronounced and reached values of 3.8, 2.2 and 2.3 C/C_0 for run 1, 2 and 3, respectively. Figure 11 shows the mass balance for the 26 and 220 nm colloids. Overall, larger amounts of 26 nm colloids are retained.

The runs within a series of experiments as well as the effective saturation levels had highly significant effect. Even release curves, whose shape was apparently alike (e.g., Figure 10A, 10C, 10D) had highly significant differences. The adjusted R^2 -values were 0.61 and 0.69 for breakthrough and release curves for 26 nm colloids and 0.82 and 0.39 for breakthrough and release curves for 220 nm colloids, respectively.

Under saturated conditions ($S_e = 1$), introduced colloids can attach to primary and secondary energy minima. That means an introduced colloid can either pass the column without attachment or the colloid can attach to a primary or secondary energy minimum. If attached to a secondary energy minimum, the particle will be released again after changing

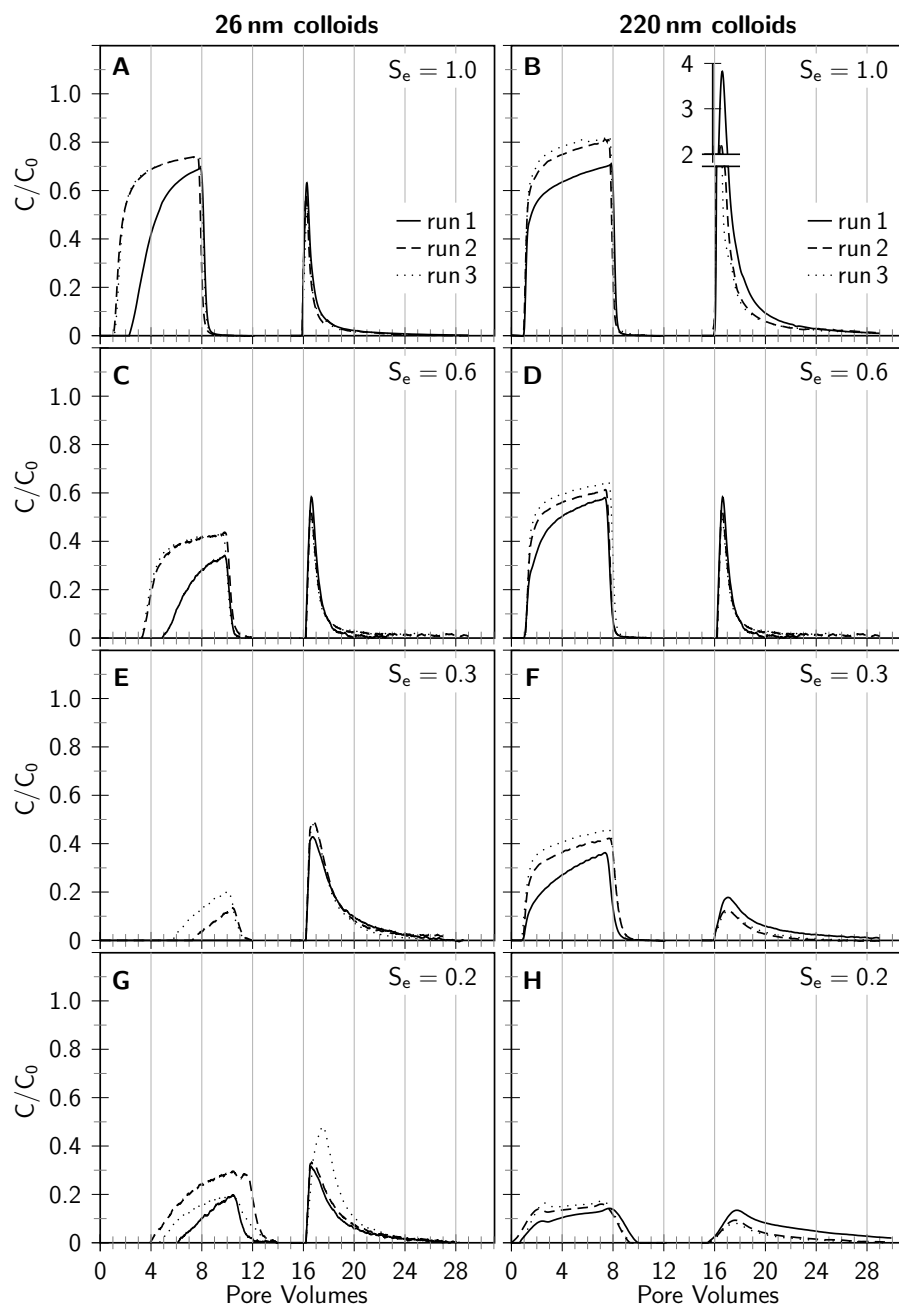


Figure 10. Overview of all breakthrough and release curves.

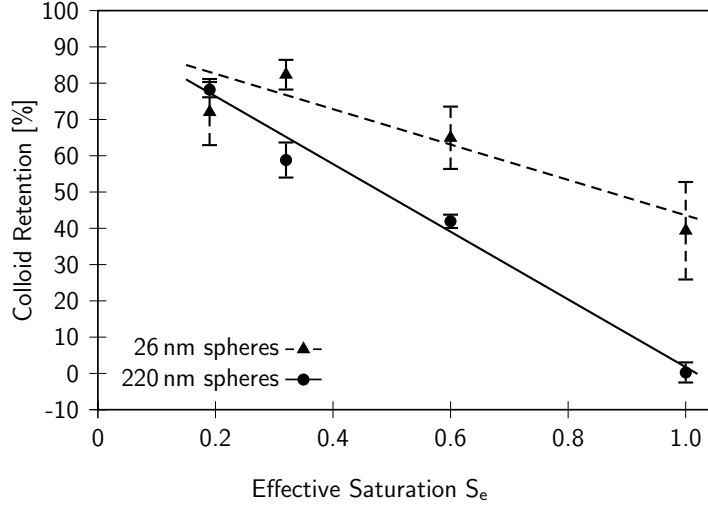


Figure 11. Colloid retention mass balance in geocentrifuge experiments.

the solution chemistry (change from phase F to G, Table 2). Consequently the secondary energy minimum will vanish and the retained colloids will be released (Figure 10). For 220 nm colloids, all colloids were leached out, i.e., colloids have only been retained in a secondary energy minimum. However, 23% of 26 nm colloids remain retained in the column. That means colloids also have to be retained in a primary energy minimum as no other attachment sites are available.

Under unsaturated conditions ($S_e < 1$), besides the mentioned primary and secondary energy minima, colloids can also attach to the liquid-gas-interface. With decreasing water content, the liquid-gas-interface is increasing and hence more attachment sites for colloids become available. For both colloid sizes, the retention increases with decreasing effective saturation (Figure 11). We assume that more colloids are retained at the liquid-gas-interface as the effective saturation is decreasing.

More detailed mass balance data are listed in Table 3. For the 26 nm colloids, the series at an effective saturation of $S_e = 0.3$ does not fit into the overall pattern. In the other series, the percentages for the breakthrough curves increase with increasing saturation from 15.9% at $S_e = 0.2$ to 55.2% at $S_e = 1$. With less saturation, less colloids pass the column after introduction. We attribute this effect to a larger liquid-gas interface. The colloids find more attachment sites at this interface. The percentage of released colloids, however, is constant for $S_e = 0.2$ and $S_e = 0.3$ as well as $S_e = 0.6$ and $S_e = 1.0$. The Kruskal-Wallis test for breakthrough, release and retention is significant at $p = 0.023$, $p = 0.036$ and $p = 0.033$, respectively.

For the 220 nm colloids, the percentages for the breakthrough curves increase with

Table 3. Mass balance for breakthrough and release curves and overall retention (in percent). Mean values and standard deviations are listed in this table. The p-values are computed with a Kruskal-Wallis test over all effective saturation values.

	effective Saturation S_e				
	0.2	0.3	0.6	1.0	p-value
26 nm colloids					
Breakthrough	15.9 \pm 8.0	4.5 \pm 4.6	29.1 \pm 10.6	55.2 \pm 14.8	0.023
Release	12.1 \pm 5.1	13.2 \pm 2.4	5.9 \pm 1.8	5.4 \pm 1.1	0.036
Retention	72.0 \pm 9.4	82.3 \pm 4.4	65.0 \pm 8.9	39.3 \pm 13.7	0.033
220 nm colloids					
Breakthrough	14.3 \pm 1.6	34.7 \pm 7.3	51.4 \pm 5.6	70.6 \pm 6.4	0.016
Release	7.5 \pm 4.0	6.5 \pm 2.6	6.6 \pm 3.7	29.1 \pm 9.3	0.092
Retention	78.2 \pm 2.4	58.8 \pm 5.1	41.9 \pm 2.1	0.3 \pm 3.1	0.016

increasing saturation from 14.3% at $S_e = 0.2$ to 70.6% at $S_e = 1$. The percentage of for the release curve is constant for unsaturated conditions and is significant higher for saturated conditions. The missing liquid-gas interface in the saturated condition obviously allows more colloids to be trapped in the secondary energy minimum. Under unsaturated conditions, the liquid-gas interface is available as attachment site and the number of colloids that are trapped in the secondary energy minimum is smaller but constant. The differences are not significant $p = 0.092$. If only the unsaturated conditions are considered in the Kruskal-Wallis test, the p-value even increases to $p = 0.837$.

Overall, the 220 nm colloids show a more consistent pattern and the mass balance data has a smaller standard deviation compared to the 26 nm colloids. However, we can determine attachments of 26 nm colloids to the solid-liquid interface in the primary energy minimum. We do not have evidence for such an attachment for the 220 nm colloids.

3.5.2 Colloid Mobilization in an Undisturbed Sediment Core under Semi-Arid Recharge Rates

(References: Liu et al., 2012)

3.5.2.1 Motivation The Hanford site is characterized by a Mediterranean, semi-arid climate where deep recharge rates are low, ranging from near zero to 100 mm/y. It is unclear whether at these low, steady-state flow rates, colloids can be mobilized and transported. Here, we used an undisturbed sediment core to (1) test whether natural colloidal materials

can be mobilized and translocated under conditions typical for the deep vadose zone at the Hanford Site and (2) to quantify the extent of the colloid mobilization. We hypothesized that under the low and steady-state recharge rate at the semi-arid Hanford site, colloid mobilization and transport is low, but existent.

3.5.2.2 Materials and Methods An undisturbed sediment core was collected from the Hanford Environmental Restoration Disposal Facility (ERDF). The core was taken from an uncontaminated layer of the sand-dominated facies association of Hanford Formation sediments from a depth of 17 meters below ground surface (Figure 12a). A flat, horizontal bench of sediment was prepared by digging into the slanted wall of the ERDF pit. Then an intact, undisturbed core sample was taken by using a stainless steel cylinder (10 GA T-304, I.D. = 50 cm, height = 59.5 cm). A front-loader with a 3-m wide bucket was used to push the cylinder into the sediments (Figure 12b). When the core was completely inserted into the sediments, the sediments around the core were excavated, and a bevelled stainless steel plate was pushed along the bottom of the core to shave the core off the underlying sediments (Figure 12c). About 17 liters of liquid nitrogen was poured onto the surface of the core to freeze the top of the core to provide stability for transportation. A wooden plate was tightened to the top of the cylinder, and the core was moved to Washington State University (Figure 12d).

The sediment core in the stainless steel column was set up as a lysimeter (Figure 12f) in a dark coldroom at 12.4 ± 0.3 °C, corresponding to the long-term average air temperature at the Hanford site. The column was irrigated uniformly by using a peristaltic pump and a sprinkler. The irrigation rate was chosen to fall within the range of annual rainfall at the Hanford site. Based on the mass balance of the sediment core, we determined the actual infiltration rate to be 0.05 mm/day (= 18.25 mm/y), which corresponds to irrigation minus evaporation rates. This rate represents a low recharge rate typical for the Hanford site; rates have reported to range from 0 to 100 mm/y. (We note that due to subsurface channeling of flow, e.g., due to flow redirection by HLW tanks, local recharge can be substantially larger). Column outflow water was analyzed for particle size and electrophoretic mobility, pH, electrical conductivity, and UV/VIS absorbance at 280 nm. Absorbance was translated to particle concentrations by using a calibration curve developed from a colloid stock solution. Selected outflow samples were analyzed by transmission electron microscopy (TEM) and energy dispersive x-ray analysis (EDX).

We used HYDRUS-1D (Version 4.14) to analyze the water flow and colloid transport in our experiments. The unsaturated hydraulic properties were parameterized by the van Genuchten-Mualem equations. The model was run in inverse mode to determine the unsaturated hydraulic properties of the sediments. For the van Genuchten-Mualem model, we fitted the parameters α , n , and K_s , with $m = 1 - 1/n$, for each of the observation nodes. For the colloid transport modeling, we assume that the pool of the colloids is ini-

tially uniformly distributed within the core and that the colloids are initially attached to the stationary sediments. We further assume that, as water flows through the core, colloids can be mobilized by a first-order kinetic colloid release:

$$\frac{\partial C}{\partial t} + \frac{\rho}{\theta} \frac{\partial S}{\partial t} = D \frac{\partial^2 C}{\partial z^2} - \frac{J_w}{\theta} \frac{\partial C}{\partial z} \quad (5)$$

$$\frac{\partial S}{\partial t} = -\beta S \quad (6)$$

where C represents the colloid concentration suspended in the aqueous phase (mg/cm^3), S is the colloid concentration attached to the sediments (mg/g), t is time (day), ρ is the bulk density (g/cm^3), z denotes the coordinate parallel to the flow direction (cm), and β is the first-order colloid release rate coefficient (d^{-1}). A zero flux condition was used at the upper boundary ($J_w C(0, t) = 0$) and a zero-gradient was used at the bottom boundary ($\frac{\partial C}{\partial x} = 0$).

3.5.2.3 Principal Results Chemical and colloidal characteristics of the sediment outflow are shown in Figure 13. Electric conductivity varied between 500 and 2000 $\mu\text{S}/\text{cm}$, corresponding to ionic strengths of 7.2 to 29 mmol/L . The critical coagulation concentration for in situ colloids from Hanford sediments has been reported to be 1.7 to 3.8 mmol/L for Ca dominated systems. As the ionic strength in our core exceed the critical coagulation concentration, we did not expect any colloid dispersion to occur. The particle counts indeed indicate that colloid transport was not prominent in our sediment core. The initial outflow samples had particle counts below 10 $\text{kCounts}/\text{s}$, which is within the background noise of the dynamic light scattering instrument. No electrophoretic mobility and size measurements could be made for such low particle counts. In 2009, the particle counts increased up to 50 $\text{kCounts}/\text{s}$, which suggests the presence of particles in the outflow. Electrophoretic mobility and size measurements were made for these samples, but have to be considered with caution, as the particle counts still did not meet the required minimum value for accurate measurements ($>50 \text{ kCounts}/\text{s}$). Electrophoretic mobility values, nonetheless, yielded reasonable results for Hanford sediments (-1 to $-3 (\mu\text{m}/\text{s})/(\text{V}/\text{cm})$). The particle concentration in the outflow ranged from generally 20 to occasionally 537 mg/L (Figure 13e), and we observed a continuous release of colloids (Figure 13f).

Figure 13f shows a continuous particle release from the sediment core at a rate of 148.1 mg/year . Over the total period of the experiment since colloid outflow was observed (967 days), a total of 0.392 g of particle were collected, corresponding to a cumulative particle flux of $0.2 \text{ mg}/\text{cm}^2$. The dispersible particles in the sediments was determined 84.1 g (0.441 g/kg sediments). The mobilized particles over 967 days constitute 0.5% (by mass) of the dispersible particles.

Model simulations could be fitted well to the experimental data (Figure 13f). The



Figure 12. Sampling of sediment core and experimental setup. (a) Location of sampling in the ERDF pit, (b) insertion of steel cylinder into sediments, (c) shave-off of cylinder from sediments, (d) lift-off, (e) sediment layering of Hanford formation, and (f) laboratory setup.

fitted colloid release coefficient was $\beta = 7 \times 10^{-6} \text{ day}^{-1}$, with lower and upper limit of 5.5 and $9.5 \times 10^{-6} \text{ day}^{-1}$, determined by adjusting the parameter β to fully encompass the experimental data (Figure 13f). Using the same model with disturbed column experiments, we had previously found a range of colloid release rates from 10.1 day^{-1} to 120 day^{-1} for a flow rates from 259.2 mm/d to 414.7 mm/d. These values are six to seven orders of magnitude higher than the rate observed in the undisturbed sediments. This large difference in release rates indicates that particle release is considerably smaller in our undisturbed core under the much lower flow rate than in disturbed, packed columns at considerable high flow rates.

Our results suggest that even in semi-arid regions, the thick vadose zone with its low water content and flow rates does not necessarily constitute a perfect filter for particle transport. The continuous particle mobilization may constitute a pathway for contaminant and colloid-facilitated contaminant transport at the US DOE Hanford site. Transport will be exacerbated when recharge locally is enhanced due to subsurface channel flow.

3.6 Field-Scale Eu Colloid Transport at the Semi-Arid Hanford Site

3.6.1 Transport of Europium Colloids in Vadose Zone Lysimeters

(References: Liu et al., 2012)

3.6.1.1 Motivation There exist no field experiments on colloid mobilization and transport at the Hanford Site. Several field lysimeter stations have been installed and operated at the Hanford site to study recharge, evapotranspiration, and mineral weathering. We used these these lysimeters to study colloid transport under field conditions.

3.6.1.2 Materials and Methods The study was conducted at the Hanford 300 Area Lysimeter site. The facility consists of six non-weighing lysimeters, each 7.6 m deep. Two of the lysimeters are 2.7 m in diameter and four lysimeters are 0.6 m in diameter (Figure 14). The 300 Area Lysimeters were installed in 1978 and all of them were kept free of vegetation for the past 34 years. These lysimeters were filled with a uniform sandy layer consisting of Hanford sediments and had a coarse sand layer at 5.7 m depth. The sandy layer's hydraulic conductivity is 173 cm/d at saturation and $9 \times 10^{-3} \text{ cm/d}$ at -5 kPa . For our study, we used four lysimeters: the South Caisson (SC) and Lysimeters 1, 2, and 3 (Figure 14).

We installed fiberglass wicks to collect pore water samples from the lysimeters under unsaturated conditions. Fiberglass wicks have been found to be useful devices to collect pore water and soil colloids. The wicks were installed into the lysimeters in horizontal orientation at 0.31, 0.61, 1.22 and 2.14 m (1, 2, 4, and 7 feet). In Lysimeter 2, the wicks were installed at 0.61, 0.92, 1.22 and 2.14 m (2, 3, 4, and 7 feet) depths, because the access port at the 1-foot depth was inaccessible. A 50-cm long piece of the wicks was used as a

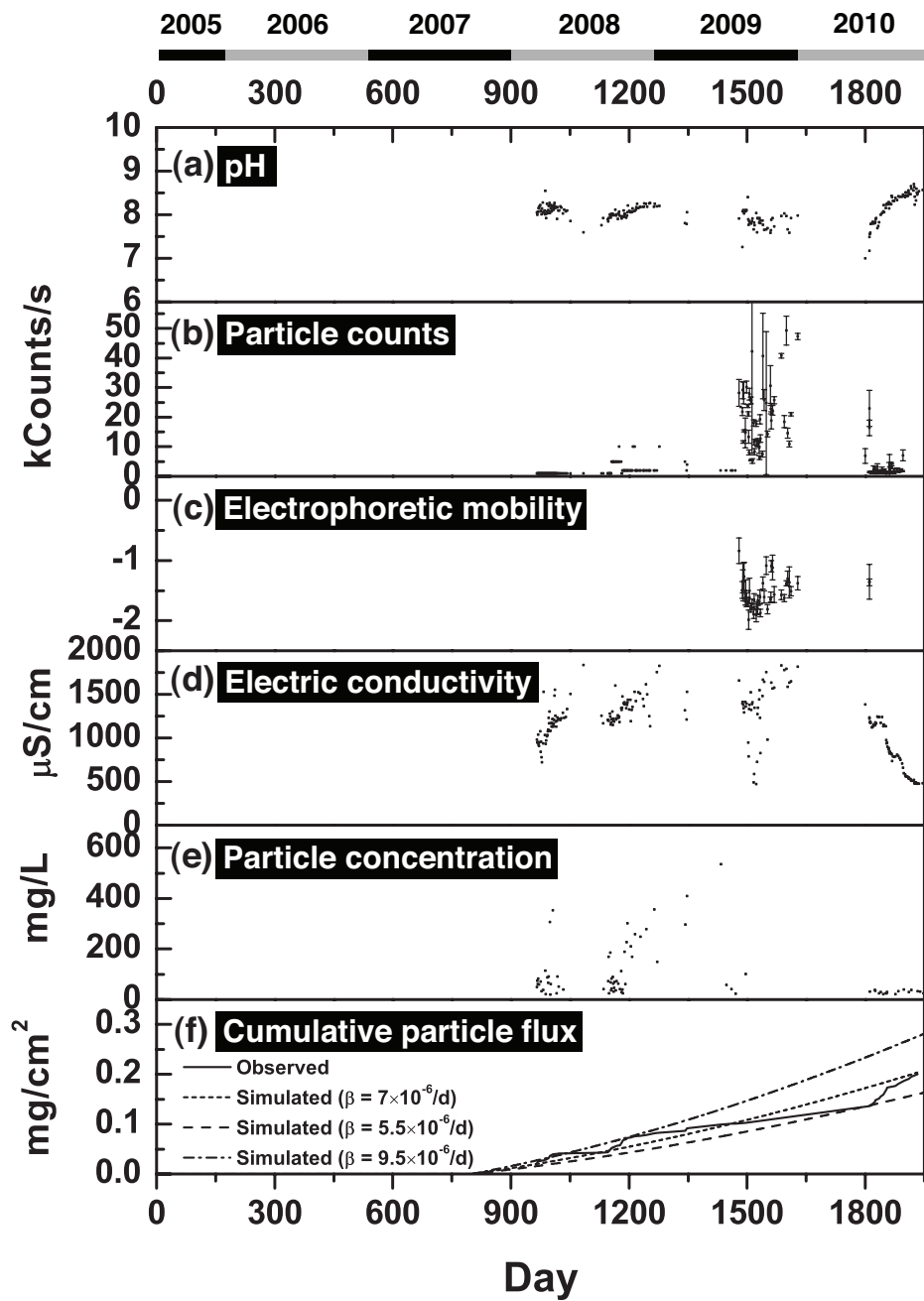


Figure 13. Characterization data of outflow from sediment core. (a) pH, (b) Particle counts, (c) Electrophoretic mobility ($(\mu\text{m/s})(\text{V}/\text{cm})$). Unit is not shown in the figure due to space limit, (d) Electric conductivity, (e) Particle concentration, (f) Cumulative particle flux.

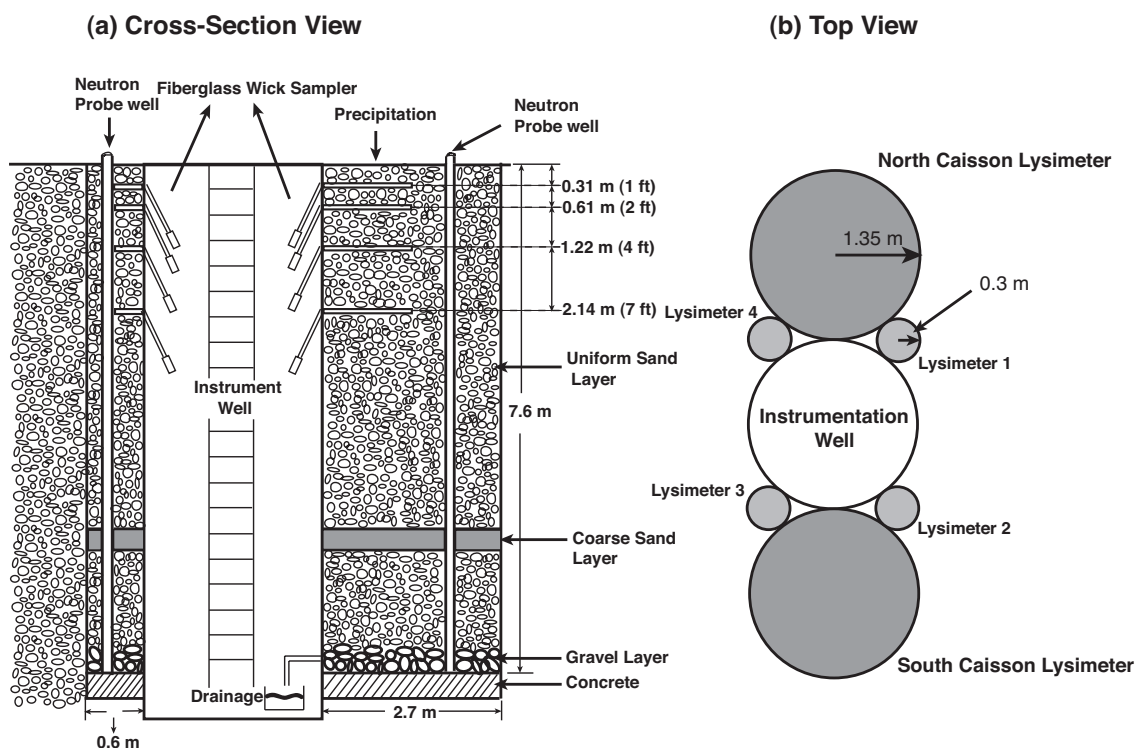


Figure 14. Schematic of Hanford 300 Area Lysimeter Facility. Only the South Caisson, Lysimeter 1, Lysimeter 2, and Lysimeter 3 were used in our experiments.

hanging water column to provide tension for pore water sampling (Figure 15). This tension matches the water potential in the lysimeters and therefore provides little disturbance of the flow field. A 250 mL polypropylene bottle was placed at the bottom of each wick sampler to collect pore water.

Eu-hydroxy-carbonate colloids ($\text{Eu}(\text{OH})(\text{CO}_3)$) were synthesized in our laboratory. A 6×10^{-3} M europium stock solution was prepared by dissolving europium chloride ($\text{EuCl}_3 \cdot 5\text{H}_2\text{O}$) in double-distilled water, and then passed through a $0.2 \mu\text{m}$ filter. The filtered solution was mixed with 1.5 M urea and small amounts of acid (7×10^{-4} M HNO_3 and 2×10^{-4} M H_2SO_4) in a 750 mL Pyrex bottle to adjust the pH to 5.1. The concentration of Eu colloids in this stock solution was 237.7 mg/L (measured gravimetrically by drying an aliquot), corresponding to a particle number concentration of 4.1×10^{13} number/L (calculated based on average colloid diameter of 108 nm and specific density of 8.78 g/cm³). We used the Eu-hydroxy-carbonate colloids as a representative intrinsic radionuclide colloid.

A colloid suspension was then manually sprayed onto the lysimeter surface. A total of 3 mm of the suspension was applied to the lysimeters on March 11, 2009. Whereas the South Caisson Lysimeter was uncovered, receiving natural precipitation, and allowing evaporation,

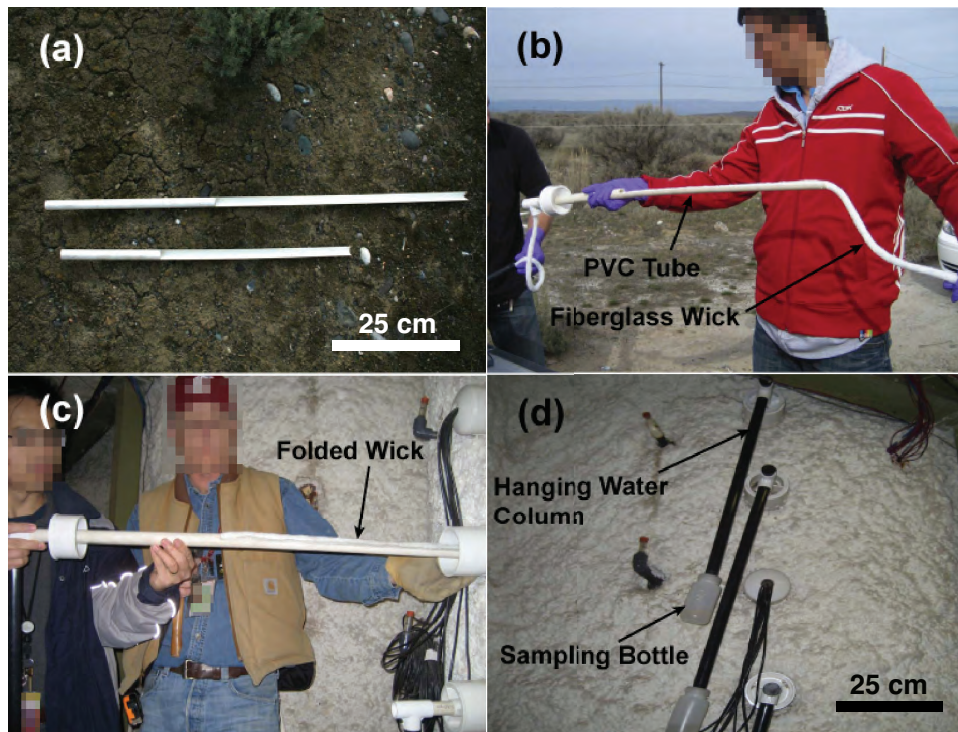


Figure 15. (a) Cut-open 3/4 inch PVC tube for wick support, (b) mounting of fiberglass wick (c) installation of wick sampler into lysimeter, (d) installed wick samplers showing the PVC tube containing hanging water column and the outflow sampling bottle.

Lysimeters 1, 2, and 3 were irrigated and then covered to minimize evaporation. Lysimeter 1 received an annual recharge of 124 mm/year, which equals twice the 26-year drainage average at the site. Lysimeter 2 was irrigated with four times the natural drainage, and Lysimeter 3 received an additional 100 mm/year simulated Chinook snowmelt event.

Outflow pore water from the fiberglass wicks was collected once a month by replacing the polypropylene bottles. Additionally, we took soil cores from the surface at different times. The collected pore water was first sonicated for 5 minutes and then analyzed for outflow volume, pH, electric conductivity, electrophoretic mobility, particle size, particle number, and particle mass concentration. Electrophoretic mobilities and particle counts were quantified by using dynamic light scattering, and repeated 5 times for each sample. Selected samples were examined microscopically using Transmission and Scanning Electron Microscopy, and Energy Dispersive X-ray analysis. The amount of Eu colloids was quantified by measuring the Eu concentration in the outflow samples or soil extracts.

3.6.1.3 Principal Results Figure 16a shows the daily natural precipitation and the irrigation from January 2009 to March 2012 for each of the lysimeters. The daily precipitation (South Caisson) was taken from the Hanford Meteorological Station and the irrigation (Lysimeters 1, 2, 3) was measured when it was applied. The natural precipitation occurred in much greater frequency than the irrigation, but the seasonal pattern was similar, not identical, because the irrigation was based on the long-term precipitation record. The Chinook events applied to Lysimeter 3 are indicated by arrows. In 2009, the Chinook simulation was applied at two separate days. The total application during a Chinook event exceeded 100 mm because the Chinook was added to the regular irrigation in that month.

While the Eu data for the South Caisson did not show a clear breakthrough pattern, we did detect Eu peaks in the irrigated lysimeters. Lysimeter 1 shows a Eu peak on June 29, 2009 at 1.22-m depth and on July 16, 2009 at 2.14-m depth. Similar patterns could be observed for Lysimeter 2 and 3. These initial peaks of Eu are corroborated by particle counts in the outflow samples (Figure 16d). Europium concentrations and particle counts declined during summer 2009 in most samples, because no outflow was collected, particularly for the top two wick samplers. The 2.14-m wick sampler showed continuous movement of Eu throughout the year in Lysimeters 1 and 2. A second peak of Eu could be detected in Spring 2010 in all lysimeters, caused by the elevated precipitation and irrigation during the preceding winter season. Particle counts, however, were not as pronounced as in 2009.

The Chinook events in Lysimeter 3 caused pronounced water infiltration and produced Eu peaks in the wick outflow, particularly in 2009. In 2010, the topmost wick (0.31 m) showed elevated Eu concentrations as a result of the Chinook event; correspondingly, there were increased particle counts in the wick outflow. The 0.61 m wick also showed elevated particle counts, however, no Eu was detected. The 2011 Chinook event, however, did not

produce an Eu peak in the outflow.

The electrophoretic mobility data indicate that the wick outflow always contained particles, with electrophoretic mobilities between -0.5 to -3 ($\mu\text{m/s}/(\text{V/cm})$). The pH of the wick outflow varied between 8.2 and 8.5. At that pH, the measured electrophoretic mobility of the water-dispersible, native colloidal fraction of the Lysimeter sediments (without Eu colloids) was -2.5 ($\mu\text{m/s}/(\text{V/cm})$), and that of the Eu colloids (from the application suspension) was -3.0 ($\mu\text{m/s}/(\text{V/cm})$). This indicates that the outflow samples contained native colloidal material from the sediments. Figure 17 shows SEM images of wick outflow from May 28, 2009. The images reveal native colloidal materials (platy clay minerals, Figure 17a) as well as spherical particles (Figure 17b), which we identified as Eu colloids with the help of energy-dispersive x-ray analysis (Figure 18).

Our results demonstrate that under field conditions with transient flow, colloid mobilization and transport occurred in Hanford sediments. Small amounts of Eu colloids could be translocated by natural precipitation or irrigation to a depth of 2.14 m within 2.5 months. Assuming steady-state flow, this corresponds to a colloid transport velocity of 3 cm/d. Estimates of recharge at the Hanford site range from 1 to 50 mm/year. Considering a volumetric water content of $0.1 \text{ m}^3/\text{m}^3$, the recharge estimates translate to a pore water velocity of 1 to 50 cm/year (equal to 0.003 to 0.14 cm/d), which is considerably slower than what we observed based on the Eu transport. This indicates that the near surface transport of Eu can be rapid, exceeding recharged-based velocity estimates by more than a factor of ten. The measured maximal transport velocity of 3 cm/d, suggests that some of the Eu was transported by preferential flow.

The observed rapid movement of Eu in the homogeneous Hanford Lysimeters was caused by transient water flow near the soil surface. Based on the mechanistic laboratory studies reported above, it is likely that the Eu colloids were mobilized and translocated by moving air-water interfaces. The main peak of Eu, however, moved at slower rate, consistent with long-term recharge.

3.6.2 Field-Scale Conceptual and Numerical Model for Colloid Mobilization and Transport

3.6.2.1 Motivation Mathematical models for colloid and colloid-facilitated transport are typically based on the advection-dispersion equation (ADE). For non-steady state flow, the ADE is usually coupled with the Richards equation describing water flow in variably-saturated porous media. The ADE for colloid-facilitated transport includes specific reactions of contaminants and colloids with the solid-water and the air-water interfaces. Alternatively, flow and transport can be modeled as two-phase flow (air-water), and a number of multiphase flow codes are available, for instance, FLOTRAN, NUFT, STOMP, and TOUGH2. These codes describe simultaneous flow of aqueous and gas phases under gravity, capillary, and viscous forces.

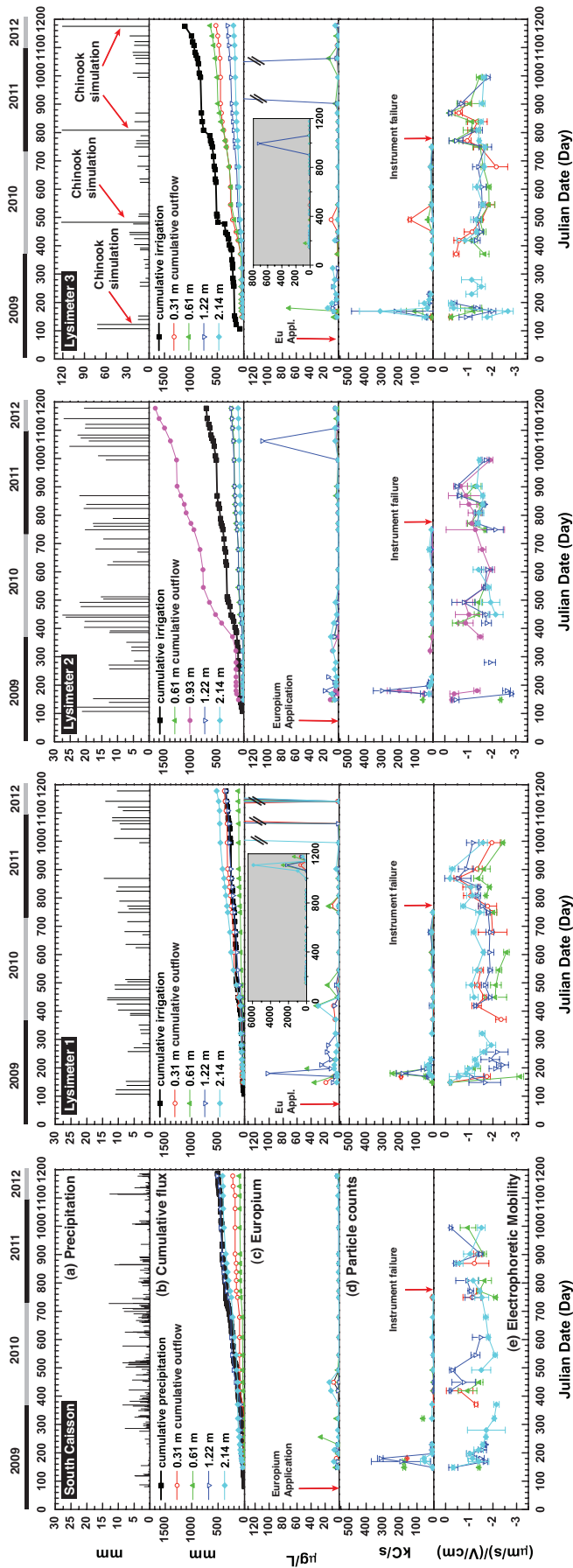


Figure 16. Time series of experimental data for each of the lysimeters. (a) Precipitation/irrigation, (b) cumulative water inflow on the surface and wick outflow, (c) Eu concentration in wick outflow (mass of Eu per volume of outflow solution); inserts show full-scale of Eu peaks observed in Fall/Winter 2011, (d) particle counts (kilocounts per s) in wick outflow , and (e) electrophoretic mobility of colloids in wick outflow.

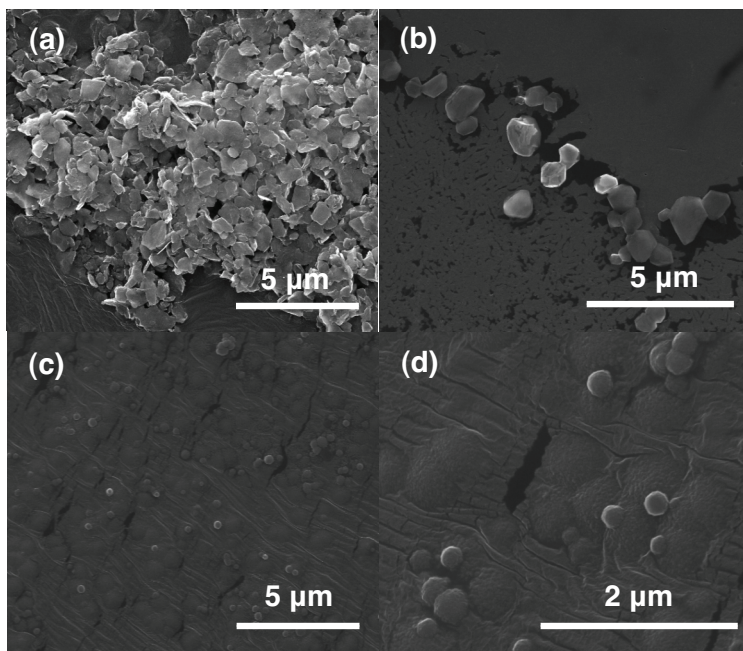


Figure 17. Scanning electron microscopy images of colloidal particles in wick outflow from different times.

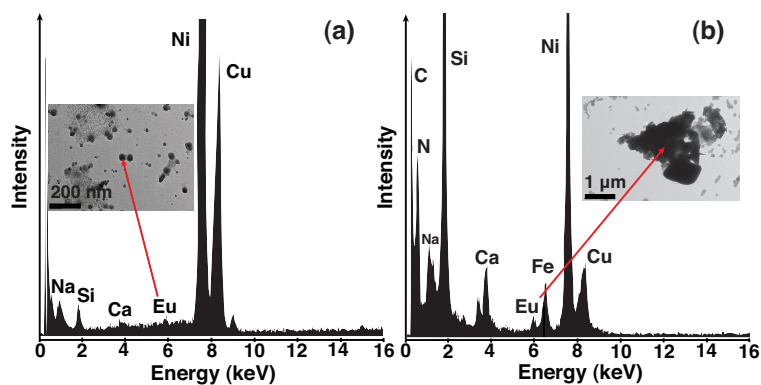
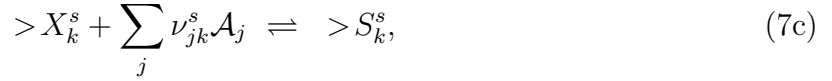
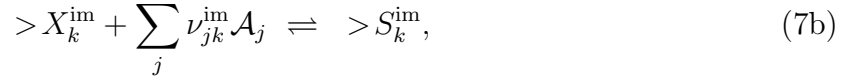
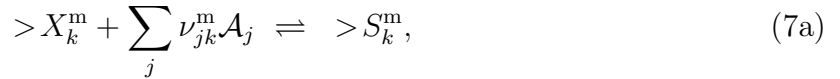


Figure 18. Energy dispersive x-ray spectra (EDX) and corresponding TEM images of wick outflow samples from (a) May 28, 2009, Lysimeter 1 (0.61-m depth), (b) June 18, 2009, Lysimeter 1 (0.31-m depth). The Eu $L\alpha$ -level emission line at 5.8 keV indicates the presence of Eu. The large peaks for C, Ni, and Cu keV are from the microscopy stub.

3.6.2.2 Materials and Methods The model PFLOTTRAN was used to simulate colloid transport through the Hanford Vadose Zone at the 200 area. FLOTTRAN is a reactive flow and transport code that simulates two-phase (air and water) flow in variably saturated, nonisothermal porous media. Flow is governed by gravity, capillary, and viscous forces, and solves mass balance equations for water, air, and energy. The code handles multicomponent reactive chemical transport involving aqueous, gaseous, and mineral species. Chemical reactions include homogeneous aqueous speciation reactions, heterogeneous gaseous speciation, mineral precipitation and dissolution reactions, ion-exchange, and sorption reactions. The rates of mineral reactions are described through kinetic rate laws.

Colloid-facilitated transport is implemented in PFLOTTRAN based on surface complexation reactions at the colloid surface. Competition between mobile and immobile colloids and stationary mineral surfaces is taken into account. Colloid filtration processes are not currently implemented into PFLOTTRAN. A colloid is treated as a solid particle suspended in solution or attached to a mineral surface. Colloids may be generated through nucleation of minerals in solution, although this effect is not included currently in the code.

Three separate competing reactions may take place involving mobile and immobile colloids and mineral surfaces



for surface complexes $>S_k^m$, $>S_k^{im}$ and $>S_k^s$ and empty sorption sites $>X_k^m$, $>X_k^{im}$, $>X_k^s$, where the superscripts s , m , and im denote mineral surfaces, and mobile and immobile colloids, respectively. The species \mathcal{A}_j form a set of primary species in terms of which all other reactions may be formulated. The corresponding reaction rates are denoted by I_k^m , I_k^{im} , and I_k^s , respectively. In addition, precipitation and dissolution reactions with minerals \mathcal{M}_s may occur with reaction rate I_s according to the reaction



The transport equations for primary species based on Richards equation, mobile (m) and immobile colloids (im), read

$$\frac{\partial}{\partial t} \varphi_{sl} \Psi_j^l + \nabla \cdot \mathbf{\Omega}_j^l = - \sum_k (\nu_{jk}^m I_k^m + \nu_{jk}^{im} I_k^{im} + \sum_s \nu_{jk}^s I_k^s) - \sum_s \nu_{js} I_s, \quad (9)$$

$$\frac{\partial}{\partial t} \varphi s_l S_k^m + \nabla \cdot \mathbf{q}_c S_k^m = I_k^m, \quad (10a)$$

$$\frac{\partial}{\partial t} S_k^{\text{im}} = I_k^{\text{im}}, \quad (10b)$$

$$\frac{\partial}{\partial t} S_k^s = I_k^s. \quad (10c)$$

In these equations \mathbf{q}_c denotes the colloid Darcy velocity which may be greater than the fluid Darcy velocity \mathbf{q} given by

$$\mathbf{q} = -\frac{k k_r}{\mu} \nabla (p - \rho g z), \quad (11)$$

with permeability k , relative permeability k_r a function of liquid saturation s_l , pressure p , fluid density and viscosity ρ , μ , acceleration of gravity g , and porosity φ . The quantities Ψ_j^l and Ω_j^l refer to the total concentration and flux of the j th primary species defined, respectively, as

$$\Psi_j^l = C_j^l + \sum_i \nu_{ji} C_i^l, \quad (12)$$

and

$$\Omega_j^l = \left(\mathbf{q} - \varphi D \nabla \right) \Psi_j^l, \quad (13)$$

with diffusion/dispersion coefficient D . The total concentration and flux account for aqueous homogeneous reactions, assumed to obey conditions of local equilibrium, given by

$$\sum_j \nu_{ji} \mathcal{A}_j \rightleftharpoons \mathcal{A}_i. \quad (14)$$

The sorption reaction rates may be eliminated from the primary species transport equations and replaced by sorbed surface complex concentrations to yield

$$\begin{aligned} \frac{\partial}{\partial t} \left[\varphi s_l \Psi_j^l + \sum_k (\varphi s_l \nu_{jk}^m S_k^m + \nu_{jk}^{\text{im}} S_k^{\text{im}} + \sum_s \nu_{jk}^s S_k^s) \right] \\ + \nabla \cdot \left(\Omega_j^l + \mathbf{q}_c \sum_k \nu_{jk} S_k^m \right) = - \sum_s \nu_{js} I_s. \end{aligned} \quad (15)$$

This result is obtained by substituting the left-hand sides of Eqns.(10a)–(10c) for the reaction rates. The mobile sorbed concentration appears in both the accumulation and flux terms, unlike the immobile and mineral sorbed concentrations. This is because of the flux term appearing in Eqn.(10a).

In the kinetic case either form of the primary species transport equations given by Eqn. (9) or (15) can be used provided it is coupled with the appropriate kinetic equations given by Eqns.(10a)–(10c).

The mobile case leads to additional equations that must be solved simultaneously with the primary species equations. A typical expression for I_k^m might be

$$I_k^m = k_k(S_k^m - S_{km}^{\text{eq}}), \quad (16)$$

with rate constant k_k and where S_{km}^{eq} is a known function of the solute concentrations.

In this case, Eqn.(10a) must be added to the primary species transport equations. Further reduction of the transport equations for the case where a flux term is present in the kinetic equation is not possible in general for complex flux terms.

Sorption Isotherm: As follows from the mass action corresponding to the surface complex reaction the equilibrium sorption concentration S_k^{eq} is given by

$$S_k^{\text{eq}} = \frac{\omega K_k Q_k}{1 + \sum_l K_l Q_l}, \quad (17)$$

and the empty site concentration by

$$S_X^{\text{eq}} = \frac{\omega}{1 + \sum_l K_l Q_l}, \quad (18)$$

for selectivity coefficients K_k , and where the ion activity product Q_k is defined by

$$Q_k = \prod_j (\gamma_j C_j)^{\nu_{jk}}. \quad (19)$$

The site concentration ω satisfies the relation

$$\omega = S_X + \sum_k S_k, \quad (20)$$

and is constant.

Retardation: Under the special circumstances of a sufficiently dilute solution so that the sorbed and aqueous concentrations can be treated as approximately constant, it is possible to define a retardation coefficient \mathcal{R}_j as

$$\mathcal{R}_j = \frac{1 + K_j^m + K_j^{\text{im}} + K_j^s}{1 + f_c K_j^m}, \quad (21)$$

where $f_c = |q_c/q| \geq 1$, and where the distribution coefficients K_j^m , K_j^{im} and K_j^s are defined

as

$$K_j^m = \frac{1}{\Psi_j^l} \sum_k \nu_{jk}^m S_k^m, \quad (22a)$$

$$K_j^{\text{im}} = \frac{1}{\varphi_{sl} \Psi_j^l} \sum_k \nu_{jk}^{\text{im}} S_k^{\text{im}}, \quad (22b)$$

$$K_j^s = \frac{1}{\varphi_{sl} \Psi_j^l} \sum_k \nu_{jk}^s S_k^s. \quad (22c)$$

With these definitions the solute transport equations ignoring diffusion/dispersion take the form

$$\frac{\partial \Psi_j^l}{\partial t} + \nabla \cdot \left(\frac{\mathbf{v}}{\mathcal{R}_j} \right) = -\frac{1}{\mathcal{R}_j} \sum_s \nu_{js} I_s, \quad (23)$$

and is valid under the assumption that $\mathcal{R}_j \simeq \text{constant}$.

Two limiting cases are of interest for Eqn.(21). In the absence of a mobile component ($K_j^m \simeq 0$), then \mathcal{R}_j reduces to the usual retardation coefficient based on sorption on stationary mineral and colloid surfaces

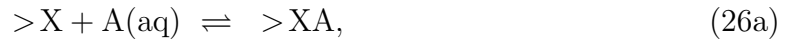
$$\mathcal{R}_j \simeq 1 + K_j^{\text{im}} + K_j^s \geq 1. \quad (24)$$

If, on the other hand, the mobile component is dominant, $K_j^m \gg K_j^{\text{im}} + K_j^s$, then

$$\mathcal{R}_j \simeq \frac{1 + K_j^m}{1 + f_c K_j^m} \leq 1, \quad (25)$$

and the solute advances unretarded and possibly more rapidly than a non-reacting tracer.

3.6.2.3 Principal Results An example is presented in Figure 19 showing the effects of competition between sorption on a stationary mineral surface and mobile and immobile colloids for conditions of local equilibrium surface complexation reactions. The concentration profiles are compared to a non-sorbing tracer. A Darcy flow velocity of 1 m/y with a porosity of 0.5 in a fully saturated porous medium is considered. A total surface site density for colloids and mineral of 50 mol/dm³ is used in the simulations with a colloid concentration of 10⁻⁷ mol/dm³. A single surface complex for colloids and a mineral is used with the complexation reactions



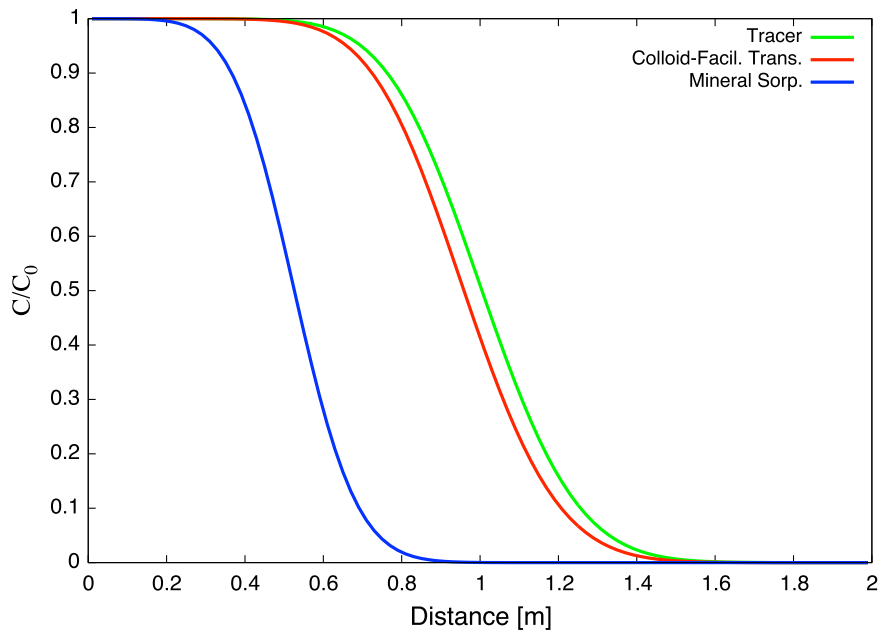


Figure 19. Normalized concentration plotted as a function of distance for a mineral sorbing solute (blue), non-sorbing tracer (green), and colloid-facilitated species transport (red).

with selectivity coefficients of 10^{-4} . The species $>cX$ and $>cXA$ refer to colloids and $>X$ and $>XA$ to the mineral. The simulations are carried out for 0.5 y.

As can be seen from the figure, the mineral sorbing solute is the most retarded and retardation of the colloid-facilitated species is intermediate between no retardation and retardation by the stationary mineral surface.

4 Products Developed

4.1 Publications Published in Peer-Reviewed Journals (in inverse chronological order)

1. Chatterjee, N., S. Lapin, and M. Flury, Capillary forces between sediment particles and an air-water interface, *Environ. Sci. Technol.*, *46*, 4411–4418, 2012.
2. Aramrak, S., M. Flury, and J. B. Harsh, Detachment of deposited colloids by advancing and receding air-water interfaces, *Langmuir*, *21*, 9985–9993, 2011.
3. Shang, J., M. Flury, J. B. Harsh, and R. L. Zollars, Contact angles of aluminosilicate clays as affected by relative humidity and exchangeable cations, *Colloids Surf. Physicochem. Eng. Aspects*, *353*, 1–9, 2010.
4. Mattson, E. D., C. D. Palmer, R. W. Smith, and M. Flury, Centrifuge techniques and apparatus for transport experiments in porous media, in *Physical Modelling in Geotechnics*, edited by Springman, Laue, and Seward, pp. 1465–1470, Taylor and Francis Group, London, 2010.
5. Shang, J., M. Flury, and Y. Deng, Force measurements between particles and the air-water interface: Implications for particle mobilization in unsaturated porous media, *Water Resour. Res.*, *45*, W06420, doi:10.1029/2008WR007384, 2009.
6. Shang, J., M. Flury, J. B. Harsh, and R. L. Zollars, Comparison of different methods to measure contact angles of soil colloids, *J. Colloid Interface Sci.*, *328*, 299–307, 2008.

4.2 Unpublished Reports and Publications in Submission or Preparation

1. Liu, Z., M. Flury, Z. F. Zhang, J. B. Harsh, G. W. Gee, C. E. Strickland, R. E. Clayton, Transport of Europium Colloids in Vadose Zone Lysimeters at the Semi-Arid Hanford Site, submitted to *Environ. Sci. Technol.*, 2012.
2. Liu, Z., M. Flury, J. B. Harsh, J. B. Mathison, C. Vogs, Long-Term Water Flow and Colloid Transport in an Undisturbed Sediment Core at the Hanford Site, submitted to *Water Resources Research*, 2012.
3. Aramrak, S., M. Flury, J. B. Harsh, R. Zollars, H. P. Davis, How Does Colloid Shape Affect Detachment of the Colloids by a Moving Air-Water Interface? (in preparation, to be submitted to *Langmuir*), 2012.
4. Knappenberger, T., M. Flury, E. Mattson, J. B. Harsh, The Role of Flow Rate and Water Content in Colloid Transport in Unsaturated Porous Media. (in preparation, to be submitted to *Environ. Sci. Technol.*), 2012.

4.3 Presentations

1. Aramrak, S., M. Flury, J. B. Harsh, E. Mattson, H. P. Davis, Z. F. Zhang, G. W. Gee, P. Lichtner, Colloid Detachment by a Moving Air-Water Interface: Effect of Particle Shapes, Soil Science Society Annual Meeting Annual Meeting, Cincinnati, Oct. 21-24, 2012.
2. Knappenberger, T., M. Flury, J. B. Harsh, E. Mattson, Using a Geocentrifuge to Study Colloid Transport in Unsaturated Porous Media, Karlsruhe Institute of Technology, Karlsruhe, Germany, May 1, 2012.
3. Knappenberger, T., M. Flury, J. B. Harsh, E. Mattson, Using a Geocentrifuge to Study Colloid Transport in Unsaturated Porous Media, University of Hohenheim, Germany, May 3, 2012.
4. Knappenberger, T., M. Flury, J. B. Harsh, E. Mattson, Z. F. Zhang, G. W. Gee, P. Lichtner, Identifying the Role of Flow Rate and Water Content in Colloid Transport in Unsaturated Porous Media, EGU Annual Meeting in Vienna, Austria, April 22-27, 2012.
5. Knappenberger, T., M. Flury, J. B. Harsh, E. Mattson, Z. F. Zhang, G. W. Gee, P. Lichtner, Using a Geocentrifuge to Study Colloid Transport in Unsaturated Porous Media, Soil Science Society Annual Meeting Annual Meeting, San Antonio, Oct 16-19, 2011.
6. Zhang, Z. F., C. E. Strickland, M. Flury, Z. Liu, G. W. Gee, J. B. Harsh, R. Clayton, Colloid-Facilitated Radionuclide Transport under Field Conditions at Hanford Washington, W1288 Regional Technical Committee Annual Meeting, Honolulu, Hawaii, Jan 2-5, 2012.
7. Cloy, J., M. Flury, J. B. Harsh, and J. B. Boyle, Interactions between Hanford Colloids and Humic Substances: Sorption Mechanisms and Colloid Stabilization, 15th International Humic Substances Society Meeting (IHSS15) on "Humic Substances and the Maintenance of Ecosystem Services", Puerto de la Cruz, Canary Islands, Spain, June 17-July 2, 2010.
8. Flury, M., J. B. Harsh, E. Mattson, Z. F. Zhang, G. W. Gee, P. Lichtner, Colloid Mobilization and Colloid-Facilitated Transport of Radionuclides in a Semi-Arid Vadose Zone, W1288 Regional Technical Committee Annual Meeting, Las Vegas, Jan 2-5, 2010.

9. Stickland, C., F. Zhang, G. Gee, M. Flury, and J. B. Harsh, Field Lysimeters to Study Colloid Transport at the Hanford Site. Annual Meeting of the Soil Science Society of America, Pittsburgh, November 2009.
10. Flury, M., Unresolved Issues in Colloid Transport in Unsaturated Porous Media. Annual Meeting of the Soil Science Society of America, Pittsburgh, November 2009.
11. Flury, M., On the Role of the Liquid-Gas Interface for Colloid Transport in Unsaturated Porous Media. Department of Chemical Engineering, Louisiana State University, Baton Rouge, April 2009.
12. Shang, J., M. Flury, and Y. Deng, Force measurements between particles and the air-water interface: Implications for particle mobilization in unsaturated porous media, *Water Resour. Res.*, 45, W06420, doi:10.1029/2008WR007384, 2009.
13. Flury, M., Colloid Transport in Unsaturated Porous Media. Environmental Science and Research (ESR), Christchurch, New Zealand, January 2009.

4.4 Web Sites

The following web sites provide information about the project. The general web site is

<http://akasha.wsu.edu>.

A list of publication is given at

<http://akasha.wsu.edu/~flury/publications.html>.

Project information is given at

<http://akasha.wsu.edu/~flury/research/colloid2.html>.

Appendix: Reprints of Publications

- Aramrak, S., M. Flury, J. B. Harsh, R. Zollars, H. P. Davis, How Does Colloid Shape Affect Detachment of the Colloids by a Moving Air-Water Interface? (in preparation, to be submitted to *Langmuir*), 2012.
- Liu, Z., M. Flury, Z. F. Zhang, J. B. Harsh, G. W. Gee, C. E. Strickland, R. E. Clayton, Transport of Europium Colloids in Vadose Zone Lysimeters at the Semi-Arid Hanford Site, submitted to *Environ. Sci. Technol.*, 2012.
- Liu, Z., M. Flury, J. B. Harsh, J. B. Mathison, C. Vogs, Long-Term Water Flow and Colloid Transport in an Undisturbed Sediment Core at the Hanford Site, submitted to *Water Resources Research*, 2012.
- Chatterjee, N., S. Lapin, and M. Flury, Capillary forces between sediment particles and an air-water interface, *Environ. Sci. Technol.*, *46*, 4411–4418, 2012.
- Aramrak, S., M. Flury, and J. B. Harsh, Detachment of deposited colloids by advancing and receding air-water interfaces, *Langmuir*, *21*, 9985–9993, 2011.
- Shang, J., M. Flury, J. B. Harsh, and R. L. Zollars, Contact angles of aluminosilicate clays as affected by relative humidity and exchangeable cations, *Colloids Surf. Physicochem. Eng. Aspects*, *353*, 1–9, 2010.
- Mattson, E. D., C. D. Palmer, R. W. Smith, and M. Flury, Centrifuge techniques and apparatus for transport experiments in porous media, in *Physical Modelling in Geotechnics*, edited by Springman, Laue, and Seward, pp. 1465–1470, Taylor and Francis Group, London, 2010.
- Shang, J., M. Flury, and Y. Deng, Force measurements between particles and the air-water interface: Implications for particle mobilization in unsaturated porous media, *Water Resour. Res.*, *45*, W06420, doi:10.1029/2008WR007384, 2009.
- Shang, J., M. Flury, J. B. Harsh, and R. L. Zollars, Comparison of different methods to measure contact angles of soil colloids, *J. Colloid Interface Sci.*, *328*, 299–307, 2008.

Transport of Europium Colloids in Vadose Zone Lysimeters at the Semi-Arid Hanford Site

Ziru Liu^a, Markus Flury^{a,*}, Z. Fred Zhang^b, James B. Harsh^c, Glendon W. Gee^b,
Chris E. Strickland^b, Ray E. Clayton^b

^a *Department of Crop and Soil Sciences, Washington State University, Puyallup, WA 98374, USA*

^b *Pacific Northwest National Laboratory, Richland, WA 99354, USA*

^c *Department of Crop and Soil Sciences, Washington State University, Pullman, WA 99164, USA*

*Corresponding author:

Markus Flury


Department of Crop and Soil Sciences

Washington State University

Puyallup, WA 98374

Phone: 1-253-445-4522

E-mail: flury@wsu.edu

1 

2 The objective of this study was to quantify transport of Eu colloids in the vadose zone at the
3 semi-arid Hanford site (Washington State). Eu-hydroxy-carbonate colloids, $\text{Eu}(\text{OH})(\text{CO}_3)$, were
4 applied to the surface of field lysimeters and migration of the colloids through the sediments was
5 monitored using wick samplers. The lysimeters were exposed to natural precipitation or artificial
6 irrigation. Wick outflow was analyzed for Eu concentrations and particle counts, supplemented
7 by electron microscopy and energy-dispersive x-ray analysis on selected samples. Small amounts
8 of Eu colloids (<1%) were detected in the deepest wick sampler (2.14 m depth) 2.5 months
9 after application and cumulative precipitation of only 20 mm. We observed rapid transport of
10 Eu colloids under both natural precipitation and artificial irrigation, i.e., the leading edge of the
11 Eu colloids moved at a velocity of 3 cm/day within the first two months after application. Large
12 water infiltration, mimicking Chinook snowmelt events in late winter/early spring, caused peaks
13 of Eu in the wick outflow. Elevated Eu concentrations were detected in 1.22 and 2.14 m depth 2.5
14 years after application, which is consistent with long-term recharge estimates at the site. However
15 the main mass of Eu remained in the top 30 cm of the soil.

16 **1 Introduction**

17 The Hanford Nuclear Reservation in Washington State was established in 1943 as a Pu
18 production facility. The site lies within the Pasco Basin of the Columbia River and is char-
19 acterized by a semi-arid, Mediterranean climate. Between 1944 and 1990 more than 100,000
20 tons of nuclear fuel were reprocessed at Hanford, and a considerable amount of radioactive
21 and hazardous waste has been released to the subsurface sediments.¹

22 Colloids are ubiquitous in the pore waters of vadose zone sediments and the movement of
23 colloids can facilitate the transport of sorbing contaminants.² In situ colloid mobilization and
24 transport has been investigated both under water-saturated^{3,4} and unsaturated conditions.^{5,6}
25 Colloid mobilization is generally hindered by increased ionic strength and low pH.⁷ However,
26 in contrast to groundwater systems, in the vadose zone physical factors play a vital role in
27 colloid mobilization.^{8,9} For instance, transient flow conditions can cause colloid mobilization
28 within unsaturated porous media.^{8,10,11}

29 In arid and semi-arid regions such as U.S. Department of Energy's Hanford site, it is
30 expected that colloid transport through the vadose zone is less pronounced than in more
31 humid regions. First, vertical water fluxes in arid and semi-arid regions are limited, and
32 recharge rates are low. Second, the low water contents of soils and sediments in arid and
33 semi-arid regions will limit colloid movement because the thickness of water films may be
34 thinner than colloids themselves, which leads to pinning of colloids to stationary soil particles
35 by capillary forces.^{11,12} However, during intense precipitation events, for instance caused by
36 thunderstorms or snowmelt, a considerable amount of water infiltrates into the soils within
37 a short period of time. This can cause a pronounced infiltration front, which in turn can
38 mobilize and move colloids. Moving infiltration fronts have been shown to mobilize colloids,

39 both in laboratory column experiments^{4,8,11} and field studies.^{5,13,14}

40 Due to their mobility in the vadose zone, colloids have the potential to facilitate the
41 transport of contaminants. Contaminants can either be sorbed to in situ colloids or form
42 colloidal particles themselves.^{2,3} Radionuclide contaminants tend to sorb strongly to soil
43 minerals and some radionuclides can form intrinsic colloids, i.e., form their own colloidal
44 phase.² Colloid-facilitated radionuclide transport is of particular concern at nuclear weapons
45 facilities and test sites. At the Nevada Test Site in the US¹⁵ and the Mayak Production Site in
46 Russia,¹⁶ colloid-facilitated radionuclide transport has been reported to have occurred under
47 water-saturated conditions, but there is currently no field evidence of such transport at the
48 semi-arid Hanford site; even though laboratory studies using Hanford sediments have shown
49 colloid-facilitated transport of Cs under both saturated^{17,18} and unsaturated conditions.^{19,20}

50 At the Hanford site, colloid-facilitated radionuclide transport is of concern for elements
51 like Cs, Sr, Pu, Am, and Eu. While Cs and Sr can associate with native colloids present in
52 the subsurface,¹⁷⁻²¹ elements like Pu, Am, or Eu can form intrinsic colloids.^{22,23} Radioactive
53 Eu and Pu are of concern in contaminated soils in the Hanford 100 Area²⁴ and also occur in
54 waste tanks.²⁵

55 Although, climatic conditions and the thick vadose zone at Hanford are not conducive
56 for colloid movement in general, there are certain circumstances when colloid transport may
57 be occurring. At Hanford, most precipitation occurs during the winter months, and some of
58 the precipitation is in form of snow.²⁶ Warm, adiabatic winds descending from the Cascade
59 Mountains occur frequently during winter time. These winds, called Chinook, can cause
60 snow to melt within a short period of time, leading to considerable water infiltration into the
61 soils and sediments.^{26,27} In addition, numerous intentional (unlined ponds, cribs, trenches)
62 and unintentional discharges (spills, waterline leaks), exceeding normal recharge rates, have

63 occurred at various locations at the Hanford site.¹ Under such conditions, colloid mobilization
64 and transport is likely.

65 Several field lysimeter stations have been installed and operated at the Hanford site to
66 study recharge, evapotranspiration, and mineral weathering.^{28,29} These lysimeters are excel-
67 lent tools to study colloid transport under field conditions. The objective of our study was
68 to quantify colloid transport under field conditions at the Hanford site using field lysimeters.
69 Eu-hydroxy-carbonate colloids were applied to the surface of field lysimeters, and the lysime-
70 ters were either exposed to natural precipitation or artificial irrigation. We hypothesized that
71 transient infiltration events are conducive for mobilization and transport of Eu colloids in the
72 near-surface vadose zone at Hanford.

73 **2 Materials and Methods**

74 **Hanford Field Lysimeters.** The study was conducted at the Hanford's 300 North Lysime-
75 ter site. A detailed description of the facility is given elsewhere.^{30,31} The facility consists of
76 six non-weighing lysimeters, each 7.6 m deep. Two of the lysimeters are 2.7 m in diameter
77 and four lysimeters are 0.6 m in diameter (Figure 1). The 300 Area Lysimeters were installed
78 in 1978 and all of them were kept free of vegetation for the past 34 years. These lysimeters
79 were filled with a uniform sandy layer consisting of Hanford sediments and had a 0.3 m thick
80 coarse sand layer at 5.7 m depth. The uniform sandy layer consists of 95% sand, 3% silt, 1%
81 clay, and 1% gravel defined as material between 2 and 10 mm.³² For our study, we used four
82 lysimeters: the South Caisson (SC) and Lysimeters 1, 2, and 3 (Figure 1).

83 Soil water content in each lysimeter from 0.3 to 7.6 m (1 to 25 feet) depth was periodically
84 monitored by using a neutron probe (Campbell Pacific Nuclear Corp., CA). The probe was

85 inserted into the lysimeters vertically through aluminum access tubes (Figure 1).

86 We installed fiberglass wicks to collect pore water samples from the lysimeters under
87 unsaturated conditions. Fiberglass wicks have been found to be useful devices to collect
88 pore water and soil colloids.^{33,34} The wicks were installed into the lysimeters in horizontal
89 orientation at 0.31, 0.61, 1.22 and 2.14 m (1, 2, 4, and 7 feet) depths. In Lysimeter 2, the
90 wicks were installed at 0.61, 0.92, 1.22 and 2.14 m (2, 3, 4, and 7 feet) depths, because the
91 access port at the 1-foot depth was inaccessible. A 50-cm long piece of the wicks, enclosed in
92 a PVC tube, was used as a hanging water column to provide tension for pore water sampling.
93 This tension matches the water potential in the lysimeters³⁰ and therefore provides little
94 disturbance of the flow field. A screw cap of a 250 mL polypropylene bottle was glued to the
95 end of the PVC tube so that a sampling bottle could be attached to the end of the wicks for
96 outflow collection. A little hole was drilled into the screw cap to allow pressure equilibration.
97 When outflow was collected, the sampling bottles were always replaced with a new, unused
98 bottle.

99 The PVC tube along the hanging water column had an access port from which we could
100 pull out fibers from the wick to examine the wick quality over the course of the experiment.
101 Figure S1 (Supporting Information) shows an example of the fiber conditions in February 2010
102 and March 2012. The images show the smooth fiber surface covered with colloidal materials,
103 i.e., native soil minerals, like kaolinite and quartz. No clogging of fibers was observed.

104 **Colloid Materials.** Eu-hydroxy-carbonate colloids ($\text{Eu}(\text{OH})(\text{CO}_3)$) were synthesized
105 in our laboratory as described in the supporting information. Europium is frequently used
106 as an analogue to study the geochemistry of radioactive actinides, such as Am(III), Cm(III),
107 and Pu(III).³⁵⁻³⁷ We used the Eu-hydroxy-carbonate colloids as a representative intrinsic

108 radionuclide colloid. The standard solubility product of $\text{Eu}(\text{OH})(\text{CO}_3)$ has been reported to
109 be $\log K_{sp} = -20$,³⁸ and the dominant species of Eu is expected to be solid $\text{Eu}(\text{OH})(\text{CO}_3)$
110 under the pH conditions of our experiments (pH 8 to 8.5).^{39,38} A flocculation test with
111 1 M CaCl_2 and Eu colloids in a Hanford pore water sample verified that indeed all Eu was
112 present in the particulate phase.

113 The Eu particles showed some non-uniformity in their size distribution, with a mean and
114 standard deviation of the diameter of 108 ± 17 nm (measured from TEM and SEM images,
115 Figure 2). The specific density of the particles was 8.78 g/cm^3 (theoretically calculated with
116 crystallographic unit-cell parameters obtained from XRD), the electrophoretic mobility was
117 $-3.2 \pm 0.1 (\mu\text{m/s})(\text{V/cm})$ (measured by dynamic light scattering at pH = 8 and 1 mM NaCl),
118 and the air-water contact angle was 64 degrees (measured by the sessile drop method using
119 a digital goniometer as described in Shang et al.⁴⁰).

120 **Colloid Application and Irrigation Scenarios.** Colloid suspension (number con-
121 centration: 4.1×10^{13} number/L; mass concentration: 237.7 mg/L) was transferred into a
122 backpack sprayer (Solo 3-Gallon Standard Piston Pump Sprayer, Gempler's). We performed
123 initial uniformity tests in the laboratory by spraying water on a filter paper and collection
124 trays were used to determine the application rate. The colloid suspension was then manually
125 sprayed onto the lysimeter surface. A total of 3 mm of the suspension was applied to the
126 lysimeters on March 11, 2009.

127 Whereas the South Caisson Lysimeter was uncovered, receiving natural precipitation,
128 and allowing evaporation, Lysimeters 1, 2, and 3 were irrigated and then covered between
129 irrigations with a styrofoam-insulated plastic cap to minimize evaporation. Lysimeter 1
130 received an annual irrigation of 124 mm/year, which equals twice the 26-year average of the

131 yearly drainage at the site.³² Lysimeter 2 was irrigated with four times the natural drainage,
132 and Lysimeter 3 received an additional 100 mm/year simulated Chinook snowmelt event
133 (Table 1).

134 Irrigation was performed with a movable sprinkler and started in April 2009. Irrigation
135 distribution and intensity were guided by the typical natural rainfall intensities recorded
136 at the Hanford Meteorological Station²⁶ and the expected recharge. In the hot summer
137 months (June, July, August), no irrigation was applied, as the small amount of precipitation
138 during these months evaporates back into the atmosphere. We scaled the remaining irrigation
139 proportional to the long-term natural rainfall (Lysimeter 1), and used multifold irrigations for
140 Lysimeters 2 and 3 (Figure 3). The chemical composition of the irrigation water mimicked
141 that of the natural precipitation at the site (we collected and analyzed rain water from
142 the Hanford Meteorological Station in February 2009): 0.0527 mM Na⁺, 0.0417 mM K⁺,
143 0.017 mM Ca²⁺, 0.0434 mM Cl⁻, 0.0395 mM NO₃⁻. The pH was 6.4 and the ionic strength
144 0.1 mM.

145 **Colloid Sampling, Characterization, and Quantification.** Outflow pore water
146 from the fiberglass wicks was collected once a month by replacing the sample bottles. The
147 collected pore water was first sonicated for 5 minutes and then analyzed for outflow volume,
148 pH, electric conductivity, electrophoretic mobility, particle size, particle counts, and Eu mass
149 concentration. Electrophoretic mobilities and particle counts were measured by using dy-
150 namic light scattering (ZetaSizer 3000HSa, Malvern Instruments Ltd., Malvern, UK), and
151 repeated 5 times for each sample. Particle counts were only used as a qualitative indicator
152 for the presence of particles in the outflow. Selected samples were examined microscopically
153 using Transmission and Scanning Electron Microscopy, and Energy Dispersive X-ray Anal-

154 ysis (JEOL 1200 EX Transmission Electron Microscope; Hitachi S-570 Scanning Electron
155 Microscope; Philips CM-200).

156 Vertical soil cores were collected on October 14, 2010 (1.5 years after start of the irriga-
157 tion) and March 23, 2012 to assess depth distribution of Eu. Three cores were taken from
158 each lysimeter from the surface to a depth of 30 cm in 5-cm increments. For the South Cais-
159 son, cores were taken with a 54-mm (i.d.) bulk density sampler (Soil Moisture Equipment
160 Co.). For Lysimeters 1, 2, and 3, soil cores with i.d. of 23 mm were taken. Europium was
161 extracted from the soil cores as described in the supporting information. No Eu was detected
162 in non-contaminated soil samples.

163 The amount of Eu colloids was quantified by measuring the Eu concentration in the
164 outflow samples or soil extracts. The pH of the samples was adjusted to pH below 3 by
165 adding HCl to dissolve the Eu particles. It is expected that $\text{Eu}(\text{OH})(\text{CO}_3)$ will completely
166 dissolve below pH 5.5.^{39,38} Then an aliquot of the sample was filtered through a 0.22 μm
167 membrane. The acidified filtrate was then analyzed for Eu by using ICP-MS (Agilent 7700,
168 Quantum Analytics, Inc.). The detection limit for Eu analysis at the 99% confidence interval,
169 determined from blank samples,⁴¹ was 0.37 $\mu\text{g}/\text{L}$. The measured concentration of dissolved
170 Eu is used as a proxy for the Eu colloids, and we hereafter report only the Eu concentrations.
171 The wick samples are presented as mass of Eu per volume of outflow water, and the soil core
172 samples are presented as mass of Eu per volume of bulk soil.

173 **3 Results**

174 **Precipitation, Irrigation, and Wick Outflow.** Figure 3 shows the daily natural precip-
175 itation and the irrigation from January 2009 to March 2012 for each of the lysimeters. The

176 daily precipitation (South Caisson) was taken from the Hanford Meteorological Station²⁶ and
177 the irrigation (Lysimeters 1, 2, 3) was measured when it was applied. The natural precipi-
178 tation occurred in much greater frequency than the irrigation, but the seasonal pattern was
179 similar, although not identical, because the irrigation was based on the long-term precipita-
180 tion record. The Chinook events applied to Lysimeter 3 are indicated by arrows. In 2009,
181 the Chinook simulation was applied on two separate days. The total application during a
182 Chinook event exceeded 100 mm because the Chinook was added to the regular irrigation in
183 that month.

184 The cumulative outflow collected from each wick sampler is shown in Figure S2 (Sup-
185 porting Information). The fiberglass wick samplers performed well in collecting soil waters
186 at different depths for all the lysimeters; i.e., all wicks collected outflow. Compared with the
187 cumulative inflow, the wicks collected generally less water; however, in some cases the wick
188 outflow exceeded the inflow. Particularly, the 0.92 m (3 feet) wick in Lysimeter 2 was efficient
189 in collecting outflow, exceeding the inflow by more than a factor two.

190 For the South Caisson, the top two wicks consistently collected less outflow than the
191 bottom two wicks, which we attribute to evaporation from the soil surface affecting the top
192 most wicks. The wick outflow in the South Caisson and Lysimeter 1 were similar, although
193 the cumulative inflow was much larger for the South Caisson. This was because Lysimeter 1
194 had a cover to prevent evaporation and the irrigation was based on long-term drainage rates.
195 Our data indicate that we indeed could mimic the long-term drainage.

196 **Colloid Transport in Lysimeters.** Figure 3 shows the Eu concentrations measured
197 in the wick outflow (as a proxy for the Eu colloids). Particle counts and electrophoretic
198 mobilities are shown in Figure S3 (Supporting Information). Europium was applied to the

199 lysimeters on March 11, 2009 (Julian day 70, indicated by the vertical arrow), and first outflow
200 samples were collected on May 18, 2009 (Julian day 138). Europium was detected in all four
201 lysimeters on the first sampling date. The upper wick samplers (0.31 and 0.61-m depth) had
202 higher Eu concentrations than the lower wicks (1.22 and 2.14-m depth). Following the first
203 detection of Eu, there was a continuous outflow of Eu in all lysimeters, with Eu concentrations
204 less than 40 $\mu\text{g/L}$. Europium concentrations in outflow waters were generally larger in the
205 irrigated lysimeters than in the non-irrigated South Caisson.

206 While the Eu data for the South Caisson did not show a clear breakthrough pattern,
207 we did detect Eu peaks in the irrigated lysimeters (Figure 3). Lysimeter 1 shows a Eu
208 peak on June 29, 2009 (Julian day 180) at 1.22-m depth and on July 16, 2009 (Julian day
209 197) at 2.14-m depth. Similar patterns could be observed for Lysimeter 2 and 3. A second
210 peak of Eu could be detected in Spring 2010 in all lysimeters, consistent with the elevated
211 precipitation and irrigation during the preceding winter season. The Chinook events in
212 Lysimeter 3 caused pronounced water infiltration and produced Eu peaks in the wick outflow,
213 particularly in 2009. In 2010, the topmost wick (0.31 m) showed elevated Eu concentrations
214 as a result of the Chinook event; correspondingly, there were increased particle counts in the
215 wick outflow. In Fall/Winter 2011, large Eu peaks were detected in Lysimeters 1, 2, and 3.
216 The Eu concentrations in the wick outflow were several orders of magnitude larger than the
217 previous concentrations, particularly in Lysimeters 1 and 3. No elevated Eu concentrations
218 were observed in the non-irrigated South Caisson though.

219 The particles in the wick outflow had electrophoretic mobilities between -0.5 to -3
220 $(\mu\text{m/s})/(\text{V/cm})$ (Figure S3, Supporting Information). At the pH of the wick outflow (pH 8.2
221 to 8.5), measured electrophoretic mobility of the water-dispersible, native colloidal fraction
222 of the Lysimeter sediments was $-2.5 (\mu\text{m/s})/(\text{V/cm})$, and that of the Eu colloids was -3.2

223 ($\mu\text{m/s})/(\text{V/cm})$. This indicates that the outflow samples contained native colloidal material
224 from the sediments, although the electrophoretic mobility data of the outflow samples have
225 to be regarded as qualitative only, because the particle counts were very low most of the time.
226 SEM images of wick outflow reveal native colloidal materials (platy clay minerals, Figure 4a)
227 as well as spherical particles (Figure 4b), which we identified as Eu colloids with the help of
228 energy-dispersive x-ray analysis (Figure S4, Supporting Information).

229 Soil cores from the top 30-cm of the lysimeters, taken on October 14, 2010 (Julian day
230 652), indicated that most of the Eu was located in the top 10 cm of the soil (Figure S5,
231 Supporting Information). There was considerable variance in the amount of Eu recovered
232 from the individual soil cores, which we attribute to analytical uncertainties and spatial
233 non-uniformity of the Eu distribution inside the lysimeter. A *t*-test showed no significant
234 differences between the mass recoveries of the soil cores (at a significance level of 5%), except
235 between Lysimeter 1 and 2. In the South Caisson, most of the Eu was located in 0 to 5-cm
236 depth, whereas in the other lysimeters, most of the Eu was in the 0 to 10-cm depth interval.
237 Another set of soil cores taken on March 23, 2012, showed that the bulk of the Eu was still
238 located in the top 30 cm of the soil (Figure S5, Supporting Information) and the variance of
239 the amount of Eu recovered was similar to the first sampling date. The *t*-test indicated no
240 significant differences among the lysimeters with respect to the mass recovery.

241 **Water Contents.** The South Caisson, which was exposed to atmospheric conditions,
242 had considerable fluctuations of the water contents in the top 2 m (Figure S6, Supporting
243 Information). These fluctuations were caused by seasonal changes in precipitation and evap-
244 oration. Infiltration of precipitation, as observed in late spring, penetrated to about 2-m
245 depth. Below 2-m depth, the water content in the South Caisson represents the long-term

246 steady-state condition.

247 The irrigated lysimeters (Lysimeter 1, 2, and 3) showed a distinct infiltration front caused
248 by the winter irrigation (Figure S6, Supporting Information). The infiltration front became
249 most pronounced in spring 2010, and the penetration depths of the fronts corresponded to the
250 amount of cumulative irrigation in each lysimeter: 2.5 m in Lysimeter 1 (120 mm infiltration
251 until March 2010), 3.5 m in Lysimeter 2 (242 mm infiltration), and 4 m in Lysimeter 3 (342
252 mm infiltration).

253 **4 Discussion**

254 **Eu Colloid and In Situ Particle Transport.** Electrophoretic mobility data and elec-
255 tron microscopy images indicate that wick outflow consisted of both Eu colloids and native
256 particles from the sediments. Given the rather small difference in electrophoretic mobility,
257 we conclude that the Eu colloids and native particles were translocated individually, but
258 via similar transport mechanisms. Movement of native particles along with radionuclide col-
259 loids has been reported from other field^{15,16} and laboratory studies¹⁷⁻²⁰ and is therefore not
260 unexpected.

261 **Total Amount of Eu Colloids Translocated.** There were considerable differences
262 in the amounts of Eu collected in the different wicks (Table 2). This was in part due to
263 considerable variability in collection efficiencies for water outflow among the wicks. This
264 different collection efficiency is likely because of non-uniform contact of the wicks with the
265 surrounding soil or non-uniform flow pathways in the lysimeters. Generally, the wicks that
266 showed larger amounts of Eu outflow also had higher water outflows (Table 2). The two
267 topmost wicks in the South Caisson were affected by evaporation, and collected less outflow

268 than the two bottom wicks and the least amounts of Eu. Over the experimental period,
269 much more Eu was recovered from the soil cores (61 to 112%) than from the wick outflow
270 (0.02 to 11%). This suggests that only a small fraction of Eu colloids was mobilized by the
271 precipitation and irrigation events into deeper soil depth, and the bulk of Eu remained close
272 to the soil surface.

273 Such significant retention of colloids and radionuclides in the surface soil was also seen
274 in other field studies. From a field study in Rocky Flats, CO, Ryan et al.⁵ reported that Pu
275 transport was largely confined to the upper 15 to 20 cm of the soil. Plutonium was associated
276 with soil particles and possibly also transported as an intrinsic colloid.⁵ Similarly, Crancon
277 et al.⁴² reported that several years after surface contamination with U, only a small fraction
278 of U moved farther than 20 cm, and this fraction was associated with water-dispersible humic
279 colloids. Burkhardt et al.⁴³ found surface applied polystyrene beads to be mainly confined
280 to the soil surface after 100 mm of rainfall simulation, with only a small fraction detected in
281 deeper layers.

282 **Eu Colloid Transport and Irrigation Patterns.** Within the first two months after
283 Eu application, the lysimeters (South Caisson, Lysimeters 1, 2, 3) received a total of 20, 29,
284 57, and 159 mm precipitation/irrigation, respectively. All lysimeters contained Eu in the
285 pore water at all sampling depths at the first sampling date; however, the concentrations
286 of Eu were larger in the irrigated Lysimeters 1, 2, and 3 than in the non-irrigated South
287 Caisson. While it is generally observed that increasing water content or flow rates lead to
288 more colloid mobilization, particularly in laboratory studies,^{10,13,20,44,45} in some field studies
289 a poor correlation between rainfall intensity and colloid transport was reported.^{5,46} Under
290 field conditions, non-uniform flow pathways such as macropore flow can cause exhaustion of

291 dispersible particles moving with the infiltration water.⁴⁷

292 Transient flow has been recognized as a major driver for colloid mobilization and trans-
293 port,^{8,11,20,47} and our results indicate that transient natural precipitation or irrigation causes
294 colloid transport. Extended dry periods between infiltration events have also been found
295 to promote colloid mobilization by inducing physical strains on soil particles during drying
296 which leads to an increase in dispersible particles.⁴⁷ At the Hanford site, the extensive dry
297 period during summer is likely conducive for colloid mobilization during the following wet
298 winter period.

299 **Mechanisms of Eu Colloid Transport.** Most of the Eu peaks were observed from
300 2009 to 2010 (Julian day 138 to 500). Afterwards, the Eu concentration curves tailed off
301 except for several larger peaks during winter 2011. In previous field studies, similar patterns
302 of tailing off of colloid concentrations have been reported.^{5,13,48,49} Although the experimental
303 time and irrigation frequency of those studies were not as long or as often as in our study, in
304 general, the first flush or initial infiltration event led to the highest colloid release followed by
305 a lower, more stable colloid release. We attribute the large peaks during winter 2011 to the
306 movement of Eu with matrix water flow, as the transport velocity for these large peaks (0.12
307 to 0.22 cm/d) is consistent with the long-term recharge estimates at the Hanford site.^{28,30,32}

308 Although Eu colloids had a negative surface charge, the bulk of the Eu was retained
309 in the top 30-cm of the soil. Such pronounced surface retention in field experiments has
310 also been reported for negatively-charged polystyrene colloids.⁴³ DLVO calculations (using
311 measured surface properties and solution chemistry and the DLVO theory described in Shang
312 et al.¹¹) indicate that our Eu colloids would not be attracted to the solid phase, as there was
313 a repulsive energy barrier of more than 100 kT. Colloids were therefore retained most likely

314 by straining or wedging,^{50,51} as well as trapping in water films.¹² Temporarily retained
315 colloids can be later dislodged and mobilized with increasing water content, moving air-water
316 interfaces, and re-connected water paths.

317 The observed rapid movement of Eu in the Hanford Lysimeters was likely caused by
318 transient water flow or preferential flow near the soil surface. Small amounts of Eu colloids
319 could be translocated by natural precipitation and irrigation to a depth of 2.14 m within
320 2.5 months. This corresponds to an overall colloid transport velocity of 3 cm/d. This ve-
321 locity suggests that some of the Eu was transported by preferential flow. Based on a review
322 of field experiments where preferential flow was reported, Nimmo⁵² deduced a maximum
323 velocity of 8 cm/d (geometric mean) for the case of intermittent infiltration. Velocities of
324 2 to 40 cm/d for preferential flow of colloids has been reported from a field study where
325 polystyrene colloids were applied to the surface of an agricultural soil followed by simulated
326 rainfall irrigation.⁴³ Although not directly comparable, our measured velocity lies within the
327 same order of magnitude as those reported from other field experiments where preferential
328 flow was inferred.⁵²

329 Based on mechanistic laboratory studies, it is likely that the fast moving Eu colloids
330 were mobilized and translocated within preferential flow pathways by moving air-water in-
331 terfaces.^{20,53-57} Moving air-water interfaces have been demonstrated to be very effective in
332 mobilizing and translocating colloids from surfaces,^{54,58,59} flow channels,^{57,60} and porous me-
333 dia.^{20,53} Repeated infiltration events, such as the ones experienced in our field experiment,
334 will likely cause colloid mobilization and translocations via air-water displacement fronts.

335 **Implications for Colloid Transport and Mobilization at Hanford Site.** Our
336 results demonstrate that under field conditions with transient flow, colloid mobilization and

337 transport occurred in Hanford sediments. Small amounts of Eu colloids could be translocated
338 by natural precipitation or irrigation to a depth of 2.14 m within 2.5 months, corresponding
339 to an overall colloid transport velocity of 3 cm/d. Estimates of recharge at the Hanford site
340 range from 1 to 100 mm/year.^{28,30,32} Considering a volumetric water content of 0.1 m³/m³,
341 the recharge estimates translate to a pore water velocity of 1 to 100 cm/year (equal to 0.003
342 to 0.3 cm/d), which is considerably slower than what we observed based on the fast Eu
343 transport. This indicates that the near surface transport of a portion of Eu can be rapid,
344 exceeding recharge-based velocity estimates by more than a factor of ten. While a small
345 portion of Eu colloids moved rapidly by preferential flow, a larger peak of Eu, however,
346 moved at slower rate, consistent with long-term recharge.

347 While semi-arid conditions in general are not conducive for colloid transport, the dry
348 summer and wet winter climate at the Hanford site leads to infiltration fronts that penetrate
349 the soil to several meters. These infiltration fronts with their associated moving air-water
350 interfaces provide a means for mobilization and transport of colloids in the near-surface vadose
351 zone.

352 **Supporting Information Available**

353 Supporting information include details on colloid synthesis, Eu extractions, images of fiber-
354 glass wicks, time series of wick outflow, energy-dispersive x-ray spectra, concentration-depth
355 profiles of Eu in lysimeters, and water content profiles for each lysimeters. This information
356 is available free of charge via the Internet at <http://pubs.acs.org>.

357 **Acknowledgments**

358 This material is based upon work supported by the US Department of Energy, Office of

359 Science (BER), under Award No. DE-FG02-08ER64660. We thank Jon Mathison for help
360 with the field experiments and Jeff Boyle for Eu colloid synthesis and Eu analysis. We thank
361 the Franceschi Microscopy & Imaging Center for access to their facility and Chris Davitt
362 for help with the use of the microscopes. We further thank anonymous reviewers for their
363 comments.

364 **Literature Cited**

- 365 (1) Gephart, R. E. *Hanford: A conversation about nuclear waste and cleanup*; Battelle
366 Press: Columbus, Ohio, 2003.
- 367 (2) Honeyman, B. D. Colloidal culprits in contamination. *Nature* **1999**, *397*, 23–24.
- 368 (3) Ryan, J. N.; Elimelech, M. Colloid mobilization and transport in groundwater. *Colloids*
369 *Surf. Physicochem. Eng. Aspects* **1996**, *107*, 1–56.
- 370 (4) Lenhart, J. J.; Sayers, J. E. Colloid mobilization in water-saturated porous media under
371 transient chemical conditions. *Environ. Sci. Technol.* **2003**, *37*, 2780–2787.
- 372 (5) Ryan, J. N.; Illangasekare, T. H.; Litaor, M. I.; Shannon, R. Particle and plutonium
373 mobilization in macroporous soils during rainfall simulations. *Environ. Sci. Technol.*
374 **1998**, *32*, 476–482.
- 375 (6) Schelde, K.; Moldrup, P.; Jacobsen, O. H.; de Jonge, H.; de Jonge, L. W.; Komatsu, K.
376 Diffusion-limited mobilization and transport of natural colloids in unsaturated macrop-
377 ous soil. *Vadose Zone J.* **2002**, *1*, 125–136.
- 378 (7) Kretzschmar, R.; Borkovec, M.; Grolimund, D.; Elimelech, M. Mobile subsurface colloids
379 and their role in contaminant transport. *Adv. Agron.* **1999**, *66*, 121–193.
- 380 (8) Sayers, J. E.; Lenhart, J. J. Colloid mobilization and transport within unsaturated
381 porous media under transient-flow conditions. *Water Resour. Res.* **2003**, *39*, 1019,
382 doi:10.1029/2002WR001370.
- 383 (9) DeNovio, N. M.; Sayers, J. E.; Ryan, J. N. Colloid movement in unsaturated porous
384 media. *Vadose Zone J.* **2004**, *3*, 338–351.

- 385 (10) Zhuang, J.; McCarthy, J. F.; Tyner, J. S.; Perfect, E.; Flury, M. In-situ colloid mo-
386 bilization in Hanford sediments under unsaturated transient flow conditions: Effect of
387 irrigation pattern. *Environ. Sci. Technol.* **2007**, *41*, 3199–3204.
- 388 (11) Shang, J.; Flury, M.; Chen, G.; Zhuang, J. Impact of flow rate, water content, and cap-
389 illary forces on *in situ* colloid mobilization during infiltration in unsaturated sediments.
390 *Water Resour. Res.* **2008**, *44*, W06411, doi:10.1029/2007WR006516.
- 391 (12) Wan, J. M.; Tokunaga, T. K. Film straining of colloids in unsaturated porous media:
392 conceptual model and experimental testing. *Environ. Sci. Technol.* **1997**, *31*, 2413–2420.
- 393 (13) El-Farhan, Y. H.; Denovio, N. M.; Herman, J. S.; Hornberger, G. M. Mobilization
394 and transport of soil particles during infiltration experiments in an agricultural field,
395 Shenandoah valley, Virginia. *Environ. Sci. Technol.* **2000**, *34*, 3555–3559.
- 396 (14) Kaplan, D. I.; Bertsch, P. M.; Adriano, D. C.; Miller, W. P. Soil-borne mobile colloids
397 as influenced by water flow and organic carbon. *Environ. Sci. Technol.* **1993**, *27*, 1193–
398 1200.
- 399 (15) Kersting, A. B.; Efurud, D. W.; Finnegan, D. L.; Rokop, D. J.; Smith, D. K.; Thompson,
400 J. L. Migration of plutonium in ground water at the Nevada Test Site. *Nature* **1999**,
401 *397*, 56–59.
- 402 (16) Novikov, A. P.; Kalmykov, S. N.; Utsunomyia, S.; Ewing, R. C.; Horreard, F.; Merkulov,
403 A.; Clark, S. B.; Tkachev, V.; Myasoedov, B. F. Colloid transport of plutonium in the
404 far-field of the Mayak production association, Russia. *Science* **2006**, *314*, 638–641.
- 405 (17) Flury, M.; Mathison, J. B.; Harsh, J. B. *In situ* mobilization of colloids and transport
406 of cesium in Hanford sediments. *Environ. Sci. Technol.* **2002**, *36*, 5335–5341.

- 407 (18) Zhuang, J.; Flury, M.; Jin, Y. Colloid-facilitated Cs transport through water-saturated
408 Hanford sediment and Ottawa sand. *Environ. Sci. Technol.* **2003**, *37*, 4905–4911.
- 409 (19) Chen, G.; Flury, M.; Harsh, J. B.; Lichtner, P. C. Colloid-facilitated transport of cesium
410 in variably-saturated Hanford sediments. *Environ. Sci. Technol.* **2005**, *39*, 3435–3442.
- 411 (20) Cheng, T.; Sayers, J. E. Colloid-facilitated transport of cesium in vadose-zone sediments:
412 the importance of flow transients. *Environ. Sci. Technol.* **2010**, *44*, 7443–7449.
- 413 (21) Turner, N. B.; Ryan, J. N.; Sayers, J. E. Effect of desorption kinetics on colloid-facilitated
414 transport of contaminants: Cesium, strontium, and illite colloids. *Water Resour. Res.*
415 **2006**, *42*, W12S09, 10.1029/2006WR004972.
- 416 (22) Kim, J. I. Actinide colloid generation in groundwater. *Radiochim. Acta* **1991**, *52/53*,
417 71–81.
- 418 (23) Runde, W. Geochemical interactions of actinides in the environment. In *Geochemistry*
419 *of Soil Radionuclides*; Zhang, P.-C.; Brady, P. V., Eds.; Soil Science Society of America,
420 Special Publication Nr. 59: Madison, WI, 2002; pp 21–44.
- 421 (24) Harmon, H. D. Trends in actinide processing at Hanford. *J. Alloys Compd.* **1994**, *213*,
422 341–343.
- 423 (25) Krupka, K. M.; Serne, R. J. *Geochemical factors affecting the behavior of antimony,*
424 *cobalt, europium, technetium, and uranium in vadose sediments*; Pacific Northwest Na-
425 tional Laboratory, PNNL-14126: Richland, Washington, 2002.
- 426 (26) Hanford Meteorological Station *Monthly and Annual Precipitation*; Pacific Northwest
427 National Laboratory: <http://hms.pnl.gov>, accessed March 2012, 2012.

- 428 (27) Gee, G. W.; Hillel, D. Recharge in arid regions: Review and critique of estimation
429 methods. *Hydrol. Processes* **1988**, *2*, 255–266.
- 430 (28) Gee, G. W.; Fayer, M. J.; Rockhold, M. L.; Campbell, M. D. Variations in recharge at
431 the Hanford site. *Northwest Sci.* **1992**, *66*, 237–250.
- 432 (29) Fayer, M. J.; Szecsody, J. E. *Recharge Data Package for the 2005 Integrated Disposal*
433 *Facility Performance Assessment*; PNNL-14744, Pacific Northwest National Laboratory:
434 Richland, Washington, 2004.
- 435 (30) Gee, G. W. Recharge at the Hanford site: Status report Technical report Pacific North-
436 west National Laboratory, Richland, WA, 1987.
- 437 (31) Gee, G. W.; Campbell, M. D.; Campbell, G. S.; Campbell, J. H. Rapid measurement of
438 low soil water potentials using a water activity meter. *Soil Sci. Soc. Am. J.* **1992**, *56*,
439 1068–1070.
- 440 (32) Gee, G. W.; Keller, J. M.; Ward, A. L. Measurement and prediction of deep drainage
441 from bare sediments at a semiarid site. *Vadose Zone J.* **2005**, *4*, 32–40.
- 442 (33) Czigany, S.; Flury, M.; Harsh, J. B.; Williams, B. C.; Shira, J. M. Suitability of fiberglass
443 wicks to sample colloids from vadose zone pore water. *Vadose Zone J.* **2005**, *4*, 175–183.
- 444 (34) Shira, J. M.; Williams, B. C.; Flury, M.; Czigany, S.; Tuller, M. Sampling silica and
445 ferrihydrite colloids with fiberglass wicks under unsaturated flow conditions. *J. Environ.*
446 *Qual.* **2006**, *35*, 1127–1134.
- 447 (35) Krauskopf, K. B. Thorium and rare-earth metals as analogs for actinide elements. *Chem.*
448 *Geol.* **1986**, *55*, 323–335.

- 449 (36) Stumpf, T.; Bauer, A.; Coppin, F.; Fanghänel, T.; Kim, J. I. Inner-sphere, outer-sphere
450 and ternary surface complexes: a TRLFS study of the sorption process of Eu(III) onto
451 smectite and kaolinite. *Radiochim. Acta* **2002**, *90*, 345–349.
- 452 (37) Rabung, T.; Pierret, M. C.; Bauer, A.; Geckeis, H.; Bradbury, M. H.; Baeyens, B.
453 Sorption of Eu(III)/Cm(III) on Ca-montmorillonite and Na-illite. Part 1: Batch sorption
454 and time-resolved laser fluorescence spectroscopy experiments. *Geochim. Cosmochim.*
455 *Acta* **2005**, *69*, 5393–5402.
- 456 (38) Rorif, F.; Fuger, J.; Desreux, J. F. Thermochemistry of selected trivalent lanthanide and
457 americium compounds: orthorhombic and hexagonal hydroxycarbonates. *Radiochim.*
458 *Acta* **2005**, *93*, 103–110.
- 459 (39) Baik, M.; Cho, W.; Hahn, P. Effects of speciation and carbonate on the sorption of Eu
460 (III) onto granite. *Environ. Eng. Res.* **2004**, *9*, 160–167.
- 461 (40) Shang, J.; Flury, M.; Harsh, J. B.; Zollars, R. L. Comparison of different methods to
462 measure contact angles of soil colloids. *J. Colloid Interface Sci.* **2008**, *328*, 299–307.
- 463 (41) Skoog, D. A.; West, D. M.; Holler, F. J. *Fundamentals of Analytical Chemistry*, 7th ed.;
464 Saunders College Publishing: Fort Worth, 1996.
- 465 (42) Crancon, P.; Pili, E.; Charlet, L. Uranium facilitated transport by water-dispersible
466 colloids in field and soil columns. *Sci. Total Environ.* **2010**, *408*, 2118–2128.
- 467 (43) Burkhardt, M.; Kasteel, R.; Vanderborcht, J.; Vereecken, H. Field study on colloid
468 transport using fluorescent microspheres. *Eur. J. Soil Sci.* **2008**, *59*, 82–93.
- 469 (44) Cherrey, K. D.; Flury, M.; Harsh, J. B. Nitrate and colloid transport through coarse

- 470 Hanford sediments under steady state, variably saturated flow. *Water Resour. Res.*
471 **2003**, *39*, 1165, doi:10.1029/2002WR001944.
- 472 (45) Gao, B.; Saiers, J. E.; Ryan, J. N. Deposition and mobilization of clay col-
473 loids in unsaturated porous media. *Water Resour. Res.* **2004**, *40*, W08602,
474 doi:10.1029/2004WR003189.
- 475 (46) Biddle, D. L.; Chittleborough, D. J.; Fitzpatrick, R. W. Field monitoring of solute and
476 colloid mobility in a gneissic sub-catchment, South Australia. *Appl. Clay Sci.* **1995**, *9*,
477 433–442.
- 478 (47) Majdalani, S.; Michel, E.; Di-Pietro, L.; Angulo-Jaramillo, R. Effects of wetting and
479 drying cycles on in situ soil particle mobilization. *Eur. J. Soil Sci.* **2008**, *59*, 147–155.
- 480 (48) Vendelboe, A. L.; Moldrup, P.; Heckrath, G.; Jin, Y.; de Jonge, L. W. Colloid and
481 phosphorus leaching from undisturbed soil cores sampled along a natural clay gradient.
482 *Soil Sci.* **2011**, *176*, 399–406.
- 483 (49) Petersen, C. T.; Holm, J.; Koch, C. B.; Jensen, H. E.; Hansen, S. Movement of
484 pendimethalin, ioxynil and soil particles to field drainage tiles. *Pest Manag. Sci.* **2002**,
485 *59*, 85–96.
- 486 (50) Bradford, S. A.; Simunek, J.; Bettahar, M.; van Genuchten, M. T.; Yates, S. R. Signifi-
487 cance of straining in colloid deposition: evidence and implications. *Water Resour. Res.*
488 **2006**, *42*, W12S15, doi:10.1029/2005WR004791.
- 489 (51) Johnson, W. P.; Li, X.; Yal, G. Colloid retention in porous media: mechanistic con-
490 firmation of wedging and retention in zones of flow stagnation. *Environ. Sci. Technol.*
491 **2007**, *41*, 1279–1287.

- 492 (52) Nimmo, J. R. Simple predictions of maximum transport rate in unsaturated soil and
493 rock. *Water Resour. Res.* **2007**, *43*, W05426, doi:10.1029/2006WR005372.
- 494 (53) Sharma, P.; Abdou, H.; Flury, M. Effect of the lower boundary condition and flotation
495 on colloid mobilization in unsaturated sandy sediments. *Vadose Zone J.* **2008**, *7*, 930–
496 940.
- 497 (54) Sharma, P.; Flury, M.; Zhou, J. Detachment of colloids from a solid surface by a moving
498 air-water interface. *J. Colloid Interface Sci.* **2008**, *326*, 143–150.
- 499 (55) Shang, J.; Flury, M.; Deng, Y. Force measurements between particles and the air-water
500 interface: Implications for particle mobilization in unsaturated porous media. *Water*
501 *Resour. Res.* **2009**, *45*, W06420, doi:10.1029/2008WR007384.
- 502 (56) Cheng, T.; Saiers, J. E. Mobilization and transport of in situ colloids during drainage
503 and imbibition of partially saturated sediments. *Water Resour. Res.* **2009**, *45*, W08414,
504 doi: 10.1029/2008WR007494.
- 505 (57) Aramrak, S.; Flury, M.; Harsh, J. B. Detachment of deposited colloids by advancing
506 and receding air-water interfaces. *Langmuir* **2011**, *27*, 9985–9993.
- 507 (58) Leenaars, A. F. M.; O'Brien, S. B. G. Particle removal from silicon substrates using
508 surface tension forces. *Philips J. Res.* **1989**, *44*, 183–209.
- 509 (59) Gomez-Suarez, C.; Noordmans, J.; van der Mei, H. C.; Busscher, H. J. Removal of
510 colloidal particles from quartz collector surfaces as simulated by the passage of liquid-
511 air interfaces. *Langmuir* **1999**, *15*, 5123–5127.
- 512 (60) Lazouskaya, V.; Wang, L.; Gao, H.; Shi, X.; Czymmek, K.; Jin, Y. Pore-scale investiga-

513 tion of colloid retention and mobilization in the presence of a moving airwater interface.

514 *Vadose Zone J.* **2011**, *10*, 1250–1260.

515 (61) Matijevic, E.; Hsu, W. P. Preparation and properties of monodispersed colloidal parti-

516 cles of lanthanide compounds. *J. Colloid Interface Sci.* **1987**, *118*, 506–523.

Table 1. Irrigation scenarios for the different lysimeters.

Lysimeter	Diameter (m)	Cover	Natural Rainfall	Irrigation (mm/year)
South Caisson	1.35	no	natural rainfall	none
Lysimeter 1	0.3	yes ^a	none	124 ^b
Lysimeter 2	0.3	yes	none	248
Lysimeter 3	0.3	yes	none	248 + 100 ^c

^a Lysimeters 1–3 were covered all the time, except when irrigation was applied.

^b 26-year average natural drainage rate is 62 mm/year.

^c Simulates a 100 mm Chinook snowmelt event, applied in spring.

Table 2. Cumulative outflow of europium (in % of the amount of Eu applied) and water (in mm) at each sampling depth from May 28, 2009 to March 23, 2012. Values are scaled by wick collection area to represent the entire lysimeter cross-section.

Lysimeter	Depth (m)	Cumulative Eu Outflow (%)	Cumulative Water Outflow (mm)
South Caisson	0.31	0.02	223
	0.61	0.02	98
	1.22	0.10	518
	2.14	0.10	417
Lysimeter 1	0.31	5.20	379
	0.61	3.62	120
	1.22	10.87	350
	2.14	10.03	529
Lysimeter 2	0.61	0.07	233
	0.93	0.54	1674
	1.22	0.33	239
	2.14	0.04	109
Lysimeter 3	0.31	0.23	528
	0.61	0.28	637
	1.22	2.06	312
	2.14	0.06	195

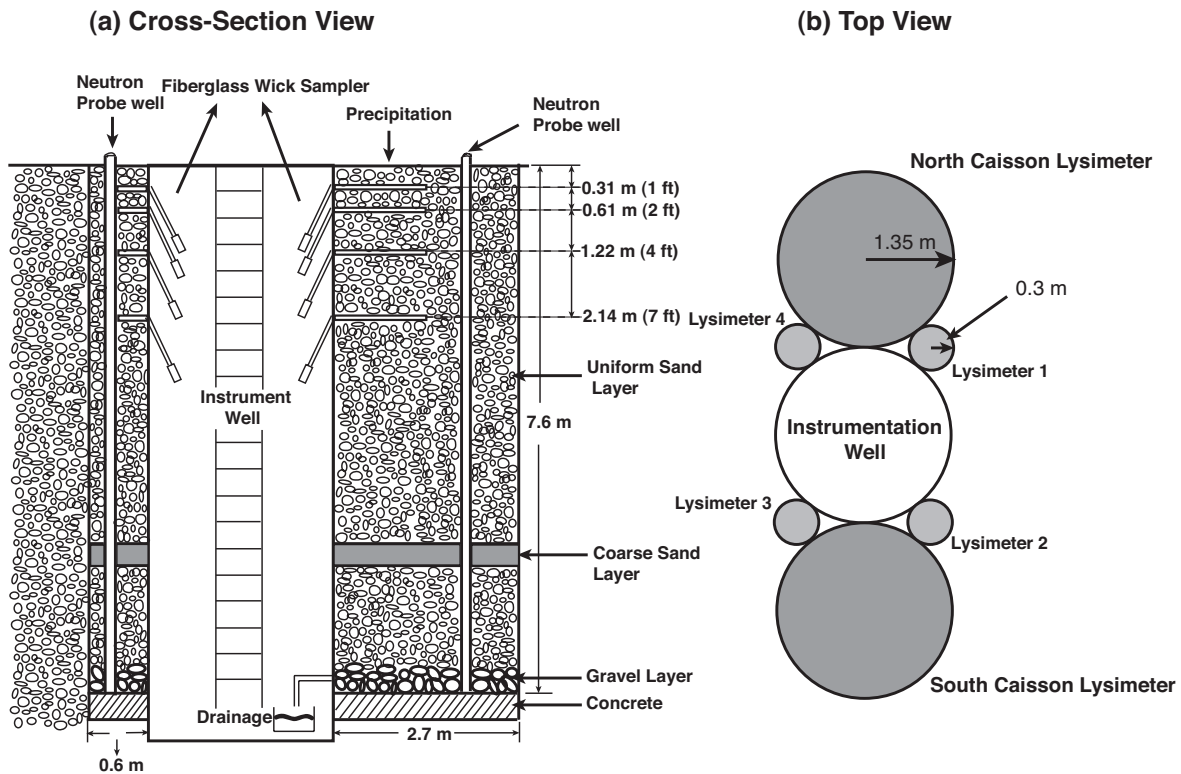


Figure 1. Schematic of Hanford's 300 North Lysimeter site. Only the South Caisson, Lysimeter 1, Lysimeter 2, and Lysimeter 3 were used in our experiments. (Note that in Lysimeter 2, the wick samplers were placed at 0.61, 0.93, 1.22, and 2.14 m.)

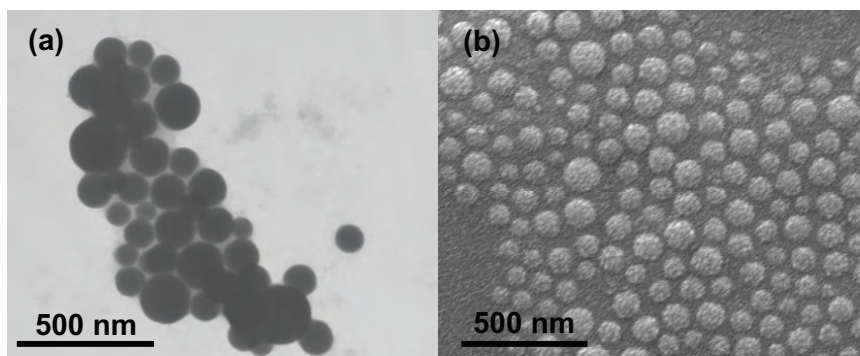


Figure 2. Electron microscope images of Eu-hydroxy-carbonate colloids applied to the field lysimeters: (a) TEM and (b) SEM images.

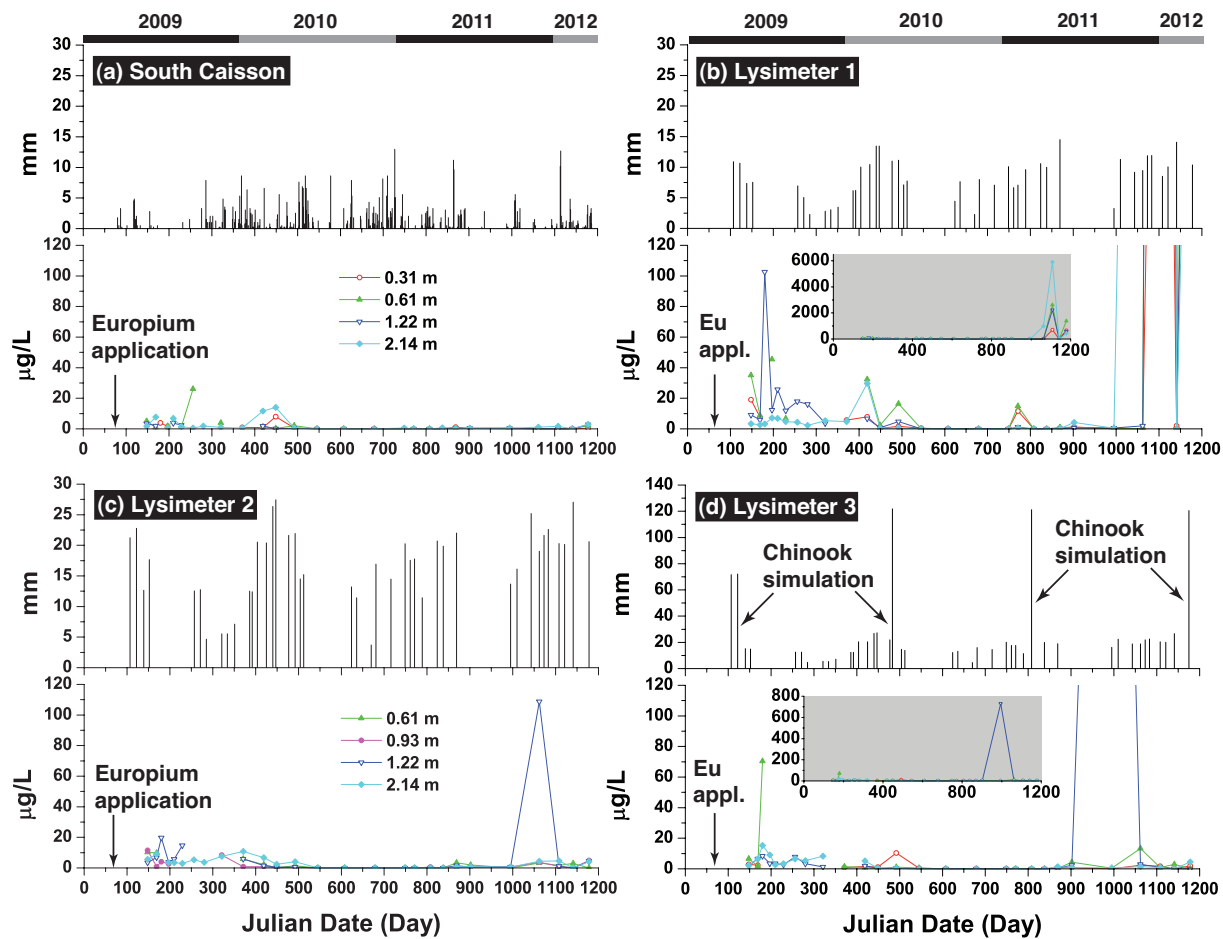


Figure 3. Time series of precipitation and Eu concentration in wick outflow (mass of Eu per volume of outflow solution) for each of the lysimeters (a to d). Inserts show full-scale of Eu peaks observed in Fall/Winter 2011. Note the different scales of the y -axis in Lysimeter 3 (precipitation) and Lysimeters 1 and 3 (inserts). (this is a color figure)

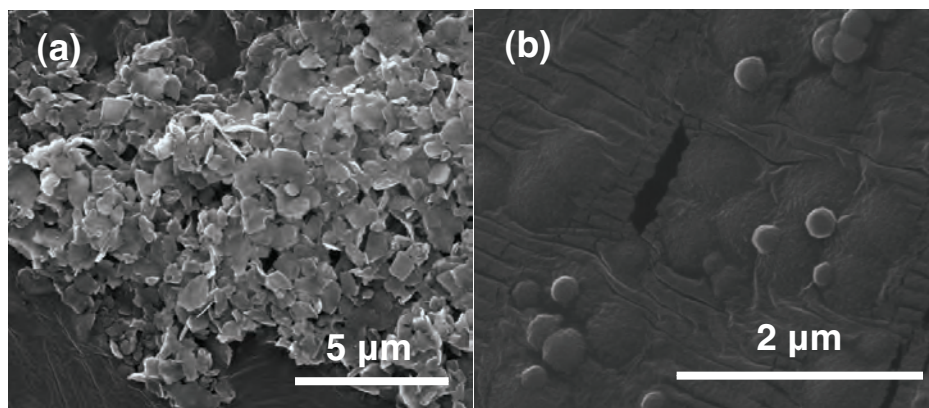


Figure 4. Scanning electron microscopy images of colloidal particles in wick outflow from May 28, 2009. (a) Platy clay minerals from Lysimeter 2, 0.61-m depth, (b) Eu colloids from South Caisson, 1.22-m depth.

518 **Transport of Europium Colloids in Vadose Zone Lysimeters at the Semi-Arid**
519 **Hanford Site**

520 Ziru Liu^a, Markus Flury^{a,*}, Z. Fred Zhang^b, James B. Harsh^c, Glendon W. Gee^b, Chris
521 E. Strickland^b, Ray E. Clayton^b

522 ^a *Department of Crop and Soil Sciences, Washington State University, Puyallup, WA 98374,*
523 *USA*

524 ^b *Pacific Northwest National Laboratory, Richland, WA 99354, USA*

525 ^c *Department of Crop and Soil Sciences, Washington State University, Pullman, WA 99164,*
526 *USA*

527

528 Supporting information include details on colloid synthesis, Eu extractions, images of
529 fiberglass wicks, time series of wick outflow, energy-dispersive x-ray spectra, concentration-
530 depth profiles of Eu in lysimeters, and water content profiles for each lysimeters. This infor-
531 mation is available free of charge via the Internet at <http://pubs.acs.org>.

532 S1 Colloid Synthesis

533 Eu-hydroxy-carbonate colloids ($\text{Eu}(\text{OH})(\text{CO}_3)$) were synthesized in our laboratory accord-
534 ing to procedures described by Matijevic and Hsu⁶¹ with some modifications outlined be-
535 low. A 6×10^{-3} M europium stock solution was prepared by dissolving europium chloride
536 ($\text{EuCl}_3 \cdot 5\text{H}_2\text{O}$) in double-distilled water, and then passed through a $0.2 \mu\text{m}$ filter. The fil-
537 tered solution was mixed with 1.5 M urea and small amounts of acid (7×10^{-4} M HNO_3 and
538 2×10^{-4} M H_2SO_4) in a 750 mL Pyrex bottle to adjust the pH to 5.1. The bottle was heated
539 in a microwave oven for about 2 min to a solution temperature of 85°C , and then put into an
540 ice bath to stop colloid formation. After cooling, the suspension was immediately dialyzed to
541 an electrical conductivity of 0.05 dS/m using dialysis tubing (Spectra/por, 45 mm, MWCO
542 of 12,000–14,000). The Eu-hydroxy-carbonate colloids were suspended in an aqueous solu-
543 tion containing 2% Liquinox with pH 7.5 and electrical conductivity of $140 \mu\text{S}/\text{m}$. Liquinox
544 was used to better disperse the particles in the stock solution. We assume that dilution
545 and washing of the particles by precipitation and irrigation would remove Liquinox from the
546 surfaces shortly after application to the Lysimeters. If the Liquinox did remain, it would be
547 expected to modify particle behavior; however, because the experiment did not require that
548 the particles consist of a clean mineral surface, this would not affect our interpretation of
549 results. After application to soil, any particle is likely to acquire organic surfactants from
550 natural organic matter that would modify surface properties.

551 The concentration of Eu colloids in the stock solution was 237.7 mg/L (measured gravi-
552 metrically by drying an aliquot), corresponding to a particle number concentration of $4.1 \times$
553 10^{13} number/L (calculated based on average colloid diameter of 108 nm and specific density
554 of $8.78 \text{ g}/\text{cm}^3$). The concentration of Eu itself in this suspension was 157.7 mg/L (calculated

555 based on Eu colloid mass concentration and the molecular weight of $\text{Eu}(\text{OH})(\text{CO}_3)$.

556 **S2 Wick Installation**

557 The fiberglass wicks (12.5 mm diameter, Catalog no. 1381, Peperell, MA) were pre-treated
558 and cleaned using the procedures described in Czigany et al.³³ The wicks were then mounted
559 onto a cut-open PVC tube (3/4 inch or 19.05 mm i.d.), and the wicks were folded once to
560 provide better contact with the surrounding soil when installed. The exposed lengths of
561 the wicks in contact with the soil were 0.56 m for the 2.7 m diameter lysimeter and 0.2 m
562 for the 0.6 m diameter lysimeter. The wicks were installed into the lysimeters in horizontal
563 orientation by drilling a 25.4 mm access hole, and manual insertion of the wick-mounted PVC
564 tube. The exposed cross-section of the wicks was used to calculate the flux of water and Eu
565 colloids.

566 **S3 Extraction of Eu from Sediments, Mass Recovery and Flocculation Experiment**

568 **Lysimeter Soil Cores:** The soil cores taken from the field lysimeters were dried at 105°C
569 and then thoroughly mixed. An aliquot of 4 grams of sediment was then extracted for Eu
570 using a 1:5 wt/wt solid:liquid ratio. The extraction solution was deionized water adjusted to
571 pH 1 by adding HCl. Europium colloids will dissolve at this pH. After 24 hours of reciprocal
572 shaking, the samples were centrifuged at 22,100 RCF for 25 min, the supernatant filtered
573 through a Nr. 42 Whatman Filter paper, and the filtrate analyzed for Eu by ICP-MS (Agilent
574 7700, Quantum Analytics, Inc., CA).

575 **Mass Recovery Testing:** Four grams of uncontaminated Hanford sediments, taken
576 adjacent to the lysimeters and oven-dried at 105°C, were spiked with 1 mL of stock solution

577 of Eu colloids mimicking the application of Eu colloids in the field experiment. After 24
578 hours of incubation at room temperature, the sediments were shaken with a HCl solution
579 (pH 1) at a solid:liquid ratio of 1:5 for 24 hours. Then the samples were centrifuged at 22,100
580 RCF for 25 min. The pH of the supernatant was checked and found to be below pH 2. The
581 supernatant was then filtered through a 0.45 μm syringe filter and analyzed for Eu with
582 ICP-MS (Agilent 7700, Quantum Analytics, Inc., CA). The Eu recovery was then calculated
583 based on mass balance. The mass recovery for Eu was $87 \pm 5\%$. We also verified the Eu
584 extraction rates for longer incubation times. For that purpose, 30 g of sediment was placed
585 into a 5-cm diameter soil can and spiked with 5.77 mL of Eu stock solution, mimicking a
586 3-mm application of stock solution of the field experiment. After 1 day, 1 week, and 1 month,
587 Eu was extracted at a 1:5 solid:liquid ratio, and Eu quantified as stated above; the mass
588 recoveries were $72 \pm 5\%$, $122 \pm 14\%$, and $123 \pm 5\%$, respectively.

589 **Flocculation Experiment:** Five outflow samples with high Eu concentrations were
590 used in a flocculation experiment to check whether Eu was present as a dissolved phase. We
591 added CaCl_2 as flocculant to 10 mL of outflow sample (CaCl_2 in the samples was 1 M).
592 Then the samples were shaken and placed in a sample holder for sedimentation for 24 hours.
593 The supernatant was then filtered through a 0.1 μm syringe filter and analyzed for Eu with
594 ICP-MS (Agilent 7700, Quantum Analytics, Inc., CA). No Eu should be detected, indicating
595 that there was no Eu in the dissolved phase.

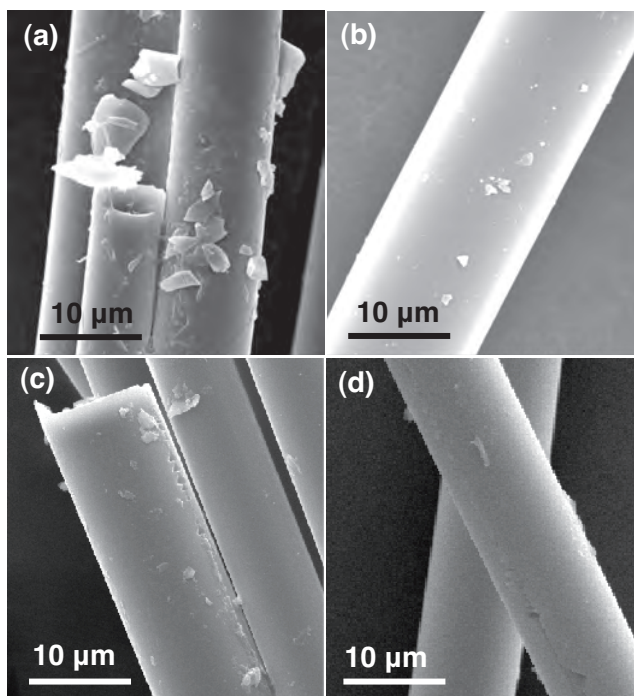


Figure S1. Scanning electron microscope images of fiberglass wicks taken from intact wick braids at the hanging water column section of the wicks. Fibers were pulled off the wick braids with clean tweezers on February 23, 2010, from (a) Lysimeter 2, 0.93-m depth, (b) Lysimeter 3, 0.31-m depth; and on March 23, 2012, from (c) South Caisson, 0.31-m depth and (d) South Caisson, 0.61-m depth.

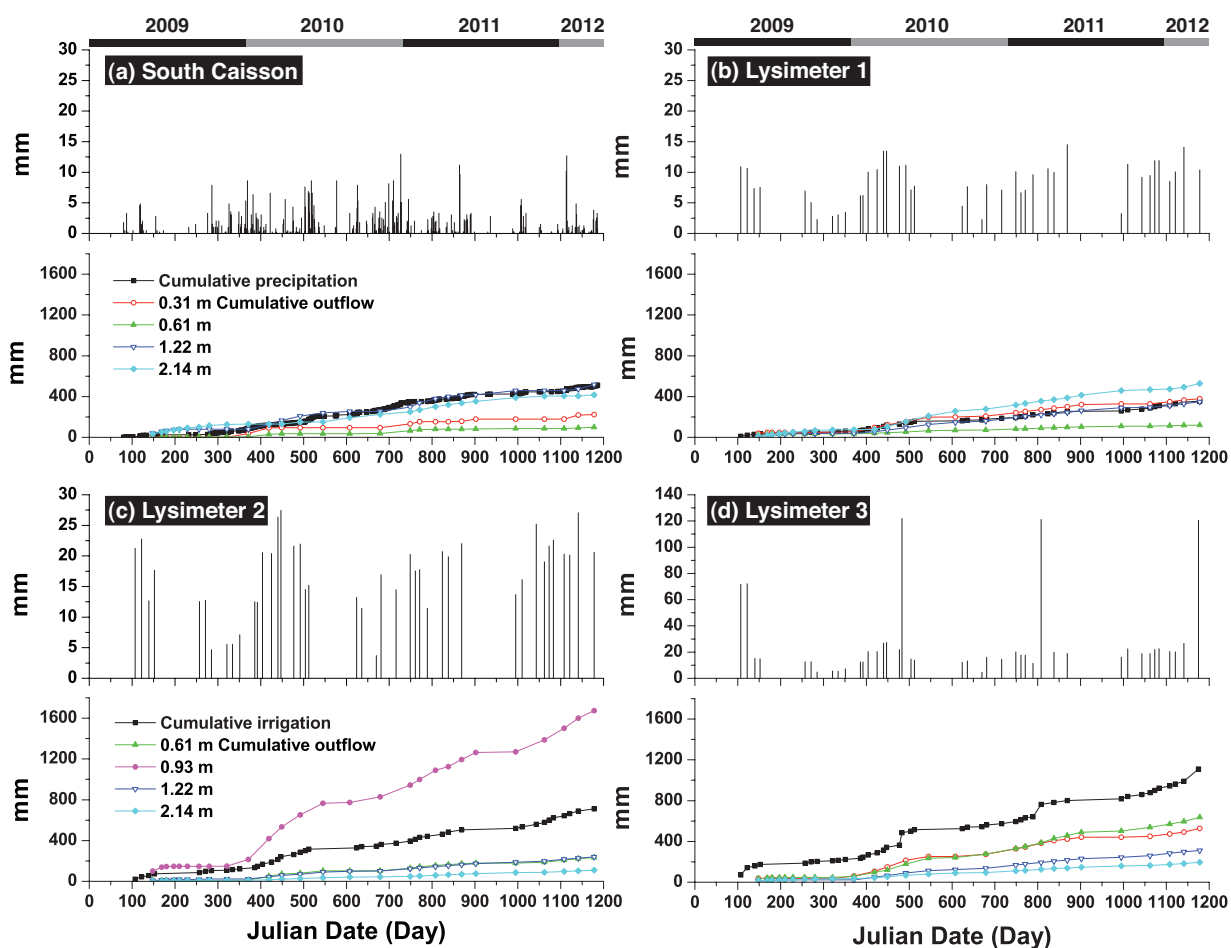


Figure S2. Time series of precipitation and wick outflow for each of the lysimeters (a to d). Note the different scales of the y -axis in Lysimeter 3 (precipitation). The volume of the outflow water (mL) was converted to a corresponding water flux (mm) by dividing by the exposed area of the wicks (diameter of the cut-open PVC tube times the length of the wick) in the lysimeter, so that inflow and outflow fluxes can be compared. (this is a color figure)

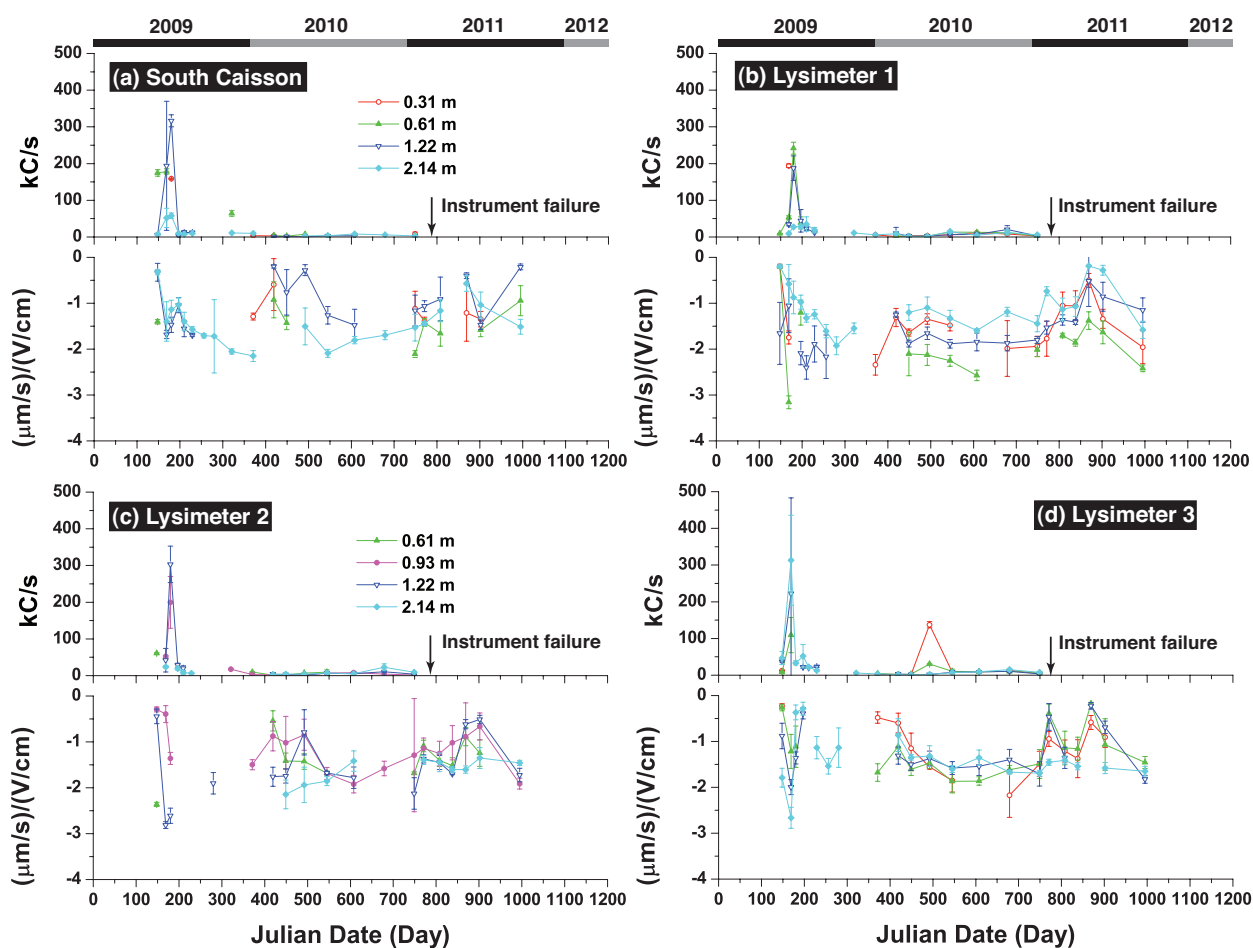


Figure S3. Time series of particle counts (kilocounts per s) and electrophoretic mobility of colloids in wick outflow. The data contain gaps, which are indicated by the broken lines and missing data points. These data gaps correspond to none or non-sufficient outflow collected from the wicks, so that no Eu and particle counts could be measured (particle count measurements were discontinued in January 2011 due to instrument failure). (this is a color figure)

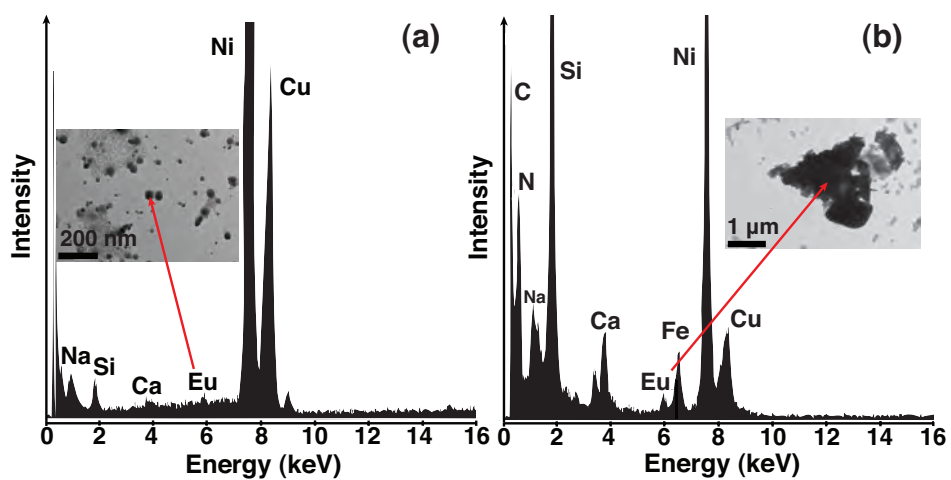


Figure S4. Energy dispersive x-ray spectra (EDX) and corresponding TEM images of wick outflow samples from (a) May 28, 2009, Lysimeter 1 (0.61-m depth), (b) June 18, 2009, Lysimeter 1 (0.31-m depth). The Eu $L\alpha$ -level emission line at 5.8 keV indicates the presence of Eu. The large peaks for C, Ni, and Cu keV are from the microscopy stub. Arrows indicate the location of the center of the x-ray beam.

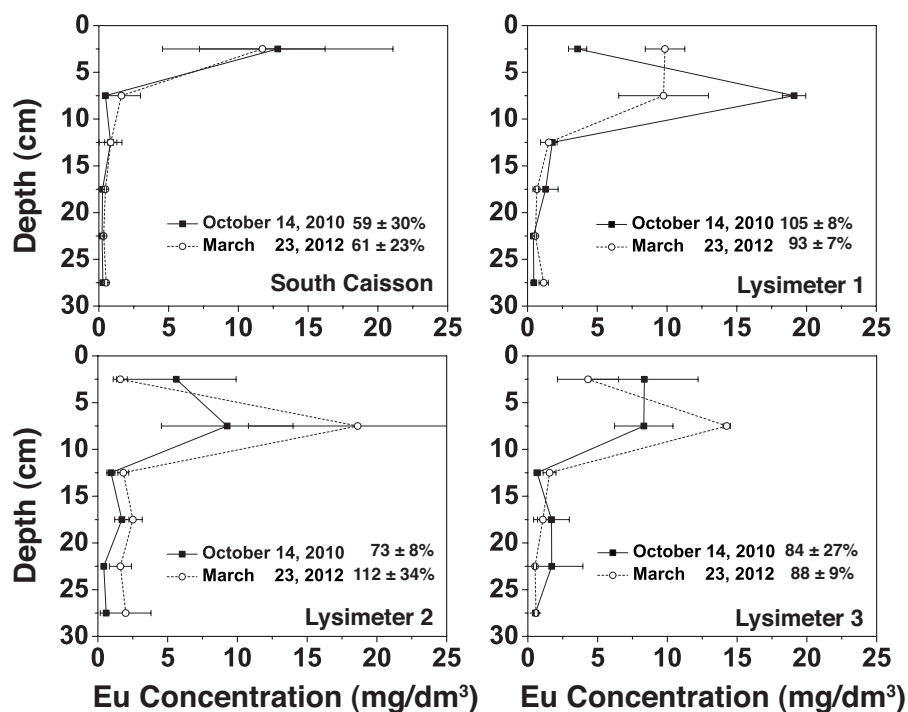


Figure S5. Depth profiles of Eu concentrations (mass of Eu per volume of bulk soil) in the top 30 cm of the lysimeters on October 14, 2010 and March 23, 2012. Error bars denote \pm one standard deviation based on three soil cores in each lysimeter. The percentage numbers represent the total amount of Eu present in the top 30 cm as percentage of the amount initially applied to the lysimeter surfaces.

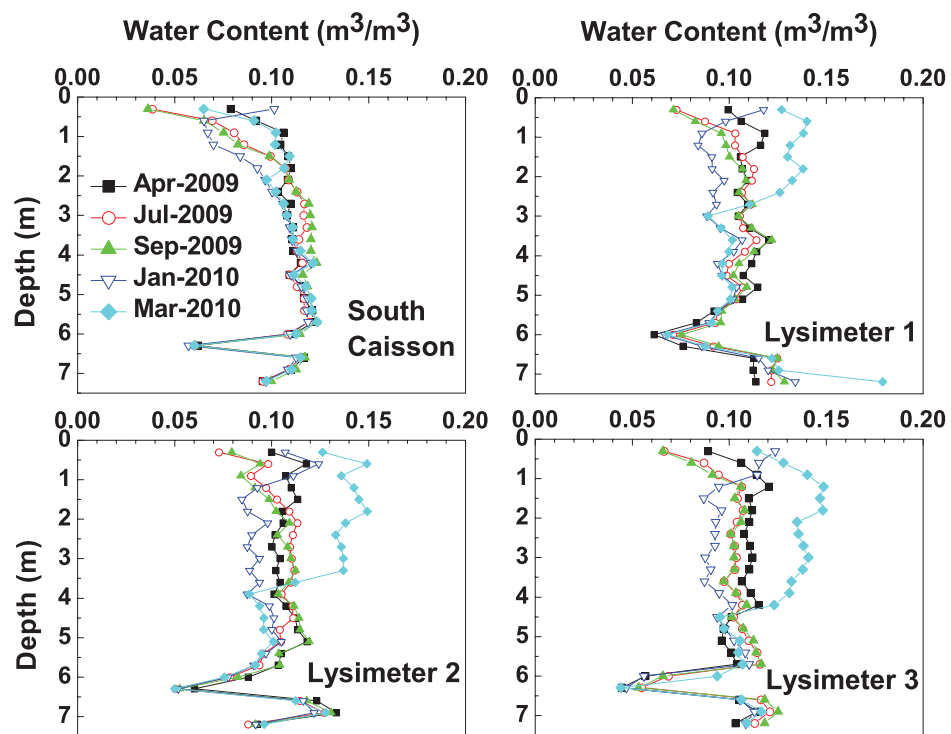
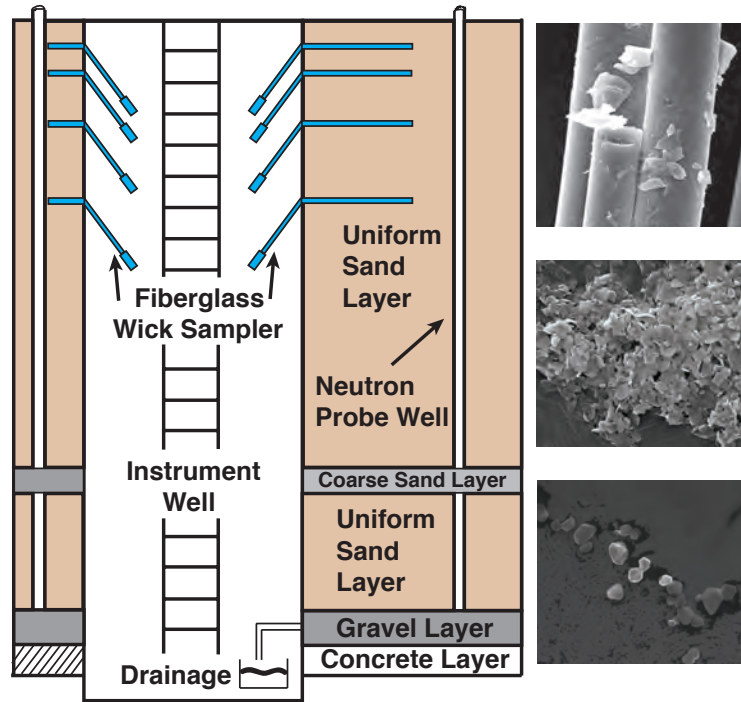


Figure S6. Water content profiles in different lysimeters from April 2009 to March 2010.

(this is a color figure)

—Table of Contents Art—



Colloid Mobilization in an Undisturbed Sediment Core under Semi-Arid Recharge Rates

Ziru Liu^a, Markus Flury^{a,*}, James B. Harsh^b, Jon B. Mathison^a, Carolina Vogs^{c,d}

^a Department of Crop & Soil Sciences, Washington State University, Puyallup, WA 98374,
USA

^b Department of Crop & Soil Sciences, Washington State University, Pullman, WA 99164,
USA

^c Institut für Geoökologie, Technische Universität Braunschweig, Braunschweig, Germany

^d currently at UFZ–Helmholtz Centre for Environmental Research, Bioanalytical Ecotoxicol-
ogy, Leipzig, Germany

*Corresponding author:

Markus Flury

Department of Crop and Soil Sciences

Washington State University

Puyallup, WA 98374

Phone: 1-253-445-4522

E-mail: flury@wsu.edu

1 **Abstract.** The semi-arid US DOE Hanford site has a deep vadose zone with low recharge
2 rates. Contaminants originating from nuclear waste processing are expected to move slowly
3 through the vadose zone. The movement of certain contaminants can be facilitated by
4 colloids. We hypothesized that the low recharge rates and low water contents in semi-
5 arid regions, however, tend to inhibit movement of colloidal particles, thereby reducing the
6 risk for colloid-facilitated contaminant transport. The goal of this study was to investigate
7 whether in situ natural colloids can be mobilized and transported in undisturbed, deep vadose
8 zone sediments at the Hanford site under typical, semi-arid recharge rates. We sampled
9 an undisturbed sediment core (50-cm i.d., 59.5-cm height) from a depth of 17 m below
10 ground at the Hanford 200 Area. The core was set up as a laboratory lysimeter and exposed
11 to an infiltration rate of 18 mm/year by applying simulated pore water onto the surface.
12 Particle concentrations were quantified in the column outflow, and selected samples were
13 examined microscopically and for elemental composition (TEM and EDX). Measured water
14 contents and potentials were used to calibrate a numerical model (HYDRUS-1D), which was
15 then applied to simulate colloid mobilization from the sediment core. During 5.3 years of
16 monitoring, natural colloids like silicates, aluminosilicates, and Fe-oxides were observed in
17 the core outflow, indicating the continuous mobilization of in situ colloids. The total amount
18 of particles mobilized during 5.3 years corresponded to 0.5% of the total dispersable colloids
19 inside the core. The fitted colloid release rate coefficient was six to seven orders of magnitude
20 smaller than coefficients reported from previous studies, where disturbed Hanford sediments
21 and higher flow rates were used. Our findings demonstrate that even under low recharge
22 rates and water contents typical for semi-arid, deep vadose zone sediments, particles can
23 continuously be mobilized, although the total mass of particles is low.

24 1 Introduction

25 The US Department of Energy Hanford site served as a Pu processing facility from 1934
26 to 1989. During the decades of Pu production, large amounts of radioactive nuclear waste
27 (including Cs, Am, U) were generated. Considerable amounts of the nuclear waste were
28 directly discharged to the ground, while much of the highly-radioactive waste was stored in
29 massive tanks buried below ground surface [Gephart, 2003].

30 Leakage from those waste tanks has been confirmed first in 1959 [Zachara *et al.*, 2007].
31 Radioactive isotopes of elements like Cs, Sr, Tc, Pu, and Am were detected in the tank
32 wastes from three of the Hanford site's largest tanks SX-108, BX-102, and T-106 [Jones
33 *et al.*, 2000a; Jones *et al.*, 2000b; Jones *et al.*, 2001]. Leaked tank wastes reacted with
34 the surrounding sediments, causing dissolution and precipitation of minerals [Mashal *et al.*,
35 2004; Mashal *et al.*, 2005a; Mashal *et al.*, 2005b; Deng *et al.*, 2006]. The more mobile tank
36 contaminants, such as anionic $^{99}\text{TcO}_4^-$, CrO_4^{2-} , and U(VI), have been reported to migrate to
37 groundwater at the Hanford site [Knepp, 2002b; Knepp, 2002a; Myers, 2005]. Less mobile
38 contaminants, such as cationic radionuclides, potentially can be transported via colloidal
39 particles [Zhuang *et al.*, 2003; Chen *et al.*, 2005; Cheng and Saiers, 2010].

40 Many radionuclides are not very mobile due to adsorption reactions on sediment surfaces
41 or precipitation in relatively insoluble solid phases. However, when the associated solid
42 phase falls in the colloidal size range, particle transport can be an important mechanism of
43 subsurface contaminant transport [McCarthy and Zachara, 1989; Honeyman, 1999]. Colloid
44 and colloid-facilitated radionuclide transport has been intensively investigated at the Hanford
45 site [Flury *et al.*, 2002; Cherrey *et al.*, 2003; Zhuang *et al.*, 2003; Zhuang *et al.*, 2004; Chen
46 *and Flury*, 2005; Chen *et al.*, 2005; Czigany *et al.*, 2005a]. These studies showed that both

47 native and neo-formed colloids can facilitate the migration of radionuclides such as ^{137}Cs ,
48 and that colloid-facilitated transport can occur under both saturated and unsaturated flow
49 conditions. Decreasing water content has been shown to lead to reduced colloid transport
50 as colloids are trapped in water films. However, transient flow conditions can lead to more
51 colloid mobilization caused by moving air-water interfaces, which can scour colloids from
52 surfaces [Saiers and Lenhart, 2003; Zhuang *et al.*, 2007; Shang *et al.*, 2008; Aramrak *et al.*,
53 2011].

54 The Hanford site is characterized by a Mediterranean, semi-arid climate [Harvey, 2000].
55 In this climate, while winter precipitation causes substantial water infiltration near the soil
56 surface, deep recharge rates are low [Hsieh *et al.*, 1973; Gee, 1987; Gee *et al.*, 1992b; Gee
57 *et al.*, 1994; Gee *et al.*, 2005b]. Using different methods to estimate recharge rates (lysimeters,
58 chloride mass balance), Gee and co-workers have reported recharge rates ranging from near
59 zero to 100 mm/y [Gee *et al.*, 1992a; Gee *et al.*, 2005a]. Model simulations performed for
60 the Hanford tank farms showed that as recharge rate decreased (50 mm/y, 30 mm/y, and
61 10 mm/y), peak arrival time of contaminants was delayed and the peak concentration was
62 reduced [Khaleel *et al.*, 2007].

63 Colloid and colloid-facilitated contaminant transport has been documented from labo-
64 ratory experiments using disturbed Hanford sediments [Cherrey *et al.*, 2003; Chen *et al.*,
65 2005; Cheng and Saiers, 2010]. A lysimeter field study at the Hanford site showed that in
66 situ colloids and Eu could be transported from the soil surface down to 2.1 m depth within
67 2.5 months under natural and forced rainfall conditions [Liu *et al.*, 2012]. While colloid and
68 Eu movement in this field study were likely caused by transients in the near-surface water
69 flow [Liu *et al.*, 2012], under deep vadose zone conditions, with its steady-state, low recharge

70 rate, colloid transport is likely less pronounced. No information, however, is available about
71 colloid movement in the deep vadose zone at Hanford.

72 Based on previous laboratory results obtained with disturbed Hanford sediments, we
73 know that colloid transport and mobilization is strongly impacted by water content or flow
74 rate—the lower the water content or flow rate, the less colloids leached from columns [*Cherrey*
75 *et al.*, 2003; *Chen et al.*, 2005; *Shang et al.*, 2008]. Similar results were found in other porous
76 materials [*Kaplan et al.*, 1993; *Saiers and Lenhart*, 2003; *Gao et al.*, 2006]. Cumulative
77 amounts of colloids mobilized from packed Hanford sediments were about 50 times smaller
78 at a water content of $0.21 \text{ cm}^3/\text{cm}^3$ than at $0.32 \text{ cm}^3/\text{cm}^3$ [*Shang et al.*, 2008]. Colloid
79 breakthrough curves at a water content of $0.11 \text{ cm}^3/\text{cm}^3$ not only showed 5 times smaller
80 peak concentration than at $0.4 \text{ cm}^3/\text{cm}^3$, but also considerable tailing [*Cherrey et al.*, 2003].
81 These results suggest that colloid transport and mobilization under the low water contents
82 in the deep vadose zone at Hanford will be limited, but nonetheless possible.

83 The objectives of this study were to (1) test whether natural colloidal materials can be
84 mobilized and translocated under conditions typical for the deep vadose zone at the semi-arid
85 Hanford site, and (2) to quantify the extent of the colloid mobilization. We hypothesized
86 that under the low and steady-state recharge rate at the semi-arid Hanford site, colloid
87 mobilization and transport is limited, but nonetheless existent. We monitored water flow and
88 colloid transport using an undisturbed sediment core, collected from 17 m below ground at
89 the Hanford site, and mimicked the natural recharge under controlled laboratory conditions.

90 2 Materials and Methods

91 2.1 Undisturbed Sediment Core

92 An undisturbed sediment core was collected on March 8, 2003 from the Hanford Environmen-
93 tal Restoration Disposal Facility (ERDF), which is located between the Hanford 200 West
94 and East areas (Figure 1). The core was taken from an uncontaminated layer of the sand-
95 dominated facies association of Hanford Formation sediments from a depth of 17 m below
96 ground surface (Figure 2a). A flat, horizontal bench of sediment was prepared by digging
97 into the slanted wall of the ERDF pit. Then an intact, undisturbed core sample was taken
98 by using a stainless steel cylinder (10 GA T-304, i.d. 50 cm, height 59.5 cm). A front-loader
99 with a 3-m wide bucket was used to push the cylinder into the sediments (Figure 2b). When
100 the core was completely inserted into the sediments, the sediments around the core were
101 excavated, and a bevelled stainless steel plate was pushed along the bottom of the core to
102 shave the core off the underlying sediments (Figure 2c). About 17 liters of liquid nitrogen
103 were poured onto the surface of the core to freeze the top of the core to provide stability
104 for transportation. A wooden plate was tightened to the top of the cylinder, and the core
105 was moved to Washington State University (Figure 2d). Small cores (5.7-cm diameter Soil
106 Core Sampler, Soilmoisture Equipment Corp, Santa Barbara, CA) and bucket samples of
107 sediments were collected for bulk density and particle size analysis.

108 The core comes from the sand-dominated facies association of the Pleistocene Hanford
109 Formation sediments [*Pace et al.*, 2003; *Reidel and Chamness*, 2007]. The sediments at
110 the sampling location had fine- and coarse-textured layers, and our core was sampled out
111 of a coarse-textured layer (Figure 2e). These coarse-textured sands consist mainly of illite,

112 smectite, kaolinite, vermiculite, mica, quartz, feldspars, and pyroxene [Mashal *et al.*, 2004].
113 The colloidal size minerals include smectite, kaolinite, illite, and quartz [Czigany *et al.*, 2005b].
114 The bulk density of the sediments was 1.6 g/cm^3 , the porosity $0.396 \text{ cm}^3/\text{cm}^3$, and the sand,
115 silt, and clay fractions were 92%, 6%, and 2%, respectively [Shang *et al.*, 2008].

116 **2.2 Experimental Setup**

117 The sediment core in the stainless steel column was set up as a lysimeter (Figure 2f) in a
118 dark coldroom at $12.4 \pm 0.3 \text{ }^\circ\text{C}$, corresponding to the long-term average air temperature at
119 the Hanford site [Hanford Meteorological Station, 2012]. We assume that the temperature
120 at 17-meters depth, where the core was taken, equals the long-term average air-temperature.
121 A schematic of the experimental setup is shown in Figure 3. Five porous cup tensiometers
122 (i.d. 0.6 mm, length 2.9 cm, Soil Moisture Equipment Corp.) and five, custom-made 3-rod
123 Time Domain Reflectometry probes (TDR, diameter of the rods = 2.5 mm, length of the
124 rods = 20 cm) were inserted into the column to monitor matric potential and volumetric
125 water content, respectively. The tensiometers and TDR probes were installed oppositely
126 at depths 9.5, 19.5, 29.5, 39.5, and 49.5 cm. The tensiometers were fitted with pressure
127 transducers (PX26, Omega Engineering, Stamford, CT) and connected to a data logger
128 (CR10X, Campbell Scientific Inc., Logan, UT). The TDR probes were connected to a TDR-
129 100 and a CR10X data logger (Campbell Scientific Inc.). Water potentials and water content
130 were monitored hourly. Tensiometers were calibrated with a hanging water column, and
131 periodic re-calibrations were made to correct for drift, and TDR probes were calibrated using
132 packed sediments with controlled water contents. Specific calibrations curves were developed
133 for each tensiometer and TDR probe.

134 A Plexiglass plate, containing 12 sections fitted with porous membranes, was attached
135 to the bottom of the column. Each section had a drain connected to a Tygon tube, through
136 which a hanging water column could be applied. The membranes had a bubbling pressure
137 of 90 cm-H₂O, corresponding to a pore size of 32 μ m, which is big enough to allow colloidal
138 particles to pass through. Due to failure of the suction system of these membranes, we
139 installed a fiberglass wick (12.5 mm diameter, Catalog no. 1381, Peperell, MA) on June
140 30, 2010 at 3 cm above the bottom. The fiberglass wick was mounted on a cut-open PVC
141 tube (3/4 inch i.d.) and inserted radially through the entire diameter of the column. A
142 57-cm hanging piece of the wick provided tension for collecting outflow (Figure 3). Outflow
143 was collected in glass vials (from the 12 sections of the bottom plate), and in a 250-mL
144 polyethylene bottle (from the wick).

145 The entire column was placed on a load-cell (AL H22-1K, capacity 500 kg, resolution
146 100 g, Indiana Scale Co.) which was monitored daily. Two UV lamps (Spectroline X-Series,
147 254 nm, Spectronics Corp, New York) were positioned close to the column surface and turned
148 on three times a day for 60 minutes to prevent microbial growth at the surface.

149 **2.3 Irrigation and Infiltration**

150 The column was irrigated uniformly by using a peristaltic pump (Ismatec CP 78001-20,
151 Glattbrugg, Switzerland) and a sprinkler. The sprinkler consisted of 48 Teflon tube drippers
152 (Western Analytical, i.d. 0.15 mm) arranged in a uniform pattern. Irrigation started in July
153 2005 with a sprinkling rate of 100 mL/d, corresponding to an irrigation rate of 0.5 mm/d (=
154 182 mm/y). As this rate was too low for continuous irrigation, sprinkling was intermittent
155 (every 35 minutes we sprinkled for a period of 5 minutes). The irrigation water consisted of

156 0.5 mM NaBr, 0.3 mM KCl, and 0.4 mM CaCl₂, adjusted to pH 8 with NaOH, to mimic the
157 chemical composition of Hanford pore water [Serne *et al.*, 2002].

158 The irrigation rate was chosen to fall within the range of annual rainfall at the Hanford
159 site [Hanford Meteorological Station, 2012]. Based on the mass balance of the sediment
160 core, we determined the actual infiltration rate to be 0.05 mm/day (= 18.25 mm/y), which
161 corresponds to irrigation minus evaporation rates. This infiltration rate represents a low
162 recharge rate typical for the Hanford site; recharge rates have reported to range from 0 to
163 100 mm/y [Gee, 1987; Gee *et al.*, 2005a]. First outflow from the column was observed in
164 March 2008. Outflow occurred from all of the outflow sections initially, but later on, several
165 sections ceased to yield outflow. Due to this inconsistent outflow pattern, we decided to
166 install a fiber glass wick in June 2010, which, after an initial spike of outflow, then collected
167 consistent outflow. The outflow was in steady-state after the wick was installed.

168 **2.4 Outflow Characterization and Data Analysis**

169 Column outflow water was analyzed for electrophoretic mobility (ZetaSizer 3000HSa, Malvern
170 Instruments Ltd., Malvern, UK), pH, electrical conductivity, and particle concentration
171 with UV/VIS absorbance at 280 nm (Ocean Optics USB4000-UV-VIS, Ocean Optics Inc.,
172 Dunedin, FL). Absorbance was translated to particle concentrations by using a calibration
173 curve developed from a colloid stock solution. The stock solution was obtained by leaching
174 a packed sediment column (i.d. 4.3 cm, length 22.5 cm) with five pore volumes of irrigation
175 solution under saturated conditions to dislodge mobile colloids. The mass of mobilized col-
176 loids was determined gravimetrically. The detection limit for the absorbance measurements
177 was 1.83 mg/L, determined following the procedure described in Skoog *et al.* [1996]. Selected

178 outflow samples were analyzed by transmission electron microscopy (TEM) and energy dis-
179 persive x-ray analysis (EDX) (JEOL 1200 EX Transmission Electron Microscope; Philips
180 CM-200). For these microscopic measurements, the outflow samples were sonicated, and a
181 drop of solution was placed on a carbon-nickel microscopy stub and air-dried.

182 The hourly monitoring data for water potential and water content were averaged on a
183 daily basis, and the time series data then smoothed with a twenty-five point, second-order
184 Savitzky-Golay algorithm. This procedure eliminated noise from the data, but preserved the
185 general shape of the curves.

186 2.5 Water Flow Modeling

187 We used HYDRUS-1D (Version 4.14, Šimůnek *et al.* [2009]) to analyze the water flow and col-
188 loid transport in our experiments. The unsaturated hydraulic properties were parameterized
189 by the van Genuchten-Mualem equations [van Genuchten, 1980]. The modeling domain was
190 discretized in 0.5-cm spaced nodes, with observation points selected at the position where
191 the sensors were installed. An additional observation point was located at the bottom of
192 the core. The initial condition was given in terms of the measured matric potentials at the
193 observation points, with linear interpolation between the points.

194 The upper boundary condition was selected as constant flow with the measured infil-
195 tration rate. In a previous study, we also modeled the water flow with a time-dependent
196 upper boundary condition, following the intermittent sprinkling, and we found no differences
197 compared with constant flow [Vogs, 2009]. The lower boundary was set as a seepage face
198 with a 2-cm H₂O matric potential, which accounts for the resistance provided by the bottom
199 plate.

200 The model was run in inverse mode to determine the unsaturated hydraulic properties
 201 of the sediments. For the van Genuchten-Mualem model, we fitted the parameters α , n ,
 202 and K_s , with $m = 1 - 1/n$, for each of the observation nodes. The core was divided in 5
 203 layers, each having distinct hydraulic properties in terms of the fitting parameters. Residual
 204 and saturated water contents (θ_r and θ_s) were fixed according to measured values, as was
 205 the parameter $l = 0.5$. Initial values for the parameter estimation were chosen from Vogs
 206 [2009]. Parameters were then determined by inverse modeling using the Levenberg-Marquardt
 207 algorithm with data from the beginning of the irrigation until day 1400, the time period for
 208 which we had continuous data for matric potential and water content. Water content and
 209 water potential data were weighted by their respective standard deviations as implemented
 210 in HYDRUS-1D.

211 2.6 Colloid Transport Modeling

212 For the colloid transport modeling, we assumed that the pool of the colloids is initially
 213 uniformly distributed within the core and that the colloids are initially attached to the sta-
 214 tionary sediments. We further assumed that, as water flows through the core, colloids can be
 215 mobilized by a first-order kinetic colloid release [Shang *et al.*, 2008]:

$$\begin{aligned}
 & 216 \\
 & 217 \frac{\partial C}{\partial t} + \frac{\rho}{\theta} \frac{\partial S}{\partial t} = D \frac{\partial^2 C}{\partial z^2} - \frac{J_w}{\theta} \frac{\partial C}{\partial z} \quad (1)
 \end{aligned}$$

$$\begin{aligned}
 & 218 \\
 & 219 \frac{\partial S}{\partial t} = -\beta S \quad (2)
 \end{aligned}$$

220 where C represents the colloid concentration suspended in the aqueous phase (mg/cm^3),
 221 S is the colloid concentration attached to the sediments (mg/g), t is time (day), ρ is the

222 bulk density (g/cm^3), z denotes the coordinate parallel to the flow direction (cm), and β
223 is the first-order colloid release rate coefficient (d^{-1}). A zero flux condition was used at
224 the upper boundary ($J_w C(0, t) = 0$) and a zero-gradient was used at the bottom boundary
225 ($\partial C/\partial z = 0$). The amount of colloids present in the column for mobilization were $C(x, 0) = 0$
226 and $S(z, 0) = S_0$, where S_0 was determined by leaching a packed sediment column as described
227 in Section 2.4. We consider that reattachment of colloids after release is considered negligible.

228 The transport model (Equations 1 and 2) was coupled with the water flow model de-
229 scribed above within HYDRUS-1D. Simulated cumulative colloid outflow from the model was
230 fitted to the experimental colloid outflow data by adjusting the first-order colloid release rate
231 coefficient β .

232 **3 Results and Discussion**

233 **3.1 Water Potentials, Water Contents, and Outflow**

234 The water monitoring data are summarized in Figure 4. The initial condition of the sediments
235 was close to a no-flow equilibrium, with the water contents ranging from 0.08 to 0.1 cm^3/cm^3 .
236 After 200 days of irrigation, the rate of increase in water potentials and water contents
237 dropped considerably. The top two water content sensors remained fairly constant, but the
238 three lower sensors indicate that the core then wetted up from the bottom. This was because
239 the porous membrane sections in the bottom plate did not yield any outflow, indicating
240 that their intended purpose of draining water under suction was not working properly, likely
241 because of air trapping under the membranes causing a break in the capillary connection.
242 After the first outflow was recorded, the top two sensors (water potential and content) indicate
243 drying of the core. After the fiber glass wicks were installed, the core started to drain at a

244 higher rate, mainly draining out the lower part of the core, as indicated by the TDR sensor
245 at 49.5-cm depth.

246 The simulated matric potentials followed the experimental data well, while the water
247 contents showed more deviations between model and data, particularly for the lower two
248 sensors (Figure 5). The overall regression coefficient of the model fit was $R^2 = 0.987$. The
249 initial infiltration phase was not fitted as well as the later, steady-state conditions. The fitted
250 model parameters are listed in Table 1.

251 3.2 Colloid Transport

252 **General Observations.** Chemical and colloidal characteristics of the outflow are shown in
253 Figure 6. The pH of the outflow remained fairly constant between pH 7.5 and 8.5, but showed
254 a lower value after the wick was installed, followed by an increase to pH 8.5. Electrolytic
255 conductivity varied between 500 and 2000 $\mu\text{S}/\text{cm}$, corresponding to ionic strengths of 7.2
256 to 29 mmol/L estimated with the Marion-Babcock equation [Sposito, 2008]. Electrolytic
257 conductivity values are in the range of those reported from pore waters from Hanford sediment
258 cores from the 200 Area; Serne *et al.* [2002] lists values of 200 to 6700 $\mu\text{S}/\text{cm}$ for pore water
259 from Hanford Formation sediments. The critical coagulation concentration for in situ colloids
260 from Hanford sediments has been reported to be 1.7 to 3.8 mmol/L for Ca dominated systems
261 [Czigany *et al.*, 2005b]. As the ionic strength in our core exceed the critical coagulation
262 concentration, we do not expect any colloid dispersion to occur.

263 The initial outflow samples had particle counts below 10 kCounts/s, which is within the
264 background noise of the dynamic light scattering and, no electrophoretic mobility could be
265 made for such low particle counts. In 2009, the particle counts increased up to 50 kCounts/s

266 and electrophoretic mobility measurements were made for these samples (Figure 6c), but
267 have to be considered with caution, as the particle counts still did not meet the required
268 minimum value for accurate measurements (>50 kCounts/s). Electrophoretic mobility values,
269 nonetheless, yielded reasonable results for Hanford colloids (-1 to -3 ($\mu\text{m/s}/(\text{V/cm})$) [*Shang*
270 *et al.*, 2008].

271 **Colloid Concentrations and Flow Rates.** The particle concentrations in the
272 outflow were generally 50 mg/L, with occasionally higher concentrations up to 400 mg/L,
273 and we observed a continuous release of colloids (Figure 6e). The particle concentrations
274 in the outflow were higher than we had expected based on previous reports. In a previous
275 study using the same coarse Hanford sediments as used in this study, *Shang et al.* [2008]
276 investigated colloid release from packed sediments under different flow rates varying from
277 0.018 to 0.288 cm/min ($= 259$ to 4147 mm/d), and observed a positive relationship between
278 the amount of colloids released and flow rate. Colloid concentration in column outflow for a
279 flow rate of 518 mm/d were reported to be 5 to 150 mg/L [*Shang et al.*, 2008]. The lowest
280 flow rates of Shang's study were three to four orders of magnitude larger than the flow rate
281 in our study here, and based on the strong dependency of the amount of colloid released on
282 flow rate (or water content) observed by *Shang et al.* [2008], we would have expected much
283 smaller colloid concentrations in our outflow samples.

284 Using coarse Hanford sediments similar to ours, *Cherrey et al.* [2003] investigated the
285 effect of different water saturations (and flow rates) on colloid transport. *Cherrey et al.* [2003]
286 did not study in situ colloid mobilization, but rather colloid transport through disturbed
287 sediments where colloidal suspensions were passed through packed sediment column under
288 different water contents and flow rates. They showed that colloids were more and more

289 retained inside the sediments as the volumetric water content decreased from saturation to
290 $0.11 \text{ cm}^3/\text{cm}^3$ (corresponding to flow rates of 59,000 to 72 mm/d, respectively). Transport
291 was inhibited, but still occurred at a water content of $0.11 \text{ cm}^3/\text{cm}^3$ [Cherrey *et al.*, 2003],
292 a water content similar to the one in our undisturbed sediment core, although the flow rates
293 in Cherrey *et al.* [2003] were three orders of magnitude higher.

294 Similar results of decreasing colloid transport and mobilization with decreasing water
295 content or flow rates in Hanford sediments have been reported by others [Chen *et al.*, 2005;
296 Cheng and Saiers, 2010]. Gamedainger and Kaplan [2001] studied colloid transport and
297 deposition in unsaturated sand and Yucca mountain tuff, and they observed that decreasing
298 water content resulted in more colloid deposition, thus less colloid transport.

299 Using a field lysimeter, Kaplan *et al.* [1993] applied a one time irrigation of 51 mm/h for
300 2 hours onto a lysimeter surface and monitored water outflow with a zero-tension drainage
301 port at 1.5-m depth. They observed colloid concentrations in the outflow ranging from 300 to
302 1700 mg/L. In a field study on an agricultural soil, Villholth *et al.* [2000] monitored particle
303 concentrations in drain lines installed at 1.1-m depth. They applied drip irrigation 12 mm/h
304 for 3 hours, and measured particle concentrations ranged from 0 to 130 mg/L [Villholth *et al.*,
305 2000]. Although some of the lowest water contents reported in previous studies are similar
306 to the ones in our study here, our flow rate was considerably lower. We are not aware of any
307 study where colloid mobilization was studied and reported under such a low flow rate as the
308 0.05 mm/d used in our study.

309 From field and laboratory studies on colloid transport and mobilization, it was reported
310 that the first flush of irrigation or rainfall generally produced the most colloid release [El-
311 Farhan *et al.*, 2000; Schelde *et al.*, 2002; Vendelboe *et al.*, 2011] and that the amount of

312 colloids released increased with increasing water content (and correspondingly increasing flow
313 rate) [Kaplan *et al.*, 1993; Villholth *et al.*, 2000; Gamerdinger and Kaplan, 2001]; however,
314 there is not always a strong correlation between colloid mobilization and rainfall intensities
315 or discharge rate [Biddle *et al.*, 1995; Jacobsen *et al.*, 1997; Ryan *et al.*, 1998; Worrall *et al.*,
316 1999]. For instance, using soil from Rocky Flats, Colorado, Ryan *et al.* [1998] reported a
317 poor correlation between particle concentrations and discharge rate. In their case, a lower
318 discharge rate of 83 mm/h mobilized more particles than a higher discharge rate of 167
319 mm/h. Such results can be explained by slow particle re-generation and diffusion-limited
320 colloid mobilization in the soil between rainfall events [Jacobsen *et al.*, 1997; Ryan *et al.*,
321 1998; Schelde *et al.*, 2002; Majdalani *et al.*, 2008].

322 **Continuous Colloid Release and Total Amounts of Colloids Released.** Fig-
323 ure 6d shows a continuous particle release from the sediment core, and based on the total
324 amount of colloids released over the experimental period, we calculated a colloid release rate
325 of 755 mg/(m²·year). Over the total period of the experiment since colloid outflow was ob-
326 served (967 days), a total of 0.392 g of particles were collected, corresponding to a cumulative
327 particle flux of 2 g/m². The total amount of dispersible particles in the sediments was esti-
328 mated to be 84.1 g (0.441 g/kg sediments). Based on this, the mobilized particles over 967
329 days constitute 0.5% (by mass) of the total dispersible particles.

330 Compared to the low recovery rate in our study, Shang *et al.* [2008] reported considerably
331 higher colloid release rates of up to 2885 mg/(m²·hour) in packed Hanford sediments having
332 volumetric water contents between 0.21 to 0.32 cm³/cm³. Disturbance and drying of the
333 sediments, as well as higher water content and flow rate, likely contributed to the differences
334 in the rates and amounts of colloids released between the Shang study and our experiments.

335 Disturbance has been found to promote colloid release also in other studies. It was for
336 instance reported that about twice as many colloids were released in disturbed compared to
337 undisturbed glacial outwash sediments [Bunn *et al.*, 2000]. As disturbance dislodges colloids
338 physically from sediment or soil particles, the increased colloid mobilization from packed
339 disturbed sediment is not unanticipated.

340 **Model Simulations.** Model simulations of colloid release could be fit well to the
341 experimental data (Figure 6d). Colloid transport parameters used for the modeling are listed
342 in Table 2. The fitted colloid release coefficient was $\beta = 7 \times 10^{-6} \text{ day}^{-1}$, with lower and
343 upper limits of 5.5 and $9.5 \times 10^{-6} \text{ day}^{-1}$, determined by adjusting the parameter β to fully
344 encompass the experimental data (Figure 6d, Table 2). Using the same model, Shang *et al.*
345 [2008] reported a range of colloid release rates from 10 day^{-1} to 120 day^{-1} for flow rates
346 from 259 mm/d to 415 mm/d. These values are six to seven orders of magnitude higher than
347 our rate. This large difference in release rates indicates that particle release is considerably
348 smaller in our undisturbed core under the much lower flow rate than in the disturbed, packed
349 column of Shang *et al.* [2008] at considerably higher flow rates and water contents.

350 **Nature of Released Colloids.** Figure 7 shows the energy dispersive x-ray spectra
351 and corresponding TEM images of outflow samples at different times. Colloid-size particles
352 were observed in all outflow samples. Energy dispersive x-ray spectra indicate the presence of
353 O, Na, Al, S, Si, Cl, K, Ca, Fe, and Br. While Na, Cl, Ca, and Br are likely contributed by the
354 irrigation solution, O, Al, Si, K, and Fe indicate the existence of silicates, aluminosilicates,
355 and Fe-oxides or hydroxides. Exact identification of minerals was not possible because not
356 enough material was available for x-ray diffraction. Although the particle counts and particle
357 concentrations were low during the experiment, colloidal-size particles could be consistently

358 found in TEM images corroborating the continuous mobilization of colloids from the sediment
359 core.

360 **3.3 Implications**

361 This study was conducted to investigate whether particles can be mobilized and translocated
362 under conditions typical for the deep vadose zone in semi-arid regions. While we had the
363 premise that particle mobilization is hindered under the low water contents and low steady-
364 state flow rates in the deep vadose zone in semi-arid regions, we did observe continuous
365 particle release. Our 5.3-year study showed that in situ colloid mobilization occurred at a
366 steady-state flow rate of 0.05 mm/d (= 18 mm/y) in an undisturbed sediment core. Although
367 release rate and mass recovery of particles were much lower than reported from previous
368 studies where colloid mobilization from disturbed, sediment columns was reported, we did
369 observe a continuous flux of particles leaving the sediment core.

370 We are not aware of other studies that have reported colloid mobilization and transport
371 in undisturbed sediments under flow rates as low as 18 mm/y, so we can not compare our
372 findings directly with other reports. However, the rates and amounts of colloid releases in our
373 study are several orders of magnitude smaller than reported from other colloid mobilization
374 studies using similar sediments, and are also smaller than amounts of colloid release reported
375 from agricultural soils.

376 Our results show that in semi-arid regions, the thick vadose zone with its low water
377 content and flow rates does not necessarily constitute a perfect filter for particle transport.
378 Even under low, steady-state flow rates, particles were mobilized. The continuous particle
379 mobilization observed here may be a possible pathway for colloid-facilitated contaminant

380 transport at the US DOE Hanford site.

381 **Acknowledgments.** This material is based upon work supported by the US Depart-
382 ment of Energy, Office of Science (BER), under Award No. DE-FG02-08ER64660. We thank
383 Bruce Bjornstad for help with the sampling of the undisturbed core. We thank, Jeff Boyle
384 for particle mobility determinations, Chris Davitt and Valerie Lynch-Holm for help with
385 TEM and EDX, and the WSU Franceschi Microscopy and Imaging Center for access to their
386 facility.

387 **References**

388

390 Aramrak, S., M. Flury, and J. B. Harsh, (2011), Detachment of deposited colloids by advanc-
389 ing and receding air-water interfaces, *Langmuir*, 27, 9985–9993.
391

392 Biddle, D. L., D. J. Chittleborough, and R. W. Fitzpatrick, (1995), Field monitoring of solute
393 and colloid mobility in a gneissic sub-catchment, South Australia, *Appl. Clay Sci.*, 9,
394 433–442.

395 Bohne, K., (2005), *An Introduction into Applied Soil Hydrology*, Catena Verlag, Reiskirchen,
396 Germany.

397 Bunn, R. A., R. D. Magelky, J. N. Ryan, and M. Elimelech, (2000), Mobilization of natural
398 colloids from an iron oxide-coated sand aquifer: Effect of pH and ionic strength, *Environ.*
399 *Sci. Technol.*, 36, 314–322.

400 Chen, G., and M. Flury, (2005), Retention of mineral colloids in unsaturated porous media
401 as related to their surface properties, *Colloids Surf. Physicochem. Eng. Aspects*, 256,
402 207–216.

403 Chen, G., M. Flury, J. B. Harsh, and P. C. Lichtner, (2005), Colloid-facilitated transport of
404 cesium in variably-saturated Hanford sediments, *Environ. Sci. Technol.*, 39, 3435–3442.

405 Cheng, T., and J. E. Saiers, (2010), Colloid-facilitated transport of cesium in vadose-zone
406 sediments: the importance of flow transients, *Environ. Sci. Technol.*, 44, 7443–7449.

407 Cherrey, K. D., M. Flury, and J. B. Harsh, (2003), Nitrate and colloid transport through

- 408 coarse Hanford sediments under steady state, variably saturated flow, *Water Resour.*
409 *Res.*, *39*, 1165, doi:10.1029/2002WR001944.
- 410 Czigany, S., M. Flury, and J. B. Harsh, (2005a), Colloid stability in vadose zone Hanford
411 sediments, *Environ. Sci. Technol.*, *39*, 1506–1512.
- 412 Czigany, S., M. Flury, J. B. Harsh, B. C. Williams, and J. M. Shira, (2005b), Suitability
413 of fiberglass wicks to sample colloids from vadose zone pore water, *Vadose Zone J.*, *4*,
414 175–183.
- 415 Deng, Y., J. B. Harsh, M. Flury, J. Young, and J. S. Boyle, (2006), Mineral formation during
416 simulated leaks of Hanford waste tanks, *Appl. Geochem.*, *21*, 1392–1409.
- 417 El-Farhan, Y. H., N. M. Denovio, J. S. Herman, and G. M. Hornberger, (2000), Mobilization
418 and transport of soil particles during infiltration experiments in an agricultural field,
419 Shenandoah valley, Virginia, *Environ. Sci. Technol.*, *34*, 3555–3559.
- 420 Flury, M., J. B. Mathison, and J. B. Harsh, (2002), *In situ* mobilization of colloids and
421 transport of cesium in Hanford sediments, *Environ. Sci. Technol.*, *36*, 5335–5341.
- 422 Gamedainger, A. P., and D. I. Kaplan, (2001), Colloid transport and deposition in water-
423 unsaturated Yucca Mountain Tuff as determined by ionic strength, *Environ. Sci. Tech-*
424 *nol.*, *35*, 3326–3331.
- 425 Gao, B., J. E. Saiers, and J. N. Ryan, (2006), Pore-scale mechanisms of colloid deposition
426 and mobilization during steady and transient flow through unsaturated granular media,
427 *Water Resour. Res.*, *42*, W01410, doi:10.1029/2005WR004233.

- 428 Gee, G. W., 1987. Recharge at the Hanford site: Status report, *Technical report*, Pacific
429 Northwest National Laboratory, Richland, WA.
- 430 Gee, G. W., J. M. Keller, and A. L. Ward, (2005a), Measurement and prediction of deep
431 drainage from bare sediments at a semiarid site, *Vadose Zone J.*, 4, 32–40.
- 432 Gee, G. W., M. D. Campbell, G. S. Campbell, and J. H. Campbell, (1992a), Rapid measure-
433 ment of low soil water potentials using a water activity meter, *Soil Sci. Soc. Am. J.*, 56,
434 1068–1070.
- 435 Gee, G. W., M. J. Fayer, M. L. Rockhold, and M. D. Campbell, (1992b), Variations in
436 recharge at the Hanford site, *Northwest Sci.*, 66, 237–250.
- 437 Gee, G. W., P. J. Wierenga, B. J. Andraski, M. H. Young, M. J. Fayer, and M. L. Rockhold,
438 (1994), Variations in water balance and recharge potential at three western desert sites,
439 *Soil Sci. Soc. Am. J.*, 58, 63–72.
- 440 Gee, G. W., Z. F. Zhang, S. W. Tyler, W. H. Albright, and M. J. Singleton, (2005b), Chloride
441 mass balance: cautions in predicting increased recharge rates, *Vadose Zone J.*, 4, 72–78.
- 442 Gephart, R. E., (2003), *Hanford: A conversation about nuclear waste and cleanup*, Battelle
443 Press, Columbus, Ohio.
- 444 Hanford Meteorological Station (2012), *Monthly and Annual Precipitation*, Pacific Northwest
445 National Laboratory, <http://hms.pnl.gov>, accessed March 2012.
- 446 Harvey, D., (2000), *History of the Hanford Site 1943–1990*, Pacific Northwest National Lab-
447 oratory, Richland.
- 448 Honeyman, B. D., (1999), Colloidal culprits in contamination, *Nature*, 397, 23–24.

- 449 Hsieh, J. J. C., L. E. Brownell, and A. E. Reisenauer, (1973), *Lysimeter experiment, de-*
450 *scription and progress report on neutron measurements*, BNWL-1711, Pacific Northwest
451 National Laboratory, Richland, Washington.
- 452 Jacobsen, O. H., P. Moldrup, C. Larson, L. Konnerup, and L. W. Petersen, (1997), Particle
453 transport in macropores of undisturbed soil columns, *J. Hydrol. (Amsterdam)*, 196,
454 185–203.
- 455 Jones, T. E., B. C. Simpson, M. I. Wood, and R. A. Corbin, (2000a), *Preliminary Inventory*
456 *Estimates for Single-Shell Tank Leaks in T, TX, and TY Tank Farms*, RPP-7218, CH2M
457 HILL Hanford Group, Richland, Washington.
- 458 Jones, T. E., M. I. Wood, R. A. Corbin, and B. C. Simpson, (2001), *Preliminary Inventory*
459 *Estimates for Single-Shell Tank Leaks in B, BX and BY Tank Farms*, RPP-7389, CH2M
460 HILL Hanford Group, Richland, Washington.
- 461 Jones, T. E., R. A. Watrous, and G. T. Maclean, (2000b), *Inventory Estimates for Single-*
462 *Shell Tank Leaks in S and SX Tank Farms*, RPP-6285, Rev. 0., CH2M HILL Hanford
463 Group, Richland, Washington.
- 464 Kaplan, D. I., P. M. Bertsch, D. C. Adriano, and W. P. Miller, (1993), Soil-borne mobile
465 colloids as influenced by water flow and organic carbon, *Environ. Sci. Technol.*, 27,
466 1193–1200.
- 467 Khaleel, R., M. D. White, M. Ostrom, M. I. Wood, F. M. Mann, and J. G. Kristofzski,
468 (2007), Impact assessment of existing vadose zone contamination at Hanford site SX
469 tank farm, *Vadose Zone J.*, 6, 935–945.

- 470 Knepp, A. J., (2002a), *Field Investigation Report for Waste Management Area B-BX-BY*,
471 RPP-10089, CH2M HILL Hanford Group, Richland, Washington.
- 472 Knepp, A. J., (2002b), *Field Investigation Report for Waste Management Area S-SX*, RPP-
473 7884, CH2M HILL Hanford Group, Richland, Washington.
- 474 Liu, Z., M. Flury, Z. F. Zhang, J. B. Harsh, G. W. Gee, C. E. Strickland, and R. E. Clayton,
475 (2012), Transport of europium colloids in vadose zone lysimeters at the semi-arid Hanford
476 site, *Environ. Sci. Technol.*, pp. (in review).
- 477 Majdalani, S., E. Michel, L. Di-Pietro, and R. Angulo-Jaramillo, (2008), Effects of wetting
478 and drying cycles on in situ soil particle mobilization, *Eur. J. Soil Sci.*, *59*, 147–155.
- 479 Mashal, K., J. B. Harsh, and M. Flury, (2005a), Clay mineralogical transformations over
480 time in Hanford sediments reacted with simulated tank waste, *Soil Sci. Soc. Am. J.*, *69*,
481 531–538.
- 482 Mashal, K., J. B. Harsh, M. Flury, A. R. Felmy, and H. Zhao, (2004), Colloid formation
483 in Hanford sediments reacted with simulated tank waste, *Environ. Sci. Technol.*, *38*,
484 5750–5756.
- 485 Mashal, K., J. B. Harsh, M. Flury, and A. R. Felmy, (2005b), Analysis of precipitates from
486 reactions of hyperalkaline solutions with soluble silica, *Appl. Geochem.*, *20*, 1357–1367.
- 487 McCarthy, J. F., and J. M. Zachara, (1989), Subsurface transport of contaminants, *Environ.*
488 *Sci. Technol.*, *23*, 496–502.
- 489 Myers, D. A., (2005), *Field Investigation Report for Waste Management Area T-TX-TY*,
490 RPP-23752, CH2M HILL Hanford Group, Richland, Washington.

- 491 Pace, M. N., M. A. Mayes, P. M. Jardine, T. L. Mehlhorn, J. M. Zachara, and B. N. Bjornstad,
492 (2003), Quantifying the effects of small-scale heterogeneities on flow and transport in
493 undisturbed cores from the Hanford Formation, *Vadose Zone J.*, *2*, 664–676.
- 494 Reidel, S. P., and M. A. Chamness, (2007), *Geology Data Package for the Single-Shell Tank*
495 *Waste Management Areas at the Hanford Site*, Pacific Northwest National Laboratory,
496 PNNL-15955, Richland, Washington.
- 497 Ryan, J. N., T. H. Illangasekare, M. I. Litaor, and R. Shannon, (1998), Particle and plutonium
498 mobilization in macroporous soils during rainfall simulations, *Environ. Sci. Technol.*, *32*,
499 476–482.
- 500 Sayers, J. E., and J. J. Lenhart, (2003), Colloid mobilization and transport within unsat-
501 urated porous media under transient-flow conditions, *Water Resour. Res.*, *39*, 1019,
502 doi:10.1029/2002WR001370.
- 503 Schelde, K., P. Moldrup, O. H. Jacobsen, H. de Jonge, L. W. de Jonge, and K. Komatsu,
504 (2002), Diffusion-limited mobilization and transport of natural colloids in unsaturated
505 macroporous soil, *Vadose Zone J.*, *1*, 125–136.
- 506 Serne, R. J., B. N. Bjornstad, H. T. Schaef, B. A. Williams, D. C. Lanigan, D. G. Horton, R. E.
507 Clayton, A. V. Mitroshkov, V. L. LeGore, M. J. O'Hara, C. F. Brown, K. E. Parker, I. V.
508 Kutnyakov, J. N. Serne, G. V. Last, S. C. Smith, C. W. Lindenmeier, J. M. Zachara, and
509 D. S. Burke, (2002), *Characterization of Vadose Zone Sediment: Uncontaminated RCRA*
510 *Borehole Core Samples and Composite Samples*, Pacific Northwest National Laboratory,
511 US Department of Energy, PNNL-13757-1, Richland, Washington.

- 512 Shang, J., M. Flury, G. Chen, and J. Zhuang, (2008), Impact of flow rate, water content,
513 and capillary forces on *in situ* colloid mobilization during infiltration in unsaturated
514 sediments, *Water Resour. Res.*, 44, W06411, doi:10.1029/2007WR006516.
- 515 Skoog, D. A., D. M. West, and F. J. Holler, (1996), *Fundamentals of Analytical Chemistry*,
516 7th ed., Saunders College Publishing, Fort Worth.
- 517 Sposito, G., (2008), *The Chemistry of Soils*, vol. Second, Oxford University Press, New York.
- 518 van Genuchten, M. T., (1980), A closed-form equation for predicting the hydraulic conduc-
519 tivity of unsaturated soils, *Soil Sci. Soc. Am. J.*, 44, 892–898.
- 520 Vendelboe, A. L., P. Moldrup, G. Heckrath, Y. Jin, and L. W. de Jonge, (2011), Colloid and
521 phosphorus leaching from undisturbed soil cores sampled along a natural clay gradient,
522 *Soil Sci.*, 176, 399–406.
- 523 Villholth, K., N. Jarvis, O. Jacobsen, and H. de Jonge, (2000), Field investigations and mod-
524 eling of particle-facilitated pesticide transport in macroporous soil, *J. Environ. Qual.*,
525 29, 1298–1309.
- 526 Vogs, C., (2009), *Modeling and Sensitivity Analysis of Water Flow and Colloid Transport*
527 *in an Undisturbed Hanford Sediment*, Institut für Geoökologie, Technische Universität
528 Carolo-Wilhelmina zu Braunschweig, Braunschweig, Germany.
- 529 Šimůnek, J., M. Šenĵy, H. Saito, M. Sakai, and M. T. van Genuchten, (2009), *The HYDRUS-*
530 *1D Software Package for Simulating the One-Dimensional movement of Water, Heat, and*
531 *Multiple Solutes in Variably-Saturated Media, Version 4.14*, Riverside, CA: Department
532 of Environmental Science, Univ. of California Riverside.

- 533 Worrall, F., A. Parker, J. E. Rae, and A. C. Johnson, (1999), A study of suspended and
534 colloidal matter in the leachate from lysimeters and its role in pesticide transport, *J.*
535 *Environ. Qual.*, *28*, 595–604.
- 536 Zachara, J. M., J. Sernr, M. Freshley, F. Mann, F. Anderson, M. Wood, T. Jones, and
537 D. Myers, (2007), Geochemical processes controlling migration of tank wastes in Han-
538 ford’s vadose zone, *Vadose Zone J.*, *6*, 985–1003.
- 539 Zhuang, J., J. F. McCarthy, J. S. Tyner, E. Perfect, and M. Flury, (2007), In-situ colloid
540 mobilization in Hanford sediments under unsaturated transient flow conditions: Effect
541 of irrigation pattern, *Environ. Sci. Technol.*, *41*, 3199–3204.
- 542 Zhuang, J., M. Flury, and Y. Jin, (2003), Colloid-facilitated Cs transport through water-
543 saturated Hanford sediment and Ottawa sand, *Environ. Sci. Technol.*, *37*, 4905–4911.
- 544 Zhuang, J., Y. Jin, and M. Flury, (2004), Comparison of natural colloid and kaolinite trans-
545 port in porous media, *Vadose Zone J.*, *3*, 395–402.

Table 1. Van Genuchten-Mualem parameters used for unsaturated water flow simulation.

The lower and upper limits of the optimized parameters indicate the 95% confidence interval.

Depth cm	θ_r^a cm ³ /cm ³	α cm ⁻¹			n [-]			K_s cm/d		
		Lower 95%	Optim.	Upper 95%	Lower 95%	Optim.	Upper 95%	Lower 95%	Optim.	Upper 95%
9.5	0.082	0.16	0.17	0.18	5.96	6.25	6.53	42	48	55
19.5	0.084	0.20	0.21	0.22	3.81	3.96	4.10	19	22	24
29.5	0.087	0.08	0.09	0.09	8.14	8.83	9.51	347	401	454
39.5	0.094	0.40	0.42	0.43	2.25	2.29	2.33	16	18	20
49.5	0.099	0.25	0.27	0.28	3.43	3.65	3.88	251	289	327

^a θ_r : measured; $\theta_s = 0.394$ cm³/cm³ for all layers, measured; $l = 0.5$ for all layers.

Table 2. Colloid transport parameters used in HYDRUS-1D.

Parameters	Unit	Value
Longitudinal dispersivity ^a	cm	3
Molecular diffusion coefficient in free water ^b	cm ² /d	5.8×10^{-4}
Bulk density ^c	g/cm ³	1.6
Colloid release rate coefficient ^d	d ⁻¹	7×10^{-6}
Colloid release rate coefficient upper limit ^e	d ⁻¹	9.5×10^{-6}
Colloid release rate coefficient lower limit ^e	d ⁻¹	5.5×10^{-6}
Initial particle concentration in liquid phase ^f	mg/cm ³	0
Initial sorbed concentration ^c	mg/g	0.441

^a *Bohne* [2005].

^b Calculated with the Stokes-Einstein equation using a particle diameter of 500 nm and a temperature of 12.4°C.

^c Measured experimentally.

^d Fitted with HYDRUS-1D.

^e Adjusted to encompass the experimental data.

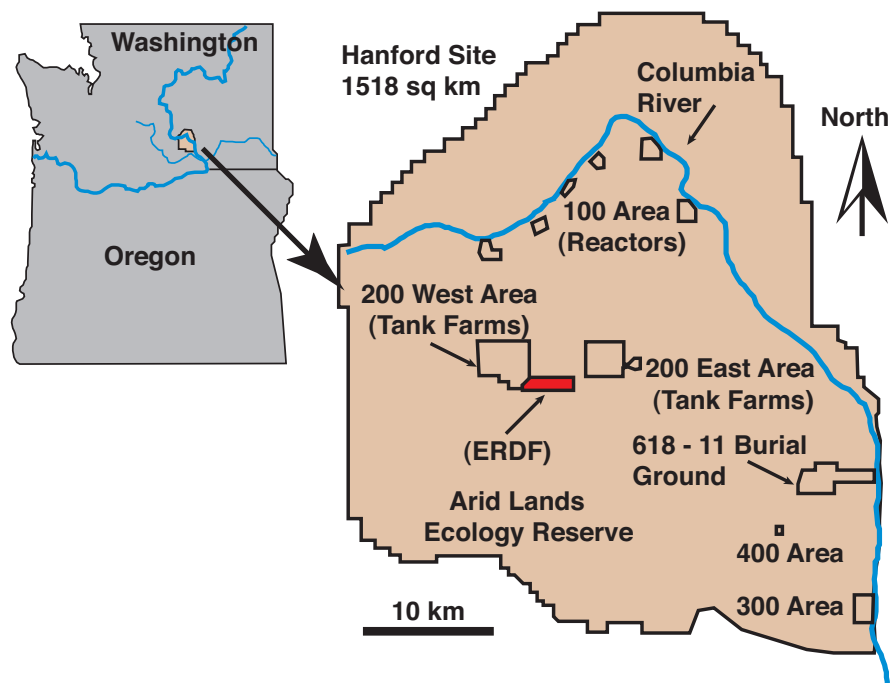


Figure 1. Map of the Hanford Site, Washington State. The sediment core was taken from the Environmental Restoration Disposal Facility (ERDF) at a depth of 17 meters below ground surface.

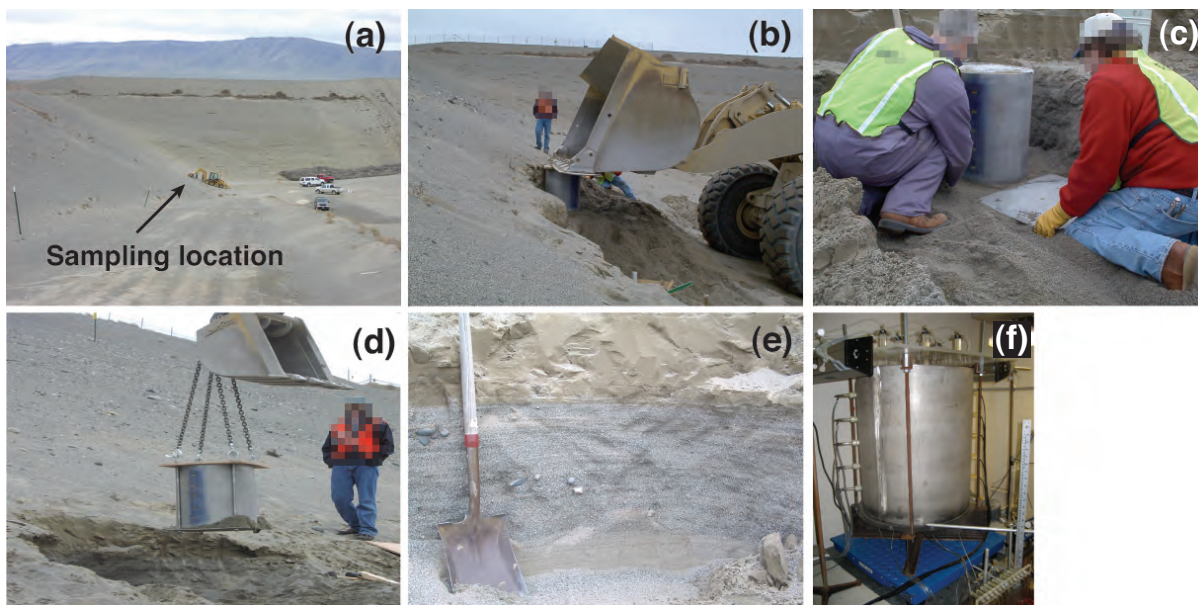


Figure 2. Sampling of sediment core and experimental setup. (a) Location of sampling in the ERDF pit, (b) insertion of steel cylinder into sediments, (c) shave-off of cylinder from sediments, (d) lift-off, (e) sediment layering of Hanford formation, and (f) laboratory setup.

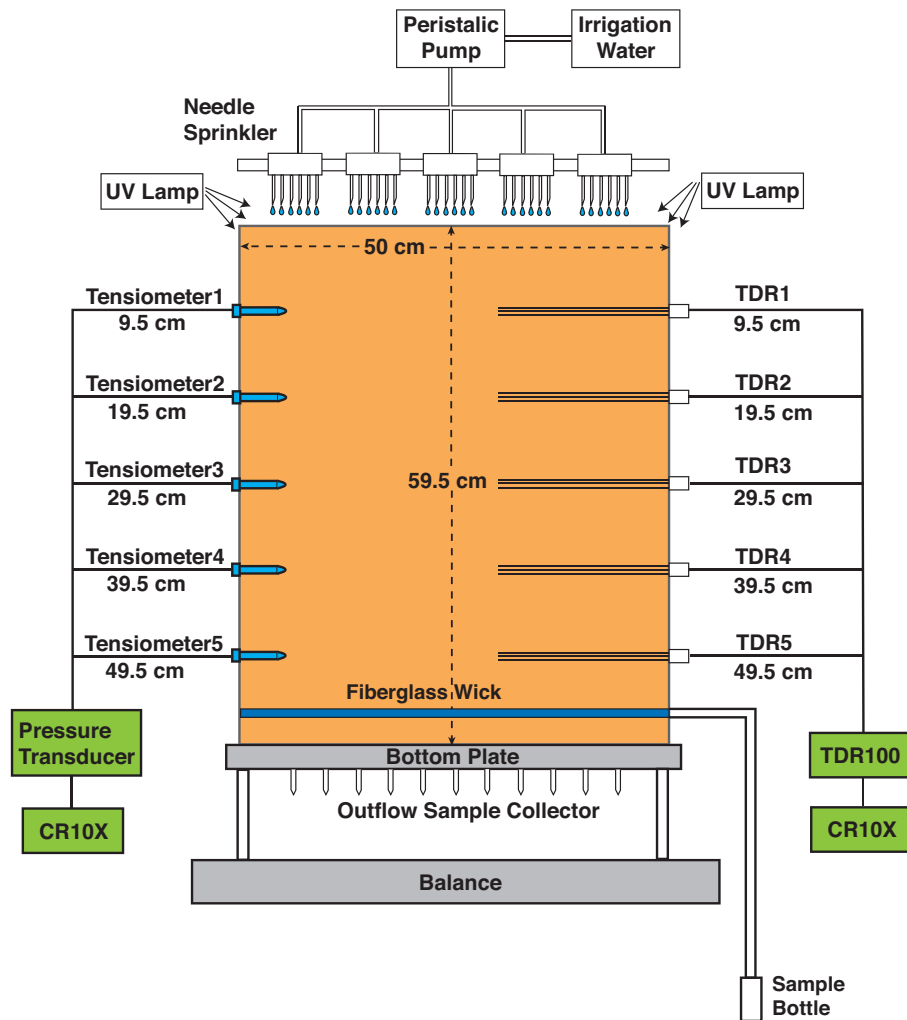


Figure 3. Schematic of the laboratory setup.

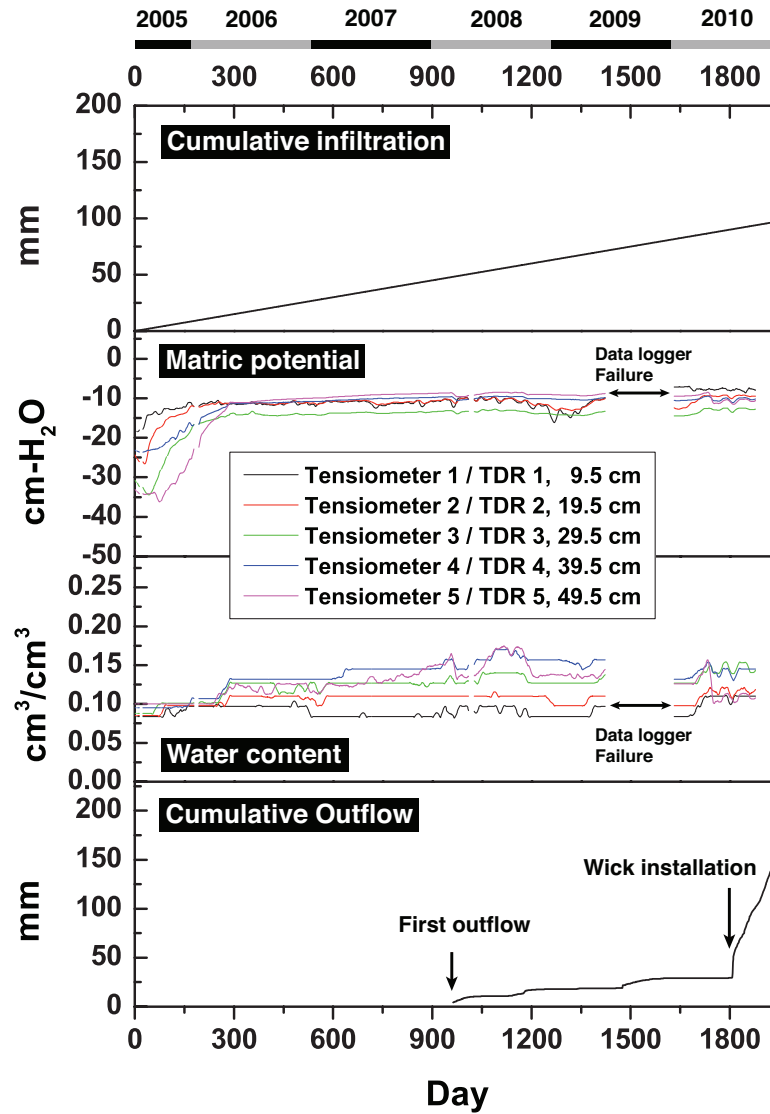


Figure 4. Cumulative infiltration, water potentials, water contents, and cumulative outflow during the course of the experiment. Data represent daily averages. (This is a color figure)

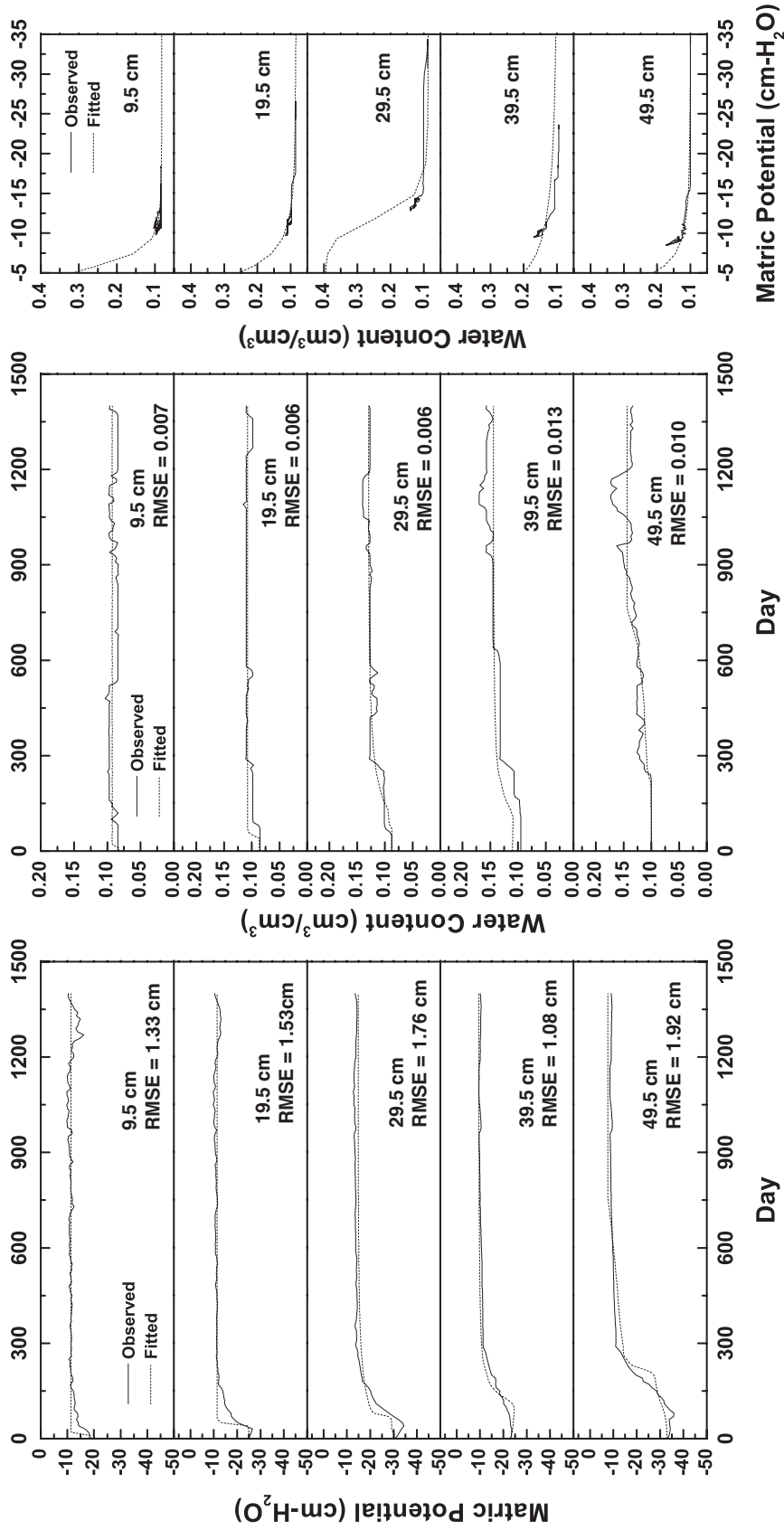


Figure 5. Observed (solid line) and fitted (dashed line) matric potentials and water contents, and water retention curves for the five different depths in the sediment core.

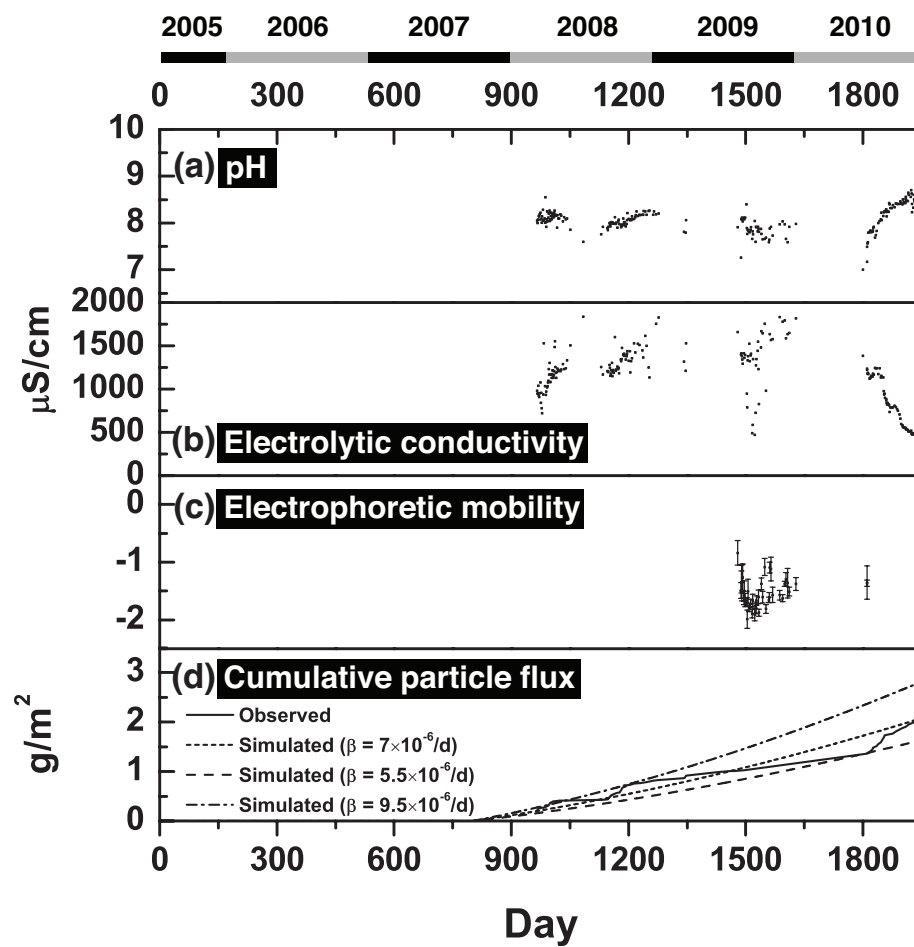


Figure 6. Characterization data of outflow from sediment core. (a) pH, (b) Electrolytic conductivity, (c) Electrophoretic mobility ($(\mu\text{m}/\text{s})(\text{V}/\text{cm})$), unit is not shown in the figure due to space limit, (d) Cumulative particle flux.

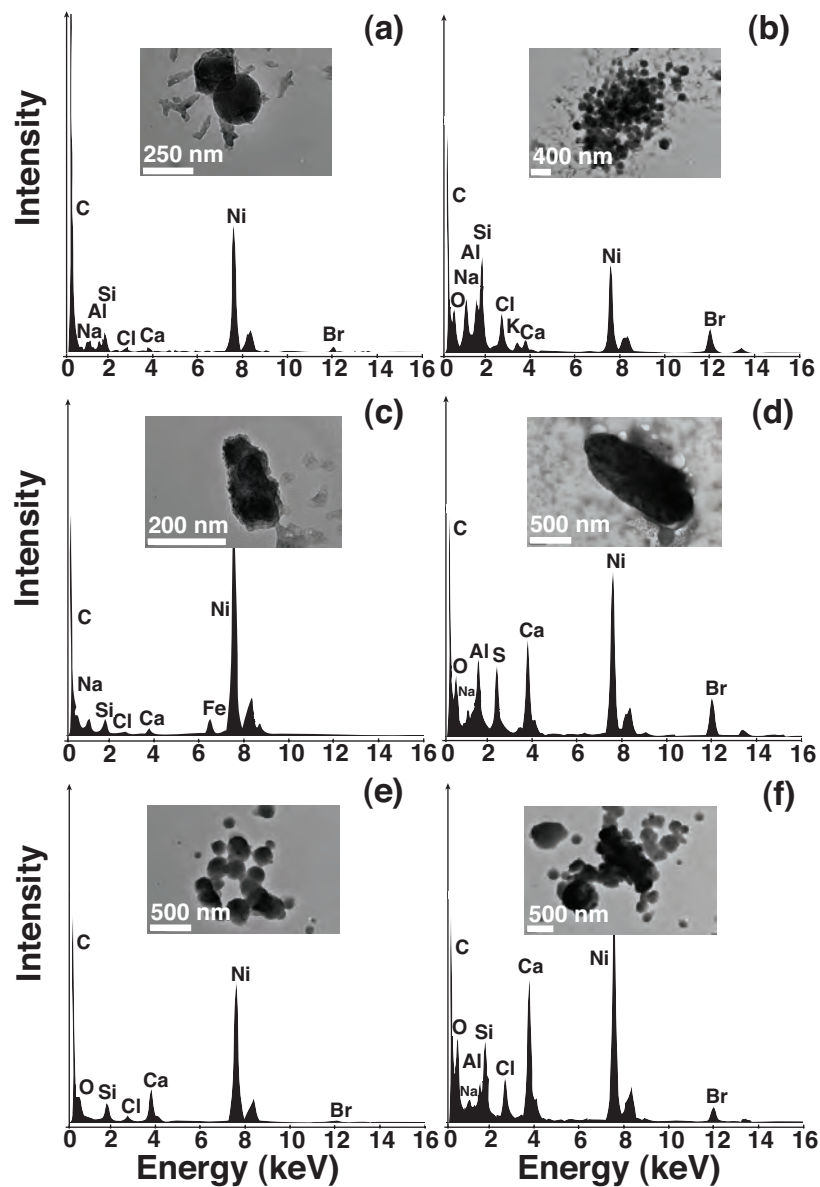


Figure 7. Energy dispersive x-ray spectra (EDX) and corresponding TEM images of selected outflow samples from (a) March 6, 2008, (b) March 6, 2008, (c) April 25, 2008, (d) May 8, 2008, (e) August 12, 2010, (f) August 12, 2010. The large peaks for C and Ni are from the microscopy stub.

How Does Colloid Shape Affect Detachment of Colloids by a Moving Air-Water Interface?

Surachet Aramrak^{a,b}, Markus Flury^{b,*}, James B. Harsh^a, Richard L. Zollars^c,
Howard P. Davis^c

^a Department of Crop and Soil Sciences, Washington State University, Pullman, WA 99164,
USA

^b Department of Crop and Soil Sciences, Washington State University, Puyallup, WA 98371,
USA

^c The Gene and Linda Voiland School of Chemical Engineering and Bioengineering, Wash-
ington State University, Pullman, WA 99164, USA

— Version 2.7, November 2, 2012; Prepared to be submitted to Langmuir

- 1 *Corresponding author:
- 2 Markus Flury
- 3 Department of Crop and Soil Sciences
- 4 Washington State University
- 5 Puyallup, WA 98371
- 6 Phone: 1-253-445-4522
- 7 E-mail: flury@wsu.edu

8 **Abstract.**

9 Air-water interfaces interact strongly with colloidal particles by capillary forces. The mag-
10 nitude of the interaction force depends, among other things, on the particle shape. Here, we
11 investigate the effects of particle shape on colloid detachment by a moving air-water interface.
12 We used hydrophilic polystyrene colloids with four different shapes (spheres, barrels, rods,
13 and oblong disks), but otherwise identical surface properties. The non-spherical shapes were
14 created by stretching spherical microspheres by using a film of polyvinyl alcohol (PVA). The
15 colloids were then deposited onto the inner surface of a glass channel. An air bubble was
16 introduced into the channel and passed through the channel, thereby generating a receding
17 and an advancing air-water interface. The detachment of colloids by the air-water inter-
18 faces was visualized by a confocal microscope, quantified by image analysis, and differences
19 in detachment were statistically analyzed. For all colloid shapes, the advancing air-water
20 interface caused pronounced colloid detachment ($>63\%$), whereas the receding interface was
21 ineffective in colloid detachment ($<1.5\%$). Among the different colloid shapes, the barrels
22 were most readily removed (94%) by the advancing interface, followed by the spheres and
23 oblong disks (80%), and the rods (63%). Colloid detachment was significantly affected by
24 colloid shape. The presence of an edge, like in a barrel-shaped colloid, promoted colloid
25 detachment because the air-water interface is being pinned at the edge. This suggests that
26 the magnitude of colloid mobilization and transport in porous media is underestimated for
27 edged particles and overestimated for rod-like particles when a sphere is used as a model
28 colloid.

29 1 Introduction

30 Particle shape is known to be an important parameter that strongly affects properties and
31 uses of colloids in research and industrial applications. In pharmacy, drug carriers are being
32 designed as a nano- and micro-fabricated particles in certain shapes and sizes for promoting
33 drug delivery [*Pan et al.*, 2011; *Elsabahy and Wooley*, 2012]. For instance, filament-shaped
34 carriers have been found to remain better in circulation than spherical carriers as they are less
35 readily taken up by immune cells, and consequently filament-shaped drug-carriers promoted
36 anticancer drug delivery and minimized tumor size in mice [*Geng et al.*, 2007]. At the same
37 adhesive strength, oblate particles have been shown to be better suited for delivery of both
38 drugs and contrast dyes than spherical particles, thus shape-optimizing designs for particles
39 are important for improving drug-delivery as well as imaging contrast [*Decuzzi and Ferrari*,
40 2006].

41 In mineral flotation, particularly at low flotabilities (i.e., in absence of a collector),
42 angular mineral particles are observed to accumulate faster than round ones, because edged
43 particles promote thinning and rupturing of air-water interfaces better than do smooth, round
44 particles [*Vizcarra et al.*, 2011]. Additionally, in filtration processes, during aerosolizing by
45 a nebulizer, cubic particles were removed from a filter less effectively than were spherical
46 particles, indicating that particle shape properties are significantly contributing to removal
47 efficiency [*Boskovic et al.*, 2005].

48 Particle shape also affects the fate and transport of colloidal particles in porous media.
49 Only few experiments have been conducted to investigate the effect of particle shape on
50 transport in porous media. Rod-like bacteria, for example, were reported to be retained
51 more than nearly spherical bacteria in saturated columns filled with quartz sand [*Weiss et al.*,

52 1995]. However, in this experiment the shape effect was not independent from the surface
53 properties of the bacteria, as different strains of bacteria were used [Weiss *et al.*, 1995]. The
54 effect of particle surface properties may be normalized or at least reduced, if shape-different
55 particles are produced from the same original particles. Spherical polystyrene can be formed
56 into different shapes by embedding them into a polyvinyl alcohol (PVA) film and subsequent
57 mechanical stretching to form rod-shaped particles [Ho *et al.*, 1993] or more complex shapes
58 [Champion *et al.*, 2007]. Such shape-modified polystyrene particles have been used to study
59 the effect of particle shape on particle transport and mobilization in porous media [Salerno
60 *et al.*, 2006; Liu *et al.*, 2010].

61 Rod-like particles modified according to the methods described by Champion *et al.* [2007]
62 were found to have increasing retention as the aspect ratio increased from 1:1 to 3:1 under
63 saturated transport in a glass bead-packed column [Salerno *et al.*, 2006]. However, retention
64 of rod-shaped polystyrene particles with an aspect ratio 7:1 was less than that of spheri-
65 cal particles, which was attributed to less straining of the rod-shaped particles [Liu *et al.*,
66 2010]. Retention of the rod-shaped particles was reported to occur in both the primary and
67 secondary energy minima, whereas the spherical particles were retained in the secondary
68 minimum [Liu *et al.*, 2010]. These different modes of particle attachment were attributed
69 to differences in electrostatic properties (i.e., electrophoretic mobility) between the particles
70 and alignment of the major axis of the rod-shaped particles with the collector [Liu *et al.*,
71 2010].

72 Under unsaturated flow conditions, air-water interfaces play an important role in particle
73 mobilization and retention. Particle shape is expected to affect the interaction forces at an air-
74 water interface. Capillary forces depend on the air-water-solid interface length, and the longer

75 the interface line, the stronger is the capillary force. These effects have been demonstrated
76 both theoretically as well as experimentally [*van Nierop et al.*, 2005; *Lehle et al.*, 2008; *Shang*
77 *et al.*, 2009; *Danov and Kralchevsky*, 2010; *Chatterjee et al.*, 2012]. Further, particles with
78 sharp edges cause the air-water interface to get pinned at these edges, causing an increase in
79 the capillary force and slip-pin behavior of the air water interface in a dynamic system [*Singh*
80 *and Joseph*, 2005; *Ally et al.*, 2012; *Chatterjee et al.*, 2012].

81 Microscopic investigations have demonstrated that moving air-water interfaces can de-
82 tach particles from stationary surfaces. Particles with different surface properties (charge,
83 contact angles), different interfacial velocities, and surface tensions have been studied [*Leenaars*
84 *and O'Brien*, 1989; *Noordmans et al.*, 1997; *Gomez-Suarez et al.*, 1999; *Gomez-Suarez et al.*,
85 2000; *Gomez-Suarez et al.*, 2001; *Sharma et al.*, 2008; *Lazouskaya et al.*, 2011]. In a recent
86 study [*Aramrak et al.*, 2011], we focused on detachment of deposited spherical particles by
87 advancing and receding air-water interfaces, and found that the advancing interface is much
88 more effective than the receding one at detaching particles from a stationary surface.

89 Here, we expand upon these studies by investigating the detachment of non-spherical
90 particles. Our objective was to quantify the effect of particle shape on particle detachment
91 from a solid surface by a moving air-water interface. We hypothesized that particles with
92 edges are most readily detached by an air-water interface, and that elongated particles are
93 the least detached because the air-water-solid interface line formed on an elongated particle
94 is the shortest if the particle is aligned parallel to the flow streamlines. We modified spherical
95 microspheres to create barrel-, rod-, and oblong disk-shaped particles and deposited them
96 onto the inner surface of a glass channel. Microscopic visualization and image analysis were
97 then used to quantify the colloid detachment caused by the passage of an air-water interface.

98 **2 Materials and Methods**

99 **2.1 Colloids and Shapes**

100 We used spherical, fluorescent, negatively charged, carboxylate-modified polystyrene colloids
101 (FluoSpheres, Lot Number 28120W, Molecular Probes Inc., Eugene, OR) with a diameter
102 of 1 μm . We modified the shape of these particles to form rods, oblong disks, and barrels.
103 These shapes represent surrogates of rod-like, plate-like, and edge-shaped particles, respec-
104 tively. The different shapes were made by enclosing the spherical particles in a polyvinyl
105 alcohol (PVA) film and stretching the film according to the methods described by *Champion*
106 *et al.* [2007]. In these methods, the resulting colloid shape is controlled by the PVA film
107 thickness, the plasticizer (glycerol), the liquefaction method (hot silicone oil or toluene), and
108 the stretching dimension (aspect ratio) and stretching order.

109 We first prepared a 5% (wt/vol) PVA solution by dissolving PVA in water at 85°C as the
110 medium for creating barrels and oblong disks, and a 10% (wt/vol) PVA solution for creating
111 rods. Glycerol at a final concentration of 0.5% and 2% (wt/vol) was subsequently added
112 to the PVA solution for barrels and oblong disks, respectively. Spherical colloids were then
113 added to the PVA solution to yield a colloid mass concentration of 0.14% (wt/vol) colloids.
114 The colloid-PVA suspension (10 mL) was then poured onto a flat 19 cm \times 24.5 cm surface of
115 a mirror glass and let evaporate at room temperature. The dried film (thickness of 35 μm for
116 the 5% PVA and 70 μm for the 10% PVA) could then be readily peeled of the glass surface.

117 The film was then cut into 2.5 cm \times 8 cm pieces and marked with a marker at a target
118 area of 2.5 cm \times 4 cm, with the edge portions being used to attach the film during the
119 stretching step. All the films were stretched in one dimension by a mechanical tension tester

120 (Model 3345, Instron[®], Canton, MA) at a stretching rate of 0.4 mm/s. The tension tester
121 instrument was equipped with a temperature-controlled container where liquids can be filled
122 in. In the case of the barrels, the film was stretched with a ratio of 1.6 before dipping the film
123 in hot silicon oil at 130°C for 12 min. For the rods, the film was first heated in silicon oil at
124 120°C for 5 min, and then stretched with a ratio of 2.4 while immersed in the hot oil. For both
125 of these cases, after stretching, the film was solidified by air cooling for 30 min. For the oblong
126 disks, the film was first immersed in toluene for 3 h, stretched with a ratio of 4.9, air-dried
127 for 10 h, and immersed in isopropanol for 12 h to remove the toluene. We intended to use the
128 toluene stretching procedure for elliptical disks as described by *Champion et al.* [2007], but
129 we instead obtained oblong disks even after repeated trials. We included the oblong disks into
130 our experiment as they had a high aspect ratio as well as edges. After the stretching step, the
131 films were dissolved in 30% isopropanol/water at 65°C and the suspension was centrifuged
132 at 13,000 rpm for 25 min ($\text{RCF} = 20,384$). The centrifugation step was repeated 10 times
133 with 30% isopropanol/water to wash all the PVA away from the colloids. The colloids then
134 were recovered, resuspended in deionized water, and kept in the dark at 4°C.

135 We also exposed spherical microspheres to the PVA treatment, heating, and extraction,
136 but without doing the stretching step, to check whether the chemical treatments and tem-
137 perature exposures would cause any changes in surface properties of the particles. These
138 spherical microspheres were used as control against which experiments with the differently
139 shaped colloids were compared. This kind of treatment of spherical colloids as controls to
140 compare against shape-modified colloids was also done by *Salerno et al.* [2006].

141 **2.2 Colloid Characterization**

142 Shape-modified colloids were examined with a scanning electron microscope (SEM) equipped
143 with a field emission electron gun (FEI Quanta 200F, FEI Co., Hillsboro, OR) to confirm their
144 expected shapes and check for uniformity. We measured characteristic lengths, i.e., major
145 and minor axes or diameters of barrels, rods, oblong disks, and spheres. Electrophoretic
146 mobilities and zeta potentials were determined by using dynamic light scattering (DelsaNano
147 C Particle Analyzer, Beckman Coulter Inc.) under a fixed background solution of 1 mM
148 CaCl_2 at different pH values. Based on the function of electrophoretic mobilities versus pH,
149 we selected pH 5.5 for the solutions to suspend the colloids for our experiments. At this pH,
150 the colloids were all negatively charged and similar among different shapes (Figure 1). All
151 the following measurements were done with colloids suspended in a solution of pH 5.5 and
152 1 mM CaCl_2 and were carried out at room temperature (18 to 20°C).

153 The advancing and receding contact angles of the colloids were determined by using
154 a manual goniometer (Model 147 50-00-115, Rame-Hart Instrument Co., Netcong, NJ). We
155 measured the contact angles of colloids which were air-dried on a soda-lime glass slide (25 mm
156 \times 75 mm, Fisher brand, Fisher Scientific). Several drops of a colloid suspension (1 mM CaCl_2
157 with pH 5.5) was air-dried on the slide to form a colloid cover. The advancing contact angle
158 was determined by dosing a drop of colloid-free solution (1 mM CaCl_2 , pH 5.5) with a syringe
159 until the measurement approached to constant value. For the receding contact angle, we
160 measured the contact angles while decreasing the drop size by withdrawing solution with the
161 syringe. Both contact angles were measured with three replications for each colloid shape.
162 These contact angles are macroscopic measurements, and may not represent microscopic
163 measurements [Decker *et al.*, 1999]. We also determined the advancing and receding contact

164 angles on the glass slide without colloid coating, which we used as a surrogate for the glass
165 channel we used for colloid deposition described below.

166 **2.3 Colloid Deposition**

167 We deposited the colloids onto the inner surface of a hydrophilic glass channel as described
168 in a previous study [Aramrak *et al.*, 2011]. The channel had a diameter of 3.7-mm diameter
169 and a length of 7.5-cm, and was cleaned with acetone, ethanol, and double-deionized water.
170 Details on the design, the cleaning procedure, and the surface characterizations of the glass
171 channel are given in Aramrak *et al.* [2011]. Electrophoretic mobility characteristics were
172 measured on a suspended powder ground from the glass channel (Figure 1).

173 A colloid suspension (pH 5.5, 1 mM CaCl₂, colloid concentration of 3.6×10^{11} particles/L)
174 was circulated through the glass channel for 2 h at a flow rate of 0.33 mL/min (mean velocity
175 of 186 cm/h). Non-deposited colloids were rinsed off by flushing with a colloid-free solution
176 (pH 5.5, 1 mM CaCl₂). The channel was then kept saturated with the aqueous solution and
177 transferred to the stage of a confocal microscope for the colloid detachment experiments.

178 **2.4 Colloid Detachment by Air-Water Interface**

179 For the air-water interface experiments, an air bubble was injected into the glass channel
180 by introducing air into the connected Tygon tubing, as described in Aramrak *et al.* [2011].
181 We used a constant flow rate of 0.9 μ L/min (mean velocity of 0.5 cm/h inside the channel
182 calculated with Hagen-Poiseuille). This flow rate corresponds to a Reynolds number of 0.01
183 ($Re = \rho_w V D_H / \mu$; where ρ_w is the density of water (kg/m³), V is the mean velocity (m/s), D_H
184 is the inner diameter of the channel (m), and μ is the dynamic viscosity of water (kg/(m·s)),
185 indicating that the flow inside the channel is laminar. Under this flow rate, the water film

186 thickness in the air-filled channel is estimated to be about $0.03 \mu\text{m}$ [Aramrak *et al.*, 2011].
187 At this water film thickness, we expect that an air-water-colloid contact line will form for all
188 our colloids when the air-bubble moved through the channel. All experiments were done at
189 room temperature (18 to 20°C) and repeated 8 times, where each replicate constitutes a new
190 glass channel.

191 **2.5 Colloid Visualization and Quantification of Detachment**

192 Deposited colloids on the glass surface were visualized with a laser scanning confocal micro-
193 scope (Axiovert 200 M equipped with LSM 510 META, Carl Zeiss Jena GmbH, Germany).
194 An area of $900 \mu\text{m} \times 900 \mu\text{m}$ at the bottom section of the horizontally-oriented glass channel
195 was scanned by the microscope. A passage of an air bubble constitutes the movement of a
196 receding (front of bubble) and an advancing (back of bubble) air-water interface. A first scan
197 with the microscope provided the initial distribution of the colloids, and subsequent scans
198 were made after passage of the receding air-water interface, during the presence of the air
199 bubble, and after passage of the advancing air-water interface.

200 The confocal microscope images were analyzed with the ImageJ software [NIH, 1999] to
201 quantify the amounts of colloids present. More details on colloid visualization and quantifi-
202 cation are given in Aramrak *et al.* [2011], where the same techniques were used.

203 **2.6 Orientation of Colloids**

204 The confocal imaging does not allow determining the orientation of the colloids, we only can
205 see whether a colloid is present or not. To visualize the orientation of deposited colloids, we
206 used SEM. For that purpose, a $2 \text{ mm} \times 8 \text{ mm}$ section of a microscopy cover glass slide was
207 inserted into the glass channel. The small glass slide was cleaned in the same manner as the

208 glass channel, marked to recognize the flow direction, inserted into the glass channel, and then
209 colloids (rods, barrels, and oblong disks) were deposited as described above. The channel was
210 then drained (i.e., a receding air-water interface moved over the deposited colloids during this
211 drainage step) and air dried. Previous experiments [Aramrak *et al.*, 2011] have shown that
212 the receding air-water interface does not detach significant amounts of colloids from the glass
213 surface. The orientation of the non-spherical colloids on the glass slide was then visualized
214 by SEM.

215 **2.7 Re-deposition of Colloids**

216 Another set of experiments was conducted to check whether colloids would re-deposit at the
217 same location when another deposition was made after a detachment experiment. We only
218 used spherical colloids for these experiments. We hypothesized that colloids would re-deposit
219 at the same location from where they have been detached. The first deposition was visualized
220 and recorded by confocal microscopy, and then followed by a detachment by a moving air-
221 water interface (receding and advancing) as previously described. The second deposition
222 step was made in situ, without moving the channel under the confocal microscope, so that
223 the positions of the colloids in the microscope view would not change. After the second
224 deposition was visualized, a second air-water interface (receding and advancing) was passed
225 over the colloids, followed by a third re-deposition. Confocal images of colloid deposition
226 were analyzed by the subtraction mode of the ImageJ software to compare the location of
227 deposited colloids. The experiment was repeated three times, with a new glass channel each
228 time.

2.8 Statistical Data Analysis

We analyzed the detachment of colloids as the function of particle shape (spheres, barrels, rods, and oblong disks) by using a one-way ANOVA with LSD and Turkey pair-wise comparison to determine statistical differences at the 95% confidence level [SAS Institute Inc., 1990].

3 Theoretical Approach

The maximum detachment force exerted by an air-water interface on a spherical colloid deposited on a flat surface is given by [Noordmans *et al.*, 1997; Sharma *et al.*, 2008; Aramrak *et al.*, 2011]:

$$F_{\gamma,max} = 2\pi R_p \gamma \sin^2 \left(\frac{\theta}{2} \right) \cos \alpha, \quad \alpha < 90^\circ \quad (1)$$

where $F_{\gamma,max}$ is the vertical component of the detachment force due to surface tension, R_p is the radius of the particle, γ is the surface tension of water, θ is the colloid-air-water contact angle, and α is the glass-air-water contact angle. The factor $2\pi R_p$ represents the length of the air-water-colloid interface line, and for non-spherical colloids this factor has to be adapted. We use two different approximations to estimate the detachment force for non-spherical colloids: (1) we consider the colloids to be spheres having the same surface area as the non-spherical colloids, i.e., surface-area-equivalent colloids, and (2) we estimate the actual air-water-interface length geometrically by considering the orientation of the colloids with respect to the movement of the air-water interface.

248 3.1 Effective Radius

249 We define an effective radius (a_{eff}) as the radius of a sphere having the same surface area as
 250 the non-spherical colloid [Salerno *et al.*, 2006; Liu *et al.*, 2010]:

$$251 \quad a_{\text{eff}} = \sqrt{\frac{S}{4\pi}} \quad (2)$$

252 where S is the surface area of the colloid, which depends on the size and shape (we do not
 253 consider roughness here). For a rod-shaped colloid, the surface area S_{rod} can be estimated
 254 as [Salerno *et al.*, 2006; Liu *et al.*, 2010]:

$$255 \quad S_{\text{rod}} = 2\pi c^2 + \left(\frac{2\pi ca}{e}\right) \arcsin e \quad (3)$$

256 where c is the minor semi-axis, a is the major semi-axis, and e is the ellipticity of the rod,
 257 which is approximated by $e = \sqrt{1 - c^2/a^2}$.

258 For a barrel, we estimate the surface area by calculating the surface area of two frustums
 259 of cones, excluding the face-to-face area of the two bases, as follows:

$$260 \quad S_{\text{barrel}} = 2 \left[\pi(r + R)s + \pi r^2 + \pi R^2 \right] - 2\pi R^2 \quad (4)$$

261 where r is the end-portion radius, s is the slanted height ($s = \sqrt{(R - r)^2 + h^2}$, where h is the
 262 height of the barrel), and R is the center portion radius. For an oblong disk, the surface area
 263 is obtained by quantitatively analyzing SEM images, i.e., measuring the area of individual
 264 segments. The effective radii of the different shapes of colloids were then determined by
 265 Equation (1).

266 3.2 Perimeter Length

267 We estimated the length of the actual air-water-colloid interface line by considering the
 268 orientation of the colloids with respect to the moving air-water interface. We consider the

269 two extreme cases of longitudinal and perpendicular alignment of the colloids along the flow
270 direction, i.e., we align the colloids either by their major or minor axis. The contact line
271 shapes for the different alignments are shown in Table 1. We measured the perimeter lengths
272 from SEM images. The perimeter lengths were then normalized by the perimeter of the
273 spherical colloid, and represented as dimensionless ratios (Table 1).

274 **3.3 DLVO Forces**

275 We calculated DLVO forces between colloids and the glass channel according to Gregory [Gre-
276 gory, 1975; Gregory, 1981; Sharma *et al.*, 2008]. For the non-spherical colloids, we assume
277 in the DLVO calculations that the colloids are spherical with a diameter of a surface-area
278 equivalent sphere [Liu *et al.*, 2010]. For spheroidal-shaped particles, DLVO forces can be cal-
279 culated based on the approach of *Bhattacharjee et al.* [2000]. The DLVO forces will depend
280 on specific orientation of particles with respect to the flat collector surface (i.e., end-on or
281 side-on configuration) [Bhattacharjee *et al.*, 2000; Adamczyk, 2006]; however, as we do not
282 have experimental evidence of the specific configuration in our flow channel, and we also have
283 non-spheroidal particle shapes, we did not quantify the DLVO forces with a shape-dependent
284 approach, but use the equivalent-shape approach as an approximation.

285 **4 Results and Discussion**

286 **4.1 Characterization of Colloids and Glass Channel Surface**

287 We speculated that the plasticization procedure with PVA, toluene, and hot silicone oil could
288 deactivate, i.e., destroy, some of carboxylate functional groups, resulting in overall less nega-
289 tive surface charges at higher pHs. The results of the electrophoretic mobility measurements

indeed confirmed that the chemical treatments used to change the colloid shape also changed the surface charges (Figure 1a). In general, the electrophoretic mobilities of colloids at $\text{pH} > 5$ increased when either toluene or silicone hot oil was used as heating source. The data for $\text{pH} < 5$ were less conclusive. PVA-treated spheres had smaller electrophoretic mobilities at $\text{pH} > 5$ and higher electrophoretic mobilities at $\text{pH} < 5$ than the non-treated spheres, suggesting that the PVA created more pH -dependent surface functional groups on the colloid surface. The hot oil and toluene treatments, however, indeed destroyed some of the carboxylate functional groups, causing the colloids to become less negative at $\text{pH} > 5$ as compared to the non-treated colloids.

Given these results, it is important, for comparative purposes, to use spheres that have undergone plasticization treatment as the control for our experiments, so that surface properties among different colloid shapes remain similar. In our case, we selected spheres treated with hot oil at 130°C to be the control treatment because of their overall electrophoretic mobilities as a function of pH falling in the same range compared to non-spherical colloids (Figure 1b).

Electrophoretic mobilities among the different shapes of the colloids generally did not vary, but were most similar between pH 5 and 6 (Figure 1b). Statistical analysis confirmed our observation, indicated by insignificant differences among colloids at pH 5.5, except for the glass channel (Table 2). We observed that the glass channel had higher negative surface charges than the colloids.

Based on Figure 1b, we selected chemical conditions at pH 5.5 for deposition and detachment experiments, which are discussed later. Table 2 summarizes geometrical and surface properties of the different colloids. Advancing and receding contact angles were not

313 significantly different among the colloids, but the static contact angles showed significant
314 differences. These data indicate that the basic surface properties (i.e., dynamic contact an-
315 gles and electrophoretic mobilities) were not significantly different among the different colloid
316 shapes, suggesting that the shape of particles, which is our physical property of interest, is
317 independent from surface properties.

318 SEM micrographs of colloid shapes after plasticization are shown in Figure 2. The rods
319 had considerably higher aspect ratio than the barrels, but a smaller aspect ratio than the
320 oblong disks. The barrel had a distinct edge at each end. The SEM micrograph insert
321 in Figure 2d also shows that the oblong disks had edges, but these were less pronounced
322 than those of the barrels. The SEM images overall also show that the shape modification
323 produced uniform particles, with little variation among the particles, as indicated by the
324 narrow standard deviation of the shape parameters (Figure 2, Table 2).

325 4.2 Effect of Shapes on Colloid Detachment by an Air-Water Interface

326 Our results here and previous results [*Aramrak et al.*, 2011] indicate that the receding air-
327 water interface could not remove substantial amounts of deposited colloids. The removal of
328 colloids was mostly from the advancing air-water interface. Figure 3 shows the visualization
329 of each shape of colloids at the initial deposition (left column) and after the passage of
330 the advancing air-water interface (right column). At the initial deposition, the amounts of
331 colloids among the different four shapes within a confocal microscopic area of $900 \mu\text{m} \times$
332 $900 \mu\text{m}$ were in the range of 65 to 85 particles. After the advancing air-water with the mean
333 velocity of 0.5 cm/h had passed over, the detachment of each shape of colloids was found to
334 be qualitatively in the following order (from more detachment to less detachment): barrel >

335 sphere \approx oblong disk $>$ rod.

336 Figure 4 shows the quantitative analysis of these detachment data. The advancing air-
337 water interface was found to dominate the receding interface in detaching deposited colloids
338 regardless different colloid shapes. Statistical differences of the detachment of rods, barrels,
339 and oblong disks compared to spheres confirmed the visual observations. Compared to the
340 spheres, the barrels were found to be significantly more detached by the advancing air-water
341 interface, but the rods were significantly less detached, while the oblong disks did not show
342 significant differences in detachment (Figure 4).

343 The detachment of rods was significantly less than that of spheres. With their higher
344 aspect ratio compared to the spheres, the rods in general have a higher surface area than the
345 spheres, so should also have a longer air-water interface line than the spheres, thereby being
346 exposed to larger surface tension forces and more detachment. However, if the rods align with
347 their major axis along the flow streamlines in the channel, then the air-water interface line
348 will be smaller than that of the spheres, thereby experiencing less surface tension energy for
349 detachment compared to spheres. That the orientation of attached rod-shaped particles with
350 respect to streamline in a porous medium affect transport behavior has also been reported
351 by others [*Salerno et al.*, 2006; *Liu et al.*, 2010].

352 Based on theoretical considerations using DLVO theory [*Bhattacharjee et al.*, 2000;
353 *Adamczyk*, 2006; *Liu et al.*, 2010], we would expect that the adhesive DLVO forces for a
354 rod-shaped colloid is different from that of a spherical colloid. The net adhesive force will
355 depend on the spatial arrangement of the colloid with respect to the planar surface of the
356 collector. For non-favorable attachment conditions, i.e., in presence of a secondary energy
357 minimum, the rod-shaped colloids would be expected to attach in an end-on configuration,

358 where the longitudinal axis of the rod is perpendicular to the planar surface [*Bhattacharjee*
359 *et al.*, 2000]. This arrangement would reduce the adhesive force as compared to side-on con-
360 figuration, or even to a spherical colloid with a surface-area equivalent radius. However, we
361 have no experimental evidence whether end-on or side-on configurations are obtained by our
362 non-spherical colloids, we cannot calculate reliable DLVO forces.

363 *Salerno et al.* [2006] and *Liu et al.* [2010] studied transport of rod-shaped particles
364 through saturated glass bead columns. They used spherical carboxylate-modified latex mi-
365 crospheres with particle diameter of 1 μm [*Salerno et al.*, 2006] and 0.5 μm [*Liu et al.*, 2010].
366 Rod-shaped particles were produced according to *Ho et al.* [1993] and *Champion et al.* [2007].
367 *Salerno et al.* [2006] reported that the collision efficiency increased when the colloid aspect
368 ratio increased from 1:1 to 2:1 and 3:1. *Liu et al.* [2010] reported that the colloid shape af-
369 fected transport, but that rod retention did not increase with higher aspect ratios, even when
370 the aspect ratio was as high 7:1. *Liu et al.* [2010] mentioned that the retention of rods oc-
371 curred in both the primary and secondary energy minima, whereas the spheres were retained
372 in the secondary minimum. These different modes of particle attachment were explained
373 by differences in electrostatic properties (i.e., electrophoretic mobility) between spheres and
374 rods, and also by differences in alignment of the rods with the collector surface [*Liu et al.*,
375 2010]. In our experiments, we maintained similar electrostatic properties (i.e., electrophoretic
376 mobility) among the different colloids by treating the spheres, used as controls, similarly as
377 the non-spherical colloids and selecting an appropriate solution chemistry for the detach-
378 ment experiments, so that differences in surface chemical properties among colloids should
379 be minimal.

380 Barrels showed significantly higher detachment by the moving air-water interface than

381 any other colloid shape in our experiments. Barrels had a higher aspect ratio than the spheres
382 (Table 2), but had edges on which the moving air-water interface could get pinned during
383 the air-bubble movement. This pinning will lead to an increased surface tension force acting
384 on the colloids. Our findings agree with current studies of theoretical and experimental
385 capillary forces of edge-shaped particles in contact with an air-water interface [*Singh and*
386 *Joseph, 2005; Shang et al., 2009; Chatterjee et al., 2012*]. *Shang et al.* [2009] reported
387 that the pinning of the air-water interface at the edge of particle increased the effective
388 contact angle and the contact line perimeter (radius), thereby generating order-of-magnitude
389 higher capillary forces than experienced by smooth spheres. We do not have capillary force
390 measurements for barrel-shaped particles, but we speculate that the edges of our barrels is
391 similar in its effect on the surface tension force as the edges in the circular cylinder reported
392 by *Shang et al.* [2009] and *Chatterjee et al.* [2012]. We therefore attribute the pronounced
393 detachment of barrels by the air-water interface to the pinning of the interface line at the
394 edges.

395 The detachment of oblong disks was not significantly different from that of the spheres.
396 The average thickness of the oblong disks was about $60 \mu\text{m}$, which was still thicker than
397 the expected water film thickness ($30 \mu\text{m}$) [*Aramrak et al., 2011*], so that a colloid-air-water
398 interface line should have formed, and consequently, colloids were detached by the moving
399 air-water interface. Although we do not have direct evidence, we suspect that the presence
400 of the edges oblong disks caused the air-water interface line to get pinned, but that the
401 perimeter of the pinned interface line was much smaller than in case of the barrels, thereby
402 making the overall detachment force less than that of the barrels.

403 4.3 Colloid Orientation

404 We expected that our non-spherical particles would align with the flow direction of the colloid
405 suspension during deposition. *Xu et al.* [2008] studied the straining of peanut-shaped particles
406 in sand columns and found that particles tended to align their major axis along the flow
407 direction when the particles entered pore-restricted space. The alignment increased as the
408 aspect ratio of the particles increased [*Xu et al.*, 2008]. In our experiments, we did not observe
409 perfect alignment of the colloids along the flow direction, rather we found some considerable
410 deviations of the alignment of the major axis, particularly for the barrels (Figure 5). The
411 quantitative analysis of the orientation showed that the angles of the major axis with respect
412 to the flow direction were $55 \pm 18^\circ$ for the barrels, $38 \pm 22^\circ$ for the rods, and $21 \pm 15^\circ$ for the
413 oblong disks. The closer the oriented angles to 0° , the more perfect was the alignment of the
414 colloids, whereas an angle of 90° would indicate perpendicular alignment. Our data generally
415 show that the higher the aspect ratio of the colloids, the better and more consistent was the
416 alignment of the major axis along the flow direction. The barrels, however, were aligned more
417 in perpendicular orientation than in axial direction of the flow rate, as their orientation was
418 $> 45^\circ$. The high standard deviation of the angles for all colloid shapes indicates a high degree
419 of non-uniformity of the attachment orientation. Non-uniform orientation of non-spherical
420 colloids with respect to the flow direction in our experiment may be explained by the fact
421 that the ratio between the colloid size and the channel diameter in our case was constant,
422 thereby no pore-space gradient from the widest to narrowest of the constriction was present
423 in our case compared to experiments reported by *Xu et al.* [2008].

424 4.4 Detachment Forces

425 Detachment forces calculated with Equation (1) are summarized in Table 1. The detachment
426 forces increase as expected with increasing effective radius (sphere = barrel < rod < oblong
427 disk), but the increase in force is not that substantial, the detachment force for the oblong
428 disk is only 12% larger than for the sphere. Calculating the interface line length based on
429 the major and minor axes provides a larger span of detachment forces, and the forces differ
430 substantially. Using the major axis for the calculations shows that the detachment force for
431 the rods increased by 110% and for the oblong disk by 132% as compared to the spheres.

432 Compared with the experimental detachment data (Figure 4), however, the theoretical
433 detachment forces do not agree well: the experimental sequence of detachment increased in
434 the order rod < sphere \approx oblong disk < barrel, which does not correspond to sequences of
435 forces shown in Table 1, neither for the effective radii nor the major or minor axes.

436 If we, however, also consider the orientation of the particles with respect to the flow
437 direction, then we find a better agreement between experimental detachment and theoretical
438 detachment forces. The rods and oblong disk tended to have their major axes aligned with the
439 direction of the air-water interface movement, i.e., exposing their minor axis to the air-water
440 interface, while the barrels were more aligned along their minor axis. This would translate
441 to increasing theoretical detachment forces as follows: oblong disk < rod < sphere < barrel,
442 which is in better agreement with the experimental data.

443 Nevertheless, the perimeter length approach does not consider the effect of the edges of
444 the colloids (i.e., barrel and oblong disk), which was reported to cause increased capillary
445 forces due to pinning of the air-water interface [*Singh and Joseph, 2005; Chatterjee et al.,*
446 2012]. The effect of the particle edges should have exacerbated detachment of the barrels and

447 oblong disks, and our experimental data qualitatively agree with this: barrels were detached
448 the most (have the largest detachment force and have edges), whereas oblong disks had the
449 smallest detachment force but have edges, and the disks were detached similarly to spheres
450 which would have a considerably higher detachment force. This suggests that the edge effect
451 was considerable and important.

452 According to the calculated DLVO profiles, we assume that most of our colloids attached
453 to the glass surface in the primary energy minimum as indicated by a low in energy barrier
454 (<35 kT) and low attractive secondary energy minima (-0.1 kT) for all four differently-
455 shaped colloids. The attachment force in the primary minimum strongly depends on the
456 colloid-glass channel separation distance. If we assume a separation distance of 0.1 nm
457 [*Weronski and Elimelech, 2008; Aramrak et al., 2011*], then the maximum attractive DLVO
458 forces for all four shapes of the colloids were in the order of 10^{-5} mN. This force is of the
459 same order of magnitude as the detachment force (Table 1). Given that the air-water interface
460 was effective in removing colloids from the glass surface, the actual detachment force must
461 have exceeded the attachment force. The attachment force is highly dependent on separation
462 distance: if we assume that attached colloids have a separation distance of 0.2 nm, then
463 the attachment force will decline to the order of 10^{-6} mN, which is one order of magnitude
464 smaller than the detachment force.

465 **4.5 Re-deposition**

466 Figure 6a shows the locations and amounts of the first colloid deposition (yellow dots). After
467 the passage of a receding and advancing air-water interface (one air bubble), the remaining
468 of the deposited colloids are shown in Figure 6b. After the second deposition of colloids,

469 none of the newly deposited colloids (white dots in Figure 6c) were found at the locations
470 were colloids had deposited in the first deposition step. The second air bubble removed all
471 of the newly deposited colloids (white dots) plus some of the colloids deposited in the first
472 deposition (yellow dots) (Figure 6d). Colloids deposited during the third deposition step
473 were all attached at locations not coinciding with previous attachment locations (red dots
474 in Figure 6e). Only two colloids from the third deposition step remained after movement of
475 the third air bubble (Figure 6f). We observed that some colloids from the first deposition
476 remained attached even after three passages of advancing air-water interfaces (yellow dots in
477 Figure 6d and f).

478 When we plot all three colloid deposition images together (Figure 7), it becomes clear
479 that the re-deposition occurred at different places every time. The colloids therefore are un-
480 likely to have a preferential location to deposit after subsequent depositions. Some colloids,
481 however, were so strongly attached that even multiple moving air-water interfaces could not
482 remove them (yellow dots Figure 6f). These locations are likely associated with preferen-
483 tial attachment locations. *Shen et al.* [2012b] theoretically and experimentally investigated
484 attachment and detachment of deposited carboxylated micro- and nanospheres from rough
485 surfaces as a function of solution ionic strength under water saturated conditions. They
486 reported that surface roughness of the collector can enhance the attachment of colloids in
487 primary minima (i.e., at the concave and the convex parts of the surface roughness) and in
488 secondary minima. Under low ionic strength (i.e., 0.001 M), two-dimensional DLVO profiles
489 also show that the secondary energy minima are deeper at the concave than the convex parts,
490 thereby the colloids deposited at the concave parts remain attached even after changing the
491 solution ionic strength [*Shen et al.*, 2012a].

492 We had expected that surface roughness of the glass channel affects the location of colloid
493 deposition, but we did not find any preferential deposition pattern from our re-deposition
494 experiment (Figures 6 and 7), implying that most of the colloids, except possibly those that
495 were not detached after multiple air-water interface passages, were randomly deposited on
496 the surface of the glass channel used in our study.

497 5 Implications

498 Previous mechanistic experimental and theoretical studies have reported that particles with
499 edges experience an increased capillary force due to a moving air-water interface as compared
500 to particles with smooth, round shapes [*Shang et al., 2009; Ally et al., 2012; Chatterjee et al.,*
501 *2012*]. Our experiments on particle detachment from a glass surface confirm such findings.
502 Our pore-scale experiments showed that the magnitude of colloid detachment depended on
503 colloid shape, with edges having the most pronounced effect. Edges are commonly found in
504 colloids present in natural porous media, such as soils and sediments, and it can therefore
505 be expected that such colloids are more likely detached and mobilized by moving air-water
506 interfaces than are smooth colloids without edges. On the contrary, we found that elongated
507 particles, such as rods, experienced less detachment than spheres. Bacteria are often in rod-
508 shaped form, and it therefore can be expected that this particular shape tends to minimize
509 capillary forces as long as the particles will orient themselves along the streamlines of the
510 water flow. Indeed, experiments in porous media have confirmed that the shape of the particle
511 affects colloid transport [*Weiss et al., 1995; Salerno et al., 2006; Xu et al., 2008; Liu et al.,*
512 *2010*]. However, the shapes of colloids in those studies were restricted to rod-like particles
513 and flow was under saturated flow conditions. Our pore-scale investigations with colloids

514 of different shapes provide a better understanding on how edge-shaped and non-spherical
515 colloids detach under unsaturated conditions.

516 **Acknowledgments.** S.A. was financially supported by the Anandamahidol Foundation,
517 under the Royal Patronage of HM the King, Bhumibol Adulyadej, Thailand. This material is
518 based upon work supported by the US Department of Energy, Office of Science (BER), under
519 Award No. DE-FG02-08ER64660. We thank the WSU Franceschi Microscopy Center for
520 access to their facility and Chris Davitt for help with the use of the confocal microscope. We
521 further thank Natalie Wall for allowing us to use the dynamic light scattering instrument.

522 **References**

523

525 Adamczyk, Z., (2006), *Particles at Interfaces: Interactions, Deposition, Structure*, Academic
524 Press, Amsterdam, The Netherlands.
526

527 Ally, J., M. Kappl, and HJ. Butt, (2012), Adhesion of particles with sharp edges to air-liquid
528 interfaces, *Langmuir*, *28*, 11042–11047.

529 Aramrak, S., M. Flury, and J. B. Harsh, (2011), Detachment of deposited colloids by advanc-
530 ing and receding air-water interfaces, *Langmuir*, *27*, 9985–9993.

531 Bhattacharjee, S., J. Y. Chen, and M. Elimelech, (2000), DLVO interaction energy between
532 spheroidal particles and a flat surface, *Colloids Surf. Physicochem. Eng. Aspects*, *165*,
533 143–156.

534 Boskovic, L., I. S. Altman, I. E. Agranovski, and R. D. Braddock, (2005), Influence of particle
535 shape on filtration processes, *Aerosol Sci. Technol.*, *39*, 1184–1190.

536 Champion, J. A., Y. K. Katare, and S. Mitragotri, (2007), Making polymeric micro- and
537 nanoparticles of complex shapes, *Proc. Natl. Acad. Sci. USA*, *104*, 11901–11904.

538 Chatterjee, N., S. Lapin, and M. Flury, (2012), Capillary forces between sediment particles
539 and an air-water interface, *Environ. Sci. Technol.*, *46*, 4411–4418.

540 Danov, K. D., and P. A. Kralchevsky, (2010), Capillary forces between particles at a liquid
541 interface: General theoretical approach and interactions between capillary multipoles,
542 *Advances in Colloid and Interface Science*, *154*, 91–103.

- 543 Decker, E. L., B. Frank, Y. Suo, and S. Garoff, (1999), Physics of contact angle measurement,
544 *Colloids Surf. Physicochem. Eng. Aspects*, 156, 177–189.
- 545 Decuzzi, P., and M. Ferrari, (2006), The adhesive strength of non-spherical particles mediated
546 by specific interactions, *Biomaterials*, 27, 5307–5314.
- 547 Elsabahy, M., and K. L. Wooley, (2012), Design of polymeric nanoparticles for biomedical
548 delivery applications, *Chem. Soc. Rev.*, 41, 2545–2561.
- 549 Geng, Y., P. Dalhaimer, S. Cai, R. Tsai, M. Tewari, T. Minko, and D. E. Discher, (2007),
550 Shape effects of filaments versus spherical particles in flow and drug delivery, *Nat. Nan-*
551 *otechnol.*, 2, 249–255.
- 552 Gomez-Suarez, C., H. C. van der Mei, and H. J. Busscher, (2000), Air bubble-induced detach-
553 ment of positively and negatively charged polystyrene particles from collector surfaces
554 in a parallel-plate flow chamber, *J. Adhesion Sci. Technol.*, 14, 1527–1537.
- 555 Gomez-Suarez, C., J. Noordmans, H. C. van der Mei, and H. J. Busscher, (1999), Removal of
556 colloidal particles from quartz collector surfaces as simulated by the passage of liquid-air
557 interfaces, *Langmuir*, 15, 5123–5127.
- 558 Gomez-Suarez, C., J. Noordmans, H. C. van der Mei, and H. J. Busscher, (2001), Air bubble-
559 induced detachment of polystyrene particles with different sizes from collector surfaces
560 in a parallel plate flow chamber, *Colloids Surf.*, 186, 211–219.
- 561 Gregory, J., (1975), Interaction of unequal double layers at constant charge, *J. Colloid Inter-*
562 *face Sci.*, 51, 44–51.

- 563 Gregory, J., (1981), Approximate expressions for retarded van der Waals interaction, *J.*
564 *Colloid Interface Sci.*, 83, 138–145.
- 565 Ho, C. C., A. Keller, J. A. Odell, and R. H. Ottewill, (1993), Preparation of monodisperse
566 ellipsoidal polystyrene particles, *Colloid Polym. Sci.*, 271, 469–479.
- 567 Lazouskaya, V., LP. Wang, H. Gao, XY. Shi, K. Crymmek, and Y. Jin, (2011), Pore-scale
568 investigation of colloid retention and mobilization in the presence of a moving air-water
569 interface, *Vadose Zone J.*, 10, 1250–1260.
- 570 Leenaars, A. F. M., and S. B. G. O'Brien, (1989), Particle removal from silicon substrates
571 using surface tension forces, *Philips J. Res.*, 44, 183–209.
- 572 Lehle, H., E. Noruzifar, and M. Oettel, (2008), Ellipsoidal particles at fluid interfaces, *Euro-*
573 *pean Physical Journal E*, 26, 151–160.
- 574 Liu, Q., V. Lazouskaya, Q. He, and Y. Jin, (2010), Effect of particle shape on colloid retention
575 and release in saturated porous media, *J. Environ. Qual.*, 39, 500–508.
- 576 NIH (1999), *ImageJ*, National Institute of Health, on-line at <http://rsb.info.nih.gov/ij>, ac-
577 cessed in January, 2012.
- 578 Noordmans, J., P. J. Wit, H. C. van der Mei, and H. J. Busscher, (1997), Detachment of
579 polystyrene particles from collector surfaces by surface tension forces induced by air-
580 bubble passage through a parallel plate flow chamber, *J. Adhesion Sci. Technol.*, 11,
581 957–969.
- 582 Pan, J., S. Y. Chan, W. G. Lee, and L. F. Kang, (2011), Microfabricated particulate drug-
583 delivery systems, *Biotechnol. J.*, 6, 1477–1487.

- 584 Salerno, M. B., M. Flamm, B. E. Logan, and D. Velegol, (2006), Transport of rodlike colloids
585 through packed beds, *Environ. Sci. Technol.*, *40*, 6336–6340.
- 586 SAS Institute Inc. (1990), *SAS/STAT User's Guide, Vers. 6*, vol. 2, 4th ed., SAS Institute
587 Inc., Cary, NC.
- 588 Shang, J., M. Flury, and Y. Deng, (2009), Force measurements between particles and the
589 air-water interface: Implications for particle mobilization in unsaturated porous media,
590 *Water Resour. Res.*, *45*, W06420, doi:10.1029/2008WR007384.
- 591 Sharma, P., M. Flury, and J. Zhou, (2008), Detachment of colloids from a solid surface by a
592 moving air-water interface, *J. Colloid Interface Sci.*, *326*, 143–150.
- 593 Shen, C., F. Wang, B. Li, Y. Jin, LP. Wang, and Y. Huang, (2012a), Application of DLVO
594 energy map to evaluate interactions between spherical colloids and rough surfaces, *Lang-*
595 *muir*, *28*, 14681–14692.
- 596 Shen, C., V. Lazouskaya, H. Zhang, F. Wang, B. Li, Y. Jin, and Y. Huang, (2012b), The-
597 oretical and experimental investigation of detachment of colloids from rough collector
598 surfaces, *Colloids Surf. Physicochem. Eng. Aspects*, *410*, 98–110.
- 599 Singh, P., and D. D. Joseph, (2005), Fluid dynamics of floating particles, *J. Fluid Mech.*,
600 *530*, 31–80.
- 601 van Nierop, E. A., M. A. Stijnman, and S. Hilgenfeldt, (2005), Shape-induced capillary
602 interactions of colloidal particles, *Europhys. Lett.*, *72*, 671–677.
- 603 Vizcarra, T. G., S. L. Harmer, E. M. Wightman, N. W. Johnson, and E. V. Manlapig,

- 604 (2011), The influence of particle shape properties and associated surface chemistry on
605 the flotation kinetics of chalcopyrite, *Miner. Eng.*, *24*, 807–816.
- 606 Weiss, T. H., A. L. Mills, G. M. Hornberger, and J. S. Herman, (1995), Effect of bacterial cell
607 shape on transport of bacteria in porous media, *Environ. Sci. Technol.*, *29*, 1737–1740.
- 608 Weronski, P., and M. Elimelech, (2008), Novel numerical method for calculating initial flux
609 of colloid particle adsorption through an energy barrier, *J. Colloid Interface Sci.*, *319*,
610 406–415.
- 611 Xu, S., Q. Liao, and J. E. Sayers, (2008), Straining of nonspherical colloids in saturated
612 porous media, *Environ. Sci. Technol.*, *42*, 771–778.

Table 1. Perimeters of interface lines and effective radii (i.e., surface-area-equivalent radii) of different colloid shapes and estimated maximum detachment forces calculated by Equation (1).


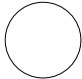
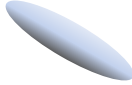
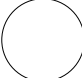

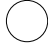
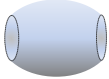
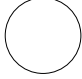
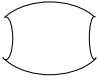

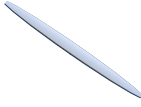
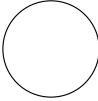


Shape	Interface Line	Interface Line Shape	Normalized Length of Interface Line	Detachment Forces (mN)
Sphere 	Real radius		1.0	3.28×10^{-5}
Rod 	Effective radius		1.1	3.70×10^{-5}
	Major axis		2.1	6.89×10^{-5}
	Minor axis		0.6	1.88×10^{-5}
Barrel 	Effective radius		1.0	3.15×10^{-5}
	Major axis		1.3	4.17×10^{-5}
	Minor axis		0.8	2.56×10^{-5}
Oblong Disk 	Effective radius		1.2	3.67×10^{-5}
	Major axis		2.4	7.61×10^{-5}
	Minor axis		0.01	2.97×10^{-7}

Table 2. Geometric and surface characterization of colloids (polystyrene microspheres) and glass channel (in 1 mM CaCl₂ and pH 5.5). Errors represent standard deviations.

Colloids	Geometric Measurement (μm)		Contact Angle ($^\circ$)*		Electrophoretic Mobility *	ζ -potential*			
Material	Major-axis	Minor-axis	Height	Aspect Ratio	Static	Advancing	Receding	($\mu\text{m/s}$)(V/cm)	(mV)
Sphere	1.01 ± 0.01	1.01 ± 0.01	—	1.0	$33 \pm 1a$	$47 \pm 2a$	$15 \pm 1a$	$-0.27 \pm 0.02a^\dagger$	$-3.5 \pm 0.2a^\dagger$
Rod	3.24 ± 0.30	0.58 ± 0.06	—	5.6	$38 \pm 2b$	$47 \pm 1a$	$14 \pm 1a$	$-0.25 \pm 0.03a$	$-3.2 \pm 0.4a$
Barrel	$0.82 \pm 0.07^\ddagger$	$0.49 \pm 0.08^\S$	1.34 ± 0.09	1.6	$39 \pm 1b$	$46 \pm 0a$	$13 \pm 1a$	$-0.30 \pm 0.03a$	$-3.9 \pm 0.4a$
Oblong disk	3.78 ± 0.30	0.46 ± 0.04	$0.06 \pm 0.02^\P$	8.2	$32 \pm 2a$	$46 \pm 1a$	$14 \pm 2a$	$-0.24 \pm 0.07a$	$-3.1 \pm 0.9a$
Glass	—	—	—	—	$14 \pm 1c$	$26 \pm 1b$	$7 \pm 1b$	$-1.52 \pm 0.04b$	$-19.5 \pm 0.5b$

* Different letters (a, b, and c) indicate statistical differences column-wise by Tukey's method at $\alpha = 0.05$.

[†] Sphere treated in hot oil; non-treated values of electrophoretic mobilities and ζ -potential are -0.70 ± 0.08 and -9.0 ± 1.0 , respectively.

[‡] Diameter of barrel center. [§] Diameter of end portion of barrel. [¶] Thickness of oblong disk.

613 **Figure Captions**

614 Figure 1. Electrophoretic mobility as function of pH for (a) spherical colloids
 615 exposed to different treatments, and (b) four differently-shaped colloids and
 616 the glass channel. All measurements were made with a 1 mM CaCl₂ solution.
 617 Error bars are \pm one standard deviation.

618 Figure 2. SEM images of four colloid shapes used in the experiments: (a) sphere,
 619 (b) rod, (c) barrel, and (d) oblong disk. Insert shows a magnification of the
 620 edge portion of the oblong disk. (Scale bar: 1 μ m)

621 Figure 3. Confocal micrographs of deposited colloid at (left) initial deposition
 622 and (right) after detachment by the advancing air-water interface (AWI). The
 623 plots show the confocal microscope view used to analyze for colloid detachment
 624 (900 μ m \times 900 μ m).

625 Figure 4. Percentage detachment of deposited colloids with different shapes by a
 626 moving air-water interface (AWI). Different letters indicate statistical differ-
 627 ences determined by LSD (uppercase letters) and by Tukey's (lowercase letters)
 628 at the 95% confidence level. Error bars are standard deviations.

629 Figure 5. Orientation of shape-modified colloids during deposition examined by
 630 field emission SEM: (a) rod, (b) barrel, and (c) oblong disk. (Scale bar: 2 μ m)

631 Figure 6. Visualization of spherical colloids deposited at (a) initial deposition, (b)
 632 colloids remaining after movement of one air bubble, (c) second deposition,
 633 (d) colloids remaining after movement of another air bubble, and (e) third
 634 deposition, (f) colloids remaining after movement of a third air bubble. Figures
 635 are not real confocal microscopy images, as the positions the colloids has been
 636 highlighted with different colored dots. Yellow, white, and red indicate colloids
 637 deposited during the first, second, and third deposition steps, respectively. The
 638 plots represent an area of $900 \mu\text{m} \times 900 \mu\text{m}$

639 Figure 7. Location of three replications of colloid deposition. Yellow, white, and
 640 red highlight the location of deposited colloids during the first, second, and
 641 third deposition, respectively.

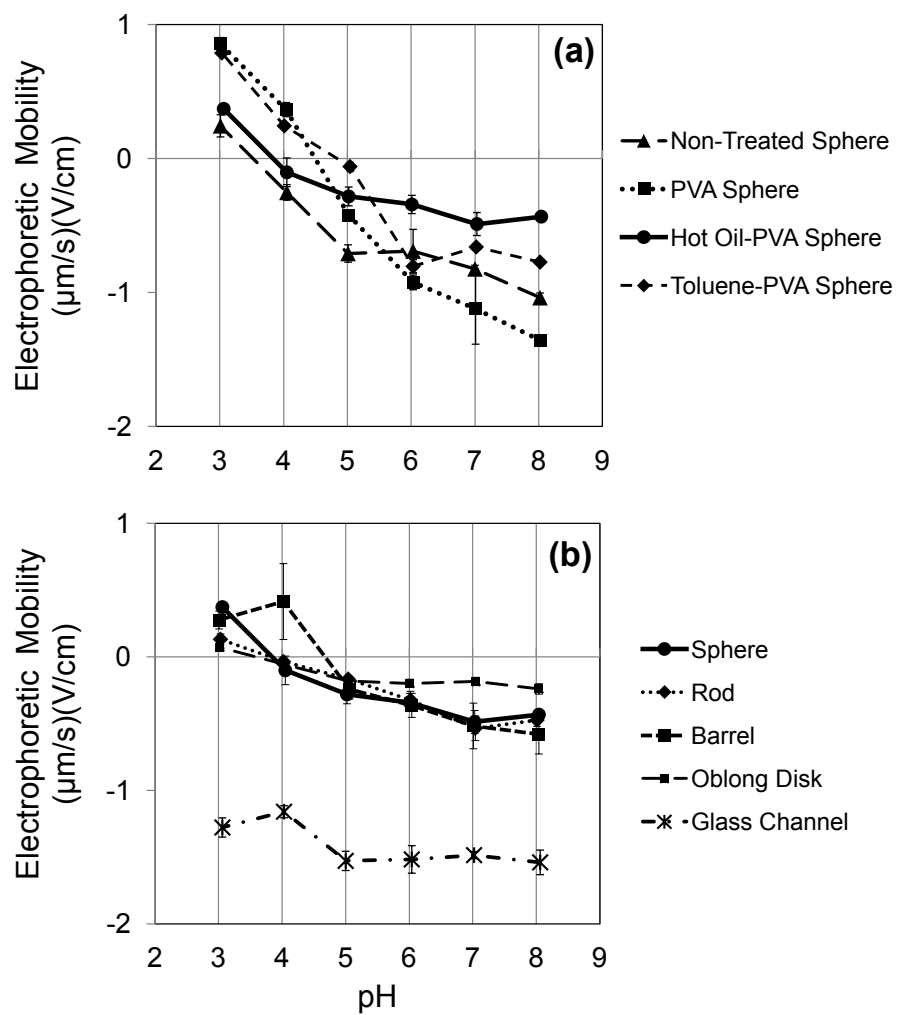


Figure 1. Electrophoretic mobility as function of pH for (a) spherical colloids exposed to different treatments, and (b) four differently-shaped colloids and the glass channel. All measurements were made with a 1 mM CaCl_2 solution. Error bars are \pm one standard deviation.

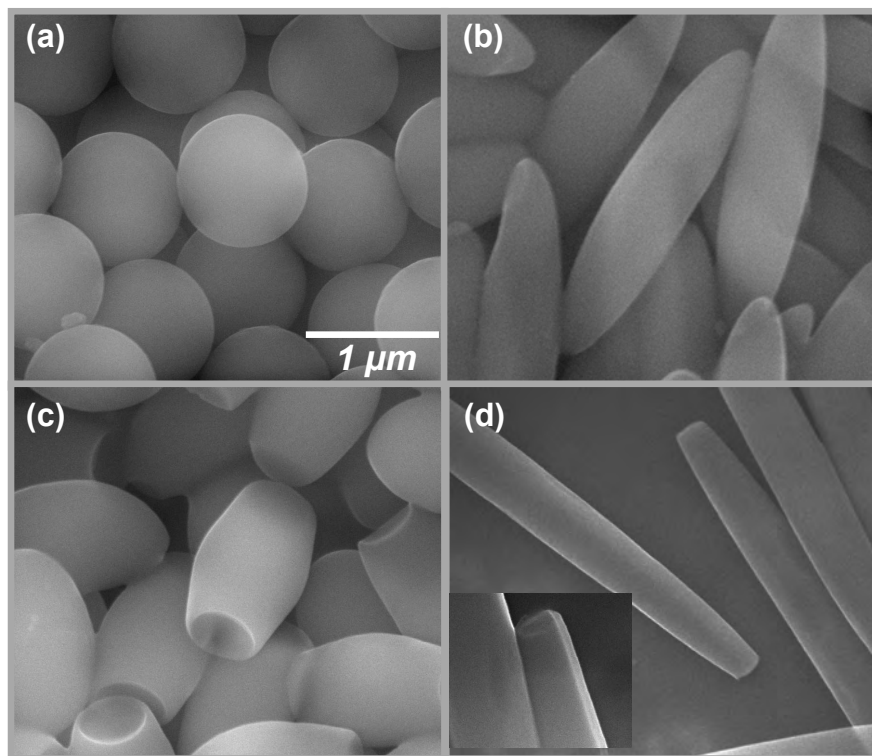


Figure 2. SEM images of four colloid shapes used in the experiments: (a) sphere, (b) rod, (c) barrel, and (d) oblong disk. Insert shows a magnification of the edge portion of the oblong disk. (Scale bar: 1 μm)

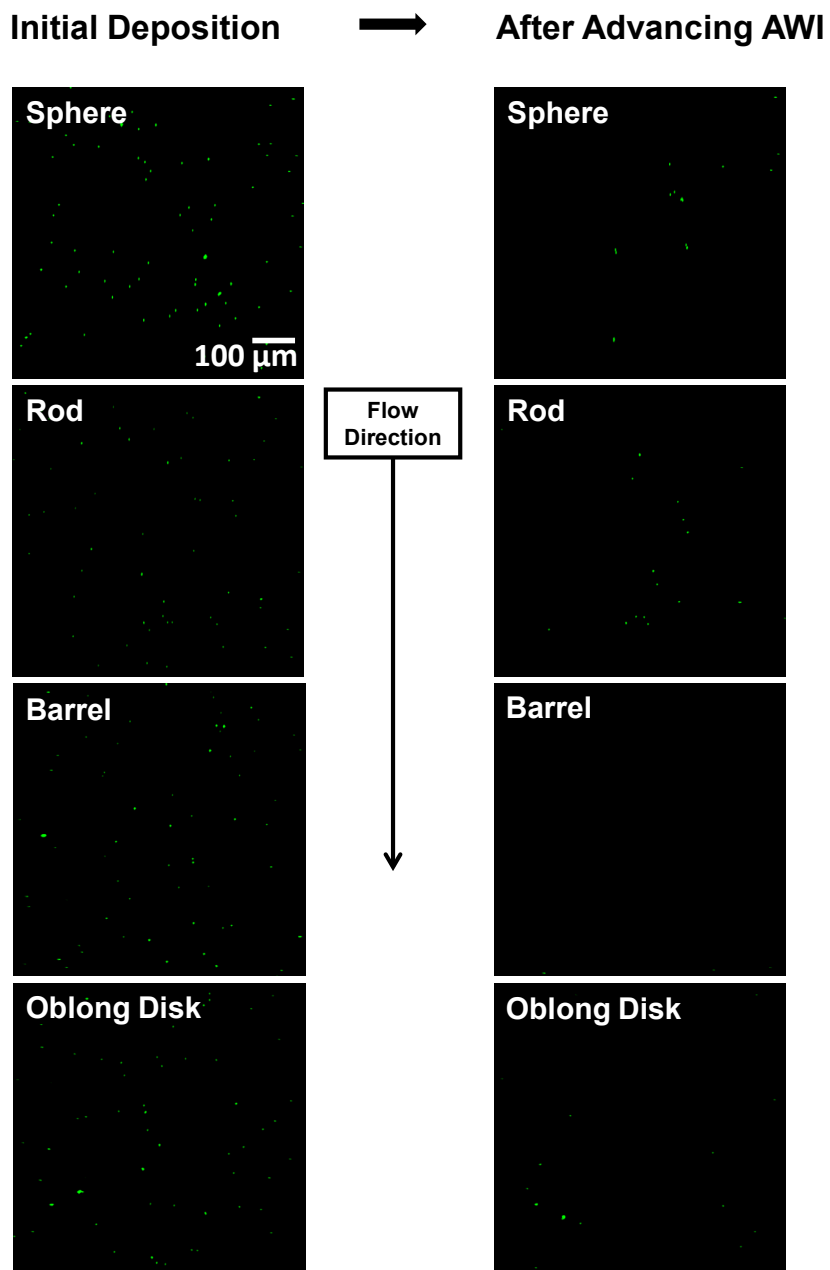


Figure 3. Confocal micrographs of deposited colloid at (left) initial deposition and (right) after detachment by the advancing air-water interface (AWI). The plots show the confocal microscope view used to analyze for colloid detachment ($900 \mu\text{m} \times 900 \mu\text{m}$).

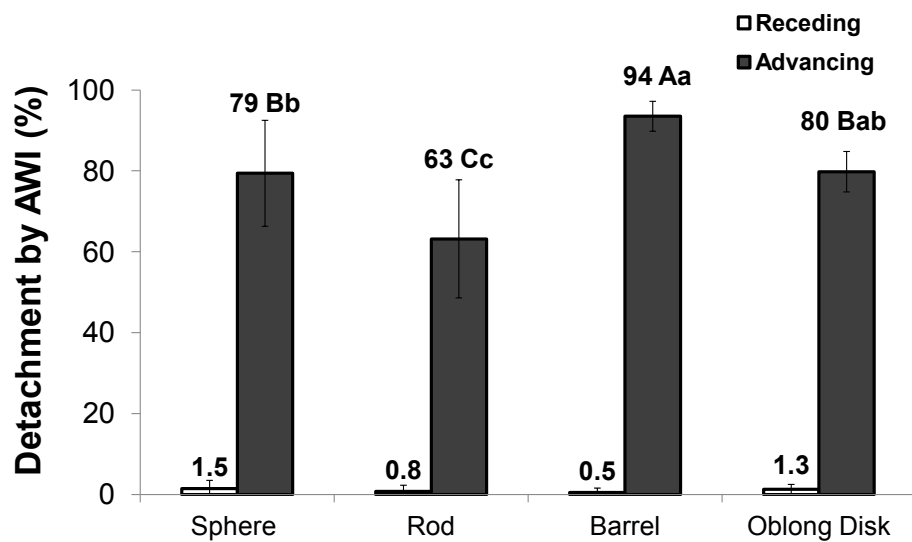


Figure 4. Percentage detachment of deposited colloids with different shapes by a moving air-water interface (AWI). Different letters indicate statistical differences determined by LSD (uppercase letters) and by Tukey's (lowercase letters) at the 95% confidence level. Error bars are standard deviations.

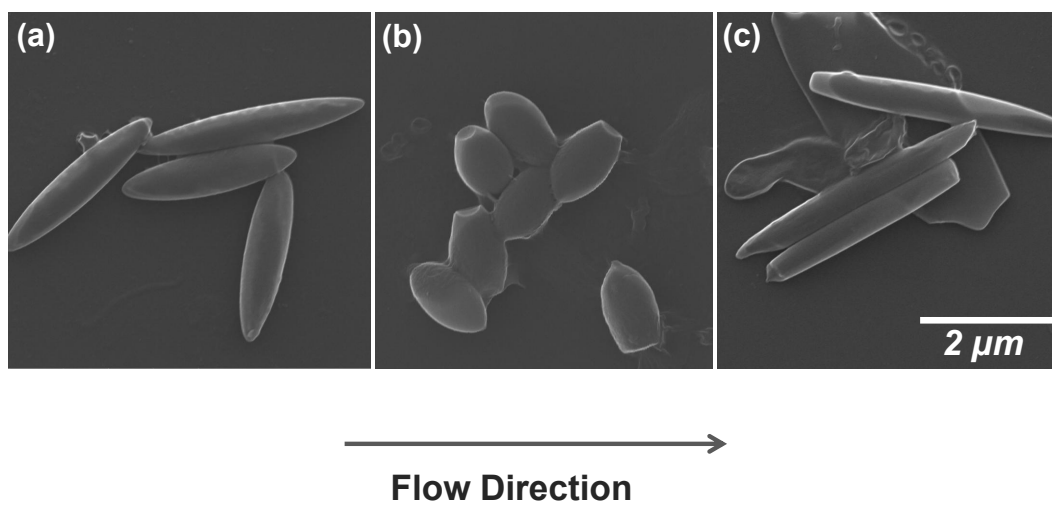


Figure 5. Orientation of shape-modified colloids during deposition examined by field emission SEM: (a) rod, (b) barrel, and (c) oblong disk. (Scale bar: 2 μm)

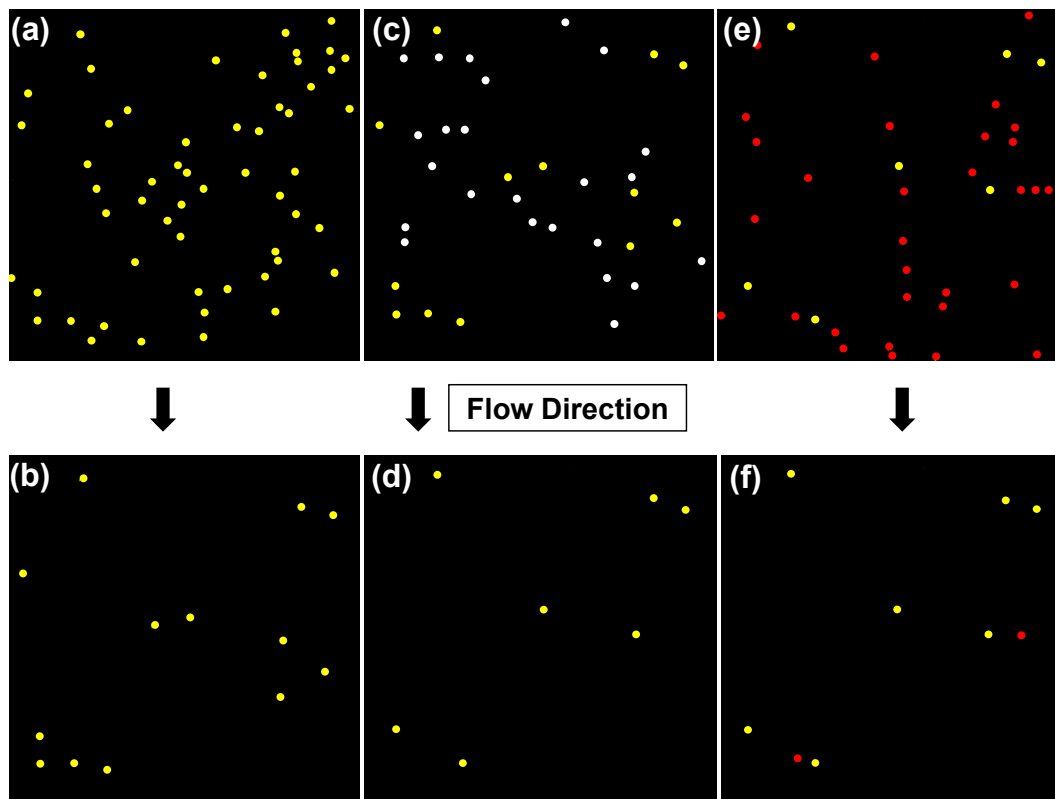


Figure 6. Visualization of spherical colloids deposited at (a) initial deposition, (b) colloids remaining after movement of one air bubble, (c) second deposition, (d) colloids remaining after movement of another air bubble, and (e) third deposition, (f) colloids remaining after movement of a third air bubble. Figures are not real confocal microscopy images, as the positions the colloids has been highlighted with different colored dots. Yellow, white, and red indicate colloids deposited during the first, second, and third deposition steps, respectively. The plots represent an area of $900 \mu\text{m} \times 900 \mu\text{m}$.

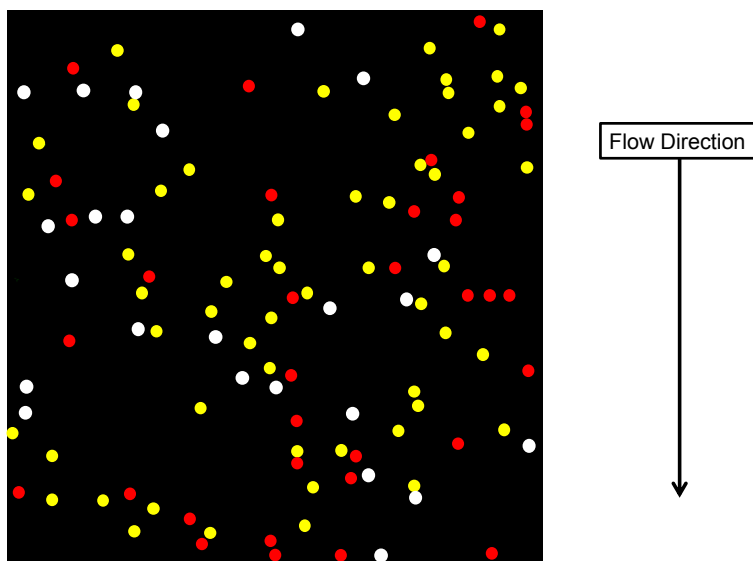


Figure 7. Location of three replications of colloid deposition. Yellow, white, and red highlight the location of deposited colloids during the first, second, and third deposition, respectively.

Capillary Forces between Sediment Particles and an Air–Water Interface

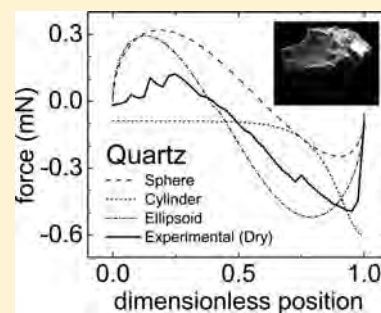
Nirmalya Chatterjee,^{*,†} Sergey Lapin,[‡] and Markus Flury[†]

[†]Department of Crop and Soil Sciences, Washington State University, Puyallup, Washington 98371, United States

[‡]Department of Mathematics, Washington State University, Pullman, Washington 99164, United States

S Supporting Information

ABSTRACT: In the vadose zone, air–water interfaces play an important role in particle fate and transport, as particles can attach to the air–water interfaces by action of capillary forces. This attachment can either retard or enhance the movement of particles, depending on whether the air–water interfaces are stationary or mobile. Here we use three standard PTFE particles (sphere, circular cylinder, and tent) and seven natural mineral particles (basalt, granite, hematite, magnetite, mica, milky quartz, and clear quartz) to quantify the capillary forces between an air–water interface and the different particles. Capillary forces were determined experimentally using tensiometry, and theoretically assuming volume-equivalent spherical, ellipsoidal, and circular cylinder shapes. We experimentally distinguished between the maximum capillary force and the snap-off force when the air–water interface detaches from the particle. Theoretical and experimental values of capillary forces were of similar order of magnitude. The sphere gave the smallest theoretical capillary force, and the circular cylinder had the largest force due to pinning of the air–water interface. Pinning was less pronounced for natural particles when compared to the circular cylinder. Ellipsoids gave the best agreement with measured forces, suggesting that this shape can provide a reasonable estimation of capillary forces for many natural particles.



1. INTRODUCTION

Soil particles in the colloidal fraction are relevant for their role in facilitation of subsurface contaminant transport.^{1,2} In unsaturated porous media, such as vadose zone sediments, the presence of the air–water interface plays an important role on fate and transport of colloids. Colloids can attach to stationary air–water interfaces in porous media.^{3,4} It has been observed that colloids can be mobilized during infiltration^{5–8} and drainage^{9,10} events. Sharma et al.¹¹ demonstrated that colloids attach and move along with air–water interfaces such as an infiltration front through a porous medium. Mechanistic studies involving pore-scale visualization confirm that colloids can be captured at the air–water interface and carried along with the moving air–water interface.^{12–17}

When a particle is attached to an air–water interface the particle experiences forces both due to surface tension and pressure differences. In a porous medium, these forces can cause a strong attraction of a particle to the stationary solid surfaces when the water saturation is low, and air–water interfaces pin the particles to solid surfaces.^{8,18,19} As water saturation increases and liquid films become thicker, this particle pinning disappears,^{19,20} and particles are even subject to a repulsive force that can lead to particle detachment from the solid surface.^{8,21} Theoretical calculations confirm that capillary forces can exceed DLVO forces.^{8,17,22,23}

Macroscopic techniques like tensiometry have been used to directly measure the capillary forces between a spherical particle and the air–water interface.^{24,25} More recently, microscopic

techniques like atomic force microscopy have been used to measure capillary forces for colloidal sized-particles.^{22,26–29} In these experiments, the measurements are usually done with spherical particles. Sphere tensiometry (i.e., using a sphere for tensiometric force measurements) has even been proposed as an alternative method to the de Nöuy ring and Wilhelmy plate methods for measuring surface tensions and contact angles.^{30,31}

Capillary forces acting on a spherical particle can be calculated from theory using numerical solutions of the Young–Laplace equation.^{24,25,32,33} For particles with non-spherical but regular shapes, especially those with sharp edges the numerical solution becomes more complicated due to additional boundary conditions that need to be applied.^{34,35} The shape and surface properties of the particle determine the orientation of the air–water interface meniscus. The scale and degree of the roughness affects the magnitude of the capillary force and also determines how the interface moves across the solid surface, i.e., whether the interface slips or jumps, and where it jumps. No-slip conditions arise due to surface roughness conditions, where the air–water interface is temporarily being pinned.^{34,35}

In previous experiments,²¹ our group has quantified capillary forces on regularly shaped particles (spheres, cylinders, cubes)

Received: November 1, 2011

Revised: March 6, 2012

Accepted: March 19, 2012

Published: March 19, 2012

using tensiometry, and we have also made some force measurements on natural subsurface particles. Here, we expand upon those previous measurements, by focusing on natural subsurface particles and by quantifying the effects of particle shape and roughness. We further investigate the effect of natural surface coatings on the magnitude of the capillary force.

2. THEORY

Forces on a Particle in Contact with an Air–Water Interface. Figure 1 shows a schematic of an ellipsoidal and an

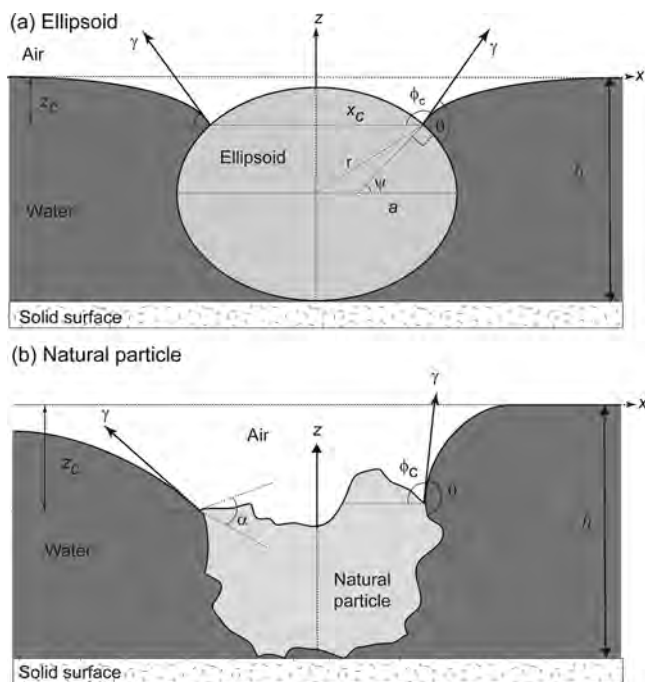


Figure 1. Forces acting (a) on a smooth, ellipsoidal particle with semiprincipal radii a, b, c , and (b) on an asymmetric, rough particle in contact with an air–water interface, where $\psi = (3\pi/2 - \theta - \phi_c)$ and α is the wedge angle for a sharp point on a surface where pinning occurs (see eq 3). Note that the interface line along the particle is undulating.

irregularly shaped particle attached to a solid surface and in contact with an air–water interface. The theory presented here follows the discussion presented in Zhang et al.²⁴ We consider that the solid surface is horizontal and that the air–water interface at $x \rightarrow \infty$ is also horizontal. The forces acting on the particle in a static system are (1) the DLVO force (f_{DLVO}), the (2) the gravity force (f_w), the (3) surface tension force (f_s), the (4) buoyancy force (f_b), and the (5) hydrostatic pressure force (f_p). The force balance on the particle is then given as²¹

$$f = f_{DLVO} + f_w + f_s + f_b + f_p \tag{1}$$

The sum of the surface tension (f_s) and hydrostatic pressure (f_p) forces is also known as the capillary force. If the particle is symmetric, the force balance f is parallel to the z -direction (Figure 1a), but if the particle is asymmetric (Figure 1b), the directions of f_s and f_p forces are determined by the contact angle of the air–water interface at the particle surface. Further, for asymmetric particles, the interface line is undulating in quadrupolar fashion.^{36–41} If $f < 0$ the particle will be detached from the solid surface, if $f > 0$ the particle will remain pinned to the solid surface.

Forces on an Ellipsoidal Particle at an Air–Water Interface. Here, we extend the theory for a spherical particle to a triaxial ellipsoid. Theoretical calculations^{36–43} of capillary forces on ellipsoidal particles showed that the contact line is of an undulating, elliptic shape rather than a flat ellipse. We calculated the length of the undulating contact line following the approach of van Nierop et al.⁴⁰ (see Supporting Information for details). The force balance on an ellipsoidal particle is then given as

$$f = 4\kappa E(e_{xy})\gamma \cos \beta \sin \phi_c + \pi ab \Delta \rho g z_c \cos^2 \beta - \frac{\pi}{3} \Delta \rho g abc (2 + 3 \sin \beta - \sin^3 \beta) \tag{2}$$

where a, b , and c are the semiprincipal axes of the ellipsoid along the three coordinate axes x, y , and z , respectively, κ is the ratio representing increase in contact line due to undulation, $E(e_{xy})$ is the complete elliptic integral of the second kind with eccentricity e_{xy} , β is the parametric latitude (Figure S.1, Supporting Information), γ is the surface tension of water, ϕ_c is the angle of inclination of the undistorted air–water interface at the three-phase contact line, $\Delta \rho = (\rho_l - \rho_g)$ is the difference between the two fluid densities ρ_l (water) and ρ_g (air), g is the acceleration due to gravity, and z_c is the deflection depth (position of the average contact line on the z -axis).

Forces on an Irregularly-Shaped Particle at an Air–Water Interface. The movement of the air–water interface (the macroscopic interface) on a solid surface is dependent on the geometry and the surface properties of the solid surface. In the case of ideally smooth surfaces, the air–water interface intersects the solid surface at an angle and a position determined by the capillary forces and the equilibrium air–water–solid contact angle.

In a dynamic system, where the air–water interface moves over a particle, surface roughness can cause the air–water interface to be pinned at surface discontinuities. While for a smooth particle, the air–water–solid interface line adjusts its position to the respective equilibrium position (Figure 1a), the pinning at surface discontinuities for rough particles causes the air–water interface to exceed its equilibrium configuration (Figure 1b). The increase in the contact angle can mathematically be formulated by the Gibbs extension of the Young equation:³⁵

$$\theta_0 < \theta < 180^\circ - \alpha + \theta_0 \tag{3}$$

where α is the wedge angle and θ_0 is the equilibrium contact angle for the vertical face (Figure 1b). The pinning causes the air–water interface to distort. These distortions cause large forces on the air–water interfaces, which tend to give way suddenly when the interface is moved beyond a critical distance, causing the contact line to snap off.

The approximation of a natural particle as a right, circular cylinder takes into consideration the maximum force due to the condition described by eq 3. The equation for the force balance on a right, circular cylinder²¹ is

$$f = -2\pi r \gamma \sin(\theta - \pi/2) - \Delta \rho g (z_0 + L) \pi r^2 \tag{4}$$

where L is the length of the cylinder.

Dimensionless Variables. The distances and forces can be represented in dimensionless form²⁴ as follows (capital letters represent dimensionless variables):

$$X = x\sqrt{c_a} \text{ and } Z = z\sqrt{c_a} \text{ and} \\ R = r\sqrt{c_a} \text{ and } H = h\sqrt{c_a} \quad (5)$$

$$R_X = r_x\sqrt{c_a} \text{ and } R_Y = r_y\sqrt{c_a} \text{ and } R_Z = r_z\sqrt{c_a} \quad (6)$$

where x , y , and z are the directions parallel and perpendicular to the undisturbed air–water interface, r is the radius of the particle measured from the z -axis, h is the distance of the base of the particle from the undisturbed interface, and c is the capillary constant $c_a = \Delta\rho g/\gamma$, where $\Delta\rho$ is the density differences between the liquid and the gas, and γ is the surface tension. The dimensionless capillary force F is given as

$$F = \frac{f}{r^3 \Delta\rho g} \quad (7)$$

where f is the dimensional force.

3. MATERIALS AND METHODS

Particles. We used three particles of well-defined, standard shape and several natural sediment particles. The standard particles were made of PTFE and consisted of a sphere, a cylindrical disk, and a tent. The natural sediment particles came from the Hanford formation at the U.S. Nuclear Hanford Reservation in south-central Washington. The sediments were collected from 20 m depth below surface from a trench face at the Hanford Environmental Restoration Disposal Facility. The sediments were air-dried and sieved through meshes with nominal sizes 1 and 2 mm; the fraction between 1 and 2 mm was collected. We placed these sediments then under a dissection scope and picked individual particles with tweezers. We selected particles with typical mineralogy for the Hanford sediments: basalt, granite, hematite, magnetite, mica, milky quartz, and clear quartz. Three particles for each type of particle were selected and stored in 20 mL glass vials. Figure S.3 (Supporting Information) shows photographic images of the particles.

Individual sediment particles were mounted on J-shaped hooks made of steel wires with diameter of 0.5 mm (Figure S.4, Supporting Information). The lower end of the hooks was flattened with a file, and the hooks were cleaned by rinsing successively with acetone, ethanol, and deionized water. Particles were then attached to the hooks with instant glue (Dr. Bond SuperGlue, ITW Inc., Solon, Ohio). The lower end of the hook was attached to the bottom of the particle so that it did not interfere with the movement of the interface when it approaches the particle surface from the top. Particles were always handled with clean tweezers to avoid surface contamination.

Particle Characterization. Particles were characterized for air–water contact angles, shape, and surface roughness. The air–water–solid contact angle was determined using a goniometer (CA Goniometer Model 50–00–115, Ramé-Hart Instrument Co., Netcong, NJ). The PTFE particles and the natural particles as obtained were mounted on a microscopy slide using double-sided tape. A microsyringe (steel needle with 0.5 mm o.d.) was used to put a drop of water (25 μ L) centered 0.3 mm away from the edge of the particle, so that the particle touched the side of the drop.

For electron microscopic characterizations, the particles were coated with platinum–palladium to a thickness of 3 nm under a sputter coater (Model 108auto, Cressington Scientific, Watford, England). The particles were then examined under an environmental scanning electron microscope (SEM) equipped with a field emission electron gun (FEI Quanta 200F, FEI Co., Hillsboro, OR). The particles were kept oriented under the SEM in the same manner as for the force-position and contact angle measurements. If observed directly from above, this gives the xy -plane view of the particle. Additional images were taken at a 90° view (xz -plane) to determine the overall cross-section of the particle. Particle dimensions were measured with the SEM measuring software. The SEM analysis was done after the contact angle and capillary force measurements (see below), because the surface properties were irreversibly altered by the sputter coating.

The particle outlines under the SEM in the xy - and xz -planes were used to determine the dimensions along the three coordinate axes. Figure 2 shows SEM images perpendicular to the xy -plane. We further calculated a root-mean-square value of the coordinates x , y , z , as well as a volume-equivalent spherical radius and ellipsoidal semimajor axes for each particle (see

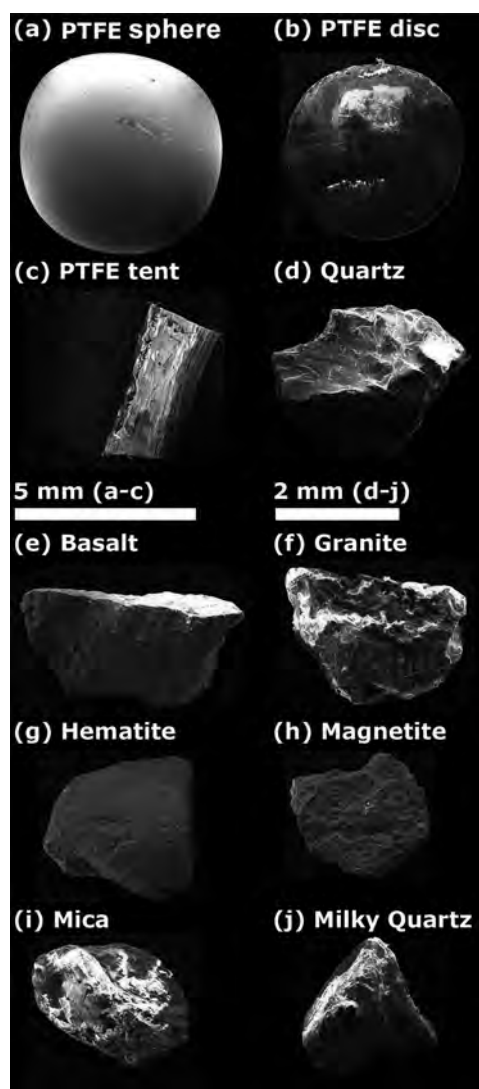


Figure 2. PTFE sphere, disk, and tent (a–c), and natural sediment particles (d–j) under field emission SEM, viewed perpendicular to the xy -plane.

Supporting Information for details on calculations and Tables S.1 and S.2 for summary of data).

Capillary Force Measurements. The capillary forces between the particles and the air–water interface were measured with a tensiometer (Process Tensiometer K100, Krüss GmbH, Hamburg, Germany). The precision of the tensiometer microbalance is 0.02 mg corresponding to a force of 0.196 μN . The J-shaped steel hook with the particle attached was fastened to the microbalance of the tensiometer (Figure S.4, Supporting Information). A glass cup (inner diameter 65.7 mm, height 37.9 mm) was filled with deionized water (electrical conductivity of 5.5 $\mu\text{S m}^{-1}$) and placed into the temperature jacket of the tensiometer (kept at 23 $^{\circ}\text{C}$).

The particle and the hook were initially in the air phase. The particle on the hook was kept stationary, while the air–water interface, formed in the glass cup below, was moved upward at a constant velocity of 1.0 mm min^{-1} , so that it approached the particle from the bottom (Figure S.4, Supporting Information). The interface made contact with the bottom part of the steel hook first, before wetting the particle itself. The tensiometer measured the force exerted on the microbalance after every position increment of 0.05 mm. These measurements were continued until the entire particle was completely immersed in water and the air–water interface had detached from the particle and passed to a position above the particle. The air–water interface was then lowered at the same velocity until the particle came back to its initial position above the interface in the air phase. By plotting force versus position, we obtained the so-called force-position curves.

Each particle was measured in a specific sequence of immersion and washing. First, the particle under air-dry conditions was mounted onto the tensiometer and immersed into the water to measure a force-position curve. This represents an initially dry particle, taken “as is” from the sediments, with its surface not modified by wetting or washing. Then, the particle was again immersed into the water, for five repeated cycles without allowing it to dry. These measurements represent force-position curves for an initially wet particle. After this sequence, the particle was washed with acetone and ethanol, and then air-dried for five minutes. The solvent rinsing was performed to remove soluble organic matter coatings on the particle surface. This cycle (one measurement for the air-dry particle and five for the wet particle) of immersion-emersion mentioned above was repeated with the cleaned particle. The data were then used to construct force-position curves for (1) dry, (2) wet, (3) cleaned-dry, and (4) cleaned-wet particles. The replicated runs for the wet (noncleaned and cleaned) particles were averaged and used to calculate error bars (standard deviations) for the force-position curves, and to determine the measurement precision.

For each particle, we used the same water in the glass cup, but we changed the water for every new particle. Surface tension of the water was measured before and after each force-position curve with the Wilhelmy plate method. The errors in force measurements are discussed in the Supporting Information.

4. DATA ANALYSIS

The force position curves were analyzed to determine the forces exerted on the particle by the moving air–water interface. We were particularly interested in the maximum detachment forces as well as the snap-off forces. The maximum detachment force is defined at the maximum force recorded by the tensiometer in

upward vertical direction, whereas the snap-off force is the force recorded when the air–water interface snaps off from the solid surface. The snap-off force was observed from the force–distance curve when the measured force decreased markedly within a short distance increment, which we found by computing the first derivative of the force–distance curve. The position where the change in force with change in position is maximal is the point of snap off.

We used the theory for a sphere (eq S.5, Supporting Information), a circular cylinder (eq 4), and a triaxial ellipsoid (eq 2) to calculate the forces acting on a particle in contact with the air–water interface as a function of the deflection depth z_c . The force plotted versus deflection depth gives the theoretical force-position curve.²⁴ We computed these theoretical curves for all particles (PTFE standard particles and natural sediment particles). To compute the forces for the natural particles, we approximated the particle shapes as spheres, cylinders, and ellipsoids, and used the measured shape parameters to calculate maximum and volume-equivalent radii and semimajor axes.

The theoretical calculations provide the maximum force; however, except for the cylindrical particle the snap-off force cannot be calculated because spheres and ellipsoids have no edges on which pinning can occur. A cylindrical particle should ideally have a snap-off force identical to the maximum force in the theoretical force-position curves.

5. RESULTS AND DISCUSSION

Interpretation of Force-Position Curves. Figure 3 shows an example of a force-position curve for a PTFE sphere. The solid line shows the measured capillary force experienced by the particle as the particle moved through the air–water interface. A zero force indicates that the particle does not experience any

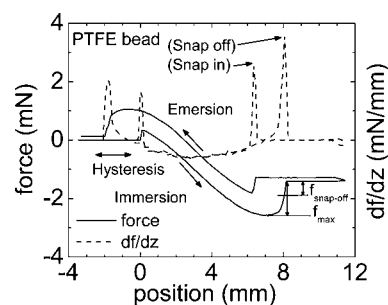


Figure 3. Example of a force-position curve for a PTFE sphere ($r = 2.78$ mm) showing the various segments of the curve during one immersion-emersion cycle and the differentiated force-position curve (dashed line).

net force due to the air–water interface. (The tensiometer balance is tared with the weight of the particle.) A positive force indicates that the particle is being pulled downward, that is, into the water phase, whereas a negative force indicates that the particle is pulled upward, that is, out of the water phase (compare Figure 1). The single-headed arrows along the plot show the direction of movement of the particle with respect to the air–water interface (immersion or emersion).

Initially, the particle is in the air-phase (net force is zero), when the particle contacts the air–water interface a downward capillary force (attractive capillary force) is recorded, indicated by the sudden occurrence of a net downward force. The magnitude of the net downward force at this position cannot be interpreted quantitatively because of the particle is attached to

the hook at the bottom; however, the snap-in can be detected unequivocally. This position of the air–water interface snap-in at the bottom of the particle is recorded for each particle and the z -value at this position is set to zero, that is, our reference position. During the immersion of the particle into the water phase, the force changes from positive to negative and reaches a minimum (or maximum negative force) at a distance of about 6.9 mm. This minimum corresponds to the maximum upward force experienced by the particle (including buoyancy). The air–water interface snaps off the particle just before the force recording becomes constant at a distance of about 8.2 mm. The constant force recorded after snap-off corresponds to the buoyancy. The maximum upward force (repulsive capillary force, f_{\max}) and the snap-off force ($f_{\text{snap-off}}$) are then determined by the difference between the recorded minimum force and the buoyancy force.

The emersion curve parallels the immersion curve, but is shifted because of hysteresis of the contact angle. The hysteresis of the contact angle not only affects the maximum forces exerted by the air–water interface, but also changes the position where the maximum forces and snap-off and snap-in occur.

The dashed curve in Figure 3 is the rate of change of the capillary force with respect to the change in position in the z -direction (df/dz) of the air–water interface. We use this curve to identify the exact position of the particle with respect to the interface where the maximum upward force ($df/dz = 0$) and the snap-off occur ($df/dz = \max$). In the following, we present the force-position curves in dimensionless form, so that different particles can be better compared with each other.

Theoretical Maximum Capillary Forces and Pressures.

Figure 4 shows theoretical force-position curves for the

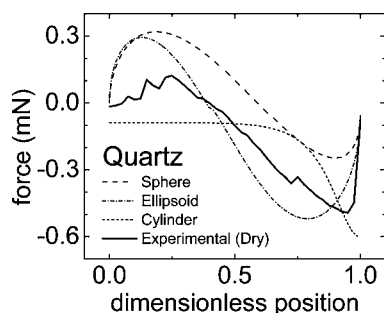


Figure 4. Force-position curves of sphere, circular cylinder, and ellipsoid (theoretical) and a dry, noncleaned quartz particle (experimental) during immersion. For the standard shapes, we used the calculated volume-equivalent dimensions (r_{ve}) of the quartz particle. [Dimensions of particles in mm are: sphere $r = 1.13$; ellipsoid $(a, b, c) = (1.47, 1.17, 0.83)$; cylinder $(r, h) = (1.47, 0.83)$; quartz $(x, y, z) = (1.54, 1.22, 0.81)$].

immersion of a sphere, an ellipsoid, and a circular cylinder compared with the measured curve for the quartz particle. For the theoretical curves, we assumed that the standard-shaped particles have the same volume as the quartz particle. The spherical particle shows the smallest forces during immersion, because it has the smallest circumference, and the cylinder shows the largest force, because the air–water interface is being pinned at the edges. The ellipsoid gives the closest approximation to the quartz particle in terms of the maximum capillary force.

Capillary forces can be translated to pressure by division by the particle cross-section. Capillary pressures associated with maximum forces were in the range of 100 Pa (Table S.3, Supporting Information). This indicates that, in porous media, the capillary forces on such millimeter-scale particles are important under fairly saturated conditions, for example during infiltration or imbibition.

Experimental Maximum and Snap-Off Capillary Forces.

Figure 5 shows the dimensionless force-position curves for the

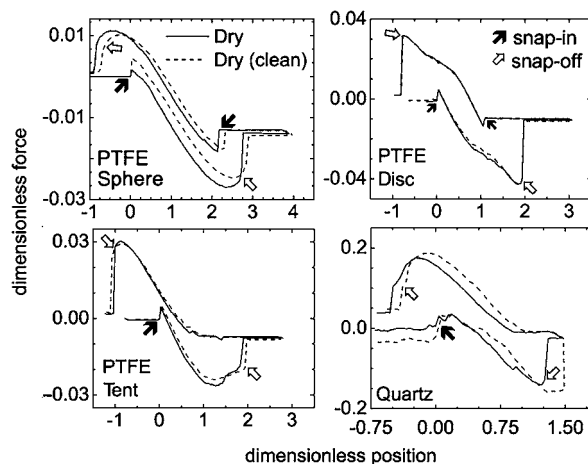


Figure 5. Experimental force-position curves of dry PTFE sphere, disk, and tent, and quartz (both cleaned and noncleaned). Filled arrows indicate snap-in, empty arrows indicate snap-off. Dimensions of particles are listed in Table S.1.

dry PTFE particles of standard shapes and for the quartz particle. We use quartz as example to illustrate the behavior of a natural sediment particle (results for the other sediment particles are shown in Figure S.6, Supporting Information). The shape of the curves for the standard particles are related to their geometries. The curves for the PTFE sphere and disk are symmetrical with the immersion and emersion curves almost exact mirror images. Both particles show a large snap-off force, with the disk showing the most pronounced snap-off effect due to interface pinning. The tent and the quartz particle also show snap-off force, due to interface pinning. However, during emersion, there was no snap-in for both the tent and the quartz particle, as the interacting surface area of the particle with the air–water interface is small.

The experimental force-position curves show that particles with a smooth surface show a more pronounced difference between maximum and snap-off forces. The PTFE sphere, with its smooth surface and minimal pinning of the air–water interface, shows a pronounced difference between maximum and snap-off force. The tent shows an even more pronounced difference between the two forces, because the snap-off force is small due the minimal interaction area of the tent tip with the air–water interface. A summary of all the experimental forces is given in Table S.4 (Supporting Information).

For the natural particles, the snap-off forces are, in general, smaller than the maximum capillary forces, but in some cases the snap-off force equals the maximum force. This occurs when the air–water interface is pinned at the particle surface strong enough so that snap-off happens under conditions represented by the Gibbs extension of the Young Equation (eq 3). The

more pronounced the pinning, the more likely the air–water interface snaps off at the maximum capillary force.

Effect of Solvent Cleaning. We expected that the solvent-cleaning would remove some organic coatings, and therefore, the cleaned particles would have a smaller contact angle than the noncleaned particles. This should manifest itself in smaller maximum upward and snap-off forces for the solvent-cleaned particles, but this was not observed in all cases. Basalt, milky quartz, hematite, and quartz showed larger forces for cleaned than for noncleaned particles (Tables S.4, Supporting Information). Closer examination of the force–distance curves shows that the snap-off forces for these four particles occurred at a greater z position for the clean particles compared to the noncleaned particles (Figure 5), suggesting that pinning was more pronounced for the clean particles. We infer that surface coatings may have covered and smoothed surface roughness, and that after solvent cleaning, more surface roughness was accessible to the air–water interface.

Figure 6 illustrates a complete measurement of force against position for the immersion of a quartz particle in the order they

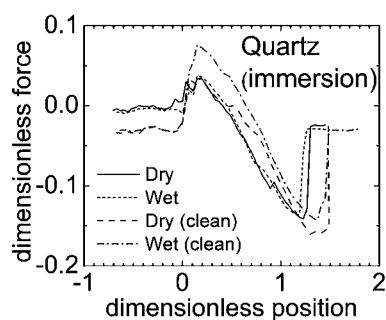


Figure 6. Force-position curves of a quartz particle during a sequence of immersion showing changes during the dry and wet stages (both cleaned and noncleaned).

were performed: first the immersion of the dry, noncleaned particle, then the wet, noncleaned particle, followed by the immersion of a cleaned and air-dried particle and last for the wet, cleaned particle. The initial, noncleaned dry particle showed large maximum and snap-off forces (solid line). After

wetting, the forces decreased, and snap off occurred earlier, indicated by the shift of the Z position to a smaller value. Similarly, the solvent-cleaned particle showed a left shift of the force–distance curve compared with the noncleaned particle. The solvent-cleaning also made the force–distance curve more symmetrical, indicating the cleaning reduced contact angle hysteresis.

Effect of Hysteresis. The immersion and emersion loops of the force–distance curves should, in the ideal case (i.e., in the absence of contact angle hysteresis and surface roughness), be symmetrical. The PTFE sphere indeed had a symmetrical curve, but the natural particles deviated from this symmetry, in some cases considerably (Figures 5 and S.6, Supporting Information). In general, the emersion curves were smoother than the immersion curves, which we attribute to the smaller contact angle during emersion (receding contact angle).

Comparison of Experimental and Theoretical Capillary Forces. Table 1 summarizes the experimental and calculated maximum capillary forces. The calculated forces are based on either the volume-equivalent or the maximum radius. The volume-equivalent radius tended to overestimate the measured radius, as shown for the PTFE sphere. For the sphere, the volume-equivalent radius was 14% higher than the measured radius. This led to a larger theoretical capillary force for the volume-equivalent radius than for the maximum radius. The theoretical calculations for the PTFE tent also overestimated the measured value. For the PTFE tent, using the volume-equivalent parameters provided close theoretical force values for both the sphere and the ellipsoidal shape. The theoretical calculations for a circular cylinder shape overestimated the force considerably, because the cylinder shape does not take into consideration the linearly reducing cross-section of the tent.

For the natural sediment particles, assuming a spherical shape (sphere) generally lead to an underestimation of the measured capillary force (Table 1). Assuming a circular cylinder, we overestimated the capillary force, whereas the ellipsoidal shape provided the best approximation of the capillary force.

6. IMPLICATIONS

Previous investigations have shown that capillary forces exerted at the air–water interface can exceed DLVO and gravity

Table 1. Maximum Capillary Forces (Experimental and Theoretical)

particle	radius (mm)		capillary force (μN)						
			experimental (dry, noncleaned)	theoretical			ellipsoid ^b		
	r_{ve} ^a	r_{max} ^c		r_{ve}	r_{max}	r_{ve}	r_{max}	r_{ve} ^d	r_{max} ^e
PTFE sphere	3.17	2.79	−1305	−2150	−1652				
PTFE disk	2.09	2.40	−1292			−1510	−1961		
PTFE tent	2.25	2.99	−1204	−1096	−1903	−1718	−3000	−1446	−1565
basalt	1.15	1.78	−537	−221	−473	−1895	−1161	−738	−423
granite	1.17	1.46	−467	−297	−414	−998	−868	−479	−388
hematite	1.00	1.22	−279	−284	−374	−515	−676	−420	−396
magnetite	0.79	1.16	−422	−180	−298	−389	−637	−377	−432
mica	0.85	1.35	−526	−116	−246	−426	−769	−559	−506
milky quartz	1.07	1.01	−7	−396	−373	−560	−524	−479	−312
quartz	1.13	1.53	−402	−247	−403	−601	−936	−472	−543

^aVolume-equivalent spherical radius. ^bUndulating contact line. ^cMaximum of the three semimajor axes. ^dUses the maximum values of the three semimajor axes of the particle to scale the volume equivalent spherical radius to give a volume-equivalent ellipsoid equal in volume to the real particle. ^eUsing the maximum values of the three semimajor axes of the particle, does not give a volume-equivalent particle.

forces,^{8,21–23} and that moving air–water interfaces during infiltration can mobilize, i.e., detach, soil particles from stationary surfaces.^{11,12,17} In porous media, while under dry conditions, the capillary force is a strong attachment force of particles to stationary surfaces, under wet conditions, the capillary force becomes a mechanism of detachment of particles from stationary surfaces. Such wet conditions occur during infiltration or drainage. Here, we quantified, such as detaching capillary forces for differently shaped particles and found that measured capillary forces on natural particles can be approximated by a volume–equivalent ellipsoid. Thus, assuming an ellipsoidal shape allows us to better predict capillary forces experienced by natural particles in porous media. Capillary forces become more important the smaller the particles are, because the gravity force decreases faster with particle size than the capillary force, and the capillary pressure scales inversely with the particle radius. Thus, particularly for particles in the colloidal size range, the capillary forces will play a dominant role.

■ ASSOCIATED CONTENT

● Supporting Information

Theoretical calculations of capillary forces on an ellipsoidal particle, data on measurement precision, and calculations of volume-equivalent dimensions, tables showing particle characterization data, experimental force measurements, and particle volume measurements, and figures showing dissection scope images of particles, experimental schematics, and force-position plots. This material is available free of charge via the Internet at <http://pubs.acs.org>.

■ AUTHOR INFORMATION

Corresponding Author

*Phone: +1-509-432-9533. E-mail: c_nirmalya@wsu.edu.

Notes

The authors declare no competing financial interest.

■ ACKNOWLEDGMENTS

This material is based upon work supported by the U.S. Department of Energy, Office of Science (BER), under Award No. DE-FG02-08ER64660.

■ REFERENCES

- (1) Kretzschmar, R.; Borkovec, M.; Grolimund, D.; Elimelech, M. Mobile subsurface colloids and their role in contaminant transport. *Adv. Agron.* **1999**, *66*, 121–193.
- (2) McCarthy, J. F.; Zachara, J. M. Subsurface transport of contaminants. *Environ. Sci. Technol.* **1989**, *23*, 496–502.
- (3) Keller, A. A.; Auset, M. A review of visualization techniques of biocolloid transport processes at the pore scale under saturated and unsaturated conditions. *Adv. Water Resour.* **2007**, *30*, 1392–1407.
- (4) Wan, J. M.; Wilson, J. L.; Kieft, T. L. Influence of the gas–water interface on transport of microorganisms through unsaturated porous media. *Appl. Environ. Microbiol.* **1994**, *60*, 509–516.
- (5) Gao, B.; Saiers, J. E.; Ryan, J. N. Deposition and mobilization of clay colloids in unsaturated porous media. *Water Resour. Res.* **2004**, *40*, W08602 DOI: 10.1029/2004WR003189.
- (6) Jacobsen, O. H.; Moldrup, P.; de Jonge, H.; de Jonge, L. W. Mobilization and transport of natural colloids in a macroporous soil. *Phys. Chem. Earth.* **1998**, *23*, 159–162.
- (7) Levin, J. M.; Herman, J. S.; Hornberger, G. M.; Saiers, J. E. Colloid mobilization from a variably saturated, intact soil core. *Vadose Zone J.* **2006**, *5*, 564–569.
- (8) Shang, J.; Flury, M.; Chen, G.; Zhuang, J. Impact of flow rate, water content, and capillary forces on in situ colloid mobilization

during infiltration in unsaturated sediments. *Water Resour. Res.* **2008**, *44*, W06411 DOI: 10.1029/2007WR006516.

(9) Cheng, T.; Saiers, J. E. Mobilization and transport of in situ colloids during drainage and imbibition of partially saturated sediments. *Water Resour. Res.* **2009**, *45*, W08414 DOI: 10.1029/2008WR007494.

(10) Zhuang, J.; McCarthy, J. F.; Tyner, J. S.; Perfect, E.; Flury, M. In-situ colloid mobilization in Hanford sediments under unsaturated transient flow conditions: Effect of irrigation pattern. *Environ. Sci. Technol.* **2007**, *41*, 3199–3204.

(11) Sharma, P.; Abdou, H.; Flury, M. Effect of the lower boundary condition and flotation on colloid mobilization in unsaturated sandy sediments. *Vadose Zone J.* **2008**, *7*, 930–940.

(12) Aramrak, S.; Flury, M.; Harsh, J. B. Detachment of deposited colloids by advancing and receding air–water interfaces. *Langmuir* **2011**, *27*, 9985–9993.

(13) Gomez-Suarez, C.; Noordmans, J.; van der Mei, H. C.; Busscher, H. J. Removal of colloidal particles from quartz collector surfaces as simulated by the passage of liquid–air interfaces. *Langmuir* **1999**, *15*, 5123–5127.

(14) Gomez-Suarez, C.; Noordmans, J.; van der Mei, H. C.; Busscher, H. J. Detachment of colloidal particles from collector surfaces with different electrostatic charge and hydrophobicity by attachment to air bubbles in a parallel plate flow chamber. *Phys. Chem. Chem. Phys.* **1999**, *1*, 4423–4427.

(15) Leenaars, A. F. M.; O'Brien, S. B. G. Particle removal from silicon substrates using surface tension forces. *Philips J. Res.* **1989**, *44*, 183–209.

(16) Noordmans, J.; Wit, P. J.; van der Mei, H. C.; Busscher, H. J. Detachment of polystyrene particles from collector surfaces by surface tension forces induced by air-bubble passage through a parallel plate flow chamber. *J. Adhesion Sci. Technol.* **1997**, *11*, 957–969.

(17) Sharma, P.; Flury, M.; Zhou, J. Detachment of colloids from a solid surface by a moving air–water interface. *J. Colloid Interface Sci.* **2008**, *326*, 143–150.

(18) Gao, B.; Steenhuis, T. S.; Zevi, Y.; Morales, V. L.; Nieber, J. L.; Richards, B. K.; McCarthy, J. F.; Parlange, J.-Y. Capillary retention of colloids in unsaturated porous media. *Water Resour. Res.* **2008**, *44*, W04504 DOI: 10.1029/2006WR005332.

(19) Wan, J. M.; Tokunaga, T. K. Film straining of colloids in unsaturated porous media: Conceptual model and experimental testing. *Environ. Sci. Technol.* **1997**, *31*, 2413–2420.

(20) Veerapaneni, S.; Wan, J.; Tokunaga, T. Motion of particles in film flow. *Environ. Sci. Technol.* **2000**, *34*, 2465–2471.

(21) Shang, J.; Flury, M.; Deng, Y. Force measurements between particles and the air–water interface: Implications for particle mobilization in unsaturated porous media. *Water Resour. Res.* **2009**, *45*, W06420 DOI: 10.1029/2008WR007384.

(22) Preuss, M.; Butt, H. J. Measuring the contact angle of individual colloidal particles. *J. Colloid Interface Sci.* **1998**, *208*, 468–477.

(23) Scheludko, A.; Toshev, B. V.; Bojadjev, D. T. Attachment of particles to a liquid surface (Capillary theory of flotation). *J. Chem. Soc., Faraday Trans. I* **1976**, *72*, 2815–2828.

(24) Zhang, L.; Ren, L.; Hartland, S. More convenient and suitable methods for sphere tensiometry. *J. Colloid Interface Sci.* **1996**, *180*, 493–503.

(25) Zhang, L.; Ren, L.; Hartland, S. Detailed analysis of determination of contact angle using sphere tensiometry. *J. Colloid Interface Sci.* **1997**, *192*, 306–318.

(26) Preuss, M.; Butt, H. Direct measurement of particle–bubble interactions in aqueous electrolyte: dependence on surfactant. *Langmuir* **1998**, *14*, 3164–3174.

(27) Gillies, G.; Kappl, M.; Butt, H. Direct measurements of particle–bubble interactions. *Adv. Colloid Interface Sci.* **2005**, *114*, 165–172.

(28) Englert, A.; Krasowska, M.; Fornasiero, D.; Ralston, J.; Rubio, J. Interaction force between an air bubble and a hydrophilic spherical particle in water, measured by the colloid probe technique. *Int. J. Miner. Process.* **2009**, *92*, 121–127.

(29) Yamamoto, T.; Harada, Y.; Fukui, K.; Yoshida, H. AFM investigation of the surface properties of silica particles dispersed by bead milling. *Colloids Surf. Physicochem. Eng. Aspects* **2010**, *362*, 97–101.

(30) Gunde, R.; Hartland, S.; Mader, R. Sphere tensiometry: a new approach to simultaneous and independent determination of surface tension and contact angle. *J. Colloid Interface Sci.* **1995**, *176*, 17–30.

(31) Ecke, S.; Preuss, M.; Butt, H. J. Microsphere tensiometry to measure advancing and receding contact angles on individual particles. *J. Adhesion Sci. Technol.* **1999**, *13*, 1181–1191.

(32) Princen, H. M. Equilibrium shape of interfaces, drops, and bubbles. Rigid and deformable particles at interfaces. *Surface Colloid Sci.* **1969**, *2*, 1–84.

(33) Zhang, P.; Johnson, W. P.; Rowland, R. Bacterial tracking using ferrographic separation. *Environ. Sci. Technol.* **1999**, *33*, 2456–2460.

(34) Hesla, T. I.; Joseph, D. D. The maximum contact angle at the rim of a heavy floating disk. *J. Colloid Interface Sci.* **2004**, *279*, 186–191.

(35) Singh, P.; Joseph, D. D. Fluid dynamics of floating particles. *J. Fluid Mech.* **2005**, *530*, 31–80.

(36) Brown, A. B. D.; Smith, C. G.; Rennie, A. R. Fabricating colloidal particles with photolithography and their interactions at an air–water interface. *Phys. Rev. E* **2000**, *62*, 951–960.

(37) Stamou, D.; Duschl, C.; Johannsmann, D. Long-range attraction between colloidal spheres at the air–water interface: The consequence of an irregular meniscus. *Phys. Rev. E* **2000**, *62*, 5263–5272.

(38) Fournier, J.-B.; Galatola, P. Anisotropic capillary interactions and jamming of colloidal particles trapped at a liquid–fluid interface. *Phys. Rev. E* **2002**, *65*, DOI: 10.1103/PhysRevE.65.031601.

(39) Danov, K. D.; Kralchevsky, P. A.; Naydenov, B. N.; Brenn, G. Interactions between particles with an undulated contact line at a fluid interface: Capillary multipoles of arbitrary order. *J. Colloid Interface Sci.* **2005**, *287*, 121–134.

(40) van Nierop, E. A.; Stijnman, M. A.; Hilgenfeldt, S. Shape-induced capillary interactions of colloidal particles. *Europhys. Lett.* **2005**, *72*, 671–677.

(41) Lehle, H.; Noruzifar, E.; Oettel, M. Ellipsoidal particles at fluid interfaces. *Eur. Phys. J. E* **2008**, *26*, 151–160.

(42) Tee, G. J. *Surface Area and Capacity of Ellipsoids in n Dimensions*; Technical Report; Department of Mathematics, University of Auckland: Auckland, New Zealand, 2004.

(43) Danov, K. D.; Kralchevsky, P. A. Capillary forces between particles at a liquid interface: General theoretical approach and interactions between capillary multipoles. *Adv. Colloid Interface Sci.* **2010**, *154*, 91–103.

—**Supporting Information**—

Detachment of deposited colloids by advancing and receding air-water
interfaces

Surachet Aramrak, Markus Flury, James B. Harsh

Table A. Colloid detachment (%) from a glass surface after the passages of air-water interfaces.

	Colloid detachment (%) at different velocities				
	1	10	100	1000	10000
	(0.5)*	(7.7)	(72)	(982)	(10,800)
	(cm/h)				
Initial state	0 Aa	0 Aa	0 Aa	0 Aa	0 Ab
Flow (no bubble)	0Aa	0.01 ± 0.01 Aa	0.01 ± 0.01 Aa	0.02 ± 0.02 Aa	0.02 ± 0.03 Ab
After receding-1	5 ± 6 Aa	5 ± 5 Aa	9 ± 6 Aa	2 ± 4 Aa	0.4 ± 0.7 Ab
After advancing-1	88 ± 10 Ba	85 ± 10 Ba	80 ± 6 Ba	72 ± 28 Ba	1 ± 2 Bb
After receding-2	0 Aa	0 Aa	0.2 ± 0.5 Aa	1 ± 2 Aa	0.1 ± 0.3 Ab
After advancing-2	3 ± 5 Aa	2 ± 4 Aa	2 ± 2 Aa	12 ± 21 Aa	0.1 ± 0.3 Ab

* Numbers in parentheses are measured velocities. Data represent means and standard deviations measured from 12 replications. Different capital letters (A, B, and C) indicate statistical differences column-wise; and different lower cases (a, b, and c) indicate statistical differences row-wise; both at $\alpha = 0.01$.

Detachment of Deposited Colloids by Advancing and Receding Air–Water Interfaces

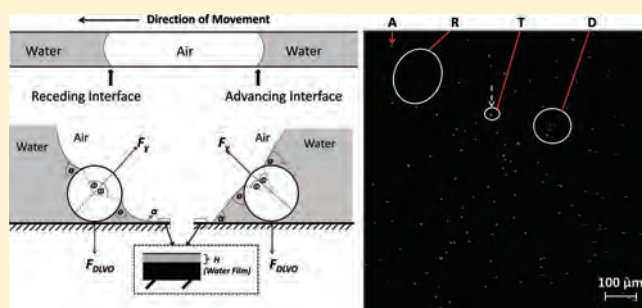
Surachet Aramrak,[†] Markus Flury,^{*,†,‡} and James B. Harsh[†]

[†]Department of Crop and Soil Sciences, Washington State University, Pullman, Washington 99164, United States

[‡]Department of Crop and Soil Sciences, Washington State University, Puyallup, Washington 98371, United States

S Supporting Information

ABSTRACT: Moving air–water interfaces can detach colloidal particles from stationary surfaces. The objective of this study was to quantify the effects of advancing and receding air–water interfaces on colloid detachment as a function of interface velocity. We deposited fluorescent, negatively charged, carboxylate-modified polystyrene colloids (diameter of 1 μm) into a cylindrical glass channel. The colloids were hydrophilic with an advancing air–water contact angle of 60° and a receding contact angle of 40° . After colloid deposition, two air bubbles were sequentially introduced into the glass channel and passed through the channel at different velocities (0.5, 7.7, 72, 982, and 10 800 cm/h). The passage of the bubbles represented a sequence of receding and advancing air–water interfaces. Colloids remaining in the glass channel after each interface passage were visualized with confocal microscopy and quantified by image analysis. The advancing air–water interface was significantly more effective in detaching colloids from the glass surface than the receding interface. Most of the colloids were detached during the first passage of the advancing air–water interface, while the subsequent interface passages did not remove significant amounts of colloids. Forces acting on the colloids calculated from theory corroborate our experimental results, and confirm that the detachment forces (surface tension forces) during the advancing air–water interface movement were stronger than during the receding movement. Theory indicates that, for hydrophilic colloids, the advancing interface movement generally exerts a stronger detachment force than the receding, except when the hysteresis of the colloid–air–water contact angle is small and that of the channel–air–water contact angle is large.



1. INTRODUCTION

One of the most striking phenomena in nature related to particle–air–water interface interactions is the rolling of water droplets on Lotus leaves.^{1,2} Due to the hydrophobic surface of Lotus leaves, water droplets roll off the slanted leaf, and as they roll downward driven by gravity, dust particles are removed from the leaf surface, resulting in a self-cleaning process, called the “Lotus-Effect”.^{2–4} The removal of dust particles is due to attachment of the particles to the air–water interface.^{3,5} This self-cleaning process observed with Lotus leaves has several industrial parallels, including cleaning of wafers in microelectronics.⁶ One of the most prominent examples of an industrial application of particle–air–water interface attachment is froth flotation, used in the mining industry to separate different minerals based on the preferential attachment to gas bubbles.^{7,8}

Moving air–water interfaces also occur in geologic media, i.e., the unsaturated subsurface or the vadose zone. The unsaturated subsurface is a three-phase system, consisting of air, water, and solid phases, and air–water interfaces move when water infiltrates or drains from the system. Such infiltration and drainage events occur frequently in nature during rainfall events. It has been reported that infiltration fronts can mobilize substantial amounts

of particles from sediments or soils.^{9–11} Particles themselves can be contaminants or can associate with contaminants, thereby providing a pathway for contaminant transport.^{12–14} Thus, the interaction of particles and moving air–water interfaces is an important process in subsurface systems with regard to environmental protection.

Particles attached to the air–water interface experience strong capillary forces.^{15–17} These forces can exceed solid–water adhesion forces by several orders of magnitude,^{10,18} and this is the basis for dust and colloid removal by moving air–water interfaces used in microelectronics.^{5,6} Several mechanistic studies on how moving air–water interfaces can be used to remove colloidal particles from a solid surface have been reported.^{6,18–22} In these studies, colloids were deposited on the inner surface of a parallel plate flow chamber^{6,18,19,21,22} or onto a microscopy slide,²³ and then removed by passing air–water interfaces over the deposited colloids. The results showed that colloid detachment by the air–water interface was more effective when colloids

Received: May 16, 2011

Revised: June 28, 2011

Published: June 29, 2011

were deposited under unfavorable as compared to favorable conditions,^{21,23} when the velocity of the air–water interface decreased,^{21,23} when colloidal size increased,²² when colloids were hydrophobic as opposed to hydrophilic,²³ and when the air–liquid surface tension increased.²¹

Experimental evidence indicates that, while colloid detachment by a moving air–water interface generally increases with decreasing interface velocity, the sensitivity of detachment to interface velocity is stronger the larger and more hydrophobic the colloids are.²² A linear relationship between the air–water interface velocity and the amount of colloid detachment was observed for velocities in the range of 700 to 5000 cm/h;²¹ however, at lower interface velocities of 0.4 to 400 cm/h, Sharma et al.²³ found no linear relationship, yet the general trend of decreasing detachment with increasing velocity was confirmed. Detachment of colloids with opposite charge to the collector surface was more sensitive to interface velocity as compared to detachment of colloids deposited on a like-charged collector surface.^{21,23}

The effect of moving air–water interfaces on the detachment of colloidal particles from both initially wet solid surfaces^{6,18,19,21,22} and initially air-dried surfaces²³ has been investigated under different physical and chemical conditions. Both initially wet and dry conditions occur often in nature. In the subsurface, the air–water interface passes over initially air-dried surfaces when water infiltrates or imbibes dry soils or sediments, while the interface passes over initially wet surfaces when water imbibes into moist soil or when drainage occurs. Column-scale experiments with porous media have shown that colloidal particles are mobilized from sediments during infiltration and drainage events,^{9,24–26} and it has indeed been demonstrated that the air–water interface is contributing considerably to the mobilization.¹¹

The interaction force between the air–water interface and a particle depends on the air–water–solid contact angle, for both the particle and the collector surface.¹⁸ As advancing and receding interfaces have different contact angles with respect to particle and collector surface, the detachment force will be different as well.^{16,20} Gomez-Suarez et al.¹⁹ showed theoretically that detachment forces are larger for advancing than receding interfaces, but no experimental evidence has been reported from microscopic-scale experiments so far.

Our objective was to experimentally test the effect of advancing and receding air–water interfaces on detachment of colloidal particles from a solid surface. We used microscopic visualization to quantify colloid detachment from a hydrophilic glass surface by a sequence of advancing and receding air–water interfaces as a function of interface velocity.

2. EXPERIMENTAL SECTION

Approach. Our general experimental approach was to deposit colloidal particles onto a glass surface and then expose the deposited colloids to successive air–water interface passages. As the air–water interface moved over the deposited colloids, we quantified the colloid removal by using confocal microscopy and image analysis. Air–water interfaces were generated by inserting air bubbles into a water-filled capillary tube. Displacement experiments were carried out with *in situ* confocal microscopy so that we could differentiate between advancing and receding interfaces. All experiments were conducted at ambient temperature (18 to 20 °C). Figure 1 shows a schematic of the experimental setup.

Glass Channel Design. A cylindrical channel (3.7 mm inner diameter and 7.5 cm length) made of soda-lime glass was used as a surrogate for a pore channel. We cleaned the channel by first using

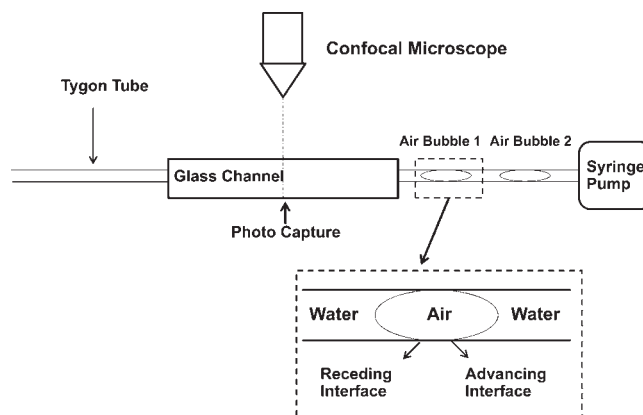


Figure 1. Schematic of experimental setup for air–water interface displacement.

compressed air to blow out dust (using a cleaning duster), then soaking in 99% acetone for 20 min, rinsing with 95% ethanol, scouring with an ethanol wet cotton swab, rinsing again with ethanol, followed by rinsing with double-deionized water. The rinsing procedures were repeated five times. The channel was finally dried at room temperature. Two 1-cm-long sections of a sterile stainless steel hypodermic needle (1.2 mm diameter, Monoject 250, Tyco) were glued with epoxy (General Purpose Epoxy, PermaPoxy, Permatex Inc., Solon, OH) to both sides of the channel. A small piece of a 6-mm-diameter glass rod with inner diameter of 1.5 mm was used to provide end-piece support for the needle tube. Two rectangularly shaped (25 mm × 10 mm) microscopy glass slides were glued to both ends of the channel to provide a support platform.

Colloids and Suspension Chemistry. Hydrophilic carboxylate-modified microspheres (FluoSpheres, lot number 28120W, Molecular Probes, Inc., Eugene, OR) were selected as the colloid models in our experiment. The microspheres were negatively charged, fluorescent with an excitation/emission wavelength of 505/515 nm (yellow–green), had a diameter of 1.0 μm, a specific density of 1.055 g/cm³, and surface charge of 0.0175 mol./g (Molecular Probes, Inc., Eugene, OR).

We intended to deposit colloids onto the inner surface of the glass channel as single, nonaggregated particles under nonfavorable conditions. We first tested solutions with different chemistry and used DLVO (Derjaguin–Landau–Verwey–Overbeek) calculations to optimize unfavorable attachment conditions. We first determined electrophoretic mobilities and ζ-potentials of the colloids and the channel at different pH values. For the glass channel, we ground the glass channel with a mortar to a fine powder and we then suspended the powder in aqueous solution. Electrophoretic mobilities were measured by dynamic light scattering (ZetaSizer 3000HSa, Malvern Instruments Ltd., Malvern, UK). All measurements were made in a solution of 1 mM CaCl₂ at different pH. Zeta potentials were derived from electrophoretic mobilities using the von Smoluchowski equation.²⁷ Using the measured zeta potentials, we then selected the pH value for the suspension that resulted in nonfavorable attachment conditions, i.e., where the DVLO profile showed a secondary energy minimum. The selected solution had pH 4.7 and 1 mM CaCl₂.

Characterization of Surface Properties of Glass Channel and Colloids. We determined advancing and receding air–liquid–solid contact angles with the tangent method by using a digital goniometer (DSA 100, Krüss, Hamburg, Germany). The liquid phase for these measurements was the aqueous solution determined above (1 mM CaCl₂ and pH 4.7). For the glass channel, we used a soda-lime microscopy slide (25 mm × 75 mm, Fisher brand, Fisher Scientific) as a surrogate. The slide was cleaned in the same manner as the glass channel described above. For colloids, a drop of a diluted microsphere

Table 1. Surface Properties of Colloids and Glass Channel (Soda-Lime Glass) (in 1 mM CaCl₂ and pH 4.7)

materials	contact angle (deg)		electrophoretic mobility ($\mu\text{m/s}$)(V/cm)	ζ -potential (mV)
	advancing	receding		
carboxylate-modified microspheres	60.1 \pm 3.0	39.7 \pm 1.0	-3.01 \pm 0.02	-38.3 \pm 0.3
glass channel	27.2 \pm 1.6	20.4 \pm 2.9	-1.93 \pm 0.05	-24.6 \pm 0.7

suspension (0.5% by weight) was evaporated on a double-sided tape attached to the microscopy slide in a laminar flow chamber. This produced a uniform layer of colloids on the slide. For the contact angle measurements, we continuously dosed liquid onto the solid surface (either glass or colloids) at a rate of 5 $\mu\text{L}/\text{min}$ and used a final drop size of 12 μL , following the procedures described by Shang et al.²⁸ The measured contact angles are macroscopic contact angles, and may differ from microscopic angles.²⁹ Electrophoretic mobilities and zeta potentials were determined as described above. Table 1 shows the characterization data.

Deposition of Colloids. Colloids were deposited onto the inner surface of the glass channel by circulating a colloid suspension through the channel. The deposition suspension was 1 mM CaCl₂, pH 4.7, and had a colloid concentration of 3.6×10^{11} particles/L. The channel was connected to Tygon tubing and a peristaltic pump (Ismatec IP4, Glattburg, Switzerland). Before the colloid suspension was introduced, the channel system was preconditioned with deionized water and the colloid-free solution for 20 min each, using a flow rate of 20 mL/h (average velocity in the channel 186 cm/h). Channel outflow of the preconditioning solution was discarded. The colloidal suspension was sonicated in an ultrasonic water bath for 1 min and then introduced into the channel. The Erlenmeyer flask containing the colloid suspension, the pump, and the channel formed a closed loop where the channel outflow recirculated into the Erlenmeyer flask at a flow rate of 20 mL/h. The colloidal suspension was recirculated for 2 h.

After the deposition, the channel was flushed for 4 h with the colloid-free solution to remove unattached colloids from the channel. After this flushing, the flow was stopped, and the channel, including the Tygon tubing, was removed from the pump. To prevent potential dust contamination, the colloidal deposition experiments were done in a laminar air-flow chamber (Laminar Airflow Cabinets, NuAire Corp., Plymouth, MN). The channel was then transferred to a confocal microscope for the interface displacement experiments.

Visualization and Quantification of Colloids. We used confocal microscopy to visualize the colloidal particles deposited inside the channel. Confocal or phase-contrast microscopy allows visualization of single colloids and has been used extensively in air–water interface displacement experiments.^{19,21,23,30} We used a laser scanning confocal microscope (Axiovert 200 M equipped with LSM 510 META, Carl Zeiss Jena GmbH, Germany) and focused the field of view at the bottom of the channel with a magnification of 10. This allowed us to identify individual colloids. We scanned a fixed area of 900 μm by 900 μm during the course of the interface displacement experiments. Scanning of one image lasted 15 s. The images were then analyzed by the *ImageJ* software³¹ to quantify the number of colloids.

Air–Water Interface Displacement Experiments. For the air–water interface displacement experiments, we used a syringe pump (KDS 200, KD Scientific, USA) to control the flow rates. One of the Tygon tubes of the channel system was connected to the pump and colloid-free solution (1 mM CaCl₂, pH 4.7) was passed through the channel at a constant flow rate. The inflow Tygon tube was bent into a U-shape and filled half with the colloid-free solution, leaving the end portions of the tube air-filled. After connecting to the channel and the pump, we had two air bubbles trapped in the inflow tube (Figure 1). These two air bubbles moved through the glass channel and provided a sequence of receding and advancing interface displacements: receding-1,

advancing-1, receding-2, and advancing-2. Scanning confocal microscopy images were recorded before and after each interface passage over the scanning area. One initial image was recorded before flow was started to check whether the solution without an air–water interface will remove colloids. In addition, we recorded a scanning image of the interface itself (which was only possible at the low flow rates due to the time required to acquire an image). Each experiment was repeated 12 times, using a new channel for each replicate, i.e., each replicate was a completely independent experiment.

To examine the effect of the air–water interface velocity on colloid detachment, we varied the velocities by using the syringe pump. Our target velocities were 1, 10, 100, 1000, and 10 000 cm/h, but we were not able to exactly obtain these values. The experimentally measured velocities were 0.5, 7.7, 72, 982, and 10 800 cm/h, respectively. Although these measured velocities did not exactly match our target velocities, they were of the same order of magnitude. In the following, we use the target velocities when discussing and presenting the results, but we use the measured velocities to represent the data in tables, in figures, and in calculations.

The lower interface velocities (1, 10, and 100 cm/h) in our experiment were in the range of those used by Sharma et al.²³ who used velocities from 0.4 to 400 cm/h, the medium velocities (1000 and 10 000 cm/h) were in the range of those used by Gomez-Suarez et al.²¹ who showed velocities from 700 to 5000 cm/h. The velocities of 1000 and 10 000 cm/h are in the range of the velocities reported for Haines jumps,^{32,33} which have velocities in the range of 1000 to 100 000 cm/h.^{34,35} The velocities used in our experiments correspond to Reynolds numbers of 0.01 to 115, indicating that the flow inside the channel was laminar at all velocities used.

To check whether the colloids removed by the moving air–water interfaces were initially deposited in the secondary energy minimum (i.e., unfavorable condition) or primary energy minimum, we conducted another set of experiments by changing the solution chemistry. We first calculated an appropriate solution chemistry using DLVO theory to determine a solution that will cause the secondary minimum to disappear. On this basis, we expected that, by changing the solution chemistry to the no-attachment condition (0.1 mM CaCl₂, pH 4.7), all colloids deposited in the secondary energy minimum would be released even without passage of air–water interfaces. We deposited the colloids into the channel as described above and then changed the solution chemistry to 0.1 mM CaCl₂ and pH 4.7. Visualization and quantification of colloids deposited on the glass channel was done before and after changing the solution chemistry at all the specific velocities indicated above. In these experiments, no air–water interface was present. As shown in the Results and Discussion section below, no colloids were removed at 0.1 mM CaCl₂ and pH 4.7, and therefore, we repeated these experiments by lowering the ionic strengths to 0.01, 0.001, and 0.0001 mM CaCl₂. Experiments were replicated three times.

Determination of the Effect of the Bubble Size. The faster the velocity of the air–water interface was, the more difficult it was to capture the colloidal images with the confocal microscope. To ease this step, we increased the size of the air bubble, providing a longer time for taking the images. To test whether the size of the air bubble in the tubing and channel affected colloid detachment, we did a series of experiments with two different bubble sizes. Air bubbles of 0.26 mL (standard bubble size used in our experiments) and 0.94 mL were introduced into the channel, and interface displacement experiments were conducted at a

velocity of 100 cm/h. Colloid detachment was visualized and quantified as described above. For each bubble size, we used 12 replicates. We found that the bubble size did not affect the experimental results, and we therefore used the bigger air bubbles for the experiments at velocities of 1000 and 10 000 cm/h.

Data Analysis. The images of colloids captured by the confocal microscope were analyzed by using the *ImageJ* software. Besides counting the total number of particles on the images, we used the mode of subtraction between images before and after interface movements to locate colloids that have remained stationary, colloids that have changed location, and colloids that have been removed. We analyzed the detachment data, i.e., the percentages of colloids detached after the passages of advancing and receding air–water interfaces, by using a one-way ANOVA and Turkey pairwise comparison to determine statistical differences at the 99% confidence level.³⁶

3. THEORETICAL CONSIDERATIONS

DLVO Forces. We calculated colloid–glass surface interaction energies and forces by using DLVO theory according to the approach presented in Sharma et al.²³ The DLVO forces were calculated by differentiating the energy profile with respect to distance. The DLVO profiles for our chosen solution chemistry (1 mM CaCl₂, pH 4.7) showed the existence of a weak secondary energy minimum, where colloids would attach under nonfavorable conditions. When we reduced the ionic strength (0.1 mM CaCl₂, pH 4.7), the secondary minimum disappeared.

Surface Tension Forces. If an air–water interface is in contact with a solid particle, the net force acting on the particle is the sum of gravity, buoyancy, and interfacial forces. For small particles (radius <500 μm), the gravity and buoyancy forces are negligible compared to the interfacial forces.^{16,23,37,38} In our experiments, we used particles with radius of 0.5 μm, and consequently, the interfacial force is the dominant force. When an air–water interface is in contact with a particle, the surface tension (interfacial) force F_γ , normal to the interface orientation can be calculated by^{6,19}

$$F_\gamma = 2\pi R_p \gamma \sin \phi \sin(\theta - \phi) \quad (1)$$

where R_p is the radius of the particle, γ is the surface tension of water, ϕ is the filling angle, and θ is the contact angle of the air–water interface with the particle. To obtain the maximum surface tension force,⁶ we can differentiate eq 1 and obtain the maximum force when $\phi = \theta/2$. In the case where the air–water interface is bounded to a solid interface at one end, like in case of an interface in a glass channel, the surface tension force vector is tilted because of the nonsymmetry caused by the air–water–solid contact angle α (Figure 2). The maximum surface tension force $F_{\gamma,\max}$ is then given by^{18,23}

$$F_{\gamma,\max} = 2\pi R_p \gamma \sin^2\left(\frac{\theta}{2}\right) \cos \alpha \quad \alpha < 90^\circ, \text{ vertical component} \quad (2)$$

and

$$F_{\gamma,\max} = 2\pi R_p \gamma \sin^2\left(\frac{\theta}{2}\right) \sin \alpha \quad \alpha < 90^\circ, \text{ horizontal component} \quad (3)$$

where α is the contact angle of the air–water interface with the glass surface. Because the contact angles θ and α are hysteretic with respect to the direction of the interface movement, it follows

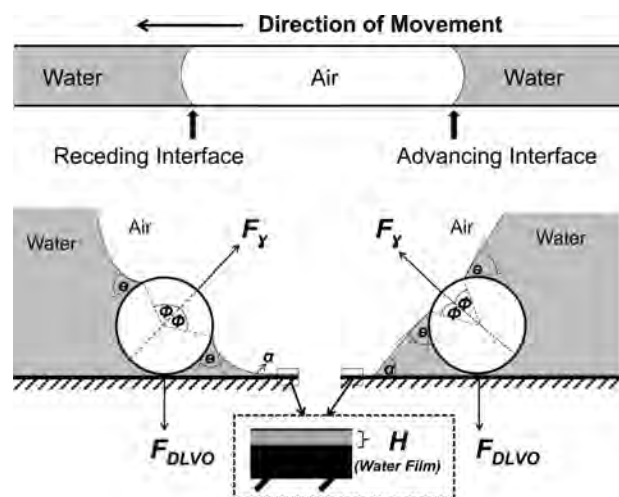


Figure 2. Schematic of surface tension force acting on a deposited colloid during receding and advancing air–water interface movement.

that the surface tension force will differ between advancing and receding interfaces. However, whether the surface tension force during advancing or receding interface movement is greater depends on the magnitude of the contact angle hysteresis and the absolute values of the contact angles.¹⁸ In our experiments, the vertical component (eq 2) of the surface tension force acts against the adhesive DLVO force, resulting in lifting the deposited colloids up from the glass surface. The horizontal component (eq 3), on the other hand, will cause sliding and translocation of the deposited colloids over the glass surface.

Shear Force. In a dynamic system, when a moving air–water interface contacts a deposited particle, in addition to the surface tension force, a shear force acts on the particle. The shear force F_s can be expressed by³⁹

$$F_s = 1.7(6\pi)\mu\left(\frac{H}{2}\right)V \quad (4)$$

where μ is the dynamic viscosity of water, H is the water film thickness, and V is the velocity of the liquid phase and the air–water interface. The shear force is maximal when the particle is completely exposed to the moving liquid, i.e., when $H/2 = R_p$.

Dynamic Thickness of Water Film. When an air bubble moves along with the fluid in a tube, a water film separates the air bubble from the tube wall; thus, the air–water interface does not make direct contact with the solid tube surface. Particles deposited on the tube surface generally will be detached by a moving air–water interface only if their diameters are larger than the water film thickness. For an air bubble moving in a tube, the thickness of the water film depends on the velocity of the air–water interface. Bretherton⁴⁰ approximated the film thickness H as function of the air bubble velocity V as

$$\frac{H}{w} = 0.643\left(\frac{3\mu V}{\gamma}\right)^{2/3} \quad (5)$$

where w is the diameter of the flow channel, μ is the dynamic viscosity, and γ is the surface tension. Equation 5 shows that increasing the velocity leads to an increased liquid-film thickness at the channel wall.

Contact and Induction Time during Colloid and Air–Water-Interface Interaction. Colloid attachment to the

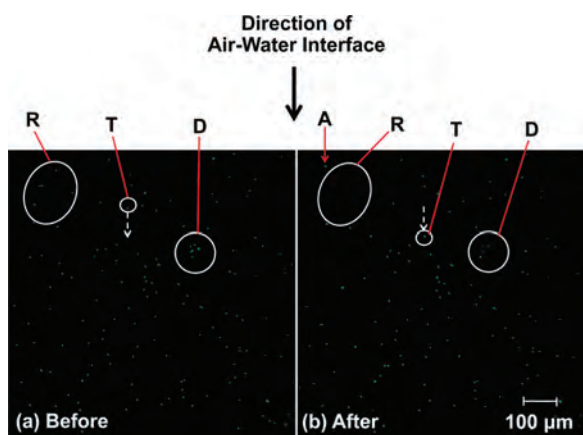


Figure 3. Modes of translocation of colloidal particles: (a) before and (b) after receding air–water interface passage. A: translocated into the field of view from upstream, R: removed from the solid surface, T: translocated to new position, and D: separated from colloid cluster. Images represent a fluid and interface velocity of 100 cm/h.

air–water interface is a time-dependent process, controlled by the contact time and the induction time.⁴¹ The contact time t_c is the time of physical contact of the colloid with the air–water interface. The induction time t_i includes the times of thinning of the water film, the film rupture, and the formation of the air–water–solid interface line. Only colloids that contact the air–water interface for a time longer than the induction time will attach to the air–water interface. Thus, only if $t_c > t_i$ can attachment occur.⁴¹

In our experimental system, the contact time t_c can be estimated by

$$t_c = \frac{2R_p}{V} \quad (6)$$

where R_p is the colloid radius and V is the interface velocity. The induction time t_i can be calculated as⁴²

$$t_i = \frac{3\mu R_f^2 R_p}{8m\gamma h_{cr}^2} \quad (7)$$

where R_f is the film radius, m is the mobility factor (1 for a completely retarded and 4 for a completely free bubble surface), and h_{cr} is the critical thickness of film rupture, which is given by⁴²

$$h_{cr} = 23.3[\gamma(1 - \cos \theta_a)]^{0.16} \quad (8)$$

where h_{cr} has units of nm, the surface tension γ is in mN/m, and θ_a is the advancing contact angle.

The film radius R_f can be approximated by^{42,43}

$$R_f = \frac{\pi R_p (656.9 - 87.4 \ln R_p) (V t_{col})^{0.60}}{180} \quad (9)$$

where V is the air–water interface velocity, and t_{col} is the collision contact time.⁴² In eq 9, the units are R_f (μm), V (cm/s), t_{col} (s).

The collision contact time can be calculated by⁴²

$$t_{col} = \sqrt{\frac{\pi^2 R_p^3 (\rho_p + 1.5\rho_{Fl})}{3\gamma}} f \quad (10)$$

where ρ_p and ρ_{Fl} are the density of the particle and water, respectively, f is a nonlinear function depending on the properties

of the particle and the surface tension of the fluid. We assumed that our f is equal to 5 according to Schulze.⁴²

4. RESULTS AND DISCUSSION

Visualization and Modes of Colloid Translocation. We observed that the deposited colloids had different modes of translocation after the passage of an air–water interface. We illustrate the different modes for the passage of a receding interface at a velocity of 100 cm/h. Figure 3 shows the position of deposited colloids before (a) and after (b) passage of the air–water interface. The flow and the direction of the interface movement in the images are from top to bottom. Arrow A shows a colloidal particle that has moved into the image from upstream, i.e., has translocated into the field of view, either by sliding along the glass surface or by redeposition. Arrow R shows an area where colloids have been removed after the passage of the interface, while Arrow T shows a colloid that has apparently translocated along the direction of flow, likely by sliding along the glass surface. Arrow D shows a colloid cluster that has been broken up after passage of the air–water interface.

Figure 4 illustrates the general patterns observed during passages of an advancing and a receding air–water interface. The initial spatial distribution of the colloids on the glass surface (a) represents our reference from which we calculate colloid detachment. As the receding air–water interface moves over the field of view (b), more colloids are visible upstream of the interface, and we consider these colloids being attached at the thinning air–water interface trailing the interface front. We could identify the interface location optically because the colloids viewed through water and air phases had different brightness in the confocal microscope. After passage of the advancing air–water interface (c), we only see colloids remaining attached to the glass surface; compared with the initial amount of colloids, only a small fraction have been removed. The following advancing air–water interface showed a pronounced accumulation of colloids at the interface (d), and after passage of the interface, a large fraction of colloids have been removed from the glass surface.

Figure 5 shows an example of the sequence of images of the colloid distribution that we used for the quantitative data analysis for each set of experiments. The images represent the condition (a) before flow was started, (b) after flow was started but just before the air–water interface passed over the field of view, (c) after passage of the first receding interface, (d) after passage of the first advancing interface, (e) after passage of the second receding interface, and (f) after passage of the second advancing interface. It can be seen that (1) the flow itself without the passage of an air–water interface could not translocate or detach colloids from the glass surface (images a versus b); (2) the passage of the first receding interface did not remove as many colloids as did the first passage of the advancing interface (images c versus d); and (3) the passage of the second receding and second advancing interface was not causing substantial additional removal of colloids from the glass surface (images c through f). While these general patterns were observed in all our experiments, the quantitative magnitude of colloid translocations differed as a function of interface velocity as discussed below.

Colloid Attachment to the Glass Surface. The DLVO calculations indicated that the colloids attached to the glass surface under unfavorable conditions. However, the secondary energy minimum was too weak (~ -0.1 kT) to keep colloids

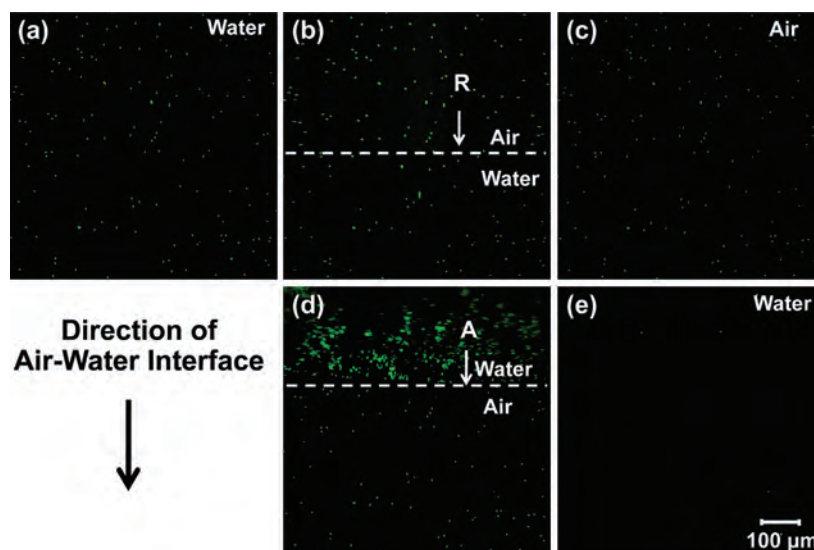


Figure 4. Detachment of deposited colloids from the solid surface by advancing and receding air–water interfaces: (a) initial condition, (b) during receding air–water interface movement, (c) after passage of receding air–water interface, (d) during advancing air–water interface movement, and (e) after passage of advancing air–water interface. R: position of receding air–water interface at the glass surface; A: position of the advancing air–water interface. Images represent a fluid and interface velocity of 100 cm/h.

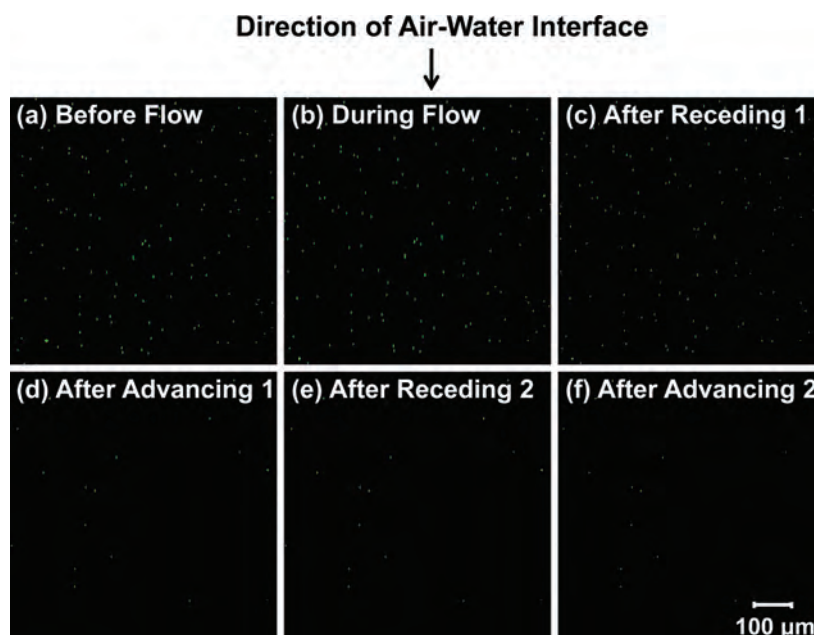


Figure 5. Detachment of deposited colloids after two successive air bubble movements: (a) initial condition before flow, (b) just before passage of the air–water interface, (c) after passage of first receding interface (receding-1), (d) after passage of first advancing interface (advancing-1), (e) after passage of second receding interface (receding-2), and (f) after passage of second advancing interface (advancing-2). Images represent a fluid and interface velocity of 100 cm/h.

attached. Our experiments showed that colloids remained attached to the glass surface after deposition and also after lowering the ionic strength to 0.1 mM CaCl_2 . The colloids did not detach even after sequentially lowering the ionic strengths to 0.01, 0.001, and 0.0001 mM CaCl_2 . We thus conclude that the attached colloids were all located in the primary energy minimum. It has been reported that chemical heterogeneities can cause differences in selectivity of attachment sites,^{44,45} and local heterogeneities on glass surfaces can provide favorable attachment sites

for negatively charged polystyrene colloids, particularly under low ionic strengths.⁴⁶ We assume that the distance between colloid and glass surface, when attached in the primary minimum, was 0.1 nm.⁴⁷

Effect of Air–Water Interface Velocity on Colloid Detachment. Figure 6 and Table A (Supporting Information) show the quantitative amounts of colloids detached after passage of the air–water interfaces as a function of interface velocity. The percent detachment represents the number of colloids detached

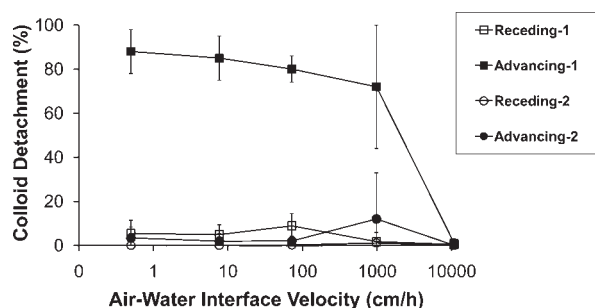


Figure 6. Detachment of deposited colloids as a function of air–water interface velocity. Solid symbols represent the advancing interface and open symbols represent receding interface. Symbols are arithmetic means and bars represent \pm one standard deviation.

by the respective air–water interface relative to the number of colloids just before the air–water interface has passed. The hydrodynamic force caused by the flow itself was not able to remove colloids from the glass surface at any velocity, as no colloids were removed during flow in absence of an air bubble (Table A, Supporting Information), and the surface tension force indeed was the dominant force causing colloid detachment. Colloid detachment was most pronounced at low flow velocities (1, 10, and 100 cm/h). The majority of the colloids were removed by the first advancing interface (advancing-1), and no significant difference in colloid detachment was observed among the three lowest velocities of 1, 10, and 100 cm/h. Indeed, for all interface passages, the amounts of colloids detached were not a function of interface velocities in the range of 1 to 100 cm/h; however, for faster velocities (1000 and 10 000 cm/h), colloid detachment drastically decreased. At a speed of 10 000 cm/h, no colloids were removed by any interface passage. While these general patterns were observed for all different interface passages, they were most pronounced for the first advancing interface (advancing-1).

Our data corroborate the results from Sharma et al.,²³ who observed the same velocity dependence of colloid detachment for carboxylate-modified polystyrene beads. Sharma et al.²³ operated with a narrower range of velocities and observed velocity-invariant detachment for velocities of 0.4, 0.8, 4, and 40 cm/h, but they observed decreased colloid detachment at an interface velocity of 400 cm/h. Gomez-Suarez et al.²⁰ found that colloid detachment from a quartz collector surface was dependent on interface velocity in the range of 700 to 5000 cm/h, with fewer colloids being detached as the velocity increased. Gomez-Suarez et al.²⁰ observed that less than 20% of colloids were detached by an air bubble (one receding and one advancing interface passage) at a velocity of 5000 cm/h. In our experiment, the detachment of colloids by the first air bubble (receding-1 and advancing-1) also decreased as the velocities increased from 100 to 1000 cm/h and was less than 1% at velocity of 10 000 cm/h (Figure 6). Our range of air–water interface velocities (1 to 10 000 cm/h) extends the ranges used in previous works, and our results and previous data indicate that the detachment of colloids significantly depends on the air–water interface velocity between 100 and 10 000 cm/h (Table A, Supporting Information).

Effect of the Sequence of Air–Water Interface Passage on Colloid Detachment. Here, we discuss the effect of the sequence of interface passages for velocities less than 100 cm/h, i.e., for velocities where colloid detachment was invariant of interface velocity. The first interface passage (receding-1) had only a small

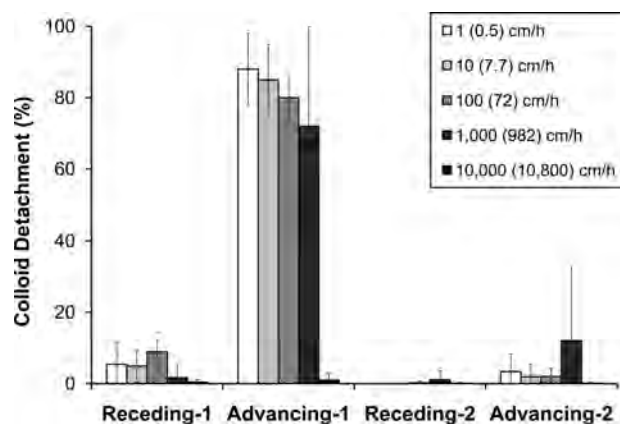


Figure 7. Percentage of colloid detachment for successive interface movements at different interface velocities. Bars are arithmetic means and lines represent \pm one standard deviation. The numbers in parentheses are the measured velocities of the air–water interface.

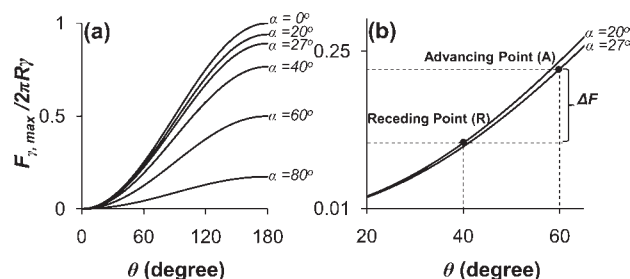


Figure 8. Maximum detachment force (eq 2, in dimensionless form ($F_{\gamma, \max}/(2\pi R\gamma)$)) exerted by an air–water interface acting on a colloid deposited on glass-channel surface as a function of colloid–air–water contact angle (θ) and glass–air–water contact angle (α). (a) Full view, and (b) detailed view showing the regions of θ and α in our experiments (see Table 1).

effect on colloid detachment: only about 5–10% of the attached colloids were detached (Figure 7). Most colloids were then detached by the first advancing interface passage (advancing-1) (80–88% (Figure 7)). The subsequent second receding interface (receding-2) caused almost no further colloid detachment, while the second advancing interface (advancing-2) again detached significant, but small, amounts of colloids (2–3%).

Comparison of Experimental Results with Theory. With the exception of the 10 000 cm/h velocity, the advancing air–water interfaces were always more effective in detaching colloids than were the receding interfaces. On the basis of theory, it is indeed expected that the surface tension force causing detachment (eq 2) is larger for an advancing interface than for a receding interface for our experimental system. Figure 8a shows the maximum detachment force in dimensionless form as a function of the contact angles θ (colloid–air–water) and α (glass–air–water). The contact angles θ and α have opposite effects on the detachment force. This behavior is not because the surface tension force itself decreases with increasing α , but because the angle of the force vector changes (see Figure 2). Increasing α will decrease the vertical component of the surface tension vector.

Figure 8b shows a magnification of the area of interest for our experiments. At a receding contact angle $\theta = 40^\circ$ and $\alpha = 20^\circ$,

Table 2. Forces Exerted on the Colloids during Passage of Advancing and Receding Air–Water Interfaces^a

forces	receding air–water interface (μN)	advancing air–water interface (μN)
F_{DLVO} at 0.1 nm separation	3.14×10^{-2}	3.14×10^{-2}
$F_{\gamma,\text{max}}$ (vertical component)	2.49×10^{-2}	5.05×10^{-2}
$F_{\gamma,\text{max}}$ (horizontal component)	9.07×10^{-3}	2.58×10^{-2}
$F_{s,\text{max}}$ at 0.5 cm/h	1.99×10^{-8}	1.99×10^{-8}
$F_{s,\text{max}}$ at 7.7 cm/h	3.06×10^{-7}	3.06×10^{-7}
$F_{s,\text{max}}$ at 72 cm/h	2.87×10^{-6}	2.87×10^{-6}
$F_{s,\text{max}}$ at 982 cm/h	3.91×10^{-5}	3.91×10^{-5}
$F_{s,\text{max}}$ at 10 800 cm/h	4.30×10^{-4}	4.30×10^{-4}

^a Forces were calculated with eqs 2, 3, and 4.

when the first interface passes over the colloids (point R), the dimensionless detachment force is $F_{\gamma,\text{max}}/(2\pi R\gamma) = 0.11$, but when the advancing interface passes (point A, where $\theta = 60^\circ$ and $\alpha = 27^\circ$), the detachment force increases to $F_{\gamma,\text{max}}/(2\pi R\gamma) = 0.22$, which constitutes an increase of 50%.

Table 2 summarizes the quantification of forces exerted on colloids during the passage of receding and advancing air–water interfaces. The DLVO and hydrodynamic forces, F_{DLVO} and $F_{s,\text{max}}$ are not a function of receding and advancing contact angles, and therefore are the same during receding and advancing events. For the vertical component of $F_{\gamma,\text{max}}$ which is opposite in direction to F_{DLVO} , the advancing $F_{\gamma,\text{max}}$ exceeded the F_{DLVO} by about 38% while the receding $F_{\gamma,\text{max}}$ was 21% less than F_{DLVO} . These force calculations corroborate our experimental results, i.e., most colloids were detached during passage of the advancing interface, but less than 1% during that of the receding interface (Figure 7). The horizontal component of $F_{\gamma,\text{max}}$ is smaller than F_{DLVO} and does not contribute to the detachment force because its direction is normal to F_{DLVO} . The hydrodynamic force $F_{s,\text{max}}$ increases linearly with air–water interface velocity, but was negligible relative to the other forces. Indeed, our experiments showed less than 1% colloid removal at the highest air–water interface velocity of 10 000 cm/h (Figure 6).

As the velocity increases, the water film thickness separating the air bubble from the channel wall increases (Figure 9). Depicted in Figure 9 are also the film thicknesses at our experimental velocities. At the three lowest velocities, the film thicknesses are all smaller than the colloid diameters, indicating that the colloids will form an air–water–solid interface with the air bubble. At a velocity of 1000 cm/h, the film thickness is larger than the colloid radius, but of similar magnitude, whereas at 10 000 cm/h, the film thickness is an order of magnitude larger than the colloid diameter. This suggests that at a velocity of 10 000 cm/h, there will be no air–water–colloid interface forming, and consequently, no colloids will be removed, as there exists no detaching surface tension force. This is corroborated by our experimental results. At a velocity 1000 cm/h, theoretically, no colloids should be removed either, but our experimental results show that colloids were removed. The amount of colloids removed was not as large as for the lower three velocities, but still,

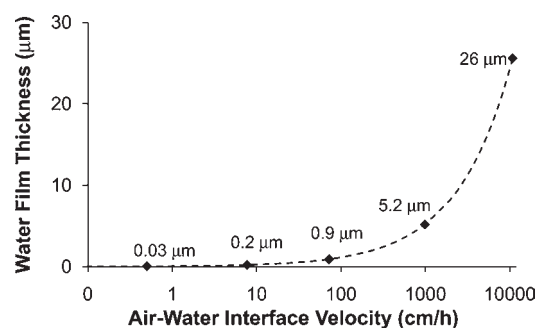


Figure 9. Water film thickness as a function of the velocity of the air–water interface. Dashed line is calculated with eq 5, symbols represent our experimental air–water interface velocities and the numbers show the corresponding water film thickness.

there was no significant difference in removal between the lower three and the 1000 cm/h velocity. We attribute this result to the fact that the colloid diameter and the film thickness at 1000 cm/h are of similar magnitude.

For colloids to be removed by an air–water interface, a colloid–air–water interface has to be formed. The critical time scales for this process are the contact time t_c and the induction time t_i (eqs 6 and 7). The contact times in our experiments were from 0.03 to 720 ms, depending on the interface velocity, whereas the induction times were on the order of 10^{-9} ms. Although the induction time, because of its empirical nature, may not be taken as an absolute value, it was several orders of magnitude smaller than the contact time, indicating that the film thinning, film rupture, and formation of the three-phase contact line was not a rate-limiting step. Overall, the theoretical calculations corroborate the experimental results, although the absolute calculations need to be considered approximate due to uncertainties in DLVO separation distances and contact angle measurements.

5. IMPLICATIONS

Moving air–water interfaces are of importance in many natural phenomena. Examples reach from sliding and rolling water droplets on leaves to the movement of water in porous media. The strong interaction of the air–water interface with colloids and particles has led to several industrial applications where moving air–water interfaces are used for colloid removal and particle separation.

Our results show the predominance of the advancing air–water interface movement over the receding interface movement on the detachment of deposited, hydrophilic colloids. Only in the special case where the colloid–air–water contact angle hysteresis is small compared to the channel–air–water contact angle hysteresis can the advancing interface movement become more dominant for hydrophilic colloids. On the basis of microscopic visualizations and pertinent theory, we can generalize the effects of advancing and receding air–water interface movements on detachment of deposited colloids. Theoretical analysis shows that the detachment force (surface tension force) is dependent on the combination of the colloid–air–water and glass–air–water contact angles.

■ ASSOCIATED CONTENT

S Supporting Information. A table showing colloid removal at different interface velocities and air–water interface

stages, including the results of the statistical significance tests. This material is available free of charge via the Internet at <http://pubs.acs.org>.

AUTHOR INFORMATION

Corresponding Author

*Markus Flury, Department of Crop and Soil Sciences, Washington State University, Pullman, WA 99164-6420. Phone: 1-253-445-4522. E-mail: flury@wsu.edu.

ACKNOWLEDGMENT

This material is based upon work supported by the U.S. Department of Energy, Office of Science (BER), under Award No. DE-FG02-08ER64660. We thank the WSU Franceschi Microscopy Center for access to their facility and Chris Davitt for help with the use of the confocal microscope.

REFERENCES

- (1) Barthlott, W.; Neinhuis, C. *Phys. Today* **1997**, *202*, 1–8.
- (2) Zhang, J.; Sheng, X.; Jiang, L. *Langmuir* **2009**, *25*, 1371–1376.
- (3) Neinhuis, C.; Barthlott, W. *Ann. Bot.* **1997**, *79*, 667–677.
- (4) Koch, K.; Neinhuis, C.; Ensikat, H. J.; Barthlott, W. *J. Exp. Bot.* **2004**, *55*, 711–718.
- (5) Fürstner, R.; Barthlott, W.; Neinhuis, C.; Walzel, P. *Langmuir* **2005**, *21*, 956–961.
- (6) Leenaars, A. F. M.; O'Brien, S. B. G. *Philips J. Res.* **1989**, *44*, 183–209.
- (7) Dai, Z.; Fornasiero, D.; Ralston, J. J. *Colloid Interface Sci.* **1999**, *217*, 70–76.
- (8) Min, Q.; Duan, Y.; Peng, X.; Mujumdar, A. S.; Hsu, C.; Lee, D. *Drying Technol.* **2008**, *26*, 985–995.
- (9) Zhuang, J.; McCarthy, J. F.; Tyner, J. S.; Perfect, E.; Flury, M. *Environ. Sci. Technol.* **2007**, *41*, 3199–3204.
- (10) Shang, J.; Flury, M.; Chen, G.; Zhuang, J. *Water Resour. Res.* **2008**, *44*, W06411, doi:10.1029/2007WR006516.
- (11) Sharma, P.; Abdou, H.; Flury, M. *Vadose Zone J.* **2008**, *7*, 930–940.
- (12) McCarthy, J. F.; Zachara, J. M. *Environ. Sci. Technol.* **1989**, *23*, 496–504.
- (13) Kretzschmar, R.; Borkovec, M.; Grolimund, D.; Elimelech, M. *Adv. Agron.* **1999**, *66*, 121–193.
- (14) Flury, M.; Mathison, J. B.; Harsh, J. B. *Environ. Sci. Technol.* **2002**, *36*, 5335–5341.
- (15) Huh, C.; Mason, S. G. *J. Colloid Interface Sci.* **1974**, *47*, 271–289.
- (16) Pitois, O.; Chateau, X. *Langmuir* **2002**, *18*, 9751–9756.
- (17) Shang, J.; Flury, M.; Deng, Y. *Water Resour. Res.* **2009**, *45*, W06420, doi:10.1029/2008WR007384.
- (18) Noordmans, J.; Wit, P. J.; van der Mei, H. C.; Busscher, H. J. *J. Adhesion Sci. Technol.* **1997**, *11*, 957–969.
- (19) Gomez-Suarez, C.; Noordmans, J.; van der Mei, H. C.; Busscher, H. J. *Langmuir* **1999**, *15*, 5123–5127.
- (20) Gomez-Suarez, C.; Noordmans, J.; van der Mei, H. C.; Busscher, H. J. *Phys. Chem. Chem. Phys.* **1999**, *1*, 4423–4427.
- (21) Gomez-Suarez, C.; van der Mei, H. C.; Busscher, H. J. *J. Adhes. Sci. Technol.* **2000**, *14*, 1527–1537.
- (22) Gomez-Suarez, C.; Noordmans, J.; van der Mei, H. C.; Busscher, H. J. *Colloids Surf.* **2001**, *186*, 211–219.
- (23) Sharma, P.; Flury, M.; Zhou, J. *J. Colloid Interface Sci.* **2008**, *326*, 143–150.
- (24) Saiers, J. E.; Lenhart, J. J. *Water Resour. Res.* **2003**, *39*, 1019, doi:10.1029/2002WR001370.
- (25) Saiers, J. E.; Hornberger, G. M.; Grower, D. B.; Herman, J. S. *Geophys. Res. Lett.* **2003**, *30*, 2083, doi:10.1029/2003GL018418.
- (26) Cheng, T.; Saiers, J. E. *Water Resour. Res.* **2009**, *45*, W08414, doi: 10.1029/2008WR007494.
- (27) Hunter, R. J. *Zeta Potential in Colloid Science*; Academic Press: London, 1981.
- (28) Shang, J.; Flury, M.; Harsh, J. B.; Zollars, R. L. *J. Colloid Interface Sci.* **2008**, *328*, 299–307.
- (29) Decker, E. L.; Frank, B.; Suo, Y.; Garoff, S. *Colloids Surf. Physicochem. Eng. Aspects* **1999**, *156*, 177–189.
- (30) Lazouskaya, V.; Jin, Y.; Or, D. *J. Colloid Interface Sci.* **2006**, *303*, 171–184.
- (31) NIH, *ImageJ*; National Institute of Health: on-line at <http://rsb.info.nih.gov/ij>, accessed in June, 2010, 1999.
- (32) Haines, W. B. *J. Agric. Sci.* **1930**, *20*, 97–116.
- (33) Morrow, N. R. *Ind. Eng. Chem.* **1970**, *62*, 32–56.
- (34) Gauglitz, P. A.; Laurent, C. M. S.; Radke, C. J. *Ind. Eng. Chem.* **1988**, *27*, 1282–1291.
- (35) Gauglitz, P. A.; Radke, C. J. *AIChE J.* **1989**, *35*, 230–240.
- (36) SAS Institute Inc., *SAS/STAT User's Guide, Vers. 6*, 4th ed.; SAS Institute Inc.: Cary, NC, 1990; Vol. 2.
- (37) Scheludko, A.; Toshev, B. V.; Bojadjev, D. T. *J. Chem. Soc., Faraday Trans. 1* **1976**, *72*, 2815–2828.
- (38) Preuss, M.; Butt, H. *Langmuir* **1998**, *14*, 3164–3174.
- (39) Sharma, M. S.; Chamoun, H.; Sita Rama Sarma, D. S. H.; Schechter, R. S. *J. Colloid Interface Sci.* **1992**, *149*, 121–134.
- (40) Bretherton, F. P. *J. Fluid Mech.* **1961**, *10*, 166–188.
- (41) Nguyen, A.; Schulze, H. *Colloidal Science of Flotation*; Marcel Dekker: New York, 2004.
- (42) Schulze, H. *Miner. Process. Extract. Met. Rev.* **1989**, *5*, 43–76.
- (43) Albijanic, B.; Ozdemir, O.; Nguyen, A.; Bradshaw, D. *Adv. Colloid Interface Sci.* **2010**, *159*, 1–21.
- (44) Song, L.; Johnson, P. R.; Elimelech, M. *Environ. Sci. Technol.* **1994**, *28*, 1164–1171.
- (45) Ryan, J. N.; Elimelech, M. *Colloids Surf. Physicochem. Eng. Aspects* **1996**, *107*, 1–56.
- (46) Wit, P. J.; Busscher, H. J. *J. Colloid Interface Sci.* **1998**, *208*, 351–352.
- (47) Weroni, P.; Elimelech, M. *J. Colloid Interface Sci.* **2008**, *319*, 406–415.

—**Supporting Information**—

Detachment of deposited colloids by advancing and receding air-water
interfaces

Surachet Aramrak, Markus Flury, James B. Harsh

Table A. Colloid detachment (%) from a glass surface after the passages of air-water interfaces.

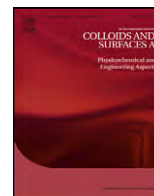
	Colloid detachment (%) at different velocities				
	1	10	100	1000	10000
	(0.5)*	(7.7)	(72)	(982)	(10,800)
	(cm/h)				
Initial state	0 Aa	0 Aa	0 Aa	0 Aa	0 Ab
Flow (no bubble)	0Aa	0.01 ± 0.01 Aa	0.01 ± 0.01 Aa	0.02 ± 0.02 Aa	0.02 ± 0.03 Ab
After receding-1	5 ± 6 Aa	5 ± 5 Aa	9 ± 6 Aa	2 ± 4 Aa	0.4 ± 0.7 Ab
After advancing-1	88 ± 10 Ba	85 ± 10 Ba	80 ± 6 Ba	72 ± 28 Ba	1 ± 2 Bb
After receding-2	0 Aa	0 Aa	0.2 ± 0.5 Aa	1 ± 2 Aa	0.1 ± 0.3 Ab
After advancing-2	3 ± 5 Aa	2 ± 4 Aa	2 ± 2 Aa	12 ± 21 Aa	0.1 ± 0.3 Ab

* Numbers in parentheses are measured velocities. Data represent means and standard deviations measured from 12 replications. Different capital letters (A, B, and C) indicate statistical differences column-wise; and different lower cases (a, b, and c) indicate statistical differences row-wise; both at $\alpha = 0.01$.



Contents lists available at ScienceDirect

Colloids and Surfaces A: Physicochemical and Engineering Aspects

journal homepage: www.elsevier.com/locate/colsurfa

Contact angles of aluminosilicate clays as affected by relative humidity and exchangeable cations

Jianying Shang^a, Markus Flury^{a,b,*}, James B. Harsh^a, Richard L. Zollars^c

^a Department of Crop and Soil Sciences, Washington State University, Pullman, WA 99164, USA

^b Department of Biological Systems Engineering, Washington State University, Pullman, WA 99164, USA

^c Voiland School of Chemical Engineering and Bioengineering, Washington State University, Pullman, WA 99164, USA

ARTICLE INFO

Article history:

Received 2 May 2009

Received in revised form 31 August 2009

Accepted 10 October 2009

Available online 17 October 2009

Keywords:

Colloids

Contact angle

Clay minerals

Cations

Relative humidity

ABSTRACT

Contact angles of aluminosilicate clays are difficult to determine. Not only does their small particle size present measurement difficulties, but contact angles may vary with relative humidity and cation composition. In this paper, we determined the effects of relative humidity and exchangeable cations on contact angles of three aluminosilicate clays (smectite, kaolinite, illite). Contact angles were measured on clay films with the sessile drop method under different relative humidity (19, 33, 75, 100%), and with clays saturated either with Na, K, Mg, or Ca. The results showed that the water contact angles on smectite increased with relative humidity between 19 and 75%, but for kaolinite and illite, little differences in water contact angles between 19 and 75% relative humidity were observed. For all three clays, however, the water contact angles decreased at 100% relative humidity as compared to the lower relative humidities. Cations affected not only the adsorption of water but also the surface charge, and both factors influenced the contact angles of the clays. Negligible effect of the different cations Na⁺, K⁺, Mg²⁺, or Ca²⁺ on contact angles was observed.

© 2009 Elsevier B.V. All rights reserved.

1. Introduction

Subsurface colloids are small, discrete solid particles indigenously present in subsurface natural porous media, which can be mobilized by means of surface and hydrodynamic forces [1]. Colloidal particles generally have dimensions between 1 nm and 2 μm [2,3]. They possess an electric surface charge, and are typically smaller than inter-granular pores in natural porous media, such as soils and sediments. In soils and sediments, there exist a variety of inorganic and organic colloidal particles, including aluminosilicate clays, oxides, hydroxides, viruses, bacteria and protozoans, and natural organic matter [4].

Inorganic colloids influence contaminant fate in soils and geological media. Colloids can facilitate the transport of contaminants [5–9]. Whether or not colloids move through the subsurface, depends on their surface properties. The surface properties of colloids control their wettability, flocculation–dispersion, ion exchange, sorption, flotation, and transport [10]. Interfacial interactions are governed, among other factors, by contact angle and surface free energy.

Contact angles are particularly important when colloidal particles are interacting with the air–water interface, such as during transport in water-unsaturated porous media or during flotation processes. When an air–water–solid interface line forms on a colloid, strong capillary forces pin colloids to the air–water interface, and the absolute magnitude of the force depends on the contact angle [11–14]. For transport of colloids in water-unsaturated porous media, the capillary force is generally the dominant force acting on the colloids [15–17].

Determining contact angles is challenging because contact angle measurement are affected by many factors, including temperature [18–21], water content [21–24], relative humidity [25], organic matter [26], particle size [21], surface roughness [27–29], surface heterogeneity [30–32], presence of hydrophobic organic compounds [10], and surface cations [33,34]. For aluminosilicate clays, the pretreatment is also important, as clays often have organic compounds and different cations associated with them [35–38]. The presence of organic materials in clays tends to increase the water contact angle [39–41].

Many surfaces possess a surface roughness or have a porous structure, both of which can affect the contact angle measurements. The use of conventional Wilhelmy plate and Washburn wicking methods to determine contact angles of porous materials has been critically reviewed and found to yield erroneous measurement results [42,43]. Similarly, surface roughness can lead to the establishment of a non-equilibrium contact angle, where

* Corresponding author at: Department of Crop and Soil Sciences, Washington State University, Pullman, WA 99164, USA. Tel.: +1 509 335 1719; fax: +1 509 335 8674.

E-mail address: flury@wsu.edu (M. Flury).

the air–water–solid contact line is pinned at surface irregularities, thereby preventing the liquid–air interface to reach the thermodynamic energy minimum [44]. Della Volpe et al. [44] proposed to mechanically disturb the measurement system by using a loud-speaker to force the system to reach the energy minimum, thereby establishing the stable equilibrium contact angle. This method of establishing the equilibrium contact angle is also called vibration-induced equilibrium contact angle, and can be used for both the Wilhelmy plate [44] as well as the sessile drop method [45,46].

It has been argued that most Wilhelmy plate and sessile drop measurements on rough surfaces have yielded non-equilibrium contact angles [44]. Della Volpe et al. [44] reported that roughnesses as low as $R_a = 3.3$ nm, where R_a is the arithmetic mean deviation of the vertical profile, caused non-equilibrium contact angles. This suggests that surface roughness is likely going to affect contact angle measurements for most surfaces. Meiron et al. [45] experimentally measured apparent contact angles and calculated ideal contact angles calculated from the Wenzel equation for water and ethylene glycol on a model surface (wax coated abrasive paper), and found the contact angles to be equal for surface roughness of $R_a = 1.3$ μm , suggesting that a surface with such a roughness could be considered smooth with respect to an equilibrium contact angle [45]. The critical surface roughness when roughness is affecting contact angle is likely dependent on the specific material used [47–49].

Shang et al. [49] compared sessile drop, Wilhelmy plate, thin-layer wicking, and column wicking methods to determine contact angles of clay minerals, and found deviations in contact angles ranging from 10° to 40° for the same clays. The results from the dynamic sessile drop method showed that the surface roughness of smectite, kaolinite, and illite had little influence on contact angles, whereas hematite showed a pronounced slip/stick pattern caused by pinning of the contact line at the rough surface [49].

Aluminosilicate clays often have a structural negative charge that is balanced by exchangeable cations. The nature of these cations changes the contact angle of the clays. Janczuk et al. [50] studied the effects of adsorbed H^+ , Na^+ , K^+ , Ca^{2+} , Mg^{2+} , Ba^{2+} , and Al^{3+} on contact angles and surface wettability of kaolinite. Contact angles ranged from 15° to 28° for water and from 21° to 34° for diiodomethane. The dispersion components coupled with different cations were not significantly different, and the non-dispersion components were affected by the type of cations due to the entropy of hydration of various ions. There were some deviations of Ba^{2+} and K^+ from the dependence between the nondispersion component and hydration energy of the ions. Similar results were also founded for bentonite, which is a mixture of clay minerals (montmorillonite, mica, feldspar and other minerals) [50]. Giese and van Oss [33] measured contact angles for smectite clays that were saturated with different cations (Li, Na, K, NH_4 , Ca, Mg, Ba, Cs, Sr) and determined surface free energy components. The authors did not report contact angles per se, but listed surface free energy components calculated from contact angles. They found that the Lifshitz–van der Waals component γ_{LW} was similar among different types of smectites and different cations on the surface. Overall, no systematic trends of surface free energy components with regard to the type of cation on the surface were observed [33]. As the cation type may affect test liquid adsorption, surface micropores, cation hydration, and surface charge density, contact angles, which were generally used to quantify surface energy, may not reflect the true surface energy [51].

The effects of cations and anions on contact angles and surface free energies of cholesterol have been studied by Chibowski et al. [34]. The presence of cations and anions increased polar acid–base interactions, especially the electron-donor component of the surface free energy, and the contact angle decreased compared to when ions were absent. Chibowski et al. interpreted this as a consequence of the presence of a hydration shell around the ions.

When the surface shows roughness, it is difficult to separate the effects of surface roughness and surface chemistry. A way to separate the effects of surface roughness and surface chemistry is to use molecularly smooth surfaces. Nishimura et al. [52] used cleaved muscovite mica, and determined contact angles for different cation treatments. They found that freshly cleaved mica had a smaller water contact angle ($< 10^\circ$) than cation-treated mica. The contact angles followed the sequence Li (10 – 15°), Mg (10 – 20°), and H and K (30 – 35°). The contact angle of a smooth solid surface, like freshly cleaved mica, is not only related to vapor pressure but also affected by the structure and properties of the adsorbed water film at the solid/gas interface [53].

Aluminosilicate clays associate with water molecules, and the amount of water and the thickness of the water films on the clay surfaces is controlled, in part, by the vapor pressure or relative humidity of the surrounding atmosphere [54,55]. It is expected that increasing water association with the clays will lower the water–solid contact angle [25]. Chassin et al. [25] equilibrated smectite at different relative humidity and determined contact angles with the sessile drop method. They found that adsorbed water molecules on the clay surface modified the free surface energy of the clay, and the higher the relative humidity, the lower were the contact angles. Similar results were reported for peat material, where contact angles decreased with increasing relative humidity [56].

The effects of cations and relative humidity on contact angle have been studied mainly for smectite clay, but little consideration has been given to the effects of the pretreatment of the clays and to different types of clays. In this study, we therefore focused on investigating the effects of pretreatment, adsorbed cations, and relative humidity on contact angles of three typical aluminosilicate clays: smectite, kaolinite, and illite. We saturated the clays with Na^+ , K^+ , Mg^{2+} , or Ca^{2+} and adjusted the relative humidity to 19, 33, 75, or 100%. We measured contact angles as a function of time by using the static sessile drop method.

2. Materials and methods

2.1. Clay minerals

We used three aluminosilicate clays: Arizona smectite (SAz1), Georgia kaolinite (KGA1b), and illite. The smectite and kaolinite were obtained from the Clay Minerals Repository (University of Missouri), and illite (No. 36, Morris, Illinois) from Ward's Natural Science (Rochester, NY). The clays, as received from the suppliers, were fractionated by gravity sedimentation in a sodium hexametaphosphate solution (0.5 g/L) to obtain particles smaller than 2 μm in diameter. Selected general properties of the clays used in this study are shown in Table 1. The particle shapes were determined by transmission electron microscopy (JEOL 1200EX TEM) (Fig. 1).

2.2. Pretreatment of clays and saturation with different cations

Subsamples of the size-fractionated clays were then treated to remove organic matter with H_2O_2 and to remove iron oxides using the citrate–dithionite method [57]. After these pretreatments, we lowered the pH of the clay suspensions to 4 by titration with 0.1 M HCl to remove acid-soluble impurities. The pH 4 suspensions were shaken for 3 h, and the supernatant decanted after centrifugation. This procedure was repeated three times. Then, the clay suspensions were washed with deionized water by shaking the suspensions for 3 h followed by centrifugation and decantation. This washing procedure was repeated until the suspensions reached pH 6.

Finally, the clays were saturated with Na, K, Mg, or Ca by treating with 1 M NaCl, 1 M KCl, 0.5 M MgCl_2 , or 0.5 M CaCl_2 , respectively.

Table 1
General properties of aluminosilicate clays used in this study.

Clay type	Origin/designation	Layer charge per half unit-cell (elementary charge, <i>e</i>)	CEC (cmol _c /kg)	<i>d</i> -spacing (nm)	Mineral composition
Smectite ^{a,c}	SAz-1	0.25–0.40	70–110	1.3–1.6	98% smectite [1% quartz, 1% other]
Kaolinite ^{b,c}	KGa-1b	< 0.01	1–10	0.7	96% kaolinite and trace dickite [3% anatase, 1% crandallite+mica and/or illite]
Illite ^{a,c}	Morris No. 36	0.60–0.90	160–230	1	na ^d

^a Mermut and Lagaly [70].^b Auerbach [71].^c Chipera and Bish [72].^d na: values not available.

The suspensions were shaken for 3 h, centrifuged, supernatant decanted, and the clays dialyzed in deionized water until the electrical conductivity of the dialysate was about 1 μS/cm [58]. With these pretreatments, we obtained two types of size-fractionated (< 2 μm) clays: (1) non-treated clays as obtained from the supplier, and (2) clays saturated with Na, K, Mg, or Ca, and dialyzed to 1 μS/cm, pretreated to remove OM, Fe, and acid-soluble impurities. All clays were stored in concentrated suspensions at room temperature until use.

Treatment-specific characteristics of the clays are shown in Table 2. Average hydrodynamic particle size and electrophoretic mobility were measured by dynamic light scattering using a Zeta-sizer 3000HAS (Malvern Instruments Ltd., Malvern, UK).

2.3. X-ray diffraction

The K-saturated smectite was analyzed by X-ray diffraction to determine interlayer characteristics (Philips XRG 3100 diffractometer equipped with a graphite monochromator and with Cu-K α radiation, Philips Analytical Inc., Mahwah NJ). X-ray diffraction patterns were recorded at room temperature and after heating the clay to 100 and 300 °C.

2.4. Preparation of clay films

Diluted stock suspensions (with deionized water) were used to coat microscope cover glass slides (2.2 cm × 2.2 cm) with clays following the procedure described by Wu [59]. The slides were first

cleaned with acetone and water, and then covered with a drop of 1.5 mL clay suspension (1–2%, w/v). The suspension was then evaporated for 2 days under laminar air flow at 20 °C. The relative humidity of the laboratory air during air-drying was about 33%.

2.5. Control of relative humidity

After air-drying, the clay-coated slides were placed into air-tight plastic boxes (volume 900 mL), in which we controlled the relative humidity at 19, 33, 75, and 100%. Humidity control was achieved by placing a beaker of silica gel desiccant, saturated MgCl₂ solution, saturated NaCl solution, or deionized water, respectively, into the box. The system was equilibrated for several days. The relative humidity was monitored by a humidity meter (Model 445814, Extech Instruments, Waltham, MA), which indicated the vapor pressure reached equilibrium after 3 h.

Aliquots of the equilibrated clay samples were removed and analyzed for their disjoining pressure using a WP4 dewpoint meter (Decagon Devices, Pullman, WA). Relative humidities and disjoining pressures of equilibrated clays are shown in Table 3. Water contents and *d*-spacings of smectite clays for different cation saturations, with data collected from the literature, are summarized in Table 4.

2.6. Electron microscopy

The clay films were examined with a field emission scanning electron microscope (FEI-Quanta 200F, FEI Company, Hillsboro, OR)

Table 2
Treatment-specific characteristics of aluminosilicate clays.

Minerals	Particle size ^a (nm)	Electrophoretic mobility ^b (μm s ⁻¹)/(V cm ⁻¹)	Particle shape ^c
Non-treated clays			
Non-treated smectite	446 ± 7	-1.21 ± 0.01	Irregular thin flakes
Non-treated kaolinite	364 ± 1	-1.70 ± 0.02	Hexagonal platy
Non-treated illite	541 ± 3	-1.50 ± 0.01	Irregular platy
Smectite dialyzed to 1 μS/cm			
Na-smectite	747 ± 57	-2.91 ± 0.03	Irregular thin flakes
K-smectite	817 ± 177	-2.97 ± 0.02	Irregular thin flakes
Mg-smectite	1031 ± 15	-1.27 ± 0.03	Irregular thin flakes
Ca-smectite	1069 ± 198	-1.12 ± 0.01	Irregular thin flakes
Kaolinite dialyzed to 1 μS/cm			
Na-kaolinite	1019 ± 159	-2.64 ± 0.06	Hexagonal platy
K-kaolinite	1145 ± 118	-1.11 ± 0.16	Hexagonal platy
Mg-kaolinite	1085 ± 110	-0.88 ± 0.07	Hexagonal platy
Ca-kaolinite	1280 ± 43	-0.24 ± 0.01	Hexagonal platy
Illite dialyzed to 1 μS/cm			
Na-illite	742 ± 58	-3.26 ± 0.04	Irregular platy
K-illite	579 ± 68	-3.14 ± 0.05	Irregular platy
Mg-illite	858 ± 48	-1.69 ± 0.06	Irregular platy
Ca-illite	915 ± 181	-1.58 ± 0.05	Irregular platy

± denotes one standard deviation.

^a Measured by dynamic light scattering.^b Measured in deionized water, 0.1 mM NaCl, KCl, MgCl₂ and CaCl₂ electrolyte background for the corresponding clays, respectively.^c Determined by electron microscopy (TEM).

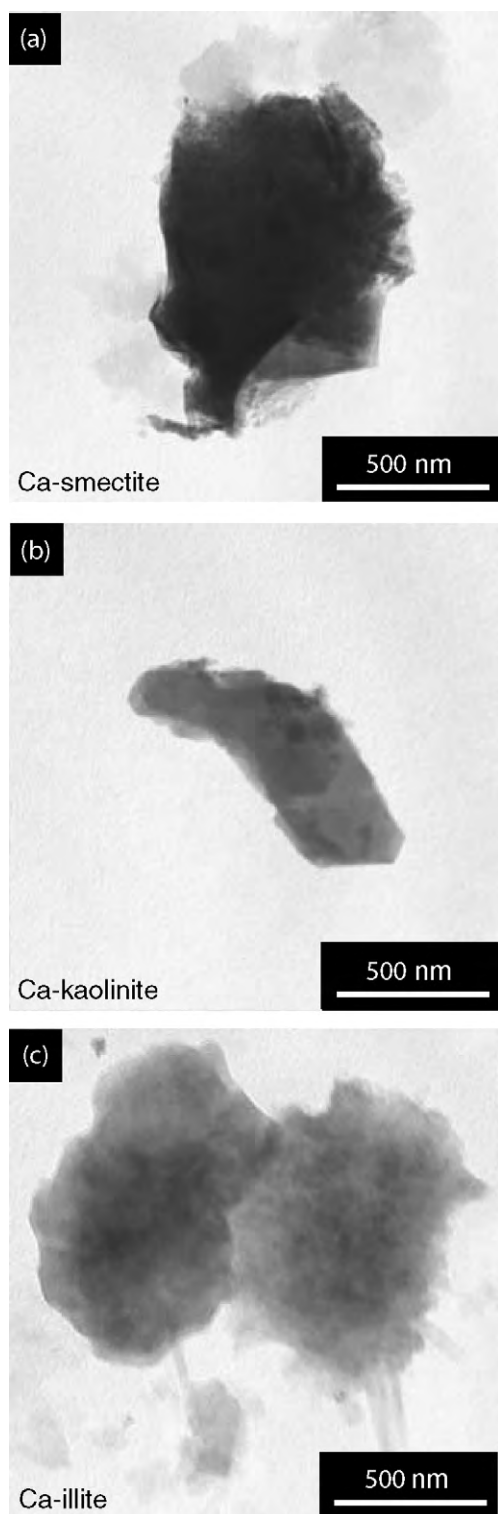


Fig. 1. Transmission electron micrographs of the aluminosilicate clays: (a) Ca-smectite, (b) Ca-kaolinite, and (c) Ca-illite.

under controlled relative humidity. The conditions in the microscope chamber were set to $-1\text{ }^{\circ}\text{C}$, and the desired vapor pressures of water were set to 19, 33, 75, and 100% relative humidity, respectively. The films for non-treated and Ca-saturated clays are shown in Fig. 2. The pictures for the Ca-saturated clays at different relative humidity were taken with the same specimen, without moving the microscope stage, so that the view remained the same. At 19% relative humidity, there was little structure visible, and the

surfaces appeared smooth. As relative humidity was increased, more surface structure appeared, but at 100% relative humidity, the surfaces appeared smoother again. Smectite swells as relative humidity increases, and it appears that the initial swelling caused the film surface to become rougher, but at complete swelling, the surface was smoothed out again. For kaolinite and illite, the 19% relative humidity sample appeared to be the smoothest; more surface roughness was visible for the 33, 75, and 100% relative humidity samples. For all clays, the films of the non-treated clays showed more surface structure than the films of the treated clays.

2.7. Contact angle measurements

Static contact angles were determined with the sessile drop method using a digital goniometer (Drop Shape Analysis System, DSA100, Krüss GmbH, Hamburg, Germany). In a comparative study, we found that the sessile drop method is the preferred method for determining contact angles of smectite, kaolinite, and illite [49]. Our goniometer was equipped with an environmental chamber and a micro-syringe steel needle of 0.5-mm diameter. We placed silica gel or a paper towel soaked with the appropriate salt solution into the environmental chamber to maintain relative humidity. For contact angle measurements, the syringe needle was positioned 0.2 mm from the surface of the clay film, and a drop of the test liquid (2 μL) was dispensed at a constant rate of 105 $\mu\text{L}/\text{min}$. The drop shape was monitored with a digital camera for 20 s, and contact angle, drop diameter, and volume were recorded. Contact angles at 0 s were deemed the most accurate angles, but the evolution of the angles for 20 s was recorded to assess the time-dependency of the measurements, which can reveal fluid imbibition or surface interactions [49]. The contact angle was calculated by the Young–Laplace method (fitting of Young–Laplace equation to the drop shape). The measurements were repeated five times for every sample.

It has been pointed out that contact angle measurements on rough and porous surfaces may not provide the true equilibrium angles, unless the system is triggered into a thermodynamic equilibrium by using vibrational disturbance [44–46]. It is therefore possible that our contact angles do not reflect the true equilibrium contact angles, but the absence of a slip/stick pattern during dynamic contact angle measurements [49] suggests that surface roughness in our samples had little, if any, effect on the contact angle.

2.8. Test liquids

We used polar and apolar liquids for the contact angle measurements: double deionized water (E-pure, Barnstead, electric conductivity $\sim 1\text{ }\mu\text{S}/\text{cm}$), formamide (99.5% purity, from Acros Organics, New Jersey, USA), and diiodomethane ($> 99\%$ purity, from Acros Organics) [49].

3. Results and discussion

3.1. Interlayer characteristics of smectite

The X-ray diffraction patterns indicated that the pretreatment procedure resulted in formation of hydroxy-Al (Al-OH) in the interlayers of smectite. The interlayer spacing reduced from 1.20 nm at room temperature to 1.02 nm at $100\text{ }^{\circ}\text{C}$, indicating a small amount of $\text{Al}_x(\text{OH})_y(3x-y)$ polymer formation in the interlayers. The further reduction of the interlayer spacing to 1.00 nm at $300\text{ }^{\circ}\text{C}$ suggests that the Al-OH interlayer was not extensive.

The electrophoretic mobility data (Table 2) indicate that the surfaces of smectite were free of the Al-OH precipitates, as the electrophoretic mobility of the untreated clays for monovalent ions

Table 3
Relative humidity and disjoining pressures of clays.

Relative humidity (%)		Disjoining pressure (10^5 J/m ³)		Humidity control (at 20 °C)
Measured	Literature ^a	Measured ^b	Calculated ^c	
19	na ^d	< -570 ^e	-2246	Silica gel desiccant Saturated MgCl ₂ solution Saturated NaCl solution Double deionized water
33	33	< -570 ^e	-1500	
75	75	-470	-389	
100	100	-0.5	0	

^a Based on saturated salt solutions from Lide [73].^b Measured with a WP4 dewpoint meter.^c Calculated from relative humidity using the Kelvin equation.^d Data not available.^e Samples were drier than the lowest measurable potential.**Table 4**
Water content and *d*-spacing of smectite saturated with different cations at different relative humidity (RH).

RH (%) (at 20–30 °C)	Water adsorption (g/g)				RH (%) (at 24.5 °C)	<i>d</i> -spacing (nm) ^d			
	Na ^{a,b}	K ^a	Mg ^b	Ca ^{a,b,c}		Na	K	Mg	Ca
19	0.06–0.067	0.035	0.307	0.15–0.21	Oven dry	1.004	1.050	1.300	1.220
33	0.1	0.055	0.33	0.19–0.24	15	1.263	1.211	1.414	1.328
75	0.19–0.21	0.28	0.43	0.30–0.31	31	1.564	1.228	1.608	1.564
94–100	0.28	0.175	0.50	0.31–0.50	88	1.640	1.232	1.639	1.610

^a SAz-1 smectite, saturated with different ions [37].^b SAz-1 smectite, saturated with different ions [74].^c Ca-montmorillonite [25].^d Ca-montmorillonite, sample C3 lamellar repeat distance [75].

was lower than those of the treated clays. This shows that external surfaces of treated smectite were “cleaner”, i.e., more free of impurities than those of the untreated smectite. The Al-OH formed during the pretreatment procedure was apparently confined to the internal surfaces of the clay, and therefore did not affect the external surfaces.

3.2. Effect of relative humidity

To assess the effects of relative humidity on contact angles, we measured contact angles at four different relative humidities (Table 5 and Fig. 3). Overall, we did not observe clear trends in contact angles as a function of relative humidity. However, contact angles with water tended to be lowest at 100% relative humidity. Correspondingly, the contact angles for the apolar diiodomethane were usually highest at 100% relative humidity.

Increasing relative humidity increases the amount of water on the clay surfaces (Tables 3 and 4). At relative humidities of 19, 33, and 75%, the water is likely present as a few molecules hydrating exchangeable cations [60]. It is likely that water is present as

islands rather than a continuous layer [60,61]. Moreover, for smectite the water is initially adsorbed into the interlayer as opposed to the external surfaces; the amount of water adsorbed for different interlayer cations is listed in Table 4. The table indicates that divalent ions, like Ca, cause more water adsorption at a given relative humidity than monovalent ions, like Na and K. Likewise, smaller cations lead to adsorption of more water than larger cations with the same charge. Related to the amount of water adsorbed, the *d*-spacings of smectite for divalent ions are generally larger than for monovalent ions at lower relative humidity. Little difference exists in the *d*-spacing between Mg and Ca [62].

According to Laird [63], water adsorption on smectite occurs initially on internal and external surfaces alike. When the relative humidity increases, water fills the interlayer with a two-layer hydrate structure (relevant to Ca and Mg saturated smectites), then water preferentially hydrates cations on external surfaces, because further expansion of the interlayer is energetically unfavorable [63]. Water at the external surface is clustering around external cations, not forming homogeneous layers [63], which would explain why there is no clear trend in contact angles for water

Table 5
Contact angles (0 s) of aluminosilicate clays for different relative humidity.

Clay mineral	Relative humidity (%)	Contact angle		
		Water (°)	Formamide (°)	Diiodomethane (°)
Ca-smectite	19	37.5 ± 0.9 A	17.2 ± 0.6 A	35.8 ± 1.2 A
	33	42.5 ± 0.4 B	14.4 ± 0.7 B	37.6 ± 0.4 B
	75	47.6 ± 0.9 C	28.1 ± 1.3 C	49.4 ± 0.8 C
	100	35.1 ± 0.7 A	44.7 ± 1.3 D	56.7 ± 0.6 D
Ca-kaolinite	19	19.9 ± 0.7 A	15.9 ± 0.8 A	18.4 ± 0.6 A
	33	17.0 ± 0.5 B	11.0 ± 0.6 B	18.0 ± 0.8 A
	75	20.6 ± 1.0 A	16.9 ± 0.8 A	23.8 ± 0.9 B
	100	17.3 ± 1.3 B	15.4 ± 0.5 A	53.5 ± 1.4 C
Ca-illite	19	28.3 ± 0.6 A	21.3 ± 0.7 A	27.7 ± 1.1 A
	33	26.1 ± 1.4 B	17.2 ± 0.8 B	27.3 ± 1.5 A
	75	24.9 ± 1.5 B	27.4 ± 1.7 C	34.0 ± 1.3 B
	100	21.6 ± 1.2 C	25.6 ± 1.4 C	51.2 ± 1.4 C

± denotes one standard deviation. Letters (A, B, C) denote statistical differences column-wise at a confidence level of 5% (*t*-test); if letters are different between two numbers for a specific clay mineral and for a given test fluid, the values are significantly different.

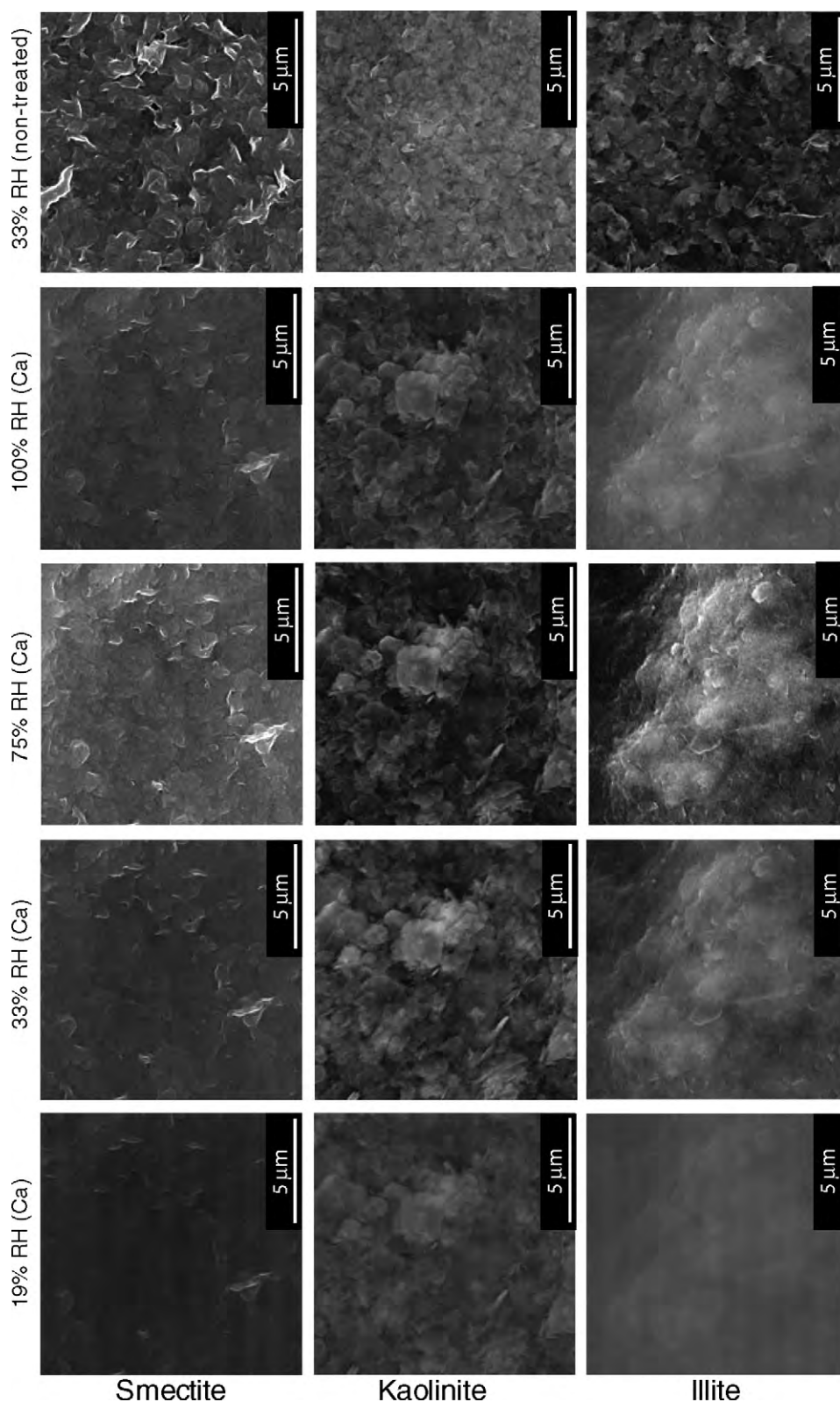


Fig. 2. Field emission scanning electron micrographs of the film surfaces at different relative humidity (RH) for smectite, kaolinite, and illite.

between 20 and 80% relative humidity observed in our experiments (Fig. 3a). The decrease in contact angle only occurs at 100% relative humidity (Fig. 3a), when the external surface is finally covered with a continuous water film.

For kaolinite, adsorption of water occurs via interaction with mineral surface groups ($-OH$) and adsorbing water molecules

encounter a more homogeneous surface (no charge sites/no exchangeable cations). Literature data indicate that adsorption of water on kaolinite is less than 0.018 g/g for relative humidities less than 80%, and 0.108 g/g for a relative humidity of 100% [64,65]. Compared with smectite (0.175–0.50 g/g at 100% relative humidity), kaolinite adsorbs little water (0.108 g/g at 100% relative

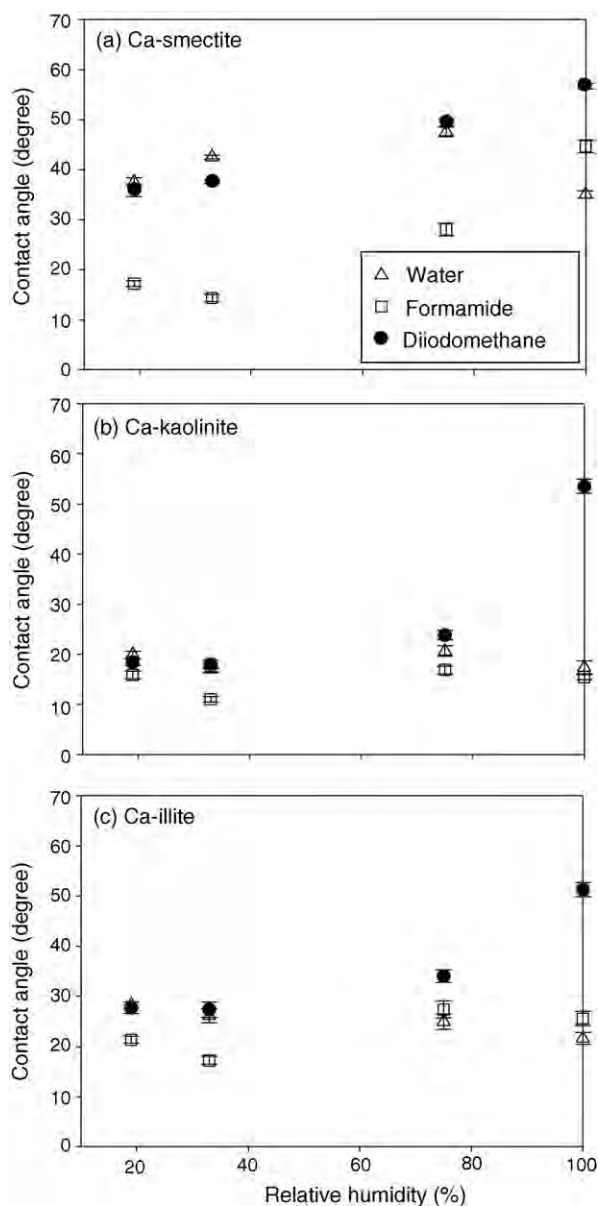


Fig. 3. Initial contact angles (0s) for aluminosilicate clays at different relative humidities. (a) Ca-smectite, (b) Ca-kaolinite, (c) Ca-illite. Error bars indicate \pm one standard deviation.

humidity) [64]. Therefore, we expect less of an effect of the relative humidity on contact angle of kaolinite (Fig. 3b). Reported water contact angles on kaolinite for the sessile drop method were about 18° under saturated water vapor [66,50].

For illite, there is higher charge density, which results in a lower contact angle compared to smectite, and a smaller change of contact angle with increasing water because the surface is more uniform, i.e., has fewer nonpolar regions (Fig. 3c).

The effects of relative humidity and cations on interlayer spacings and water adsorption on smectite are summarized in Table 4. Both interlayer spacing and amount of water adsorbed increase monotonously with relative humidity (Table 4); however, the water contact angles only increase between 19 and 75% relative humidity, and then decrease for 100% relative humidity (Table 5). A similar observation was reported by Chassin et al. [25], who noted that at high relative humidity ($> 90\%$), the properties of the solid are masked by a continuous water film. Chassin et al. [25] categorized the wetting properties of Ca-smectite into three stages: (1) below

Table 6

Contact angles (0s) of aluminosilicate clays for different types of cations at relative humidity 33%.

Clay mineral	Contact angle		
	Water ($^\circ$)	Formamide ($^\circ$)	Diiodomethane ($^\circ$)
Non-treated smectite	23.8 ± 1.7 A	10.8 ± 1.2 A	42.1 ± 2.5 A
Ca-smectite	42.5 ± 0.4 B	14.4 ± 0.7 B	37.6 ± 0.4 B
Na-smectite	39.2 ± 0.6 B	14.3 ± 0.7 B	37.1 ± 0.2 B
K-smectite	38.5 ± 1.0 B	10.1 ± 0.8 A	37.1 ± 1.0 B
Mg-smectite	40.9 ± 0.9 B	10.7 ± 1.1 A	37.6 ± 0.8 B
Non-treated kaolinite	16.9 ± 0.7 A	13.3 ± 1.4 A	21.8 ± 1.7 A
Ca-kaolinite	17.0 ± 0.5 A	11.0 ± 0.8 A	18.0 ± 0.4 B
Na-kaolinite	17.1 ± 1.4 A	12.8 ± 0.8 A	22.6 ± 0.8 A
K-kaolinite	17.1 ± 1.9 A	12.2 ± 0.7 A	21.3 ± 1.8 A
Mg-kaolinite	17.5 ± 1.6 A	12.2 ± 0.8 A	19.3 ± 0.9 A,B
Non-treated illite	34.2 ± 0.9 A	11.9 ± 1.5 A	27.6 ± 1.2 A
Ca-illite	26.1 ± 1.4 B	17.2 ± 0.8 B,C	27.3 ± 1.5 A
Na-illite	24.1 ± 1.5 B	15.8 ± 0.6 C	27.3 ± 1.0 A
K-illite	26.0 ± 1.2 B	19.7 ± 0.5 B	28.0 ± 1.1 A
Mg-illite	23.3 ± 0.7 B	16.8 ± 1.0 B,C	26.5 ± 0.6 A

\pm denotes one standard deviation. Letters (A, B, C) denote statistical differences column-wise at a confidence level of 5% (*t*-test); if letters are different between two numbers for a specific clay mineral, the values are significantly different.

18% relative humidity (water content < 0.15 g/g), the hydration of Ca ions masks the surface oxygen atoms, and both polar and dispersive components of the surface free energy decrease as compared to oven-dry conditions; (2) between 20 and 90% relative humidity (water content 0.2 to 0.5 g/g), increasing water coverage of the surface decreases the dispersive component; and (3) above 90% relative humidity (water content > 0.5 g/g), the adsorbed water approximates that of liquid water in terms of wetting. A similar conceptual model has been presented by Cases et al. [67]. Our experimental data qualitatively corroborate this conceptual model.

3.3. Effect of exchangeable cations

We tested the effect of different cations on contact angles by using a constant relative humidity of 33%. The two different pre-treatments resulted in different composition of the exchangeable cations on the clay surfaces. The non-treated clays contained trace amounts of organic matter, and different types of cations on the surface. For the Ca-saturated clay dialyzed to $1 \mu\text{S}/\text{cm}$, all the exchangeable cations were replaced by Ca.

Electrophoretic mobilities measured for the different treatments shown in Table 2 show an interesting trend: for all clay minerals, the Na-saturated clay had lower (more negative) electrophoretic mobility than the non-treated clays. By and large, the Na-saturated clays also showed lower electrophoretic mobility than other cation saturations; for smectite and illite the Na and K electrophoretic mobility were similar. Saturation with Ca and Mg generally resulted in the highest (least negative) electrophoretic mobility. This effect of bivalent cations on electrophoretic mobility is expected based on their strong attraction to the mineral surfaces, i.e., they form outer sphere complexes with clay surfaces [68].

The contact angle measurements showed good reproducibility, as indicated by small standard deviations ranging from 0.5° to 2.5° (Table 6). The non-treated smectite had significantly smaller water contact angles than the dialyzed smectites. The surface cation composition of the non-treated smectite was 2.2% Mg, 4.0% Ca, 0.047% Na, and 0.16% K [69]. Our water contact angle of 23.8° on the non-treated smectite was similar to the value of 21.8° measured on smectite where no organic matter, Fe, or acid-soluble impurities were removed [59]. On the contrary, non-treated illite had a larger contact angle than the dialyzed illite. The surface cations reported for dry samples were 0.25% Mg, 0.03% Ca, and 0.037% Na [69]. We

found no differences in contact angles among treatments for kaolinite. Generally, we observed little differences in contact angles among the different treatments after dialysis, suggesting that the specific cation on the surface of the clays did not significantly affect contact angles.

The effect of cations was, in part, confounded by the different water contents of the clays. Different cations caused clays to have different water contents at a constant relative humidity (Table 4). The greater the hydration energy of the cation, the larger the water content of the clay (Table 4). Based on the water content, we would expect the contact angles to increase in the following sequence $Mg < Ca < Na < K$. Our experimental data, however, do not follow this trend (Table 6), likely because the differences in water contents are not pronounced enough, or because water structure is as important as water content and cations with more negative hydration energies will alter the structure of the water.

4. Conclusions

Our results showed that contact angles of aluminosilicate clays were little affected by relative humidity between 19 and 75%, but a smaller contact angle was observed at 100%, caused likely by the expansion of the adsorbed water film on the clay surface at 100% relative humidity. The type of exchangeable cations did not cause a significant change in contact angles as cations affect multiple factors related to contact angle. While for illite, the contact angles decreased after the pretreatment, i.e. the mineral became more hydrophilic, the opposite was found for smectite, where the mineral became more hydrophobic after pretreatment. Kaolinite contact angles were not affected by the pretreatment.

References

- [1] T.K. Sen, K.C. Khilar, Review on subsurface colloids and colloid-associated contaminant transport in saturated porous media, *Adv. Colloid Interface Sci.* 119 (2006) 71–96.
- [2] P.C. Hiemenz, R. Rajagopalan, *Principles of Colloid and Surface Chemistry*, 3rd ed., Marcel Dekker, New York, 1997.
- [3] R.J. Hunter, *Foundations of Colloid Science*, 2nd ed., Oxford University Press, Oxford, 2001.
- [4] J.F. McCarthy, L.D. McKay, Colloid transport in the subsurface: past, present, and future challenges, *Vadose Zone J.* 3 (2004) 326–337.
- [5] J.F. McCarthy, J.M. Zachara, Subsurface transport of contaminants, *Environ. Sci. Technol.* 23 (1989) 496–502.
- [6] J.F. McCarthy, C. Degueudre, Sampling and characterization of groundwater colloids for studying their role in the subsurface transport of contaminants, in: J. Buffle, H. van Leeuwen (Eds.), *Environmental Particles*, vol. II, Lewis Publisher, Boca Raton, FL, 1993, pp. 247–315.
- [7] J.F. McCarthy, Colloid-facilitated transport of contaminants in groundwater: mobilization of transuranic radionuclides from disposal trenches by natural organic matter, *Phys. Chem. Earth* 23 (1998) 171–178.
- [8] M. Flury, J.B. Mathison, J.B. Harsh, In situ mobilization of colloids and transport of cesium in Hanford sediments, *Environ. Sci. Technol.* 36 (2002) 5335–5341.
- [9] J. Zhuang, M. Flury, Y. Jin, Colloid-facilitated Cs transport through water-saturated Hanford sediment and Ottawa sand, *Environ. Sci. Technol.* 37 (2003) 4905–4911.
- [10] J.M. Breiner, M.A. Anderson, H.W.K. Tom, R.C. Graham, Properties of surface-modified colloidal particles, *Clays Clay Miner.* 54 (2006) 12–24.
- [11] A. Scheludko, B.V. Toshev, D.T. Bojadjev, Attachment of particles to a liquid surface (capillary theory of flotation), *J. Chem. Soc. Faraday Trans. 1* 72 (1976) 2815–2828.
- [12] M. Preuss, H. Butt, Direct measurement of particle–bubble interactions in aqueous electrolyte: dependence on surfactant, *Langmuir* 14 (1998) 3164–3174.
- [13] G. Gillies, M. Kappl, H. Butt, Direct measurements of particle–bubble interactions, *Adv. Colloid Interface Sci.* 114 (2005) 165–172.
- [14] J. Shang, M. Flury, Y. Deng, Force measurements between particles and the air–water interface: implications for particle mobilization in unsaturated porous media, *Water Resour. Res.* 45 (2009) W06420, doi:10.1029/2008WR007384.
- [15] P. Sharma, H. Abdou, M. Flury, Effect of the lower boundary condition and flotation on colloid mobilization in unsaturated sandy sediments, *Vadose Zone J.* 7 (2008) 930–940.
- [16] P. Sharma, M. Flury, J. Zhou, Detachment of colloids from a solid surface by a moving air–water interface, *J. Colloid Interface Sci.* 326 (2008) 143–150.
- [17] J. Shang, M. Flury, G. Chen, J. Zhuang, Impact of flow rate, water content, and capillary forces on in situ colloid mobilization during infiltration in unsaturated sediments, *Water Resour. Res.* 44 (2008) W06411, doi:10.1029/2007WR006516.
- [18] P.M. King, Comparison of methods for measuring severity of water repellence of sandy soils and assessment of some factors that affect its measurement, *Aust. J. Soil Res.* 19 (1981) 275–285.
- [19] L.W. Dekker, C.J. Ritsema, K. Oostindie, O.H. Boersma, Effect of drying temperature on the severity of soil water repellency, *Soil Sci.* 163 (1998) 780–796.
- [20] H.Y. She, B. Sleep, The effect of temperature on capillary pressure–saturation relationships for air–water and perchloroethylene–water systems, *Water Resour. Res.* 34 (1998) 2587–2597.
- [21] L.W. DeJong, O.H. Jacobsen, P. Moldrup, Soil water repellency: effects of water content, temperature, and particle size, *Soil Sci. Soc. Am. J.* 63 (1999) 437–442.
- [22] L.W. Dekker, C.J. Ritsema, Wetting patterns and moisture variability in water repellent Dutch soils, *J. Hydrol. (Amsterdam)* 231 (2000) 148–164.
- [23] L.W. deJong, P. Moldrup, O.H. Jacobsen, Soil–water content dependency of water repellency in soils: effect of crop type, soil management, and physical–chemical parameters, *Soil Sci.* 172 (2007) 577–588.
- [24] J. Bachmann, M. Deurer, G. Arye, Modeling water movement in heterogeneous water-repellent soil. 1. Development of a contact angle-dependent water-retention model, *Vadose Zone J.* 6 (2007) 436–445.
- [25] P. Chassin, C. Jounay, H. Quiquampoix, Measurement of the surface free-energy of calcium–montmorillonite, *Clay Miner.* 21 (1986) 899–907.
- [26] S.K. Woche, M.O. Goebel, M.B. Kirkham, R. Horton, R.R. Van der Ploeg, J. Bachmann, Contact angle of soils as affected by depth, texture, and land management, *Eur. J. Soil Sci.* 56 (2) (2005) 239–251.
- [27] J. Eick, R. Good, A. Neumann, Thermodynamics of contact angles. II. Rough solid surfaces, *J. Colloid Interface Sci.* 53 (2) (1975) 235–238.
- [28] J. Oliver, C. Huh, S. Mason, An experimental study of some effects of solid surface roughness on wetting, *Colloids Surf.* 1 (1) (1980) 79–104.
- [29] J. Drelich, J. Miller, R. Good, The effect of drop (bubble) size on advancing and receding contact angles for heterogeneous and rough solid surfaces as observed with sessile-drop and captive-bubble techniques, *J. Colloid Interface Sci.* 179 (1) (1996) 37–50.
- [30] R.E.J. Johnson, R.H. Dettre, Contact angle hysteresis. III. Study of an idealized heterogeneous surface, *J. Phys. Chem.* 68 (7) (1964) 1744–1750.
- [31] R.H. Dettre, R.E.J. Johnson, Contact angle hysteresis. IV. Contact angle measurements on heterogeneous surfaces, *J. Phys. Chem.* 69 (5) (1965) 1507–1515.
- [32] J. Long, M. Hyder, R. Huang, P. Chen, Thermodynamic modeling of contact angles on rough, heterogeneous surfaces, *Adv. Colloid Interface Sci.* 118 (2005) 173–190.
- [33] R.F. Giese, C.J. van Oss, *Colloid and Surface Properties of Clays and Related Minerals*, CRC Press, Oxford, 2002.
- [34] E. Chibowski, M.L. Kerker, F. González-Caballero, Effect of inorganic-ions on changes in the energetic heterogeneity of the cholesterol surface, *Langmuir* 9 (10) (1993) 2491–2495.
- [35] R. Kretzschmar, H. Sticher, Transport of humic-coated iron oxide colloids in a sandy soil: influence of Ca^{2+} and trace metals, *Environ. Sci. Technol.* 31 (1997) 3497–3504.
- [36] J. Tarchitzky, Y. Chen, A. Banin, Humic substances and pH effects on sodium- and calcium-montmorillonite flocculation and dispersion, *Soil Sci. Soc. Am. J.* 57 (1993) 367–372.
- [37] C.T. Chiou, D.W. Rutherford, Effects of exchanged cation and layer charge on the sorption of water and EGME vapors on montmorillonite clays, *Clays Clay Miner.* 45 (1997) 867–880.
- [38] J. Cuadros, Interlayer cation effects on the hydration state of smectite, *Am. J. Sci.* 297 (1997) 829–841.
- [39] K. Rogers, E. Takacs, M.R. Thompson, Contact angle measurement of select compatibilizers for polymer–silicate layer nanocomposites, *Polym. Test* 24 (4) (2005) 423–427.
- [40] D. Dharaiya, S.C. Jana, Thermal decomposition of alkyl ammonium ions and its effects on surface polarity of organically treated nanoclay, *Polymer* 46 (2005) 10139–10147.
- [41] G. Malucelli, S. Ronchetti, N. Lak, A. Priola, N.T. Dintcheva, F.P. Mantia, Intercalation effects in LDPE/o-montmorillonites nanocomposites, *Eur. Polym. J.* 43 (2007) 328–335.
- [42] M. Brugnara, E. Degasperri, C. Della Volpe, D. Maniglio, A. Penati, S. Siboni, Wettability of porous materials. II. Can we obtain the contact angle from the Washburn equation? in: K.L. Mittal (Ed.), *Contact Angle, Wettability and Adhesion*, vol. 4, VSP, Boston, MA, 2006, pp. 143–164.
- [43] M. Brugnara, C. Della Volpe, D. Maniglio, S. Siboni, M. Negri, N. Gaeti, Wettability of porous materials. I. The use of Wilhelmy experiment: the cases of stone, wood and nonwoven fabric, in: K.L. Mittal (Ed.), *Contact Angle, Wettability and Adhesion*, vol. 4, VSP, Boston, MA, 2006, pp. 115–142.
- [44] C. Della Volpe, D. Maniglio, M. Morra, S. Siboni, The determination of a ‘stable-equilibrium’ contact angle on heterogeneous and rough surfaces *Colloids Surf. Physicochem. Eng. Aspects* 206 (2002) 47–67.
- [45] T.S. Meiron, A. Marmor, I.S. Saguy, Contact angle measurement on rough surfaces, *J. Colloid Interface Sci.* 274 (2004) 637–644.
- [46] A. Pegoretti, A. Dorigato, M. Brugnara, A. Penati, Contact angle measurements as a tool to investigate the filler–matrix interactions in polyurethane–clay nanocomposites from blocked prepolymer, *Eur. Polym. J.* 44 (6) (2008) 1662–1672.
- [47] J. Drelich, K. Bukka, J. Miller, F. Hanson, Surface-tension of toluene-extracted bitumens from Utah oil sands as determined by Wilhelmy plate and contact-angle techniques, *Energy Fuels* 8 (1994) 700–704.

- [48] A. Gilboa, J. Bachmann, S. Woche, Y. Chen, Applicability of interfacial theories of surface tension to water-repellent soils, *Soil Sci. Soc. Am. J.* 70 (2006) 1417–1429.
- [49] J. Shang, M. Flury, J.B. Harsh, R.L. Zollars, Comparison of different methods to measure contact angles of soil colloids, *J. Colloid Interface Sci.* 328 (2008) 299–307.
- [50] B. Janczuk, E. Chibowski, M. Hajnos, T. Biaepiotrowic, J. Stawinski, Influence of exchangeable cations on the surface free-energy of kaolinite as determined from contact angles, *Clays Clay Miner.* 37 (1989) 269–272.
- [51] F. Wypych, K.G. Satyanarayana, *Clay Surfaces: Fundamentals and Applications*, Academic Press, San Diego, 2004.
- [52] S. Nishimura, S. Biggs, P.J. Scales, T.W. Healy, K. Tsunematsu, T. Tateyama, Molecular-scale structure of the cation modified muscovite mica basal plane, *Langmuir* 10 (1994) 4554–4559.
- [53] D.H. Bangham, Z. Saweris, The behavior of liquid drops and adsorbed films at cleavage surfaces of mica, *Trans. Faraday Soc.* 34 (1938) 554–569.
- [54] P.F. Low, Principles of ion diffusion in clays, in: D.E. Baker (Ed.), *Chemistry in the Soil Environment*, ASA Special Publication No. 40, American Society of Agronomy, Madison, WI, 1981, pp. 31–45.
- [55] R.I. Papendick, G.S. Campbell, Theory and measurement of water potential, in: J.F. Parr, W.R. Gardner, L.F. Elliot (Eds.), *Water Potential Relations in Soil Microbiology*, Soil Science Society of America, Madison, WI, 1981, pp. 1–22.
- [56] J.C. Michel, L.M. Riviere, M.N. Bellon-Fontaine, Measurement of the wettability of organic materials in relation to water content by the capillary rise method, *Eur. J. Soil Sci.* 52 (3) (2001) 459–467.
- [57] G.G.S. Holmgren, A rapid citrate–dithionite extractable iron procedure, *Soil Sci. Soc. Am. Proc.* 31 (1967) 210–211.
- [58] M. Chorom, P. Rengasamy, Dispersion and zeta potential of pure clays as related to net particle charge under varying pH, electrolyte concentration and cation type, *Eur. J. Soil Sci.* 46 (4) (1995) 657–665.
- [59] W. Wu, Baseline studies of The Clay Minerals Society Source Clays: colloid and surface phenomena, *Clays Clay Miner.* 49 (2001) 446–452.
- [60] D. Beaglehole, E.Z. Radlinska, B.W. Ninham, Inadequacy of Lifshitz theory for the liquid-films, *Phys. Rev. Lett.* 66 (16) (1991) 2084–2087.
- [61] D. Beaglehole, Aspects of vapor adsorption on solids, *Physica A* 244 (1997) 40–44.
- [62] K.M. Dontsova, L.D. Norton, C.T. Johnston, J.M. Bigham, Influence of exchangeable cations on water adsorption by soil clays, *Soil Sci. Soc. Am. J.* 68 (2004) 1218–1227.
- [63] D.A. Laird, Layer charge influences on the hydration of expandable 2:1 phyllosilicates, *Clays Clay Miner.* 47 (1999) 630–636.
- [64] E. Chibowski, P. Staszczuk, Determination of surface free-energy of kaolinite, *Clays Clay Miner.* 36 (5) (1988) 455–461.
- [65] A.K. Helmy, E.A. Ferreira, S.G. de Bussetti, The surface energy of kaolinite, *Colloid Polym. Sci.* 283 (2004) 225–228.
- [66] B. Janczuk, T. Bialopiotrowicz, Components of surface free energy of some clay minerals, *Clays Clay Miner.* 36 (1988) 243–248.
- [67] J.-M. Cases, I. Berend, M. Francois, J.-P. Uriot, L. Michot, F. Thomas, Mechanism of adsorption and desorption of water vapor by homoionic montmorillonite. 3. The Mg^{2+} , Ca^{2+} , Sr^{2+} and Ba^{2+} exchanged forms, *Clays Clay Miner.* 45 (1997) 8–22.
- [68] J.B. Harsh, S. Xu, Microelectrophoresis applied to the surface chemistry of clay minerals, *Adv. Soil Sci.* 14 (1990) 131–165.
- [69] R.M. Ahmet, F.C. Angel, Baseline studies of The Clay Minerals Society Source Clays: chemical analysis of major elements, *Clays Clay Miner.* 49 (2001) 381–386.
- [70] A.R. Mermut, G. Lagaly, Baseline studies of The Clay Minerals Society Source Clays: layer-charge determination and characteristics of those minerals containing 2:1 layers, *Clays Clay Miner.* 49 (2001) 393–397.
- [71] S.M. Auerbach, K.A. Carrado, P.K. Dutta, *Handbook of Layered Materials*, 1st ed., CRC Press, Boca Raton, FL, 2004.
- [72] S.J. Chipera, D.L. Bish, Baseline studies of The Clay Minerals Society Source Clays: powder X-ray diffraction analyses, *Clays Clay Miner.* 49 (2001) 398–409.
- [73] D.R. Lide, *CRC Handbook of Chemistry and Physics*, 75th ed., CRC Press, Boca Raton, FL, 1994.
- [74] W.Z. Xu, C.T. Johnston, P. Parker, S.F. Agnew, Infrared study of water sorption on Na-, Li-, Ca-, and Mg-exchanged (SWy-1 and SAz-1) montmorillonite, *Clays Clay Miner.* 48 (2000) 120–131.
- [75] L. Raymond, J.R. Kerns, J.M. Charles, Structural charge site influence on the interlayer hydration of expandable three-sheet clay minerals, *Clays Clay Miner.* 16 (1968) 73–81.

Centrifuge techniques and apparatus for transport experiments in porous media

E.D. Mattson & C.D. Palmer

Idaho National Laboratory, Idaho Falls, Idaho, USA

R.W. Smith

University of Idaho, Idaho, Idaho Falls, USA

M. Flury

Washington State University, Pullman, Washington, USA

ABSTRACT: This paper describes experimental approaches and apparatus that we have developed to study solute and colloid transport in porous media using Idaho National Laboratory's 2-m radius centrifuge. The experimental techniques include water flux scaling with applied acceleration at the top of the column and sub-atmospheric pressure control at the column base, automation of data collection, and remote experimental control over the internet. These apparatus include a constant displacement piston pump, a custom designed liquid fraction collector based on switching valve technology, and modified moisture monitoring equipment. Successful development of these experimental techniques and equipment is illustrated through application to transport of a conservative tracer through unsaturated sand column, with centrifugal acceleration up to 40 g. Development of such experimental equipment that can withstand high accelerations enhances the centrifuge technique to conduct highly controlled unsaturated solute/colloid transport experiments and allows in-flight liquid sample collection of the effluent.

1 INTRODUCTION

The selection and design of subsurface environmental restoration strategies (including monitored natural attenuation) frequently relies on the use of sophisticated numerical models that couple transport and biogeochemical processes to predict the fate and transport of contaminants and introduced remediation agents in heterogeneous subsurface media. These models are typically validated by comparing modeling results to 'large-scale' field research demonstrations and 'small-scale' laboratory experiments. Although controlled field experiments have the advantage of being representative of the field-scale problem, such experiments are costly, difficult to conduct, limit the use of relevant contaminants, and offer little direct control over boundary conditions. Conversely, laboratory column experiments, which are generally inexpensive and better controlled, are of limited value because they do not closely mimic field conditions. Reactive transport studies conducted in unsaturated porous media compounds these limitations due to the extensive length of time need to transport a tracer through the porous media (e.g. up to 300 days

in laboratory sand packed column experiments (Jardine et al. 1993a, b). Experiments conducted on large centrifuges can help bridge the gap between field and lab experiments because the experimental packages are large enough to incorporate critical field-scale conditions. They can also significantly reduce the time necessary for unsaturated transport experiments because flow rates through the porous media can be controlled at prescribed moisture content conditions.

A mathematical description of a steady-state, unsaturated flow field in a centrifuge has been described by Nimmo et al. (1987). Numerous authors have presented scaling laws for water flow and solute transport in centrifuge experiments (e.g., Garnier et al. 2000). These scaling relationships allow us to design experiments where we can increase the velocity of water through the sample while maintaining moisture potential and water content essentially unaffected. This increases solute advection reduces the time necessary for vertical flow experiments; for example, a solute transport experiment that might take a year to conduct on the bench top could be completed in a week in a centrifuge operating at 50-gs.

Although commercially available cabinet-size centrifuges (Conca & Wright 1990, 1998, Gamedinger & Kaplan 2000) have been used to evaluate miscible solute transport in unsaturated soil, their application is limited to small samples (5.2 cm length \times 3.3 cm diameter or \sim 45 cm³) of homogeneous materials. In addition, most small centrifuges are limited to simplistic controlled flux application at the surface and free drainage at the lower boundary and lack in-flight monitoring of moisture contents, pressures and solute concentrations. Measurements of these variables are physically acquired after stopping the centrifuge.

Large centrifuges overcome many of the limitations of the cabinet-size centrifuge in conducting solute transport experiments in unsaturated soils. Advantages include large sample sizes (both in diameter and length), better experimental control of the boundary conditions, in-flight monitoring of the state variables, and multi-dimensional testing. CCD cameras can be mounted and used to monitor the movement of non-aqueous phase liquids (NAPL) and dyes, and record other changes in the experimental system. Flow-through conductivity cells can be mounted in the system (e.g., Hensley & Savvidou, 1993) to obtain in-flight tracer breakthrough-curves. Fraction collectors (see Methods section) can be added to collect effluent samples for subsequent chemical analyses.

The addition on computers on the hub of large centrifuge systems essentially permit "bench-scale" type experiments to be conducted under enhanced accelerations with fully automated control. At the Idaho National Laboratory (INL), we have developed tools and techniques to conduct flux controlled unsaturated solute transport experiments with collection of the column effluent while in-flight. This advancement in automation and control extends the limits of miscible solute transport in unsaturated soils to solute concentrations that better represent those in the prototype. This paper describes the equipment and controls necessary to conduct such experiments and verifies its applicability using a one-dimensional sand-packed column experiment conducted over a range of centrifugal acceleration.

2 IDAHO NATIONAL LABORATORY CENTRIFUGE FACILITY

The Idaho National Laboratory centrifuge is a 2-m radius, 50 g-tonne Actidyne Systemes model C61-3 centrifuge (Figure 1) that can carry an experimental package as large as 70 cm long by 50 cm thick by 60 cm high and 500 kg mass at accelerations up to 130 g (Smith et al. 2002). An experimental package is built in a cage-like aluminum support

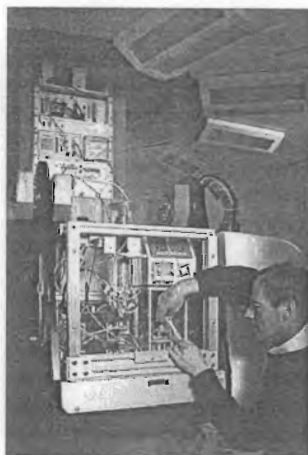


Figure 1. Photograph of the experimental package installed on the platform of the INL 2-meter centrifuge. Note the column (center), solute tank (upper left), pump (upper right), and effluent sampling system (lower right).

structure that both supports the experiment and provides secondary containment in case of leakage or failure.

In-flight experimental control and monitoring of experiments is accomplished using a data acquisition system employing a wireless network hub. The hub links computers in the control room with National Instruments data acquisition systems mounted directly on the centrifuge. Real-time monitoring data is collected using LabVIEW software and stored and displayed on control room computers where collaborating researchers can access the data via the web.

3 METHODS

Tracer experiments through unsaturated soil are typically conducted by packing a column with soil, applying a solution to the surface until a steady-state flow field is established through the column, switching the background solution to one that contains a tracer, and measuring the tracer concentration as a function of time at the bottom of the soil column.

The experimental setup is illustrated in Figure 2. Two tanks under atmospheric pressure contain a 330-ppm KBr background solution and a 2000-ppm KBr tracer solution. A solenoid 3-way valve controls which of the solutions is pumped to the column. A remotely controlled Encynova pump (model 2-4) is used to adjust the flow rate to the top of the soil column. An experiment is conducted by placing the experimental package on the

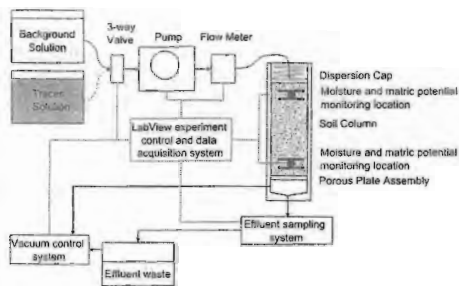


Figure 2. A schematic illustrating the major experimental components of solute transport experiments through unsaturated porous media.

centrifuge platform and spinning the centrifuge at a constant speed to obtain the desired centrifugal acceleration. The 3-way valve is set to the 330-ppm KBr background solution and a constant flux is delivered to the top of the column via the pump. A constant vacuum is applied to the effluent collection system at the base of the soil column. The vacuum is adjusted until the monitoring equipment (capacitance probes and tensiometers) indicates that the water flux through the soil column is in steady state. At this time, the 3-way valve is switched to the 2000-ppm KBr tracer solution and the fraction collector is activated to collect discrete effluent samples at a predetermined rate.

The test column is constructed from a 5.7-cm diameter by 28-cm long multi-piece Lexan cylinder (Figure 3) and packed with a 2-to 0.075-mm diameter sandy soil. At the top of this test column, a cap with a porous stone diffuser was used to spread the input solution over the surface of the column. The cap was not rigidly attached to the column but was pressed against the soil surface using a large compression spring, to ensure good contact with the soil. The moisture content and matric potential were monitored in the soil column at two locations approximately 4.5 cm from each end. Soil moisture was measured using a Decagon Echo 10 probe, where the electrodes have been modified to wrap around the inner circumference of the experimental column (Mattson et al. 2006). Small 0.5-cm diameter porous ceramic cups were attached to Honeywell 26PCCFA6D pressure transducers (0 to 15 psi range) to measure the soil matric potential. The bottom of the column was set as a constant pressure boundary using a Versapor 1.2 um diameter filter supported by a porous stone between the soil and the lower fluid collection chamber. A constant vacuum was applied to the lower fluid collection chamber.

The experiment is remotely controlled and monitored using a computer program written using LabVIEW software. This program controls

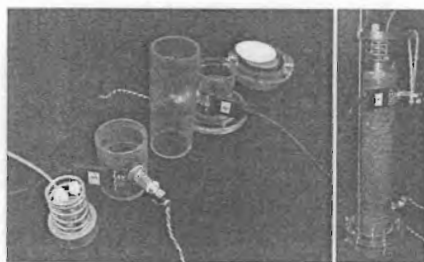


Figure 3. Multi-piece lexan column used for 1 dimensional solute transport experiments. A key feature of the columns is the installed capacitance water content probes and the mini tensiometers.

the 3-way valve switching of the influent background and tracer application, the pump rate, and the effluent collection system. Monitoring of the experiment is also accomplished using LabVIEW programs. Influent water flow rate, soil moisture, soil matric potential, applied vacuum at the lower boundary, and the effluent electrical conductivity can all be monitored at a user specified interval. Influent flow rates are recorded using a Sensirion ASL-1430-24 liquid mass flow meter capable of measuring rates as low as 150 nL min^{-1} . The lower boundary vacuum is controlled by adjusting the pressure of air supplied through the centrifuge rotary joint to a venturi vacuum pump (Cole-Parmer) mounted on the rotating centrifuge. The vacuum is monitored using a Honeywell pressure transducer (26PCCFA6D, 0 to 15 psi range). Electrical conductivity of the effluent solution was measured using a Microelectrode (model 16-900) flow-thru conductivity electrode.

When samples are required for chemical analyses, the method has been to periodically stop the centrifuge to physically remove an effluent sample (e.g., Antoniadis & McKinley, 2000). A better approach is to collect samples in flight, however commercially available fraction collectors fail to operate on the centrifuge due to their inability to physically operate at high accelerations. Due to this failure, we designed and built an effluent sampling system capable of working in our centrifuge experiments (Figure 4). A fundamental difference between our sampling system and commercially available fraction collectors is the reliance on valves and air pressure to move fluids to stationary sample vials rather than attempting to move the sample vials. Column effluent is allowed to fill a sample accumulation connection tube between two large bore stainless steel 3-way valves (Figure 4a). Once the effluent valve connection tube is full, effluent flows into a waste container. To collect a sample, both valves are activated (Figure 4b). When in the 'B' position, the top valve isolates the column from

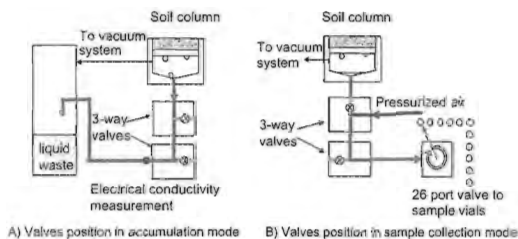


Figure 4. Schematic of the geotechnical centrifuge effluent collection system. Porous media.

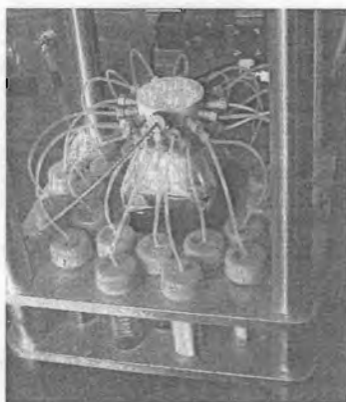


Figure 5. Photograph of the centrifuge effluent collection system (shown schematically in Figure 4b). Note the 26 position high pressure rotor valve (center).

the effluent collection chamber and the bottom valve isolates the collection tube from the waste container. Pressurized air is used to transport the effluent in the collection tube to a 26-port switching valve connected to 15-ml sample collection vials (Figure 5). With the valves in the 'B' position, effluent from the column accumulates above the upper 3-way valve. After a sufficient time has passed to empty the accumulation tube, the valves switch back to their original position to collect the next sample. Valve switching is performed via a LabVIEW program that allows automated operation of the effluent collection for subsequent laboratory analyses. Timing of the sample collection is operator controlled. Multiple 26-port switching valves can be daisy-chained together to allow additional samples to be collected.

4 RESULTS AND DISCUSSIONS

The experimental design and equipment was tested in a series of preliminary experiments to verify the establishment of a one-dimensional flow field at high accelerations and that the tracer output could be accurately measured. To confirm that flow was

effectively unidirectional through out the column, red dye was added to the tracer solution for one test. The test was conducted similar to a normal tracer experiment except the test was stopped when the red dye nearly reached the end of the column. Subsequent visual inspection of the dye distribution at the top of the soil surface confirmed that there is sufficient capillary dispersion in the porous stone to evenly spread the influent across the top of the soil. Subsequent destructive sampling of the column indicated an even red staining of the sand throughout the column.

A second equipment test was conducted to evaluate the comparability of solute break through curves determined by the in-flight electrical conductivity cell and post-experimental analysis of bromide concentration. Our results suggest a good correspondence between the breakthrough curves derived from the conductivity measurements and the Br concentrations determined by ion chromatograph (Dionex DX-320) analysis of collected effluent samples (Figure 6). A single value for the velocity (0.13 cm min^{-1}) and the dispersion coefficient ($0.040 \text{ cm}^2 \text{ min}^{-1}$) were estimated using a non-linear parameter estimation spreadsheet program and an analytical solution to the convection-dispersion equation (Wraith & Or 1998). The breakthrough curves calculated from these values describe both the normalized bromide effluent samples and the normalized conductivity measurements. This result suggests that for the experiments involving only the KBr tracers described in this report, breakthrough curves derived from the easier-to-collect continuous electrical conductivity measurements are reflective of breakthrough curves collected using the effluent sampling system and that breakthrough curves can be defined solely from the in-line conductivity measurements. Experiments using multiple reactive and/or conservative tracers would, however, require the use of the effluent sampling system and subsequent post-experimental chemical analysis.

Success of the equipment testing experiments gave confidence that tracer transport experiment in unsaturated soil could be conducted on the INL centrifuge at 1, 10, 20, 30, and 40 times earth's gravitational acceleration. Since the vertical flux of water through soil is dependent on the body force experienced by the water, the applied water flux should therefore be proportional to the applied centrifugal acceleration. Adjusting the flow rate leads to an advantage of using a centrifuge for unsaturated solute transport experiments; the time required to conduct an experiment can be decreased by increasing the applied acceleration. Comparison of breakthrough results from experiments conducted on the centrifuge at 1 g to 40 g is illustrated in Figure 7a. Although not exactly inversely proportional to applied acceleration (discussed

later), the 40-g experiment required significantly less time to achieve breakthrough ($C/C_0 = 0.5$) when compared with the 1 g experiment.

To analyze these data sets, time is normalized using the applied flux and the column moisture

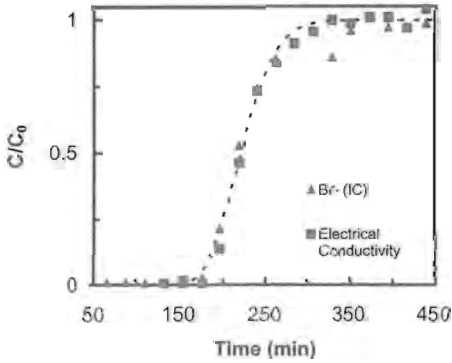


Figure 6. Breakthrough curve showing the correspondence between real time in line electrical conductivity measurements and post-experiments analyses of Br by ion chromatography.

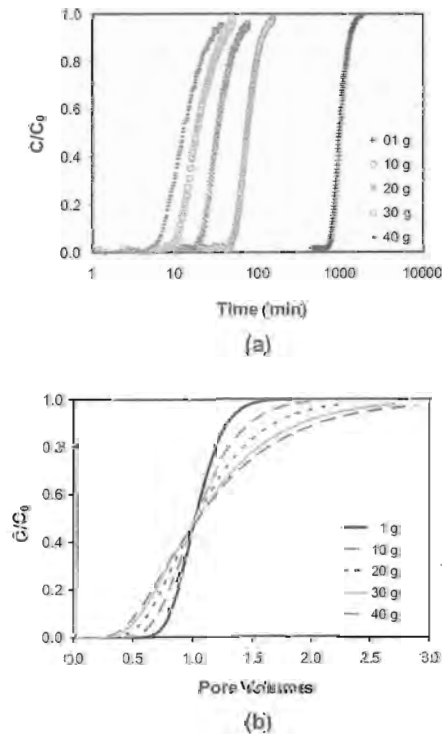


Figure 7. Comparison of breakthrough curves for 1, 10, 20, 30 and 40-g column experiments in terms of experimental time (upper, 7a) and pore volume (lower, 7b).

content from each experiment, then the data are plotted in terms of pore volume (e.g., dimensionless time). The normalized breakthrough curves for experiments conducted at 1, 10, 20, 30, and 40 g respectively are shown in Figure 7b. The average pore-water velocity, dispersion coefficient, moisture content and breakthrough time (at $C/C_0 = 0.5$) calculated from these breakthrough curves using a non-linear parameter estimation spreadsheet program (Wraith & Or 1998) are presented in Table 1. The parameter N is the dimensionless applied acceleration and is calculated by dividing the centrifugal acceleration by earth's gravity. The applied water flow rate through the column was adjusted based on a simple linear scaling with g in an attempt to maintain the same water content in all experiments. Although mostly successful, the measured water content of the column decreased with increasing N, likely due to non-linear competition between gravitational (scaled in centrifuge experiments) and capillary (not scaled in centrifuge experiments) forces.

The time of arrival of the $C/C_0 = 0.5$ relative concentration at the effluent end of the column increases linearly with $1/N$ (Figure 8). Although the variability of water content in the column tests is relatively small (0.090 to 0.187, Table 1), there is a significant variation with N. The hydraulic conductivity of the unsaturated soil is a function of the moisture content and since the measured moisture content is not exactly the same between the experiments, the solute transport results will deviate some of the scaling relationships. For example, the time for the breakthrough ($C/C_0 = 0.5$) at $N = 10$ is not exactly twice the time for breakthrough at $N = 20$ (see Table 1). Extrapolation of a regression through the 10 to 40 g breakthrough times to 1 g results in a breakthrough time of 808 minutes, approximately 20 percent less than the measured value.

A second important parameter that is calculated from these experiments is the dispersion coefficient. Culligan & Savvidou (1995) calculated the dispersion coefficient as

$$D = D_m + \alpha N v \quad (1)$$

Table 1. Parameters derived from breakthrough curves data.

N	Q (mL/min)	v (cm/min)	D (cm ² /min)	θ	($C/C_0 = 0.5$) (min)
1	0.014	0.0292	0.015	0.187	993
10	0.14	0.3974	0.51	0.137	73.0
20	0.28	0.892	2.19	0.122	32.5
30	0.42	1.528	6.2	0.103	18.3
40	0.56	2.416	12.1	0.090	12.0

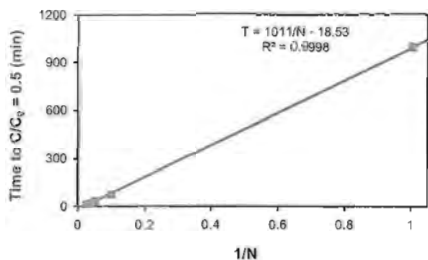


Figure 8. Arrival times for the $C/C_0 = 0.5$ relative concentration at the effluent end of the column.

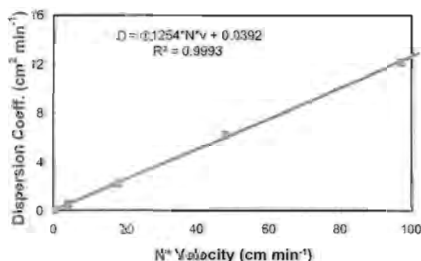


Figure 9. A plot of D vs Nv yields a straight line with a slope of 0.125 cm and an intercept of 0.039 $\text{cm}^2 \text{min}^{-1}$.

where D_m is the effective diffusion coefficient in the porous medium and α is the dispersivity. In our results since the velocity is a linear function of N , it follows that D varies with N^2 . A plot of D versus Nv (Figure 9) yields a straight line suggesting that the experimental apparatus on the centrifuge is operating correctly.

5 CONCLUSIONS

The improved moisture probes, new fraction collector, and general experimental setups developed at the INL represent significant advancements in the techniques needed to conduct in-flight sampling and monitoring on the centrifuge. The centrifuge allows experiments to be completed more quickly than tests conducted at 1-g, and permits experiments to be conducted under a range of conditions that would be difficult or impossible using conventional approaches. Despite some deviation in the moisture content between experimental runs, the transport parameters could be scaled to the 1-g tests using previously published scaling laws. Our ability to control the upper and lower boundary of the experiment and collect effluent samples for subsequent analyses allows for realistic solute transport experiments in unsaturated soils to be conducted in a centrifuge.

Disclaimer: Commercial products named in this article are for the reader's reference and do not represent endorsement by the INEL.

Work supported by the U.S. Department of Energy, Office of Environmental Management, under DOE Idaho Operations Office Contract DE-AC07-05ID14517.

REFERENCES

- Antoniadis, V. & McKinley, J.D. 2000. Leaching tests in a laboratory centrifuge on zinc migration in london clay. J. Garnier, L. Thorel & E. Haza (eds.), *International Symposium on Physical Modelling and Testing in Environmental Geotechnics, La Baule, 15-17 May 2000*, 53-60. Paris: LCPC.
- Conca, J.L. & Wright, J.V. 1990. Diffusion coefficients in gravel under unsaturated conditions. *Water Resour. Res.* 26: 1055-1066.
- Conca, J.L. & Wright, J.V. 1998. The UFA Method for Rapid, Direct Measurements of Unsaturated Soil Transport Properties. *Australian J. of Soil Research* 36: 291-315.
- Culligan-Hensley, P.J. & Savvidou, C. 1995. Environmental geomechanics and transport processes. In R.N. Taylor (ed.), *Geotechnical Centrifuge Technology*: 196-263. London: Chapman and Hall.
- Gamerding, A.P. & Kaplan, D.I. 2000. Application of a continuous-flow centrifugation method for solute transport in disturbed, unsaturated sediments and illustration of mobile-immobile water. *Water Resour. Res.*, 36:1747-1755.
- Garnier, J., Thorel, L. & Haza, E. (eds). 2000. *International Symposium on Physical Modelling and Testing in Environmental Geotechnics, La Baule, 15-17 May 2000*, 191-260. Paris: LCPC.
- Hensley, P.J. & C. Savvidou. 1991. "Modelling coupled heat and contaminant transport in groundwater", *Int. J. Numerical Anal. Meth. Geomech.* 17: 493-527.
- Jardine, P.M., Jacobs, G.K. & O'Dell, J.D. 1993a. Unsaturated transport processes in undisturbed heterogeneous porous media: II. Co-contaminants, *Soil Sci. Soc. Am. J.* 57: 954-962.
- Jardine, P.M., Jacobs, G.K. & Wilson, G.V. 1993b. Unsaturated transport processes in undisturbed heterogeneous porous media: I. Inorganic contaminants, *Soil Sci. Soc. Am. J.* 57: 945-953.
- Mattson, E.D., Baker, K.E., Palmer, C.D., Breckenridge, C.R., Svoboda, J.M. & Smith, R.W. 2006. A Flexible Water Content Probe for Unsaturated Soil Column Experiments, *Vadose Zone Journal* 5: 805-808.
- Nimmo, J.R., Rubin, J. & Hammermeister, D.P. 1987. Unsaturated flow in a centrifugal field: Measurement of hydraulic conductivity and testing of Darcy's law. *Water Resour. Res.* 23: 124-134.
- Smith, R.W., Payne, S.J. & Miller, D.L. 2002. INEEL Environmental Geocentrifuge Facility Developments. In R. Phillips, P.J. Guo & R. Popescu (eds.), *Physical Modelling in Geotechnics: ICPMG '02, St. Johns, Canada, 10-12 July 2002*, 55-58. Lisse: A.A. Balkema Publishers.
- Wraith, J.M., & Or, D. 1998. Nonlinear parameter estimation using spreadsheet software. *J. Nat. Resour. Life Sci. Educ.* 27: 13-19.

Force measurements between particles and the air-water interface: Implications for particle mobilization in unsaturated porous media

Jianyong Shang,¹ Markus Flury,^{1,2} and Youjun Deng³

Received 23 August 2008; revised 9 February 2009; accepted 31 March 2009; published 16 June 2009.

[1] Capillary forces acting at the air-water interface play an important role in colloid fate and transport in subsurface porous media. We quantified capillary forces between different particles (sphere, cylinder, cube, disk, sheet, and natural mineral particles) and a moving air-water interface. The particles had different sizes and contact angles (ranging from 14° to 121°). Theoretical calculations using the Young-Laplace equation were used to support and generalize the experimental data. When the air-water interface moved over the particles, there were strong capillary forces acting on the particles in the direction of the moving interface. The measured maximum capillary forces were similar to those calculated by the Young-Laplace equation. The larger the contact angles and the larger the particle size, the stronger were the capillary forces. Particles with irregular shape and sharp edges experienced greater forces than smooth particles. Generalization of the results indicates that capillary forces exerted by a moving air-water interface can readily exceed attractive Derjaguin-Landau-Verwey-Overbeek (DLVO) and gravity forces for typical subsurface particles, and a moving air-water interface is therefore an effective mechanism for mobilization of particles in porous media. Particles in the colloidal size range are particularly susceptible for mobilization by a moving air-water interface.

Citation: Shang, J., M. Flury, and Y. Deng (2009), Force measurements between particles and the air-water interface: Implications for particle mobilization in unsaturated porous media, *Water Resour. Res.*, 45, W06420, doi:10.1029/2008WR007384.

1. Introduction

[2] Interfacial capillary forces between solid, liquid, and gas phases can cause solid particles to be attracted to, or repelled from, each other, depending on the contact angle forming at the solid-liquid-gas interface and the movement of the liquid-gas interface relative to the solids. It has been commonly observed that liquid bridges can cause strong attraction between particles [Hunter, 2001; Sur and Pak, 2001; Steenhuis *et al.*, 2006; Gao *et al.*, 2008]. When there is a liquid film on a flat surface, strong capillary forces will pin the particles to the surface, but when the liquid film expands, the particles may be lifted off the flat surface because the particles are being strongly attached to the liquid-gas interface. Surface tension, contact angles, particle densities, sizes, and shapes determine whether the detachment of a particle from a surface by liquid film happens and determine the order of magnitude of the forces involved [Gillies *et al.*, 2005].

[3] Colloids play an important role in subsurface contaminant transport. Mobile colloids can enhance and facilitate transport of contaminants [Kretzschmar *et al.*, 1999].

Whether this colloid-facilitated transport of contaminants occurs depends on whether colloids are present, mobile, and associate with contaminants [Honeyman, 1999]. In unsaturated soils and sediments, colloids are often attached to larger mineral particles, and for such colloids to become an effective carrier for contaminants, the colloids have to be mobilized, i.e., detached from the larger soil minerals. Chemical as well as physical factors play a role in colloid mobilization [McCarthy and McKay, 2004; Flury and Qui, 2008]. In this paper we focus on the physical factors related to the liquid-gas interface.

[4] While the importance of liquid-gas interfaces on colloid mobilization and transport in porous media has been recognized, it is not clear what the exact mechanisms of colloid mobilization by liquid-gas interfaces are. Colloids may be trapped in pendular liquid rings [Wan and Tokunaga, 1997], strained in thin liquid films [Veerapaneni *et al.*, 2000; Saiters and Lenhart, 2003], attached to the liquid-gas interface [Wan *et al.*, 1994; Abdel-Fattah and El-Genk, 1998b; Sirivithayapakorn and Keller, 2003; Auset *et al.*, 2005; Lazouskaya and Jin, 2008], or attached to the solid-liquid-gas phase interface [Chen and Flury, 2005; Crist *et al.*, 2005]. Colloid mobilization can occur when liquid films expand, thereby releasing trapped colloids from pendular liquid rings. It has also been shown that capillary forces acting between colloids and the liquid-gas interface can mobilize colloids [Shang *et al.*, 2008a, 2008b; Sharma *et al.*, 2008a, 2008b]. Theoretical considerations indicate that capillary forces can exceed Derjaguin-Landau-Verwey-Overbeek (DLVO) forces [Scheludko *et al.*, 1976; Preuss

¹Department of Crop and Soil Sciences, Washington State University, Pullman, Washington, USA.

²Department of Biological Systems Engineering, Washington State University, Pullman, Washington, USA.

³Department of Soil and Crop Sciences, Texas A&M University, College Station, Texas, USA.

and Butt, 1998a, 1998b; Shang *et al.*, 2008a]. Experiments with natural colloids in sediments [Sharma *et al.*, 2008a] and synthetic polystyrene beads [Sharma *et al.*, 2008b] showed that a moving liquid-gas interface can indeed capture and mobilize particles that are initially attached to stationary surfaces.

[5] When colloids are at the liquid-gas interface, it is energetically unfavorable for the colloids to detach from the interface [Israelachvili, 1992; Abdel-Fattah and El-Genk, 1998b, 1998a]. When a colloid is attached to a liquid-gas interface, the attachment is considered irreversible [Abdel-Fattah and El-Genk, 1998a]. Colloids can aggregate at a stationary liquid-gas interface [Williams and Berg, 1992] and can also aggregate when an air bubble slowly dissolves in a porous medium [Sirivithayapakorn and Keller, 2003]. While colloid attachment to liquid-gas interfaces has been investigated extensively in the past, as mentioned above, the quantification of the forces acting on particles already attached to the liquid-gas interface has not received as much attention.

[6] Colloid attachment onto the gas-liquid interface is important for industrial solvent extraction and surface cleaning processes. During solvent extraction processes, colloidal particles tend to aggregate at the liquid-gas interface [Williams and Berg, 1992; Abdel-Fattah and El-Genk, 1998a]. Foams and emulsions are stabilized by the strong attachment of particles at the liquid-gas or liquid-liquid interface [Binks, 2002; Du *et al.*, 2003; Gonzenbach *et al.*, 2006]. In most cases, the attachment or assembly of colloidal particles at air-water interfaces is controlled by adjusting the surface hydrophobicity of colloidal particles. For surface cleaning, surfactants are used to change the property of the gas-liquid interface where “dirty” colloidal particles or droplets can be detached [Hiemenz and Rajagopalan, 1997; Abdel-Fattah and El-Genk, 1998a].

[7] The forces acting between a particle and a liquid-gas interface can be measured by tensiometry [Zhang *et al.*, 1996, 1997] or atomic force microscopy [Preuss and Butt, 1998a, 1998b; Gillies *et al.*, 2005]. In most cases, spherical particles are used for force measurements, and sphere tensiometry has even been proposed as an alternative to du Noüy ring and Wilhelmy plate methods for measuring surface tensions and contact angles [Gunde *et al.*, 1995; Ecke *et al.*, 1999].

[8] The capillary forces acting on a spherical particle at the liquid-gas interface can be described by the Young-Laplace equation, and numerical solutions have been developed for spherical particles [Princen, 1969; Zhang *et al.*, 1996, 1997, 1999]. For particles with sharp edges, the boundary condition for the contact angle at the sharp edges requires additional assumptions [Hesla and Joseph, 2004; Singh and Joseph, 2005], making the solution of the Young-Laplace equation more complicated. For particles with irregular shape, neither experimental measurements nor theoretical calculations are available.

[9] We hypothesize that capillary forces play an important role in the mobilization and transport of colloids in porous media. Under relatively dry conditions, when solid surfaces are covered with a thin water film, colloid particles will be pinned to the porous media surface by capillary forces, but when water films expand, the same capillary forces can cause particles to detach and move along with moving liquid-gas interfaces.

[10] The overall objective of this study was to quantify the forces acting on a solid particle when an air-water interface passes over the particle, with the goal to clarify the role of moving air-water interfaces on colloid mobilization in porous media. Specifically, we (1) quantify, both experimentally and theoretically, the forces acting on particles of different shape as a function of air-water interface position and (2) discuss the implications for colloid mobilization under unsaturated flow conditions in porous media.

2. Theory

2.1. Force Balance for a Particle in Contact With a Liquid Film

[11] Consider a particle attached to a flat surface covered by a liquid film (Figure 1). We assume that the density (ρ_a) of the gas phase is much smaller than that of the liquid (ρ_l) and the solid phases (ρ_s) and thus can be neglected. We use the following conventions: (1) the position of the horizontal bottom line of the particle is the reference position, (2) the position above the reference position is positive, and (3) downward forces are positive and upward forces negative. The vertical components of the forces acting on the particle are as follows: (1) DLVO forces (f_{DLVO}) between the particle and the surface (downward or upward depending on surface charges and solution chemistry), (2) weight (f_w) of the particle (downward), (3) surface tension force (f_s) (downward or upward depending on contact angle), (4) buoyancy force (f_b) (upward), and (5) hydrostatic pressure force (f_p).

[12] If the sum of the above forces,

$$F = f_{DLVO} + f_w + f_s + f_b + f_p, \quad (1)$$

is negative, $F < 0$, then the particles will detach from the solid surface and will float at the air-water interface (upward repulsive force); if $F > 0$, the particle will be pinned to the solid surface (downward attractive force). The sum of surface tension and hydrostatic pressure force is commonly called the capillary force, f_{cap} .

[13] For a particle of constant size, the force balance in equation (1) depends on the thickness, H , of the liquid film, such that the net force can either be positive or negative. In the following, we discuss the forces acting at the particle-liquid-gas interface as a function of liquid film thickness. We discuss the theoretical forces and compare with experimental measurements.

2.2. Forces on a Sphere at a Liquid-Gas Interface

[14] The forces acting on a sphere at a liquid-gas interface have been worked out in relation to flotation and sphere tensiometry [Princen, 1969; Huh and Mason, 1974, 1976; Schulze, 1977; Fieber and Sonntag, 1979; Zhang *et al.*, 1996; Singh and Joseph, 2005]. We assume that a spherical bead with radius R is adhering to point B on a horizontal solid surface and that the contact angle of the bead is θ (Figure 1a). When a water film builds up on the flat solid surface, the water film forms a meniscus and a contact line (AC) around the sphere. We designate the immersion angle as ψ , the distance from the center bottom B of the bead to the horizontal air-water interface as y , and the deflecting depth of the water film as z_0 (Figure 1a). The vertical components of the forces exerted on the sphere are (see

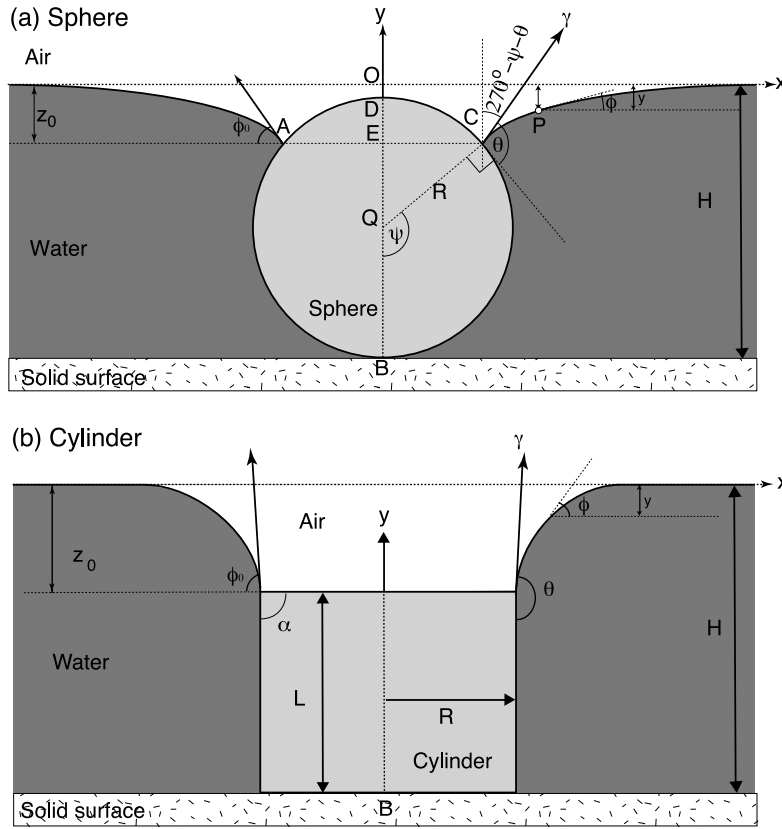


Figure 1. (a) A sphere and (b) a cylinder adhering to a horizontal solid surface in contact with a water film of height H .

also the notation section for explanation of symbols and their dimensions)

$$f_w = \frac{4}{3} \pi R^3 \rho_s g \quad (2)$$

$$f_b = -\frac{\pi}{3} R^3 (1 - \cos \psi)^2 (2 + \cos \psi) \rho_l g, \quad (3)$$

where R is the radius of the sphere or cylinder, ρ_s is the density of the solid phase, g is the gravitational acceleration, ψ is the filling angle between the center of the colloidal sphere and the water-colloid contact line, and ρ_l is the density of the liquid phase. The vertical component of the surface tension force (downward if $\psi + \theta < 180^\circ$, upward if $\psi + \theta > 180^\circ$) can be calculated as [Zhang *et al.*, 1996; Singh and Joseph, 2005]

$$f_s = -(2\pi R \sin \psi) \gamma \cos(270 - \psi - \theta) = (2\pi R \sin \psi) \gamma \sin(\psi + \theta), \quad (4)$$

where γ is the liquid surface tension and θ is the water contact angle of the particle. The hydrostatic pressure force is given as [Zhang *et al.*, 1996; Singh and Joseph, 2005]

$$f_p = \pi(R \sin \psi)^2 \Delta p = \pi(R \sin \psi)^2 \rho_l g z_0, \quad (5)$$

where Δp is the pressure difference and z_0 is the deflection depth. To simplify the discussion, we can take

the weight of the particle in the air phase to be 0 by a balance, and we assume for the moment that the net DLVO force f_{DLVO} is 0. We will expand the discussion to the more general case later. Then, equation (1) can be written as

$$F = -(2\pi R \sin \psi) \gamma \sin(\psi + \theta) - \frac{\pi}{3} R^3 (1 - \cos \psi)^2 (2 + \cos \psi) \rho_l g + \pi(R \sin \psi)^2 \rho_l g z_0. \quad (6)$$

The deflection depth z_0 is related to the height of the water film H by [Zhang *et al.*, 1996]

$$H = z_0 + R(1 + \cos \psi). \quad (7)$$

2.3. Forces on a Cylinder at a Liquid-Gas Interface

[15] For particles with sharp edges or rims, such as cylinders, cubes, and prisms, the contact line moves along the smooth vertical surfaces as the liquid film expands or shrinks until it comes to rest at the sharp edge of the top surface (Figure 1b). Further movement of the liquid-gas interface will not change the contact line; rather, the contact angle changes. This is in conflict with the Young equation, which states that the equilibrium contact angle is constant. In this case, we can use the Gibbs extension to Young's equation [Singh and Joseph, 2005]:

$$\theta_0 < \theta < 180^\circ - \alpha + \theta_0, \quad (8)$$

where α is the wedge angle and θ_0 is the equilibrium contact angle for the vertical face. The angles θ_0 and $180^\circ - \alpha + \theta_0$ are the limits of the contact angle θ according to the Gibbs extension (Figure 1b).

[16] We describe the forces exerted on a cylindrical particle as follows [Princen, 1969; Hesla and Joseph, 2004; Singh and Joseph, 2005]. We assume that a cylinder with radius R and length L is adhered to point B on a horizontal solid surface and that the contact angle between the water-air interface and the vertical edge of the cylinder is θ (Figure 1b). When a liquid film builds up on the flat solid surface, the water film forms a meniscus around the cylinder, and the contact angle is the advancing contact angle between the cylinder and the liquid. When the liquid-gas interface reaches the sharp edge of the top surface of the cylinder, the contact angle θ increases from $\theta = \theta_0$ to maximal $\theta = 180^\circ - \alpha + \theta_0$. The vertical components of the forces exerted on the cylinder are

$$f_w = \pi R^2 \rho_s g L \quad (9)$$

$$f_b = -\pi R^2 \rho_l g L, \quad (10)$$

where L is the height of cylinder. If the contact angle θ at the pinned interface is larger than 90° , the surface tension and pressure forces are given by [Singh and Joseph, 2005]

$$f_s = -2\pi R \gamma \sin(\theta - 90^\circ) \quad (11)$$

$$f_p = -\rho_l g (H - L) \pi R^2. \quad (12)$$

When the weight of the particle is tared in the air phase with a balance and we neglect the DLVO forces for the moment, equation (1) becomes

$$F = -2\pi R \gamma \sin(\theta - 90^\circ) - \rho_l g H \pi R^2. \quad (13)$$

For the calculation of the pressure force, we need to know the height of the water film H as a function of the deflection depth z_0 [Singh and Joseph, 2005]:

$$H = z_0 + L. \quad (14)$$

Equations (6) and (7) (for the sphere) and (13) and (14) (for the cylinder) can be solved numerically as described in section 2.4 and allow us to calculate the force exerted by the liquid-gas interface as a function of water film height.

2.4. Numerical Solution

[17] The solutions of equations (6), (7), (13), and (14) require knowledge of the relation between the angular inclination of the interface ϕ and the height of water film H . This relation can be obtained by solving the Young-Laplace equation. We consider an unbounded liquid-gas interface in contact with an axisymmetric particle (Figure 1). The Young-Laplace equation describes the shape of the

axisymmetric meniscus [Princen, 1969; Veerapaneni et al., 2000]:

$$\gamma \left\{ \frac{d^2 y / dx^2}{[1 + (dy/dx)^2]^{3/2}} + \frac{dy/dx}{x[1 + (dy/dx)^2]^{1/2}} \right\} - g \rho_l y = 0 \quad (15)$$

together with the boundary conditions,

$$\frac{dy}{dx} = -\tan \phi_0 \quad \text{at} \quad x = x_0 \quad (16)$$

$$\frac{dy}{dx} = 0 \quad \text{at} \quad x \rightarrow \infty, \quad (17)$$

where x is the horizontal distance measured from the axis of symmetry, y is the vertical distance from the liquid-gas interface, x_0 is the horizontal distance to the intersection of the particle and the liquid-gas interface, and ϕ_0 is the angular inclination of the interface to the horizontal line at the intersection. By scaling with the capillary constant $c = \sqrt{\rho_l g / \gamma}$ we can define the following dimensionless variables [Princen, 1969; Veerapaneni et al., 2000]:

$$\hat{x} = cx \quad \text{and} \quad \hat{y} = cy, \quad (18)$$

where \hat{x} is the dimensionless horizontal distance measured from the axis of symmetry and \hat{y} is the dimensionless vertical distance from the interface. The Young-Laplace equation can then be transformed into a system of dimensionless differential equations [Princen, 1969; Veerapaneni et al., 2000]:

$$\frac{d \sin \phi}{d \hat{x}} + \frac{\sin \phi}{\hat{x}} - \hat{y} = 0, \quad (19)$$

$$\frac{d \hat{x}}{d \phi} = \frac{-\hat{x} \cos \phi}{\hat{x} \hat{y} + \sin \phi}, \quad (20)$$

$$\frac{d \hat{y}}{d \phi} = \frac{\hat{x} \sin(\phi)}{\hat{x} \hat{y} + \sin \phi}, \quad (21)$$

with the boundary conditions [Princen, 1969; Veerapaneni et al., 2000]

$$\phi = \phi_0, \quad \hat{y} = \hat{y}_0 \quad \text{at} \quad \hat{x} = \hat{x}_0 \quad (22)$$

$$\phi = 0, \quad \hat{y} = 0 \quad \text{at} \quad \hat{x} \rightarrow \infty, \quad (23)$$

where ϕ is the angular inclination of the interface to the horizontal, ϕ_0 is the angular inclination of the interface, and (\hat{x}_0, \hat{y}_0) are the dimensionless coordinates of the intersection of the particle and the liquid-gas interface.

[18] Equations (19)–(23) have to be solved by numerical integration. Because the integration starts at infinity, an appropriate starting point has to be chosen. We followed the approach described by Zhang et al. [1996], which uses

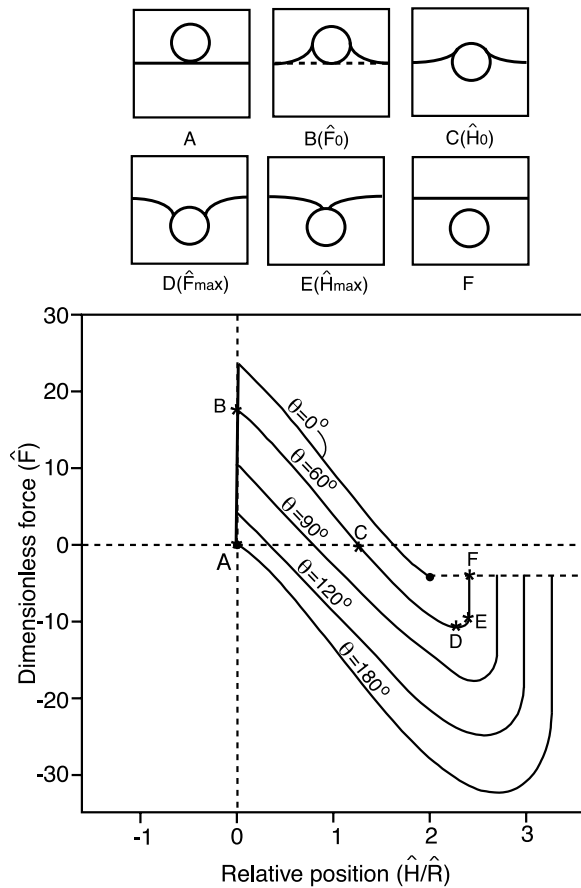


Figure 2. Examples of theoretical force-position curves for a sphere with $\hat{R} = 0.5$. Contact angles of water on the spheres are noted. The weight of the sphere in air is tared to 0. Letters indicate geometrical configurations and respective positions in the force-position curves shown for $\theta = 60^\circ$.

modified Bessel functions to find the starting point:

$$\sin(\phi^*) = Bk_1(\hat{x}^*), \quad (24)$$

$$\hat{y}^* = Bk_0(\hat{x}^*), \quad (25)$$

$$\hat{y}^* = \frac{k_0(\hat{x}^*)}{k_1(\hat{x}^*)} \sin(\phi^*), \quad (26)$$

where $(\hat{x}^*, \hat{y}^*, \phi^*)$ is an initial point on the liquid-gas interface used for the integration, ϕ^* is the dimensionless angle of the initial point on the liquid-gas interface, and k_0 and k_1 are modified Bessel functions of the second kind of order 0 and order 1, respectively, and B is an integration constant.

[19] The solution of the Young-Laplace equation has to satisfy the following conditions at the contact line with the particle:

For a sphere

$$\hat{x}_0 = \hat{R} \sin \psi \quad (27)$$

For a cylinder

$$\hat{x}_0 = \hat{R}, \quad (28)$$

where \hat{R} is the dimensionless radius of the sphere or cylinder. We solved the system of equations (equations (19)–(28)) by a fourth-order Runge-Kutta method using MATLAB (version 6.5.1, The MathWorks, Natick, Massachusetts).

[20] The solution of the Young-Laplace equation in combination with equations (6), (7), (13), and (14) can be used to develop force-position relationships [Huh and Mason, 1974; Fieber and Sonntag, 1979; Gunde et al., 1995; Zhang et al., 1996]. An example of such a relation for a sphere, which is initially in the air phase and which is subsequently passing through a liquid-gas interface, is shown in Figure 2. The schematic at the top of Figure 2 shows the relative movement of the particle and the liquid-gas interface. The particle is moved through the liquid-gas interface, and we neglect the presence of the solid-liquid interface, as we are interested in just the liquid-gas interface for the moment. In Figure 2 (bottom), we plotted the calculated dimensionless force $\hat{F} = F/(R^3 \rho_w g)$, where ρ_w is the density of water versus relative position \hat{H}/\hat{R} (dimensionless form $\hat{H} = cH$ and $\hat{R} = cR$) for contact angles $\theta = 0^\circ$, 60° , 90° , 120° , and 180° .

[21] We illustrate the behavior of the force for a spherical particle with a contact angle of 60° that is denser than the fluid. The curve begins at point A, where the sphere just touches the liquid-gas interface; then the liquid-gas interface jumps to its equilibrium condition at the sphere (point B), and an attractive capillary force is exerted. As the sphere moves downward, the capillary force decreases, and the buoyancy force starts to increase until at point C no net force ($\hat{F} = 0$) is exerted. When the sphere moves farther down, the net force becomes negative, i.e., in the upward direction, until a maximum upward force is reached at point D; further downward movement of the sphere causes the upward force to reduce again, until at point E the maximum deformation at the liquid-gas interface is reached; then the interface snaps off the sphere, and the force recovers to $\hat{F} = -4\pi/3$, corresponding to the dimensionless buoyancy force.

[22] For $\theta = 0^\circ$, the snap off occurs at point (2, $-4\pi/3$), where $\hat{F} = -4\pi/3$ is the buoyancy force. If the contact angle θ is greater than 0° , surface tension and pressure cause an additional upward force, as shown by the increasing maximal upward force in Figure 2. The larger the contact angle, the larger is the maximum upward force and the larger is the maximum deformation of the liquid-gas interface.

[23] In contrast to a sphere, for a cylindrical particle the liquid-gas interface pins at the sharp edge when the interface reaches the edge. The contact angle θ between cylinder and interface will increase as the liquid-gas interface moves upward. The contact angle is bounded by the Gibbs extension (equation (8)). If the equilibrium contact angle $\theta_0 < 120^\circ$, then the maximum upward capillary force occurs at $\theta = 180^\circ - 90^\circ + \theta_0$. If $\theta_0 > 120^\circ$, then the maximum force occurs when $\theta < 180^\circ - 90^\circ + \theta_0$.

[24] The theoretical force-distance curves can be used to determine the maximum upward force \hat{F}_{\max} (point D in Figure 2) and the maximum immersion depth H_{\max} at which the snap off occurs. The results for the total maximum upward forces ($\hat{F}_{\max} = \hat{f}_{\text{cap,max}} + \hat{f}_b$) are plotted in Figure 3a

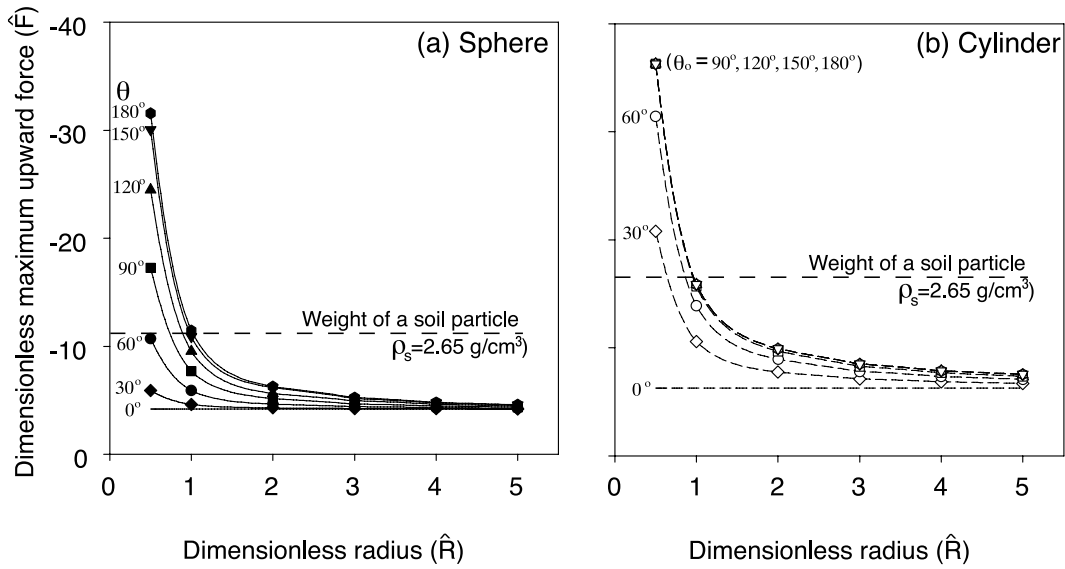


Figure 3. Theoretical total maximum upward force ($\hat{F}_{\max} = \hat{f}_{\text{cap,max}} + \hat{f}_b$, dimensionless) (a) spheres and (b) cylindrical cylinders ($\hat{L} = 2\hat{R}$) for different radii and contact angles θ . The dimensionless radius is defined as $\hat{R} = cR$, where c is the capillary constant. Also shown is the dimensionless weight of a typical spherical and cylindrical soil particle with density $\rho_s = 2.65 \text{ g cm}^{-3}$.

for spheres and Figure 3b for cylinders. Figure 3 shows that (1) for a given radius \hat{R} , the maximum upward force increases with contact angle θ ; (2) for a given contact angle $\theta > 0$, the maximum upward force and maximum deformation (dimensionless) increase when the size of the particle is reduced; and (3) for a given contact angle $\theta > 0$, the slopes of the maximum force-radius curve and of the maximum immersion depth-radius curve become increasingly steeper when \hat{R} is reduced. The forces for the cylinders exceed those of the spheres with the same radii and contact angles. If the contact angle is larger than 90° , little differences in the maximum capillary forces for the cylinders are observed, particularly if the particle size is small (Figure 3b).

[25] Figure 3 can be used to determine whether a particle can float at the air-water interface. For instance, the weight of a spherical particle with density of 2.65 g cm^{-3} , typical of soils and sediment particles, is $\frac{4}{3}\pi R^3 \rho_s g$. The dimensionless weight for such a particle using water as the fluid for the scaling is $\hat{f} = \frac{4}{3}\pi R^3 \rho_s g / (R^3 \rho_w g) = \frac{4}{3}\pi \rho_s / \rho_w = 11.1$. When the particle size \hat{R} decreases to a certain value, e.g., $\hat{R} \approx 0.5$ for $\theta = 60^\circ$, the upward force equals the weight of the particle, and the particle will float on the interface. When the surface of the particle becomes more hydrophilic, the size of the particle must become smaller before flotation can occur.

2.5. DLVO Forces

[26] If we assume that the soil particles are spherical, we can use DLVO theory for a sphere-plate system to calculate colloid-sediment interaction energies. The total interaction energy can be calculated as [Gregory, 1975, 1981]

$$\Delta G_{\text{tot}} = 64\pi\epsilon R \left(\frac{kT}{ve}\right)^2 \Upsilon_1 \Upsilon_2 \exp(-\kappa h) - \frac{AR}{6h} \left[1 - \frac{5.32h}{\lambda_0} \ln\left(1 + \frac{\lambda_0}{5.32h}\right) \right], \quad (29)$$

where the left-hand term is the electrostatic and the right-hand term is the van der Waals interactive energy, respectively; ϵ is the dielectric permittivity of the liquid; k is the Boltzmann constant; T is the absolute temperature; v is the ion valence; e is the electron charge; κ is the Debye-Hückel reciprocal length; h is the separation distance; and A is the Hamaker constant; $\Upsilon_i = \tanh[v e \psi_{0,i} / (4kT)]$, where $\psi_{0,i}$ are the surface potential of the colloids and the sediments, respectively; and λ_0 is a characteristic length of 100 nm. The total DLVO or adhesive force is

$$f_{\text{DLVO}} = \frac{d}{dh}(\Delta G_{\text{tot}}). \quad (30)$$

We assumed a separation distance of $h = 0.3 \text{ nm}$ [Elimelech *et al.*, 1995; Sharma *et al.*, 2008a] to calculate the value of the total DLVO force.

3. Materials and Methods

3.1. Particles Used for Force Measurements

[27] We used particles of well-defined geometry as well as natural soil particles for the force measurements. The particles of well-defined geometry consisted of spheres, cylinders, disks, and sheets (Table 1). These particles were all purchased from McMaster-Carr (Santa Fe Springs, California) and were cleaned by sequential immersion in acetone (once), ethanol (once), and deionized water (more than three times). The dimensions of the particles were measured with a micrometer caliper with an error of $\pm 0.01 \text{ mm}$. The density of the each type of material was calculated from the average weight and average volume.

[28] The natural subsurface particles were obtained from the sediments of the Hanford Environmental Restoration Disposal Facility, located 8 miles from the Columbia River between the 200 east and 200 west areas of the Hanford site (south-central Washington State, United States). Five dif-

Table 1. Characteristics of Spherical Beads and Sharp-Edged Particles

Shape	Material ^a	Diameter/ Length (mm)	Sphericity ^b / Height (mm)	Density (g cm ⁻³)	Contact Angle (deg)
Sphere	glass	2.37 ^c , 3.16 ^c , 3.95 ^c , 4.76, 6.34	<0.01	2.46	64 ± 1
Sphere	steel	1.00 ^c , 2.00, 3.00, 4.00, 5.00	<0.01	7.85	83 ± 1
Sphere	PTFE	2.37 ^c , 3.17 ^c , 3.97 ^c , 4.76 ^c , 6.35	<0.01	2.16	121 ± 3
Cylinder	steel	4.76	4.76	7.85	83 ± 1
Cylinder	PTFE	4.76	4.76	2.16	121 ± 3
Cube	steel	4.76	4.76	7.85	83 ± 1
Cube	PTFE	4.76	4.76	2.16	121 ± 3
Disk	steel	4.76	2.00	7.85	83 ± 1
Disk	PTFE	4.76	2.00	2.16	121 ± 3
Sheet	steel	4.76	2.00	7.85	83 ± 1
Sheet	PTFE	4.76	2.00	2.16	121 ± 3

^aGlass, heat-resistant borosilicate; steel, bearing-quality aircraft-grade E52100 alloy, chrome coated; PTFE, virgin electrical grade fluoropolymer.

^bDifference between measured maximum and minimum diameters.

^cParticles can be floated by pure water (on the basis of a flotation experiment).

ferent types of particles (three particles each) with size between 1 and 5 mm were selected (Table 2 and Figure 4). Particles were identified optically and microscopically. The particles were cleaned by sequential immersion in ethanol for 24 hours and deionized water for 24 hours, followed by air drying.

[29] The particles were mounted onto U-shaped hooks made of steel wire (Figure 5). We used these U-shaped hooks so that we could investigate the forces acting on the particles when a liquid-gas interface expands and moves over the particles. As the hook is attached to the bottom of the particle, it does not interfere with the liquid-gas interface. Two different diameter wires were used; a 0.5-mm wire was used for the three smallest spheres, the regular-shaped polytetrafluoroethylene (PTFE) objects, and a 0.78-mm

wire was used for the two largest spheres and the regular-shaped steel objects. The wires were cut to about 7-cm-long segments and were bent into hooks. The tips of the hooks were flattened with a file to ensure enough contact area with spheres and regular-shaped objects. The hooks were cleaned in the same manner as the particles. The glass and steel particles were then glued onto the hooks using Instant Krazy Glue (Elmer's Products, Inc., Columbus, Ohio). As the PTFE particles were difficult to glue to the hooks, a hole was drilled into each PTFE object with a microdrill (Dremel Moto-Tool model 395, Dremel, Racine, Wisconsin). A small amount of glue was applied into the hole, and the tip of the hook was inserted into the hole. The natural subsurface particles were glued onto the tip of the hook in the middle of one side.

3.2. Contact Angle Measurement

[30] We determined the advancing air-water-solid contact angle on the particles by using a goniometer (Drop Shape Analysis System, DSA100, Krüss GmbH, Hamburg, Germany). A spherical bead (4 or 4.76 mm in diameter) or a natural Hanford sediment particle (≈ 3 mm in diameter) was mounted on a microscopy slide using double-sided tape. A microsyringe with a steel needle (outer diameter 0.5 mm) was used to deposit a drop of water next to the bead or particle a short distance apart (0.2 mm). The test liquid ($5 \mu\text{L}$ of water) was then continuously dispensed at a flow rate of $5 \mu\text{L min}^{-1}$. The advancing contact angle was continuously measured by the goniometer.

3.3. Force-Position Curve Measurements

[31] We measured the forces between the particles and the air-water interface by using a tensiometer (Process Tensiometer, K100, Krüss GmbH, Hamburg, Germany). The hook with an attached particle was mounted onto the microbalance of the tensiometer. The air inside the sample chamber of the tensiometer was saturated with moisture by keeping wet paper towels inside the chamber. A cup with 65 mm inner diameter was used to hold the water in which the particle was immersed. Nanopure water with an electri-

Table 2. Characteristics and Maximum Capillary Force of Natural Hanford Sediments With Irregular Shape

Sediments	Number of Particle	Maximum Length (mm)	Maximum Width (mm)	Maximum Height (mm)	Angle Contact (deg)	Maximum Capillary Force ^a		
						Experimental (μN)	Theoretical	
							Sphere (μN)	Cylinder (μN)
Basalt	1	1.57	1.50	1.12	23 ± 3	-220 ± 15	-14	-148
	2	2.99	1.97	1.04	23 ± 3	-370 ± 20	-27	-308
	3	3.37	2.60	1.32	23 ± 3	-247 ± 11	-31	-356
Quartz	1	2.11	1.91	1.08	37 ± 3	-321 ± 17	-49	-319
	2	3.23	2.80	1.24	37 ± 3	-254 ± 12	-76	-527
	3	3.86	3.23	1.55	37 ± 3	-523 ± 20	-92	-653
Granite	1	1.97	1.71	1.11	22 ± 3	-194 ± 15	-16	-183
	2	4.32	3.34	1.29	22 ± 3	-197 ± 19	-37	-466
	3	3.42	2.92	1.04	22 ± 3	-265 ± 13	-29	-392
Biotite	1	1.49	1.58	1.20	37 ± 4	-103 ± 9	-34	-216
	2	2.45	2.45	0.20	37 ± 4	-427 ± 17	-57	-378
	3	3.13	2.75	0.11	37 ± 4	-496 ± 27	-74	-505
Calcite	1	3.1	2.68	1.77	14 ± 3	-13 ± 2	-11	-207
	2	3.85	3.12	1.78	14 ± 3	-95 ± 7	-13	-234
	3	3.28	2.92	1.05	14 ± 3	-94 ± 38	-11	-216

^aHere \pm denotes one standard deviation. Theoretical calculations of maximum capillary forces for spheres and cylinders are based on maximum lengths of Hanford sediments and are therefore maximum expected forces.

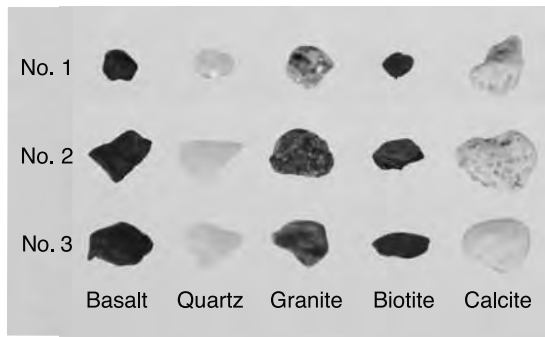


Figure 4. Five different natural Hanford sediment particles (basalt, quartz, granite, biotite, and calcite) with irregular shapes.

cal conductivity of $1.0 \mu\text{S m}^{-1}$ was used. Temperature of the water in the cup was controlled by a temperature jacket with a circulating water bath at $20 \pm 0.5^\circ\text{C}$. The precision of the tensiometer was 0.02 mg or $0.196 \mu\text{N}$.

[32] At the beginning of the measurements, the hook and the particle were in the air phase, and the tensiometer balance was tared to 0. The particle was then successively immersed into the water by raising the water cup, whose velocity was controlled by the tensiometer. The force on the object was recorded in 0.05-mm position increments as the particle passed through the air-water interface. When the particle was completely immersed in the water, the water cup was lowered at the same velocity until the particle was in its original position above the air-water interface. This sequence was repeated five times for each particle. The data were then used to construct force-position curves.

[33] As the force measured is dependent of the surface tension of the fluid, we verified the surface tension of the water in the cup using the Wilhelmy plate method. The surface tensions of water before and after immersion of the objects did not change significantly. Average surface tension was $72.4 \pm 0.4 \text{ mN m}^{-1}$ before each force-position measurement cycle and $72.0 \pm 0.3 \text{ mN m}^{-1}$ after the measurements.

[34] An initial test was performed to assess the effect of immersion velocity on the force measurements. For this test, we used only one size (4.8 or 5.0 mm) of each sphere type. We determined force-position curves at interface velocities ranging from 0.25 to 10 mm min^{-1} . Standard errors of the force for different velocities were within 4% , suggesting that the air-water interface reached equilibrium with the bead at speeds up to at least 10 mm min^{-1} . We selected an

immersion speed of 1.0 mm min^{-1} for the experimental measurements.

4. Results and Discussion

4.1. Force-Position Curves

[35] Figure 6 shows examples of measured force curves. These curves can be categorized into the following segments. Before the hook touches the air-water interface, the weight of the sphere and hook was tared to 0; no net force is recorded (stage a). When the bottom of the hook touches the water, a downward attractive (positive) force, due to the capillary force on the hook itself, is recorded (stage b). When the hook is further immersed into water, the attractive force reduces, and when the air-water interface bends downward, capillary and buoyancy forces on the hook cause an upward lifting (negative) force (stage c). The upward force reaches its maximum just before the air-water interface detaches from the horizontal part of the hook and the force recovers to nearly zero (stage d). Once the particle touches the air-water interface, a maximum downward attractive force is recorded (stage e). As the particle continues to be immersed into the water, the surface tension and buoyancy forces cause the force to become smaller until it becomes an upward lifting (negative) force; the force reaches a minimum and then increases slightly (stage f). When the maximum deformation of the air-water interface is reached, the deformed air-water interface snaps back to its original flat surface (stage g). The surface tension force on the wire and the buoyancy forces on the object and wire contribute to the upward force thereafter; the slight slope observed as the particle is continued to be immersed corresponds to the increase of the buoyancy force (stage h).

[36] During emersion the forces are downward (positive) throughout the emersion process, except for the portion of the curve where the particle is completely immersed in the fluid and the buoyancy force points upward. The hysteresis observed between immersion and emersion is due to contact angle hysteresis (advancing versus receding). In addition, the nonsymmetry due to the presence of the hook contributes to hysteresis.

[37] The measured force-position curves are, for the large part, affected by the interactions of the hook with the air-water interface. The relevant sections for the particle interactions with the air-water interface are stages e, f, g, and h. We are particularly interested in the magnitude of the upward lifting forces during particle immersion and the maximum upward force just before snap off of the particle from the air-water interface. The maximum upward capil-

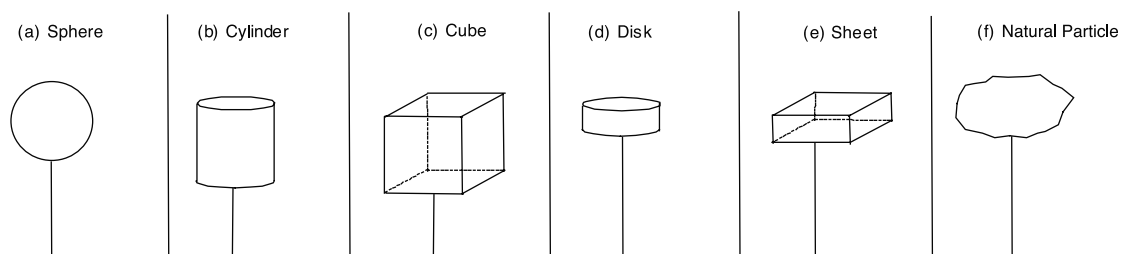


Figure 5. Different shape particles: (a) sphere, (b) cylinder, (c) cube, (d) disk, (e) sheet, and (f) natural particle with hooks.

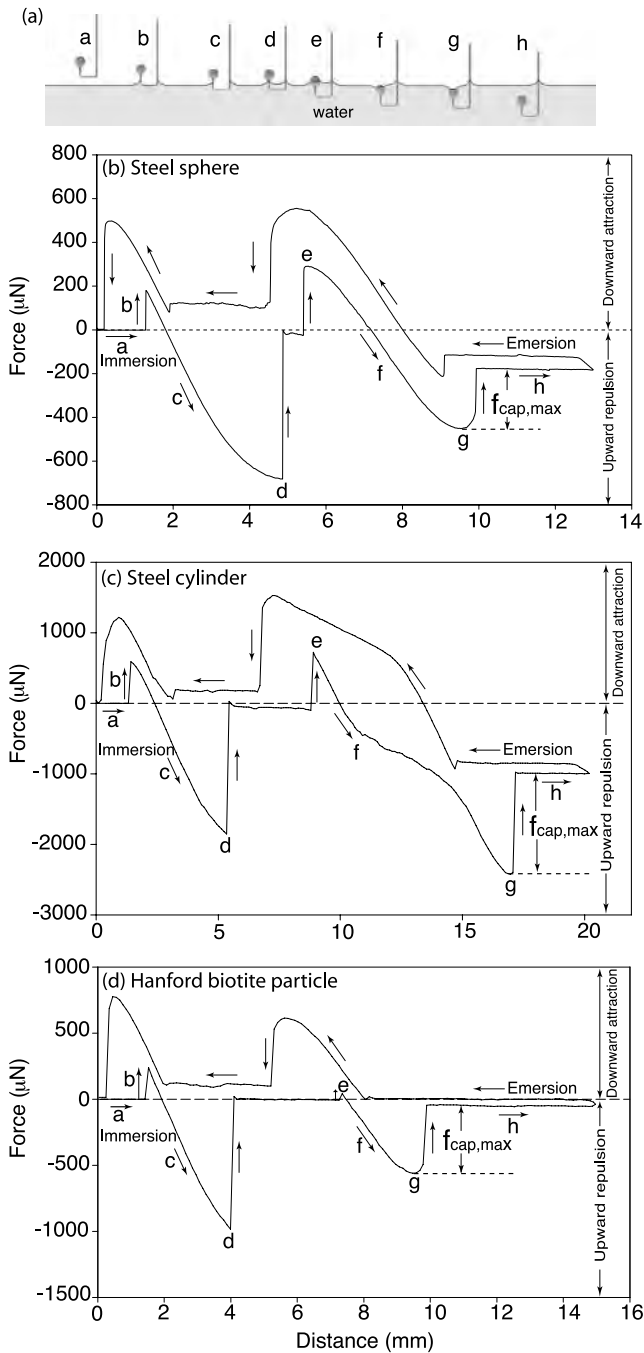


Figure 6. (a) Schematic of immersion of a particle into water, (b) corresponding measured force-position curve for a 3-mm diameter steel sphere, (c) a 4.76 mm diameter and 4.76 mm height steel cylinder, and (d) a Hanford biotite particle. Here $f_{\text{cap,max}}$ is the maximum upward capillary force.

lary force $f_{\text{cap,max}}$ can be determined from the force-position curves as the difference Δf between the maximum upward force before snap off and the force just after snap off between stage g and stage h (Figure 6). As there is only an insignificant movement of the horizontal section of the air-water interface with respect to the particle during snap off, the measured force $f_{\text{cap,max}}$ is not affected by buoyancy differences.

[38] Figure 6 also shows that for all the particles investigated in our study, we measured upward repulsion forces, i.e., the air-water interface caused an upward force when the interface moved over the particles. The tensiometer measurements were well suited to quantify the forces, even for the irregular-shaped sediment particles.

4.2. Maximum Capillary Force

[39] For spherical particles, the maximum capillary force $f_{\text{cap,max}}$ increased with radius and hydrophobicity of the beads (Figure 7a). Experimental data generally agreed well with calculated values. For PTFE, the relative errors were less than 5%, and for steel they were less than 9%. For glass, the errors were greater (up to 43% for the smallest sphere), which was likely caused by the small forces measured. In dimensionless form (Figure 7b), the maximum capillary force, $\hat{f}_{\text{cap,max}}$, decreased when the particle size increased, and the slopes of the curve were steeper for small particle sizes.

[40] Figure 8 shows the theoretical maximum capillary forces for spheres and cylinders with different contact angles. The theoretical maximum capillary forces for the cylinders are always greater than those for spheres with the same diameter and contact angle. In contrast to the sphere, the liquid-gas interface pins at the sharp edge of the cylinder, and as a consequence, the effective contact angle exceeds the equilibrium contact angle (Gibbs extension). The pinning increases not only the effective contact angle but also the effective perimeter (radius) on which the surface tension force acts, thereby contributing to additional increase of the maximum capillary force as compared to a smooth spherical particle. These factors cause particles with sharp edges to have larger negative capillary forces than particles with smooth edges.

[41] Figure 8 also shows that the maximum capillary force drastically increases as the dimensionless particle size becomes smaller. Although we do not have experimental data to verify the forces at small particle size, the calculations imply that for colloidal particles (size $<10 \mu\text{m}$), capillary forces are becoming exceedingly important.

[42] The experimental and theoretical forces for the steel and PTFE particles with sharp edges are summarized in Table 3. The cubes and sheets had the strongest experimental maximum capillary forces because their perimeter was the largest. No theoretical calculations for the rectangular perimeters were done, so we cannot compare with theory. For the cylindrical particles (cylinder and disk), the experimental data agree well with theoretical calculations.

[43] The sediment particles with irregular shapes have sharp edges on the surface, which will increase the maximum capillary forces, causing the particle to float or detach from a solid surface. Table 2 shows that the sediment particles had negative capillary forces as the air-water interface passed over the particles. We cannot calculate the capillary forces for the natural particles theoretically, but we can approximate the maximum capillary force by using a sphere and cylinder equivalent, i.e., a sphere and cylinder having a diameter equal to the maximum length of the natural particle. The maximum repulsive (upward) forces measured for the sediment particles were considerably larger than theoretical values for equivalent spheres (Table 2). The values for a cylinder are generally closer to the experimental values, although deviations of up to a

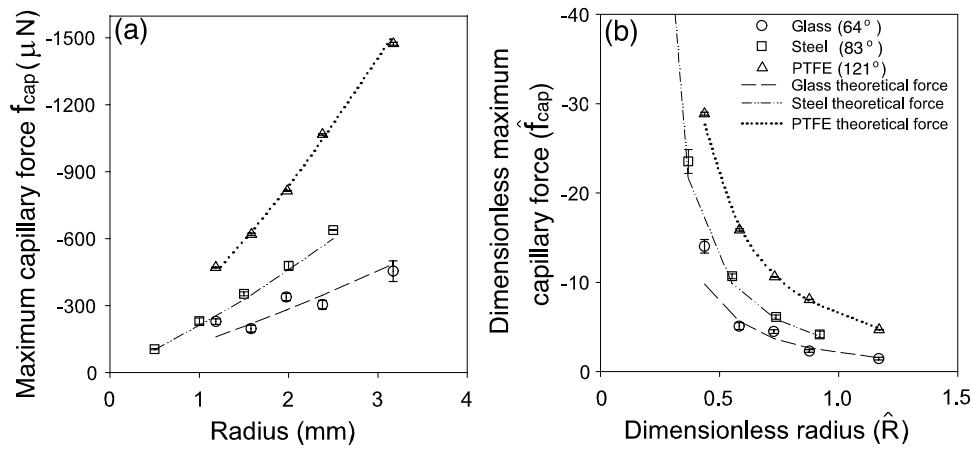


Figure 7. Measured (open symbols) and theoretical (dashed lines) maximum capillary force of spherical beads as a function of sphere radius: (a) dimensional and (b) dimensionless form. Error bars represent plus or minus one standard deviation.

factor of 2 were observed (Table 2). For calcite, the experimental values were closer to the sphere than to the cylinder calculations, which can be explained by the relatively smooth surface of the calcite particles (Figure 4).

4.3. Force Balance Considerations

[44] Now we discuss the more general case in which the DLVO forces are considered. If the particle is in contact with a solid-liquid interface, the particle experiences DLVO forces, which can be calculated with equation (30). We are interested in colloid detachment and mobilization in natural

subsurface media, so we consider the case of natural subsurface particles here. For illustrative purposes, we are using DLVO parameters as used by *Shang et al.* [2008a]: particle radius = 250 nm, electrophoretic mobility = -3.18 ± 0.07 ($\mu\text{m s}^{-1}/(\text{V cm}^{-1})$), ζ potential = -40.1 ± 0.9 mV, and water contact angle = $25.9 \pm 2.5^\circ$. Sediments (the stationary phase) and particles are assumed to have the same properties. The sediments are assumed to be flat plates.

[45] To illustrate the importance of the DLVO forces, we plotted the different forces as a function of ζ potential for a particle with radius 250 nm and contact angle $\theta = 25.9^\circ$

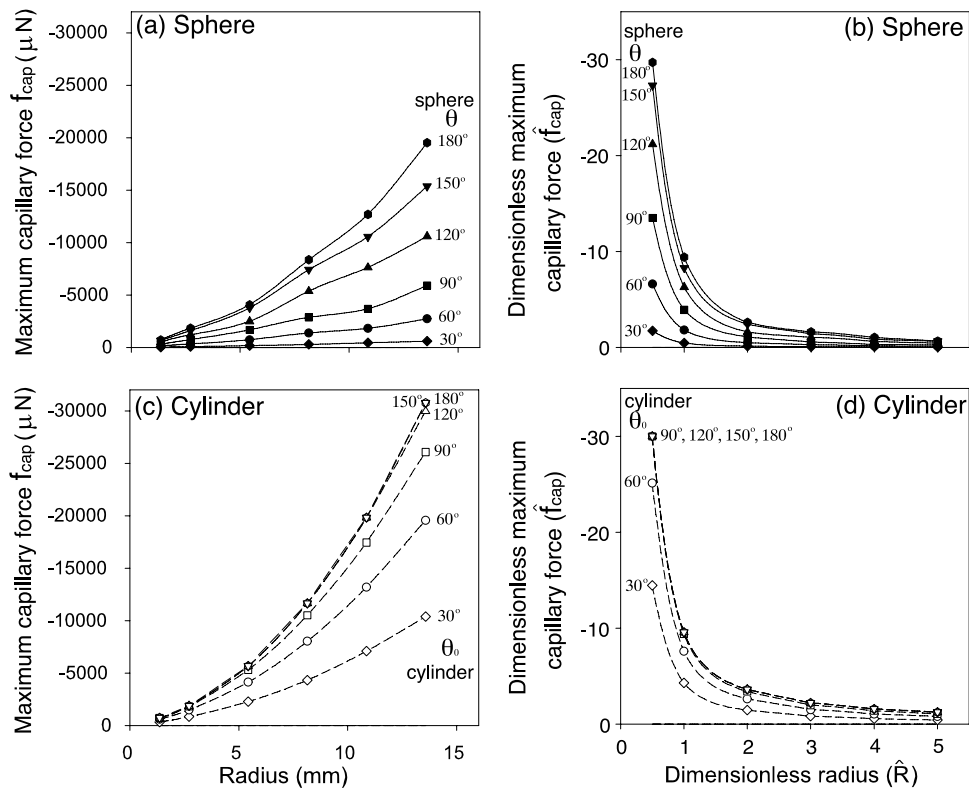


Figure 8. Theoretical maximum capillary force ($f_{\text{cap,max}}$) on (top) a sphere with radius R and (bottom) a cylindrical cylinder ($L = 2R$) for different radii and contact angles: (a, c) dimensional and (b, d) dimensionless form.

Table 3. Maximum Capillary Forces (Upward Forces) for Regular-Shaped Particles With Sharp Edges

Material	Shape	Size (mm × mm)	Contact Angle (deg)	Maximum Capillary Force	
				Experimental Force (μN)	Theoretical Force ^a (μN)
Steel	cylinder	4.76×4.76	83 ± 1	-1468 ± 17	-1497
	cube	4.76×4.76	83 ± 1	-1608 ± 10	na
	disk	4.76×2.00	83 ± 1	-1497 ± 6	-1497
	sheet	4.76×2.00	83 ± 1	-1554 ± 26	na
PTFE	cylinder	4.76×4.76	121 ± 3	-1545 ± 3	-1553
	cube	4.76×4.76	121 ± 3	-1580 ± 36	na
	disk	4.76×2.00	121 ± 3	-1565 ± 2	-1553
	sheet	4.76×2.00	121 ± 3	-1634 ± 2	na

^aNa means theoretical data not available.

(Figure 9). This particular size and contact angle were chosen on the basis of experimental measurements with sediments taken from the Hanford site [Chen and Flury, 2005; Shang et al., 2008a]. The contact angle is also within the range of experimentally measured contact angles for various subsurface colloids [Shang et al., 2008b]. Figure 9 shows that for colloids with radius 250 nm and contact angle $\theta = 25.9^\circ$, the attractive net DLVO force is always smaller than the maximum repulsive capillary force, even though the net DLVO force increases when ζ potential increases from -100 to $+100$ mV. No matter what the surface charge of particles, the DLVO forces at the separation distance 0.3 nm are smaller than the repulsive capillary force.

[46] The different forces acting on a spherical particle as a function of particle size and contact angle are shown in Figure 10. Figure 10a shows that for a particle with contact angle $\theta = 25.9^\circ$ (1) the maximum capillary force and the DLVO forces are dominant in the system when particle radius is less than about 0.1 mm, and (2) the buoyancy and weight forces become more important when particle radius

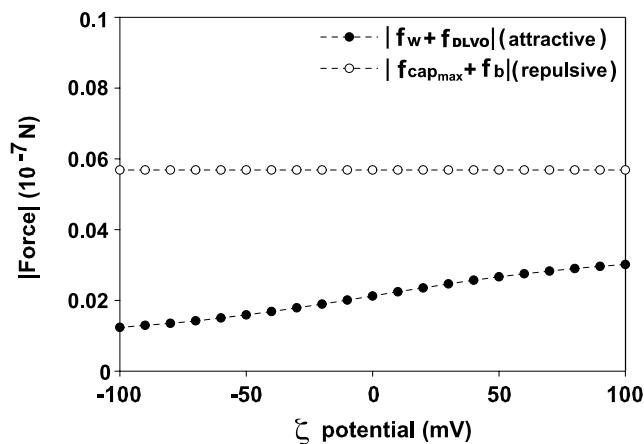


Figure 9. Net attractive and net maximum repulsive forces acting on a spherical particle in contact with an air-water interface as a function of ζ potential for fixed particle radius 250 nm, contact angle 25.9° , and density of 2.65 g cm^{-3} . Here f_w is weight, f_{DLVO} is the sum of van der Waals force and electrostatic force, $f_{cap,max}$ is the maximum upward capillary force, and f_b is the buoyancy force. The ζ potential of sediments is fixed to -40.1 mV.

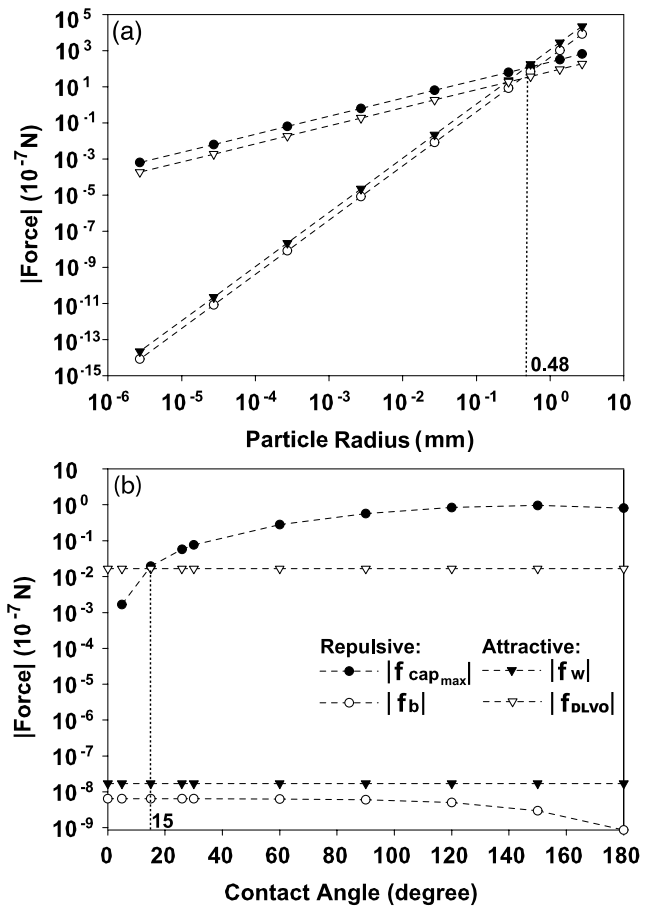


Figure 10. Attractive and repulsive forces acting on spherical particle with ζ potential -40.1 mV in contact with an air-water interface as a function of (a) particle radius for a fixed contact angle (25.9°) and (b) contact angle for a fixed particle radius (250 nm).

is larger than about 0.1 mm. The net forces show that the maximum repulsive forces are dominating up to a particle size of 0.48 mm, after which attractive forces start to dominate. This means that particles less than 0.48 mm can be lifted off the sediment surfaces by the maximum total upward force (the sum of maximum capillary and buoyancy force).

[47] To show the effects of the contact angle, the different forces are plotted as a function of contact angle for a particle with radius 250 nm (Figure 10b). Figure 10b shows that (1) the buoyancy and weight forces are small compared to other two forces, and (2) for colloids with radius 250 nm, the maximum repulsive capillary force and the attractive net DLVO force are the dominant forces to determine colloid retention and release. For contact angles less than 15° , attractive forces are dominant; above this contact angle repulsive forces dominate. This suggests that the repulsive forces are dominant for a large range of surface charges, particle sizes, and contact angles.

[48] In the previous considerations, the gravity force is considered to be pointing in the opposite direction from the repulsive capillary force, and the gravity force contributes an attractive component between the particle and the sediment surface. If the gravity force points in the direction parallel to or in the direction of the repulsive capillary force,

it will contribute an additional detachment force. According to our calculations of the torque balances, the gravity force (weight), however, is considerably smaller than capillary and DLVO forces for colloidal particles; only for large particles, the gravity force will become important (Figure 10).

5. Implications for Colloid Mobilization in the Vadose Zone

[49] Our experiments demonstrate that capillary forces acting at the air-water interface in porous media can cause strong repulsion of particles from the stationary surfaces when water films expand or move through the porous medium. No matter whether the surface charge of particles is negative or positive, the maximum repulsive capillary force is larger than the net DLVO force. For particles in the size range of fine sands, silt, and clay, the repulsive capillary force also exceeds attractive DLVO and gravity forces. The capillary force is therefore a dominant force in colloid mobilization in unsaturated soil and sediments. The repulsive capillary force becomes more dominant the smaller the particle; that is, particles in the colloidal size fraction (diameter $<2 \mu\text{m}$) will be most affected by the repulsive capillary force. In addition, a rough and irregular surface shape causes the capillary force to increase as compared to a smooth, spherical shape, making natural particles even more prone to detachment and mobilization due to moving air-water interfaces.

[50] For the repulsive capillary force to be effective, a liquid film must build up around particles and the film must expand beyond the diameter of the particles themselves so that a lift off can occur. In soils and sediments, some of the small particles are likely already completely covered with a liquid film, so the repulsive capillary force will not act on all the particles, even when an infiltration or drainage front moves through the medium. This will cause only a fraction of the colloids to be detached and mobilized by moving water fronts. On the other hand, if soils are initially dry, then it is expected that an infiltration front will remove more particles than if the soil is initially wet. This is in qualitative agreement with experimental observations of colloid mobilization in field soils, which showed that more colloids were mobilized after periods of drying [Totsche *et al.*, 2007; Majdalani *et al.*, 2008].

[51] While the capillary forces discussed in this paper may be dominant in coarse-textured soils and sediments, other mechanisms likely will also contribute to colloid mobilization in silty and clayey soils. Majdalani *et al.* [2008] hypothesized that capillary stresses during drying cause flaws and cracks in pore walls, which subsequently promotes colloid mobilization during infiltration. Prolonged drying, however, may lead to increased cohesion between particles, particularly in clayey soils, so fewer colloids will be removed during subsequent infiltration [Kjaergaard *et al.*, 2004; Majdalani *et al.*, 2008]. Nonetheless, repulsive capillary forces will play an important role, even in fine-texture soils and sediments.

Notation

Latin symbols

- A Hamaker constant [$M L^2 T^{-2}$].
 B integration constant [dimensionless].

- c capillary constant $c = \sqrt{\rho_l g / \gamma}$ [L^{-1}].
 e electron charge (1.6×10^{-19} C) [Q].
 f_{DLVO} sum of van der Waals force and electrostatic force between the particle and the surface (downward or upward depending on surface charges and solution chemistry) [$M L T^{-2}$].
 f_b buoyancy force (upward) [$M L T^{-2}$].
 f_p pressure force due to pressure difference across the curved air-water interface [$M L T^{-2}$].
 f_{cap} sum of surface tension and hydrostatic pressure force [$M L T^{-2}$].
 $f_{\text{cap,max}}$ maximum upward capillary force [$M L T^{-2}$].
 f_s surface tension force (downward or upward depending on contact angle) [$M L T^{-2}$].
 f_w weight of the particle (downward) [$M L T^{-2}$].
 \hat{f} dimensionless force.
 \hat{f}_{cap} sum of dimensionless surface tension and dimensionless hydrostatic pressure force.
 F sum of f_{DLVO} , f_w , f_s , f_b , and f_p [$M L T^{-2}$].
 \hat{F} dimensionless sum of forces of f_{DLVO} , f_w , f_s , f_b , and f_p .
 \hat{F}_{max} dimensionless maximum upward force.
 g gravitational acceleration [$L T^{-2}$].
 h separation distance [L].
 H height of water film [L].
 \hat{H} dimensionless height of water film above reference line.
 \hat{H}_{max} dimensionless maximum height of water film above reference line.
 k Boltzmann constant (1.38×10^{-23} J K $^{-1}$) [$M L^2 T^{-2} \theta^{-1}$].
 $k_0(x)$ modified Bessel function of the second kind of order 0 [dimensionless].
 $k_1(x)$ modified Bessel function of the second kind of order 1 [dimensionless].
 L height of cylinder [L].
 R radius of sphere or cylinder [L].
 \hat{R} dimensionless radius of sphere or cylinder.
 T absolute temperature [θ].
 ν ion valence [dimensionless].
 x horizontal distance measured from the axis of symmetry [L].
 \hat{x} dimensionless horizontal distance measured from the axis of symmetry.
 \hat{x}_0 dimensionless horizontal distance measured from the axis of symmetry to where the liquid-gas interface meets the particle.
 \hat{x}^* dimensionless horizontal distance of the initial point on the liquid-gas interface.
 y vertical distance measured upward/downward from the interface [L].
 \hat{y}^* dimensionless vertical distance of the initial point on the liquid-gas interface.
 \hat{y} dimensionless vertical distance measured upward/downward from the interface.

- z_0 deflection depth related to the length of the water film [L].
- \hat{y}_0 dimensionless vertical distance measured upward/downward from the interface to where the liquid-gas interface meets the particle.
- Greek symbols
- α wedge angle [degrees].
- γ liquid surface tension [$M T^{-2}$].
- ΔG_{tot} total interaction energy [$M L^2 T^{-2}$].
- Δp pressure difference [$M L^{-1} T^{-2}$].
- ϵ permittivity of the liquid [$L^2 T^4 L^{-3} M^{-1}$].
- Υ_i surface potential of the colloids and the sediments or the liquid-gas interface [$M T^{-3} L^2 I^{-1}$].
- ρ_a density of air phase [$M L^{-3}$].
- ρ_l density of liquid phase [$M L^{-3}$].
- ρ_s density of solid phase [$M L^{-3}$].
- ρ_w density of water [$M L^{-3}$].
- θ water contact angle of the particle [degrees].
- θ_0 equilibrium contact angle for the vertical face of the particle with sharp edges [degrees].
- ϕ angular inclination of the interface to the horizontal [degrees].
- ϕ_o angular inclination of the interface to the horizontal line when the interface meets the particle surface [degrees].
- ϕ^* dimensionless angle of the initial point on the liquid-gas interface.
- κ Debye-Hückel reciprocal length [L^{-1}].
- λ_0 characteristic length of system [L].
- ψ filling angle between the center of the colloidal sphere and the water-colloid contact line [degrees].
- Fieber, C., and H. Sonntag (1979), Theoretical consideration on the applicability of the sphere method for measuring interfacial tension and contact angle, *Colloid Polym. Sci.*, 257, 874–881.
- Flury, M., and H. Qiu (2008), Modeling colloid-facilitated contaminant transport in the vadose zone, *Vadose Zone J.*, 7, 682–697.
- Gao, B., T. S. Steenhuis, Y. Zevi, V. L. Morales, J. L. Nieber, B. K. Richards, J. F. McCarthy, and J.-Y. Parlange (2008), Capillary retention of colloids in unsaturated porous media, *Water Resour. Res.*, 44, W04504, doi:10.1029/2006WR005332.
- Gillies, G., M. Kappel, and H.-J. Butt (2005), Direct measurements of particle-bubble interactions, *Adv. Colloid Interface Sci.*, 114, 165–172.
- Gonzonbach, U. T., A. R. Studart, E. Tervoort, and L. J. Gauckler (2006), Ultrastable particle-stabilized foams, *Angew. Chem. Int. Ed.*, 45, 3526–3530.
- Gregory, J. (1975), Interaction of unequal double layers at constant charge, *J. Colloid Interface Sci.*, 51, 44–51.
- Gregory, J. (1981), Approximate expressions for retarded van der Waals interaction, *J. Colloid Interface Sci.*, 83, 138–145.
- Gunde, R., S. Hartland, and R. Mader (1995), Sphere tensiometry: A new approach to simultaneous and independent determination of surface tension and contact angle, *J. Colloid Interface Sci.*, 176, 17–30.
- Hesla, T. I., and D. D. Joseph (2004), The maximum contact angle at the rim of a heavy floating disk, *J. Colloid Interface Sci.*, 279, 186–191.
- Hiemenz, P. C., and R. Rajagopalan (1997), *Principles of Colloid and Surface Chemistry*, 3rd ed., Marcel Dekker, New York.
- Honeyman, B. D. (1999), Colloidal culprits in contamination, *Nature*, 397, 23–24.
- Huh, C., and S. G. Mason (1974), The flotation of axisymmetric particles at horizontal liquid interfaces, *J. Colloid Interface Sci.*, 47, 271–289.
- Huh, C., and S. G. Mason (1976), Sphere tensiometry: An evaluation and critique, *Can. J. Chem.*, 54, 969–978.
- Hunter, R. J. (2001), *Foundations of Colloid Science*, 2nd ed., Oxford Univ. Press, Oxford, U. K.
- Israelachvili, J. (1992), *Intermolecular and Surface Forces*, Academic, London.
- Kjaergaard, C., L. W. de Jonge, P. Moldrup, and P. Schjonning (2004), Water dispersible colloids: Effects of measurement method, clay content, initial soil matric potential, and wetting rate, *Vadose Zone J.*, 3, 403–412.
- Kretzschmar, R., M. Borkovec, D. Grolimund, and M. Elimelech (1999), Mobile subsurface colloids and their role in contaminant transport, *Adv. Agron.*, 66, 121–193.
- Lazouskaya, V., and Y. Jin (2008), Colloid retention at air-water interface in a capillary channel, *Colloids Surf. A*, 325, 141–151.
- Majdalani, S., E. Michel, L. Di-Pietro, and R. Angulo-Jaramillo (2008), Effects of wetting and drying cycles on in situ soil particle mobilization, *Eur. J. Soil Sci.*, 59, 147–155.
- McCarthy, J. F., and L. D. McKay (2004), Colloid transport in the subsurface: Past, present, and future challenges, *Vadose Zone J.*, 3, 326–337.
- Preuss, M., and H.-J. Butt (1998a), Direct measurement of particle-bubble interactions in aqueous electrolyte: Dependence on surfactant, *Langmuir*, 14, 3164–3174.
- Preuss, M., and H.-J. Butt (1998b), Measuring the contact angle of individual colloidal particles, *J. Colloid Interface Sci.*, 208, 468–477.
- Princen, H. M. (1969), Equilibrium shape of interfaces, drops, and bubbles. Rigid and deformable particles at interfaces, *Surf. Colloid Sci.*, 2, 1–84.
- Saier, J. E., and J. J. Lenhart (2003), Colloid mobilization and transport within unsaturated porous media under transient-flow conditions, *Water Resour. Res.*, 39(1), 1019, doi:10.1029/2002WR001370.
- Scheludko, A., B. V. Toshev, and D. T. Bojadjev (1976), Attachment of particles to a liquid surface (capillary theory of flotation), *J. Chem. Soc. Faraday Trans. 1*, 72, 2815–2828.
- Schulze, H. D. (1977), New theoretical and experimental investigations on the stability of bubble/particle aggregates in flotation: A theory on the upper particle size on floatability, *Int. J. Miner. Process.*, 4, 241–259.
- Shang, J., M. Flury, G. Chen, and J. Zhuang (2008a), Impact of flow rate, water content, and capillary forces on in situ colloid mobilization during infiltration in unsaturated sediments, *Water Resour. Res.*, 44, W06411, doi:10.1029/2007WR006516.
- Shang, J., M. Flury, J. B. Harsh, and R. L. Zollars (2008b), Comparison of different methods to measure contact angles of soil colloids, *J. Colloid Interface Sci.*, 328, 299–307.
- Sharma, P., H. Abdou, and M. Flury (2008a), Effect of the lower boundary condition and flotation on colloid mobilization in unsaturated sandy sediments, *Vadose Zone J.*, 7, 930–940.

[52] **Acknowledgment.** This material is based upon work supported by the U.S. Department of Energy, Office of Science (BER), under award E-FG02-08ER64660.

References

- Abdel-Fattah, A. I., and M. S. El-Genk (1998a), On colloidal particle sorption onto a stagnant air-water interface, *Adv. Colloid Interface Sci.*, 78, 237–266.
- Abdel-Fattah, A. I., and M. S. El-Genk (1998b), Sorption of hydrophobic, negatively charged microsphere onto a stagnant air/water interface, *J. Colloid Interface Sci.*, 202, 417–429.
- Auset, M., A. A. Keller, F. Brissaud, and V. Lazarova (2005), Intermittent filtration of bacteria and colloids in porous media, *Water Resour. Res.*, 41, W09408, doi:10.1029/2004WR003611.
- Binks, B. P. (2002), Particles as surfactants—Similarities and differences, *Curr. Opin. Colloid Interface Sci.*, 7, 21–41.
- Chen, G., and M. Flury (2005), Retention of mineral colloids in unsaturated porous media as related to their surface properties, *Colloids Surf. A*, 256, 207–216.
- Crist, J. T., Y. Zevi, J. F. McCarthy, J. A. Troop, and T. S. Steenhuis (2005), Transport and retention mechanisms of colloids in partially saturated porous media, *Vadose Zone J.*, 4, 184–195.
- Du, Z., M. P. Bilbao-Montoya, B. P. Binks, E. Dickinson, R. Ettelaie, and B. S. Murray (2003), Outstanding stability of particle-stabilized bubbles, *Curr. Opin. Colloid Interface Sci.*, 19, 3106–3108.
- Ecke, S., M. Preuss, and H. J. Butt (1999), Microsphere tensiometry to measure advancing and receding contact angles on individual particles, *J. Adhesion Sci. Technol.*, 13, 1181–1191.
- Elimelech, M., J. Gregory, X. Jia, and R. A. Williams (1995), *Particle Deposition and Aggregation: Measurement, Modelling, and Simulation*, Butterworth-Heinemann, Oxford, U. K.

- Sharma, P., M. Flury, and J. Zhou (2008b), Detachment of colloids from a solid surface by a moving air-water interface, *J. Colloid Interface Sci.*, *326*, 143–150.
- Singh, P., and D. D. Joseph (2005), Fluid dynamics of floating particles, *J. Fluid Mech.*, *530*, 31–80.
- Sirivithayapakorn, S., and A. Keller (2003), Transport of colloids in unsaturated porous media: A pore-scale observation of processes during the dissolution of air-water interface, *Water Resour. Res.*, *39*(12), 1346, doi:10.1029/2003WR002487.
- Steenhuis, T., et al. (2006), Biocolloid retention in partially saturated soils, *Biologia*, *61*, S229–S233.
- Sur, J., and H. K. Pak (2001), Capillary force on colloidal particles in a freely suspended liquid thin film, *Phys. Rev. Lett.*, *86*, 4326–4329.
- Totsche, K. U., S. Jann, and I. Kögel-Knabner (2007), Single event-driven export of polycyclic aromatic hydrocarbons and suspended matter from coal tar-contaminated soil, *Vadose Zone J.*, *6*, 233–243.
- Veerapaneni, S., J. Wan, and T. Tokunaga (2000), Motion of particles in film flow, *Environ. Sci. Technol.*, *34*, 2465–2471.
- Wan, J. M., and T. K. Tokunaga (1997), Film straining of colloids in unsaturated porous media: Conceptual model and experimental testing, *Environ. Sci. Technol.*, *31*, 2413–2420.
- Wan, J. M., J. L. Wilson, and T. L. Kieft (1994), Influence of the gas-water interface on transport of microorganisms through unsaturated porous media, *Appl. Environ. Microbiol.*, *60*, 509–516.
- Williams, D. F., and J. C. Berg (1992), The aggregation of colloidal particles at the air-water interface, *J. Colloid Interface Sci.*, *152*, 218–229.
- Zhang, L., L. Ren, and S. Hartland (1996), More convenient and suitable methods for sphere tensiometry, *J. Colloid Interface Sci.*, *180*, 493–503.
- Zhang, L., L. Ren, and S. Hartland (1997), Detailed analysis of determination of contact angle using sphere tensiometry, *J. Colloid Interface Sci.*, *192*, 306–318.
- Zhang, P., W. P. Johnson, and R. Rowland (1999), Bacterial tracking using ferrographic separation, *Environ. Sci. Technol.*, *33*, 2456–2460.

Y. Deng, Department of Soil and Crop Sciences, Texas A&M University, College Station, TX 77843, USA.

M. Flury and J. Shang, Department of Crop and Soil Sciences, Washington State University, Pullman, WA 99164-6420, USA. (flury@wsu.edu)



Comparison of different methods to measure contact angles of soil colloids

Jianying Shang^a, Markus Flury^{a,b,*}, James B. Harsh^a, Richard L. Zollars^c

^a Department of Crop and Soil Sciences, Center for Multiphase Environmental Research, Washington State University, Pullman, WA 99164, USA

^b Department of Biological Systems Engineering, Washington State University, Pullman, WA 99164, USA

^c Department of Chemical Engineering, Washington State University, Pullman, WA 99164, USA

ARTICLE INFO

Article history:

Received 29 July 2008

Accepted 12 September 2008

Available online 20 September 2008

Keywords:

Colloids

Contact angle

Silicates

Clay

Wilhelmy plate

Thin-layer wicking

Sessile drop

ABSTRACT

We compared five different methods, static sessile drop, dynamic sessile drop, Wilhelmy plate, thin-layer wicking, and column wicking, to determine the contact angle of colloids typical for soils and sediments. The colloids (smectite, kaolinite, illite, goethite, hematite) were chosen to represent 1:1 and 2:1 layered aluminosilicate clays and sesquioxides, and were either obtained in pure form or synthesized in our laboratory. Colloids were deposited as thin films on glass slides, and then used for contact angle measurements using three different test liquids (water, formamide, diiodomethane). The colloidal films could be categorized into three types: (1) films without pores and with polar–liquid interactions (smectite), (2) films with pores and with polar–liquid interactions (kaolinite, illite, goethite), and (3) films without pores and no polar–liquid interactions (hematite). The static and dynamic sessile drop methods yielded the most consistent contact angles. For porous films, the contact angles decreased with time, and we consider the initial contact angle to be the most accurate. The differences in contact angles among the different methods were large and varied considerably: the most consistent contact angles were obtained for kaolinite with water, and illite with diiodomethane (contact angles were within 3°); but mostly the differences ranged from 10° to 40° among the different methods. The thin-layer and column wicking methods were the least consistent methods.

© 2008 Elsevier Inc. All rights reserved.

1. Introduction

The most common methods to determine contact angles are the sessile or pendant drop and the Wilhelmy plate methods. For porous materials, the wicking or capillary rise method is often used [1]. For spherical particles, methods have been developed to determine contact angles based on force measurements [2,3], confocal microscopy [4], and film trapping [5]. The contact angle of colloidal particles, however, is difficult to measure because the small particle size (<2 μm in diameter) poses considerable challenges with existing contact angle measurement methods.

Different methods have been described in the literature to determine contact angles of colloids. The sessile drop method can be used to measure static and dynamic contact angles of colloids. As the sessile drop method requires a flat surface upon which a liquid drop can be placed, colloids are often deposited as a film onto a microscope slide or filter paper [6–10]. Smooth films have been made with synthetic colloids, such as Latex microspheres [11], mineral colloids, such as smectites and hematite [9,

12], bacteria, such as *Pseudomonas cepacia* 3N3A, *Arthrobacter* sp., *Escherichia coli* [13,14], and viruses, such as hepatitis A [15]. Spherical, monodisperse particles, like microspheres are often used with the sessile drop method [11]. Among soil colloids, smectites are particularly suitable for the sessile drop method, because these clays are swelling, and form a water impermeable surface [9]. If the colloidal film is porous, then the liquid drop will penetrate into the film, and as a consequence the contact angle changes with time [9,16]. Kaolinite, for instance, forms a porous film, into which water readily infiltrates [9].

The sessile drop method has also been used to determine contact angles for soil particles. Bachmann and coworkers [17–19] used double-sided adhesive tape to mount a layer of powdered or sieved soil particles on a glass microscope slide. They determined static contact angles for different soil types, varying in texture, mineral and organic matter composition, and geographic origin [19].

The Wilhelmy plate method is commonly used for materials with a well-defined wetting length, so that the contact angle can be calculated from the measured capillary force. The Wilhelmy plate method has been used to determine contact angles of gold colloids [20] and soil materials [19,21], where the particles were deposited or glued to a flat plate, which was then used as the Wilhelmy plate.

* Corresponding author at: Department of Crop and Soil Sciences, Center for Multiphase Environmental Research, Washington State University, Pullman, WA 99164, USA. Fax: +1 509 335 8674.

E-mail address: flury@mail.wsu.edu (M. Flury).

Table 1
Characteristics of colloids.

Sample	Particle diameter ^a (nm)	Electrophoretic mobility ^a ($\mu\text{m s}^{-1}/(\text{V cm}^{-1})$)	ζ potential ^b (mV)	Particle shape ^c
Ca-smectite (SAz1)	1069 ± 198	-1.12 ± 0.01	-14.2 ± 0.1	Irregular thin flakes
Ca-kaolinite (KGa1b)	1280 ± 43	-0.24 ± 0.01	-3.0 ± 0.1	Hexagonal platy
Ca-illite (No. 36)	915 ± 181	-1.58 ± 0.05	-20.1 ± 0.6	Irregular platy
Goethite	1814 ± 38	2.10 ± 0.04	26.6 ± 0.6	Acicular
Hematite	146 ± 1	2.77 ± 0.02	35.2 ± 0.3	Spherical

± denotes one standard deviation.

^a Measured by dynamic light scattering at pH 6.0 and 0.1 mM CaCl₂ electrolyte background.

^b Calculated from the von Smoluchowski equation.

^c Determined by electron microscopy (SEM and TEM).

Table 2
Density, viscosity, air-liquid surface tension γ_L , and surface-tension components of test liquids at 20 °C. [γ_L^{LW} : Lifshitz-van der Waals component (apolar); γ_L^+ : electron-acceptor component (polar); γ_L^- : electron-donor component (polar)].

Liquid	Density (kg m ⁻³)	Dyn. viscosity (Ns m ⁻²)	γ_L (mJ m ⁻²)	γ_L^{LW} (mJ m ⁻²)	γ_L^+ (mJ m ⁻²)	γ_L^- (mJ m ⁻²)
Hexane	663 ^a	0.00029 ^a	18.4	18.4	0	0
Water	998	0.00100	72.8	21.8	25.5	25.5
Formamide	1130 ^a	0.00376 ^a	58.0	39.0	2.28	39.6
Diiodomethane	3320 ^a	0.00280 ^a	50.8	50.8	0	0

Surface tensions and surface tension components are from van Oss [8].

^a From J.T. Baker and Acros Organic.

For powdered or porous materials, contact angles are often determined with the column wicking method [8]. In this method, the speed of the capillary rise into the porous medium is measured, from which the contact angle can be determined. For successful use of the column wicking method, the geometry of the porous material should remain constant during the capillary rise. However, soil colloids, such as clay minerals, tend to cluster or shrink and swell, causing the pore structure to change.

To prevent this problem, colloidal particles can be deposited on a flat surface, forming a rigid thin layer of porous material [16,22]. This method is known as thin-layer wicking [16]. It has been used for a variety of particles, such as illite [16], kaolinite [9], attapulgite [9], talc [16,23], hydrotalcite [24], hematite [12], dolomite [23], calcite [23], basalt [25], limestone [25], silica [26,27], and feldspar [28]. Costanzo et al. [12] have shown that for cubic hematite particles, thin-layer wicking yields identical contact angles as the sessile drop method.

More recently, contact angle methods based on film and gel trapping [5,29], atomic force microscopy [3,30,31], and scanning confocal microscopy [4] have been developed. These methods are particularly useful for spherical particles in the micrometer size range, but less suitable for soil colloids, which have irregular shapes.

The determination of contact angles for soil colloids remains challenging, and no ideal method has yet been described. It is likely that different methods are optimal for different types of colloids. The objective of this paper was, therefore, to compare different methods to determine contact angles of soil colloids. We used the sessile drop, Wilhelmy plate, column wicking, and thin-layer wicking methods to determine contact angles of five major types of soil colloids (swelling and non-swelling aluminosilicate clays, and (hydr)oxides). We discuss advantages and disadvantages of the different methods, and make recommendations on the optimal methods for specific colloids.

2. Materials and methods

2.1. Soil colloids

We used five typical soil colloids: three aluminosilicate clays and two (hydr)oxides (Table 1). Arizona smectite (SAz1) and Geor-

gia kaolinite (KGa1b) were obtained from the Clay Minerals Repository (University of Missouri), and illite (No. 36, Morris, Illinois) was obtained from Ward's Natural Science (Rochester, NY). All the clays (smectite, kaolinite, illite), as received from the suppliers, were fractionated by gravity sedimentation to obtain particles smaller than 2 μm in diameter. Hematite and goethite were synthesized in our laboratory following Schwertmann and Cornell [32].

The fractionated clay minerals were treated with H₂O₂ to remove organic matter and the citrate-dithionite method was used to remove iron oxides. Then, to prevent Al³⁺ precipitation on the clay surfaces, the pH of the clay suspensions was lowered to about 4 by titration with 0.1 M HCl. The suspensions were shaken for 3 h, and the supernatant was decanted after centrifugation. This procedure was repeated three times. Finally, the clay suspensions were washed with deionized water. Deionized water was added, equilibrated for 3 h, and decanted after centrifugation. This washing procedure was repeated until the suspensions reached pH 6. Finally, the clay minerals were made homoionic and Ca-saturated by washing with 0.5 M CaCl₂, and dialyzed with deionized water until free from chloride [33,34]. All colloids were stored in concentrated suspensions at room temperature until use.

Average hydrodynamic particle size and electrophoretic mobility were measured by dynamic light scattering using a Zetasizer 3000HAS (Malvern Instruments Ltd., Malvern, UK). The particle shapes were determined by scanning and transmission electron microscopy (Hitachi S520 SEM, JEOL 1200EX TEM). Selected properties of the colloids are shown in Table 1.

2.2. Test liquids

Polar and apolar liquids were used for the contact angle measurements (Table 2): double deionized water (electrical conductivity 0.58 $\mu\text{S}/\text{cm}$, E-pure, Barnstead), formamide (99.5% purity, from Acros Organics, Morris Plains, NJ), diiodomethane (99% purity, from Acros Organics, Morris Plains, NJ), and hexane (100% purity, J.T. Baker, Phillipsburg, NJ). Hexane was used as the low energy liquid with contact angle of 0 degree, and was used to obtain the capillary constant for the wicking methods.

2.3. Sessile drop method (static and dynamic)

For the sessile drop method, a microscope cover glass slide (2.2 cm × 2.2 cm), cleaned with acetone and deionized water, was coated with colloids following the procedure described by Wu [9]. For the coating, concentrated colloid stock suspensions were first diluted with deionized water to a concentration of about 1–2% wt/vol, and stirred with a magnetic stir bar for several hours. Then, 1.5 mL suspension was placed on the microscope slide, evaporated for two days under laminar air flow, and finally dried in an oven at 105 °C for 12 h. Glass slides were kept horizontal during the drying process.

The contact angles were determined using a goniometer (Drop Shape Analysis System, DSA100, Krüss GmbH, Hamburg, Germany), equipped with an environmental chamber and a microsyringe steel needle of 0.5-mm diameter. The environmental chamber helped to minimize evaporation. For static contact angle measurements, the syringe needle was positioned 0.2 mm from the surface of the colloidal film, and a drop of the test liquid (2 µL) was dispensed at a rate 1.75 µL s⁻¹. After dispensing, the drop shape was monitored with a digital camera for 20 s, and contact angle, drop diameter, and volume were recorded. To determine the contact angle, the drop contour was mathematically described by the Young–Laplace equation using DSA100, and the contact angle was determined as the slope of the contour line at the three-phase contact point. For dynamic contact angle measurements, the drop volume was continuously increased and then decreased as contact angles were recorded. We used a liquid dispensation rate of 5 µL min⁻¹ to increase the drop volume from 0 to 5 µL (advancing contact angle), and then reversed the flow at the same rate to decrease the drop volume again (receding contact angle). The contact angle was taken as the average angle after the contact angle vs time curve had reached a plateau.

2.4. Wilhelmy plate method

For the Wilhelmy plate method, we coated a cleaned microscope cover glass on both sides with colloids. A 1.5-mL drop of 3% wt/vol colloid suspension was placed on the glass slides and evaporated for 12 h under laminar air flow. Then, the slide was turned over and the other side was coated with the same procedure. The slide was dried for two days under laminar flow and then heated in an oven at 105 °C for 12 h. With this procedure, the slide was completely covered with a thin film of colloids.

The contact angles were determined using a tensiometer (K100, Krüss GmbH, Hamburg, Germany). The wetted length of the coated slides was measured by a digital micrometer caliper (precision 0.01 mm). The slide was suspended from the electronic microbalance (precision 1 µg) and moved in and out of the test liquids at a speed of 1 mm min⁻¹. The force acting on the balance was continuously measured. Advancing and receding contact angles were obtained from immersion and emersion, respectively. The contact angle was calculated according to $\cos\theta = (F - F_b)/(P\gamma_L)$, where F is the measured vertical force (N), F_b is the buoyancy force (N), P is the wetted length (m), and γ_L is the surface tension of the test liquid (J m⁻²). The wetting length was measured with the caliper for each colloid-covered slide. The colloidal film remained stable on the glass slides during the contact time with the liquids (measurements lasted 10 min).

2.5. Thin-layer wicking method

For the thin-layer wicking method, we prepared thin films of colloids on a glass slide (2.4 cm × 4 cm), using the same procedure as described for the Wilhelmy plate method. Because the slide was

larger than the ones used for the Wilhelmy plate method, we used a 3 mL drop of colloid suspension.

The capillary constant was determined with hexane as the test fluid. Before the hexane measurements, the coated slides were equilibrated in a glass container with saturated hexane vapor for one hour to equalize the spreading pressure [9]. For the wicking, the slides were vertically dipped to a depth of 5 mm into the test liquids contained in a sealed cylindrical glass container to prevent evaporation. As soon as the slide was immersed into the liquid, the wicking height was recorded with a video camera (iSight, Apple Inc.). Recording was stopped when the wicking height was 2 cm. The Washburn equation was used to calculate contact angles [35]:

$$x^2 = \frac{R_{\text{eff}}\gamma_L \cos\theta}{2\eta} t \quad (1)$$

where x is the wicking distance (m) in the porous layer, t is time (s), R_{eff} is the effective pore radius (m) of the interparticle capillaries in the porous layer, γ_L is the surface tension of test liquid (J m⁻²), and η is the liquid viscosity (N s m⁻²).

2.6. Column wicking method

For the column wicking method, colloid suspensions were dried, ground into powders, and passed through sieves to obtain aggregates between 106 and 250 µm in diameter. Spherical glass beads (diameter of 120 µm) were used as standards. The sample holder was an aluminum tube with an inner diameter of 12 mm (Krüss GmbH, Hamburg, Germany). A 30-µm mesh membrane was placed into the sample holder to prevent the sample powder from falling out. Two grams of dry powder were placed into the sample holder with manual tapping (several times) to obtain uniform packing of the aggregates. The packing densities were 1.11 g cm⁻³ for smectite, 0.93 g cm⁻³ for kaolinite, 1.00 g cm⁻³ for illite, 0.50 g cm⁻³ for goethite, and 1.00 g cm⁻³ for hematite; the differences arose because of different particle densities, sizes, and shapes. After packing, the holder was placed onto the electronic balance of the tensiometer. The weight gain of the sample holder after contact with test liquids was recorded. The modified Washburn equation was used to calculate contact angles [36]: $w^2 = ct\rho^2\gamma_L \cos\theta/\eta$, where w is the weight increase of the column (kg), ρ is the liquid density (kg m⁻³), and c is the capillary constant (m⁵). The capillary constant c was determined using hexane as the test fluid.

2.7. Sample storage, measurement replication, and data reporting

After sample preparation as described for the individual methods above, the samples were stored in a desiccator until use for the contact angle measurements. Samples were taken out from the desiccator and used immediately. The relative humidity in the atmosphere during the measurements was 33%; except for the thin-layer wicking method, which was performed in a sealed cylinder, and the vapor pressure was therefore close to saturation.

All measurements were replicated 5 times, except the tensiometer measurements (Wilhelmy plate and column wicking method), which were replicated 3 times. Data are reported as means and standard deviations of the replicates. Statistical differences were analyzed at the 5% confidence level with a t -test.

3. Results and discussion

3.1. Colloid films

The thin colloid films prepared by deposition of colloids on the glass slides are shown in Fig. 1. The electron micrographs show that surface roughness varied among the films. Smectite, kaolinite,

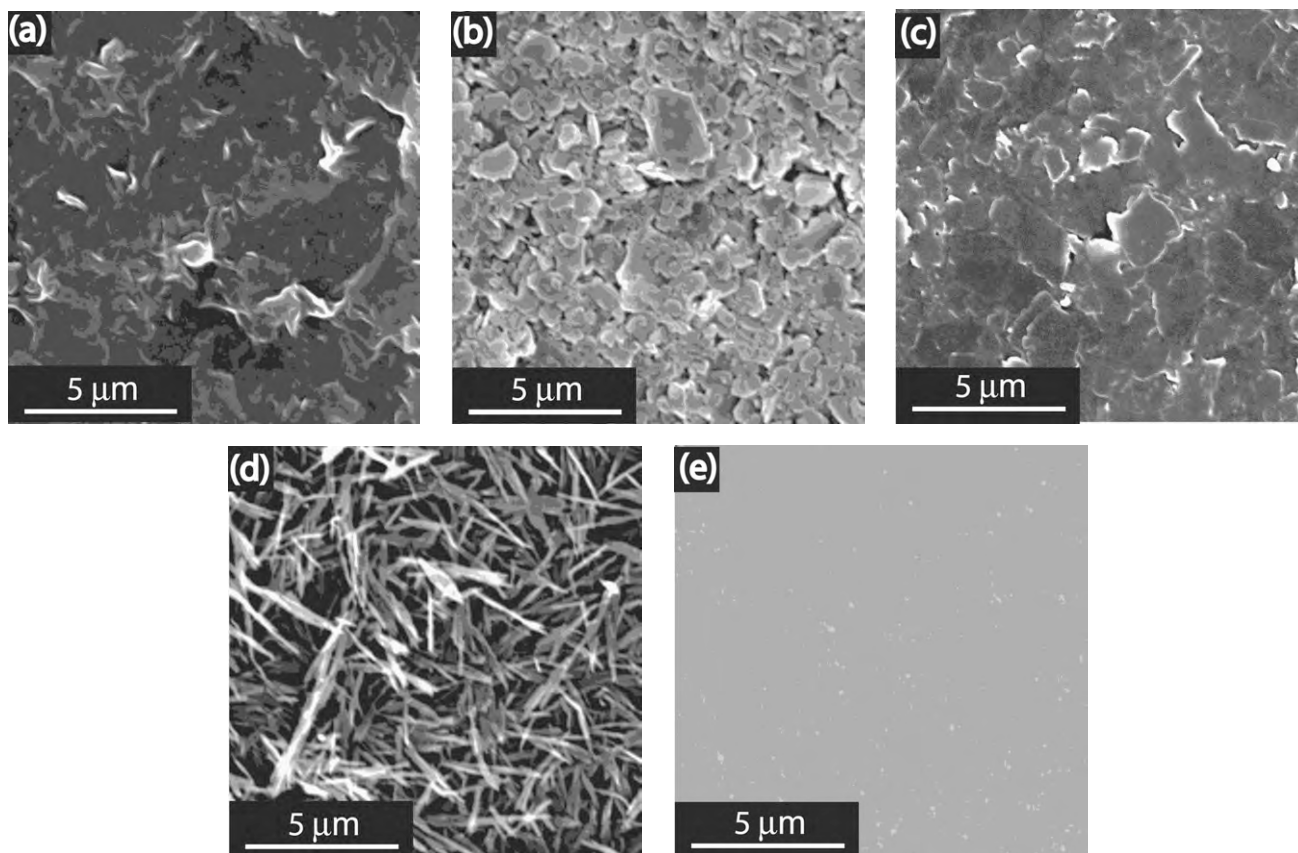


Fig. 1. Scanning electron micrographs of the film surfaces: (a) smectite, (b) kaolinite, (c) illite, (d) goethite, and (e) hematite.

illite, and goethite films all had considerable roughness, whereas the hematite surface appeared smooth at the scale of the micrographs. The smooth surface obtained for hematite was because of the small and spherical particle size of the hematite colloids (Table 1). Kaolinite, illite, and goethite surfaces show also the presence of pores.

3.2. Sessile drop method (static)

Fig. 2 shows the contact angles, drop diameters, and drop volumes determined as a function of time after the liquid drop was placed onto the colloid film. Only the data for smectite, kaolinite, and hematite are shown; illite and goethite patterns were similar to kaolinite, and are therefore not shown. Table 3 shows contact angles at three time intervals for all colloids.

For smectite, contact angles of water and formamide decreased and drop diameters increased with time, whereas the drop volumes remained constant (Fig. 2). Contact angles, drop diameters, and drop volumes of diiodomethane remained constant. The constant drop volume indicates that there was no penetration of liquid into the colloid film. Smectite swells in contact with water and in the process seals the film surface [9]. The decreasing contact angles of the polar liquids, water and formamide, may be explained by hydration [37] and polar (acid–base) interactions [38].

For kaolinite the liquid drops infiltrated into the pores of the colloid film, as indicated by the decrease in drop volume (Fig. 2). As the drop volume decreased, the drop diameter for water and formamide increased, and the contact angle decreased. The increase in drop diameter was caused by two processes: (1) polar (acid–base) interactions between the solid and the polar liquids, and (2) drop imbibition into the pores of the colloid film. The former process is similar to what was observed for smectite. The latter process, however, causes false contact angle readings, as the

shape of the liquid–gas interface changes because of the imbibition. Correct contact angle readings should therefore be done at 0 s, i.e., before imbibition begins. The use of a digital goniometer, such as the Krüss Drop Shape Analysis System, allows to determine the contact angle immediately when the drop is placed on the substrate, so that accurate readings at 0 s can be made. For diiodomethane, the drop volume also decreased, but at a much lower rate than compared to water and formamide. The colloid film imbibed the diiodomethane, but the imbibition was slow because of the high fluid viscosity. Illite and goethite showed very similar behavior to kaolinite (Table 3).

Contact angles for kaolinite and smectite with water were reported in the literature. Reported values for the sessile drop method range from 17.4° to 34° and 21.8° to 42.5° for kaolinite and smectite, respectively [9,39–42].

For hematite, contact angles, drop diameters, and drop volumes remained constant during the 20-s measurement period (Fig. 2). This indicates that there were no interactions or imbibition of liquid into the colloid film. We believe that this was because of the spherical shape of the hematite particle, which formed a non-porous film with a periodical surface roughness. Contact angles for hematite reported in the literature vary considerably. This is likely due to different types of hematite used in different studies. Values reported for cuboid hematite by Costanzo [12] are generally smaller than our values.

Based on the experimental results, we can distinguish three types of mechanisms during contact angle measurements with soil colloids. For swelling films, like smectite, the colloid film seals itself when in contact with a polar liquid, but acid–base interactions can cause the drop shape to change with time. The contact angle change with time reflects the modification of the surface with time. For non-swelling, porous films, such as kaolinite, illite, and goethite, the drop shape changes because of both acid–base inter-

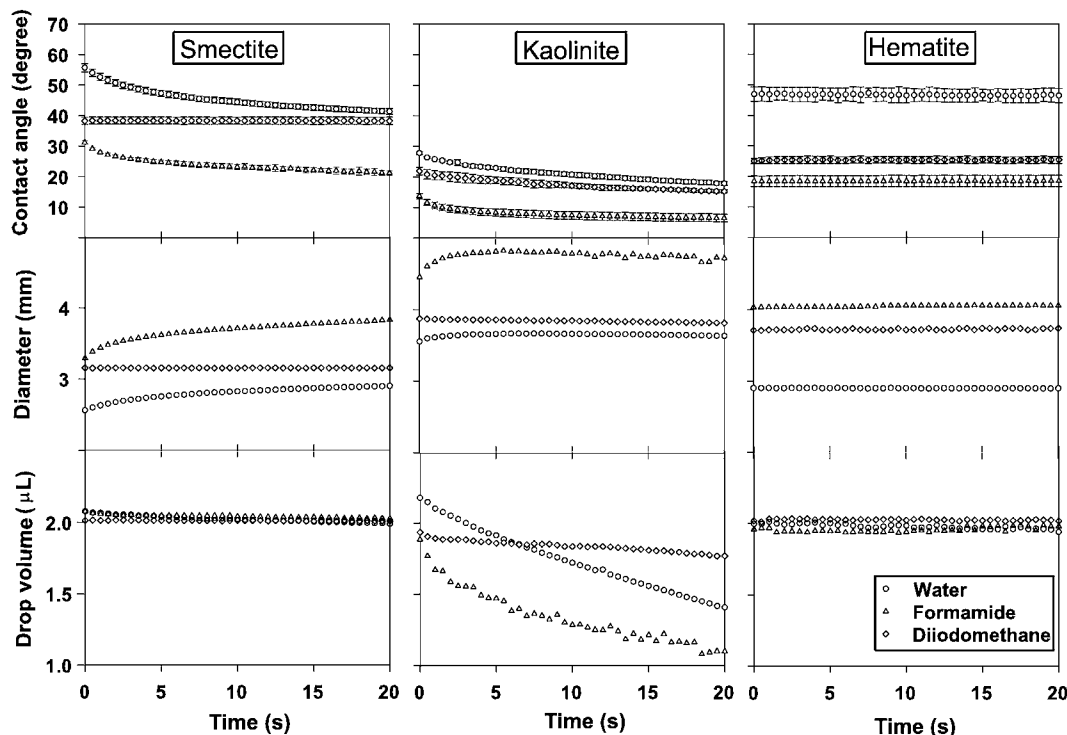


Fig. 2. Contact angles, drop diameters, and drop volumes as a function of time determined with static sessile drop method. Error bars (only shown for contact angles) indicate standard deviations of five measurements.

Table 3 Contact angles of subsurface colloids determined using static sessile drop method.

Subsurface colloids	Time (s)	Contact angle		
		Water (degree)	Formamide (degree)	Diiodomethane (degree)
Ca-smectite	0	55.7 ± 1.4	31.2 ± 0.6	38.3 ± 1.2
	10	44.5 ± 0.9	23.2 ± 0.9	38.3 ± 1.1
	20	41.4 ± 0.9	21.2 ± 0.8	38.3 ± 1.2
Ca-kaolinite	0	27.8 ± 0.4	13.7 ± 0.9	21.9 ± 1.3
	10	20.8 ± 0.8	7.4 ± 1.3	17.1 ± 0.9
	20	17.8 ± 0.6	6.5 ± 1.2	15.3 ± 0.5
Ca-illite	0	43.3 ± 0.3	21.1 ± 0.7	30.8 ± 1.4
	10	31.9 ± 1.1	17.4 ± 1.8	30.0 ± 1.6
	20	29.3 ± 1.3	16.8 ± 1.5	29.6 ± 1.6
Goethite	0	22.8 ± 1.8	24.1 ± 1.0	19.4 ± 0.4
	10	0 ± 0	15.3 ± 3.0	12.8 ± 0.1
	20	0 ± 0	0 ± 0	8.1 ± 0.4
Hematite	0	46.9 ± 2.3	18.5 ± 1.7	25.0 ± 0.8
	10	46.5 ± 2.4	18.5 ± 1.8	25.5 ± 1.0
	20	46.4 ± 2.4	18.5 ± 1.8	25.4 ± 1.1

± denotes one standard deviation of 5 replicates.

actions and imbibition, thereby causing false contact angle readings after the initial drop has been put on the colloid film surface. Because of interactions and imbibition, the most accurate contact angle should be the initial contact angle. For a non-swelling, non-porous films, such as hematite, the drop shape remains stable over time.

3.3. Sessile drop method (dynamic)

The dynamic sessile drop method can provide advancing and receding contact angles as a function of time. We again only show the data for smectite, kaolinite, and hematite, as illite and goethite showed similar behavior as kaolinite (Fig. 3). The dashed lines in

the figure separate increasing from decreasing drop volume, as controlled by the liquid supply syringe.

For smectite, as the drop volume of water and formamide increased, the contact angles initially decreased and reached a plateau (Fig. 3a). This plateau represents the mean advancing contact angle [43]. For diiodomethane, the contact angle was constant because there were no interactions with the solid surface. When the drop volume was decreased after 60 s, the drop diameters for formamide still increased, and then decreased. Receding contact angles decreased for all three liquids, and did not reach a constant value. For water and diiodomethane, the drop diameter remained constant, indicating a non-slip boundary at the air-liquid-solid interface [44], which will cause the contact angle to continuously decrease as fluid is withdrawn from the drop.

For kaolinite, the advancing contact angles were fairly constant for the three liquids (Fig. 3b). The diameters of the liquid drop increased when the drop volume increased, and remained constant for a few seconds after flow was reversed, and then decreased quickly. The colloid film imbibed all three liquids, but the rate of imbibition was much smaller than the rate of drop volume increase, therefore, the imbibition had negligible effect, and the advancing contact angles remained constant.

For hematite, the drop diameters for water and formamide remained initially constant when the drop volume was increased, but the contact angles increased at a high rate (Fig. 3c). When the drop size exceeded a critical limit, the drop diameter jumped to a new position, and remained constant again. This led to a typical slip/stick pattern of the advancing contact angle [44–46]. The slip/stick pattern was bounded by a lower and upper critical contact angle, and the range was larger for water than for formamide. No distinct slip/stick pattern was observed for diiodomethane. The different behavior among the three liquid drops can be explained by their different Bond numbers: the water drop had the smallest Bond number ($Bo = 37$), and could keep its shape better than the formamide drop ($Bo = 46$), and the diiodomethane drop ($Bo = 184$).

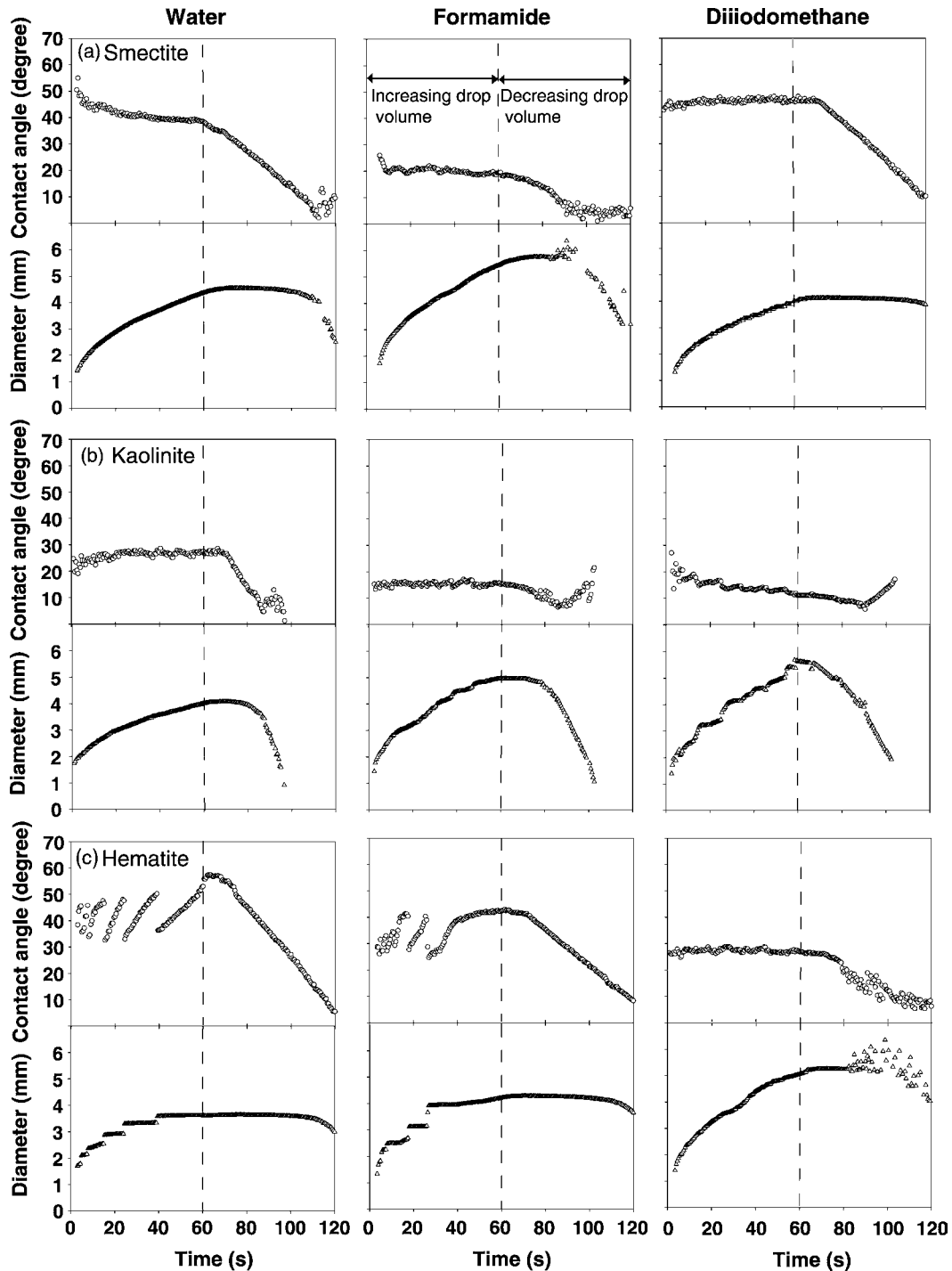


Fig. 3. Dynamic contact angles and drop diameters of test liquids as a function of time determined by the dynamic sessile drop method: (a) smectite, (b) kaolinite (illite and goethite were similar to kaolinite), (c) hematite. Dashed lines separate increasing from decreasing drop volume.

3.4. Wilhelmy plate method

From the Wilhelmy plate method, both advancing and receding contact angles can be obtained by immersion and emersion of the coated colloid films. The forces measured as a function of immersion depth for complete immersion–emersion loops were used to construct force–distance curves. Only the linear portions of the force curves were used to calculate the contact angles. The force curves show a distinct contact angle hysteresis, with the advancing contact angles always larger than the receding ones (Table 4). The largest hysteresis was observed for smectite and hematite

with water. We attribute this pronounced contact angle hysteresis to swelling behavior (smectite) and surface roughness (hematite). Hematite has the most pronounced surface roughness in the sense of a periodic arrangement of its spherical particles, leading to both acute and obtuse angles, which causes pronounced contact angle hysteresis.

For kaolinite, illite, and goethite, the receding contact angles were zero for all liquids (Table 4). Zero-degree receding contact angles were also reported by Bachmann et al. [19], who measured contact angles of soil particles (diameter < 0.063 or 2 mm) with the Wilhelmy plate method. The zero-degree contact angles are

Table 4

Contact angles of test liquids for subsurface colloids using static sessile drop, dynamic sessile drop, Wilhelmy plate, and thin-layer wicking methods.

Subsurface colloids	Contact angles (degree)		
	Water	Formamide	Diiodomethane
Static sessile drop method (equilibrium contact angle)			
Ca-smectite	55.7 ± 1.4 A	31.2 ± 0.6 A	38.3 ± 1.2 A
Ca-kaolinite	27.8 ± 0.4 A	13.7 ± 0.9 A	21.9 ± 1.3 A
Ca-illite	43.3 ± 1.4 A	21.1 ± 0.7 A	30.8 ± 1.4 A
Goethite	22.8 ± 1.9 A	24.1 ± 1.0 A	19.4 ± 0.4 A
Hematite	46.9 ± 2.3 A	18.5 ± 1.7 A	25.0 ± 0.8 A
Dynamic sessile drop method (advancing contact angle)			
Ca-smectite	41.9 ± 2.5 B	17.2 ± 1.4 B	46.9 ± 0.7 B
Ca-kaolinite	26.2 ± 2.0 A	14.9 ± 3.6 A,B	10.8 ± 1.9 B
Ca-illite	24.0 ± 3.2 B	13.8 ± 1.6 B	32.4 ± 3.2 A
Goethite	25.0 ± 2.9 A	41.2 ± 4.8 B	13.8 ± 0.8 B
Hematite	42.5 ± 11.4 A	35.4 ± 8.3 B	26.4 ± 1.6 A
Wilhelmy plate method (advancing contact angle)			
Ca-smectite	57.1 ± 2.5 A	34.7 ± 2.1 A	50.9 ± 0.6 B,D
Ca-kaolinite	27.3 ± 1.3 A	11.1 ± 0.9 A	20.8 ± 1.9 A
Ca-illite	30.0 ± 0.4 C	20.0 ± 1.7 A	30.6 ± 2.0 A
Goethite	14.2 ± 2.4 B	17.8 ± 1.4 C	8.7 ± 2.3 B
Hematite	71.7 ± 2.0 B	42.3 ± 1.0 C	35.5 ± 0.6 B
Wilhelmy plate method (receding contact angle)			
Ca-smectite	9.9 ± 2.3 C	5.3 ± 1.0 C	25.6 ± 1.7 C
Ca-kaolinite	0 B	0 C	0 C
Ca-illite	0 D	0 C	0 B
Goethite	0 C	0 D	0 C
Hematite	32.3 ± 1.1 C	5.8 ± 0.7 D	23.4 ± 0.4 C
Thin-layer wicking method (advancing contact angle)			
Ca-kaolinite	29.3 ± 2.2 A	19.8 ± 0.3 B	52.0 ± 3.1 D
Ca-illite	56.8 ± 3.4 E	39.1 ± 5.5 D	34.2 ± 4.9 A
Goethite	34.1 ± 3.4 D	20.9 ± 1.8 A	46.7 ± 2.9 D

± denotes one standard deviation of 5 replicates (except for Wilhelmy plate method, where 3 replicates were used). Letters (A, B, C, D, E) denote statistical difference column-wise for identical colloids; if letters are different between two methods, then there is a significant difference at the 5% confidence level between the methods.

likely caused by imbibition of liquid into the porous films or aggregates during plate immersion. The Wilhelmy plate method has successfully been used to determine contact angles for other types of colloidal and porous materials, such as gold colloids [20] and soil particles [19,21].

The Wilhelmy plate method generally leads to an underestimation of the advancing contact angle when the plate surface is rough, because the effective plate perimeter is larger than that determined by a caliper [47]. For our colloids, we cannot quantify the magnitude of this error, because we do not have a quantitative measure of the surface roughness.

3.5. Thin-layer wicking method

We chose kaolinite, illite, and goethite as the samples for the thin-layer wicking clay, because the films formed by these colloids have microporous characteristics (Fig. 1). Smectite and hematite films, which swell and have no microporosity, respectively, cannot be used for the thin-layer wicking. Results for kaolinite, illite, and goethite are shown in Fig. 4 and Table 4.

The experimental data follow the theoretical trend given by Eq. (1) (Fig. 4), indicating that the thin-layer wicking method was suited to calculate the contact angles. The effective pore sizes R_{eff} of kaolinite, illite, and goethite were 233, 173, and 387 nm, which are all smaller than the particle diameters (Table 1). This is a consequence of the platy and rodlike particle shape of the colloids, which upon deposition orient themselves in a thin film, causing the pore size to become smaller than the particle size [24]. To show that the glass slide itself did not affect the liquid wicking speed, we peeled off the thin colloidal film from the glass slide

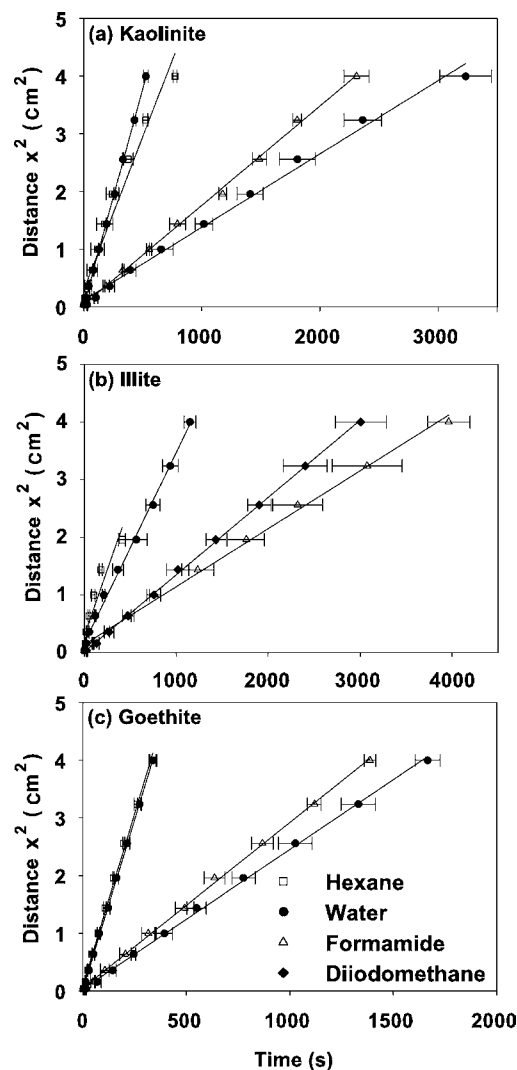


Fig. 4. Wicking distance squared versus time for different test liquids using thin-layer wicking: (a) kaolinite, (b) illite, (c) goethite. The lines are linear trendlines of the form $x^2 = at$, where a is a fitting parameter given as $a = (R_{\text{eff}})^2 \cos^2 \theta / (2\eta)$. Error bars indicate standard deviations of three measurements.

(this could only be done for illite, the other colloidal films broke apart when attempting to peel them off). The wicking results with the illite film alone were identical to the ones with the illite film on the glass slide. This confirmed that the glass slide itself did not affect the measurement.

The contact angles obtained from the thin-layer wicking method (Table 4) are different than those reported in the literature. For kaolinite and the thin-layer wicking method, Wu [9] reported contact angles of 46.1° for water, 27.2° for formamide, and 34.5° for diiodomethane. For illite and goethite, we did not find literature data. The values reported by Wu [9] are larger than ours, likely because Wu [9] did not pretreat their kaolinite (no removal of organic matter and iron oxides).

3.6. Column wicking method

Fig. 5a shows the results for three replicates of the glass bead measurements with hexane to check the method performance. Three stages can be distinguished in the weight-time curves [48]: in stage 1, at very short times, the bottom boundary of the sample holder affects the measurements; in stage 2, interparticle pores are filled, and a linear increase of the weight-time curve is obtained; in stage 3, the pore space is either completely filled, resulting in a

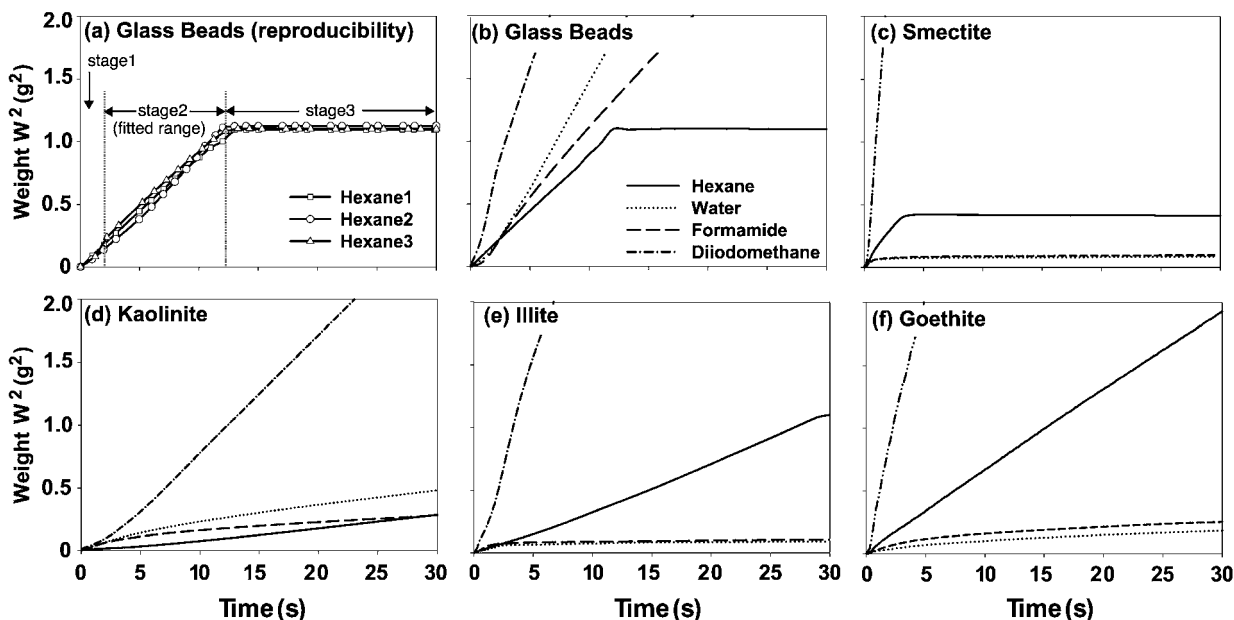


Fig. 5. Capillary rise curves, wicking weight versus time for different test liquids using the column wicking method: (a) glass beads in hexane (reproducibility), (b) glass beads, (c) smectite, (d) kaolinite, (e) illite, and (f) goethite.

cease of the weight gain, or intraparticle pores begin to fill, resulting in a non-linear weight-time response. For our glass beads, no intraparticle pores were present, and we obtained an ideal weight-time response for hexane (Fig. 5a) as well as for the other fluids (Fig. 5b).

For the soil colloids, however, most of the time no distinct stage 2 could be identified (Figs. 5c–5f), and therefore, no contact angles could be calculated. The pore structure of the packed soil colloids changed as the fluid was imbibed, thereby, invalidating the assumptions inherent in the Washburn equation. Colloids dispersed in water and formamide and, in addition, smectite swelled. Thin-layer wicking, on the other hand, was better suited for contact angle measurements because the colloids on the plates formed a more rigid porous structure, and did not easily disperse [1].

Column wicking data for natural hematite data reported in the literature for water (contact angle = 46°) [49] were very similar to our sessile drop data of 46.9° . Nonetheless, the column wicking method should be used with caution. In addition to the change in pore structure, the column wicking method has the disadvantage that it requires the validity of the Young equation. This requirement may not be fulfilled for all liquid–solid combinations. The same potential shortcoming regarding the Young equation applies also for the thin-layer wicking method.

3.7. Comparison of contact angles

The contact angle measurements are affected by many factors (e.g., temperature, relative humidity, solid surface roughness, surfaces preparation, sample pretreatment). It is therefore not surprising that a large variation of contact angles for soil colloids is reported in the literature.

The contact angles obtained from the different methods in our study are summarized in Table 4. The data show that there were considerable differences in the contact angles determined using the different methods. The best agreements among the different methods were obtained with kaolinite (except for diiodomethane). For water, the static and advancing contact angles with kaolinite were within 3° for the different methods, and no significant differences were observed (Table 4). For formamide, the static and advancing contact angles with kaolinite were within 9° and, except

for the thin-layer wicking, the angles were again not statistically different. Larger differences were observed for diiodomethane.

The other colloids generally showed large differences among methods, but the differences among the methods and the colloids were not consistent. For instance, for smectite, the static sessile drop and the Wilhelmy plate method (advancing) gave similar contact angles with water and formamide; but for illite, goethite, and hematite, these two methods gave significantly different contact angles (Table 4). For illite, goethite, and hematite, no consistent patterns among different methods were observed. Differences in contact angles among the methods ranged from 20° to 33° for water, 20° to 25° for formamide, and 4° to 40° for diiodomethane (Table 4).

The thin-layer wicking method often produced contact angles that deviated considerably from those determined from other methods (Table 4). Although thin-layer wicking has been frequently used for powders [9,25–27], it appears that for our soil colloids, its suitability is limited. The column-wicking method was also not suited for contact angle measurement; similar observations were reported by others using powdered liposomes [50], microporous membranes [51], and soil materials [19,48].

Contact angles determined with a single method usually showed a standard deviation of up to about 3 degrees (Table 4), so the precision of the individual methods was good. However, the inter-method variability was often much larger than the intra-method variability. Thus, whereas the precision of a single method was good, the method may not provide accurate results. The optimal (most accurate) method for a given colloid has to be determined on a case by case basis.

Based on all our measurements, and requiring that at least two methods should give similar contact angles, we can make the following recommendations for water (Table 5). For kaolinite, all methods except column wicking were suitable and gave similar results. For smectite, the static sessile drop and the Wilhelmy plate method are recommended. For illite, all methods gave significantly different results, but dynamic sessile drop and Wilhelmy plate methods gave the most similar contact angles. For goethite and hematite, static and dynamic sessile drop methods are recommended.

Table 5

Recommended contact angle measurement methods for subsurface colloids with water.

Subsurface colloid	Contact angle measurement method				
	Static sessile drop	Dynamic sessile drop	Wilhelmy plate	Thin-layer wicking	Column wicking
Ca-smectite	×	○	×	○	○
Ca-kaolinite	×	×	×	×	○
Ca-illite	○	×	×	○	○
Goethite	×	×	○	○	○
Hematite	×	×	○	○	○

× denotes recommended method.

○ denotes not recommended method.

4. Conclusions

Our results showed that large differences can exist between contact angles of soil colloids measured with different methods. Given the large differences among measurement methods, it is important to report contact angle always together with its detailed measurements methods. Based on our systematic comparison of different methods, we can recommend specific methods for typical soil colloids (Table 5).

In terms of the contact angles themselves, our data show that soil colloids generally have fairly large contact angles (equilibrium and advancing): kaolinite and goethite had a contact angle of about 25°, smectite 40° to 50°, illite 25° to 45°, and hematite 45°. There was a pronounced contact angle hysteresis—receding contact angles were 10° for smectite, 32° for hematite, 0° for kaolinite, illite, and goethite. Under natural subsurface conditions, colloids are often coated with organic matter, which will make their contact angles larger than the ones reported here.

Acknowledgment

This research was supported in part by the Office of Science (BER), US Department of Energy, Grant No. DE-FG02-08ER64660.

References

- [1] E. Chibowski, R. Perea-Carpio, *Adv. Colloid Interface Sci.* 98 (2002) 245.
- [2] L. Zhang, L. Ren, S. Hartland, *J. Colloid Interface Sci.* 180 (1996) 493.
- [3] M. Preuss, H.J. Butt, *J. Colloid Interface Sci.* 208 (1998) 468.
- [4] R. Mohammadi, A. Amirfazli, *J. Dispersion Sci. Technol.* 25 (2004) 567.
- [5] A. Hadjiiski, R. Dimova, N.D. Denkov, I.B. Ivanov, R. Borwankar, *Langmuir* 12 (1996) 6665.
- [6] C.J. van Oss, C.F. Gillman, *J. Reticuloendothel. Soc.* 12 (1972) 283.
- [7] C.J. van Oss, C.F. Gillman, *J. Reticuloendothel. Soc.* 12 (1972) 497.
- [8] C.J. van Oss, *Interfacial Forces in Aqueous Media*, second ed., CRC Press, New York, 2006.
- [9] W. Wu, *Clays Clay Miner.* 49 (2001) 446.
- [10] R.F. Giese, C.J. van Oss, *Colloid and Surface Properties of Clays and Related Minerals*, CRC Press, Oxford, 2002.
- [11] J.M. Wan, J.L. Wilson, *Water Resour. Res.* 30 (1994) 857.
- [12] P.M. Costanzo, W. Wu, R.F. Giese, C.J. van Oss, *Langmuir* 11 (1995) 1827.
- [13] J.M. Wan, J.L. Wilson, T.L. Kieft, *Appl. Environ. Microbiol.* 60 (1994) 509.
- [14] N.I. Abu-Lail, T.A. Comesano, *Colloids Surf. B* 51 (2006) 62.
- [15] I. Kukavica-Ibrulj, A. Darveau, J. Jean, I. Fliss, *J. Appl. Microbiol.* 97 (2004) 923.
- [16] C.J. van Oss, R.F. Giese, Z. Li, K. Murphy, J. Norris, M.K. Chaudhury, R.J. Good, *J. Adhesion Sci. Technol.* 6 (1992) 413.
- [17] J. Bachmann, R. Horton, R.R. Van der Ploeg, S. Woche, *Soil Sci. Soc. Am. J.* 64 (2000) 564.
- [18] J. Bachmann, A. Ellies, K.H. Hartge, *J. Hydrol. (Amsterdam)* 231 (2000) 66.
- [19] J. Bachmann, S.K. Woche, M.O. Goebel, *Water Resour. Res.* 39 (2003) 1353, doi:10.1029/2003WR002143.
- [20] K. Abe, H. Takiguchi, K. Tamada, *Langmuir* 16 (2000) 2394.
- [21] S.K. Woche, M.O. Goebel, M.B. Kirkham, R. Horton, R.R. Van der Ploeg, J. Bachmann, *Eur. J. Soil Sci.* 56 (2005) 239.
- [22] R.F. Giese, P.M. Costanzo, C.J. van Oss, *Phys. Chem. Miner.* 17 (1991) 611.
- [23] W. Wu, J.R.F. Giese, C.J. van Oss, *Powder Technol.* 89 (1996) 129.
- [24] Z. Li, R.F. Giese, C.J. van Oss, *Langmuir* 10 (1994) 330.
- [25] P. Teixeira, J. Azeredo, R. Oliveira, E. Chibowski, *Colloids Surf. B* 12 (1998) 69.
- [26] E. Chibowski, L. Holysz, *Langmuir* 8 (1992) 710.
- [27] E. Chibowski, F. González-Caballero, *Langmuir* 9 (1993) 330.
- [28] C. Karagüzel, M.F. Can, E. Sónmez, M.S. Celik, *J. Colloid Interface Sci.* 285 (2005) 192.
- [29] V.N. Paunov, *Langmuir* 19 (2003) 7970.
- [30] M. Preuss, H.J. Butt, *Langmuir* 14 (1998) 3164.
- [31] M. Preuss, H.J. Butt, *Int. J. Miner. Process.* 56 (1999) 99.
- [32] U. Schwertmann, R.M. Cornell, *Iron Oxides in the Laboratory: Preparation and Characterization*, VCH, Weinheim, 1991.
- [33] M. Chorom, P. Rengasamy, *Eur. J. Soil Sci.* 46 (1995) 657.
- [34] J. Jerez, M. Flury, J. Shang, Y. Deng, *J. Colloid Interface Sci.* 294 (2006) 155.
- [35] E. Washburn, *Phys. Rev.* 17 (1921) 273.
- [36] A. Siebold, A. Walliser, M. Nordin, M. Oppliger, J. Schultz, *J. Colloid Interface Sci.* 186 (1997) 60.
- [37] M.B. McBride, in: J.B. Dixon, S.B. Weed (Eds.), *Minerals in the Soil Environment*, Soil Science Society of America, Madison, WI, 1989, pp. 35–88.
- [38] C.J. van Oss, *Interfacial Forces in Aqueous Media*, Marcel Dekker, New York, 1994.
- [39] B. Janczuk, T. Bialopiotrowicz, *Clays Clay Miner.* 36 (1988) 243.
- [40] P.M. Costanzo, R.F. Giese, C.J. van Oss, *J. Adhesion Sci. Technol.* 4 (1990) 267.
- [41] J. Norris, R.F. Giese, C.J. van Oss, P.M. Costanzo, *Clays Clay Miner.* 40 (1992) 327.
- [42] J.M. Breiner, M.A. Anderson, H.W.K. Tom, R.C. Graham, *Clays Clay Miner.* 54 (2006) 12.
- [43] C.N.C. Lam, N. Kim, D. Hui, D.Y. Kwok, M.L. Hair, A.W. Neumann, *Colloids Surf. Physicochem. Eng. Aspects* 189 (2001) 265.
- [44] C.N.C. Lam, R. Wu, D. Li, M.L. Hair, A.W. Neumann, *Adv. Colloid Interface Sci.* 96 (2002) 169.
- [45] D.Y. Kwok, R. Lin, M. Mui, A.W. Neumann, *Colloids Surf. Physicochem. Eng. Aspects* 116 (1996) 63.
- [46] D.Y. Kwok, C. Lam, A. Li, A. Leung, R. Wu, E. Mok, A.W. Neumann, *Colloids Surf. Physicochem. Eng. Aspects* 142 (1998) 219.
- [47] G. Buckton, P. Darcy, D. McCarthy, *Colloids Surf. Physicochem. Eng. Aspects* 95 (1995) 27.
- [48] M. Goebel, J. Bachmann, S.K. Woche, W.R. Fischer, R. Horton, *Soil Sci. Soc. Am. J.* 68 (2004) 383.
- [49] U. Akdemir, *Powder Technol.* 94 (1997) 1.
- [50] R.D. Tejas, L. Dongqing, H.F. Warren, P.W. Jonathan, *Colloids Surf. Biointerfaces* 22 (2001) 107.
- [51] J. Tröger, K. Lunkwitz, K. Grundke, W. Burger, *Colloids Surf. Physicochem. Eng. Aspects* 134 (1998) 299.